

# 3D diffractive optics for linear interconnects and nonlinear processing

Présentée le 25 janvier 2024

Faculté des sciences et techniques de l'ingénieur  
Laboratoire d'optique  
Programme doctoral en photonique

pour l'obtention du grade de Docteur ès Sciences

par

**Niyazi Ulaş DINÇ**

Acceptée sur proposition du jury

Prof. I.-C. Benea-Chelmus, présidente du jury  
Prof. D. Psaltis, Prof. C. Moser, directeurs de thèse  
Prof. A. Ozcan, rapporteur  
Prof. S. Gigan, rapporteur  
Prof. R. Fleury, rapporteur



*“To oppose something is to maintain it.  
They say here “all roads lead to Mishnory.” To be sure, if you turn your back on Mishnory and walk  
away from it, you are still on the Mishnory road.  
To oppose vulgarity is inevitably to be vulgar.  
You must go somewhere else;  
you must have another goal;  
then you walk in a different road.”*

— Ursula K. Le Guin, *The Left Hand of Darkness*



# Acknowledgements

I would like to express my sincere gratitude to my thesis directors, Prof. Demetri Psaltis and Prof. Christophe Moser, for the incredible opportunity to conduct research at EPFL. Their extensive knowledge across a range of subjects, coupled with their encouragement to explore these areas creatively, has provided me the liberty to pursue fascinating research directions. I deeply appreciate all your support. Special thanks go to Prof. Psaltis for initially welcoming me into his lab and for our collaborative work since my master's studies. I would also like to extend my sincere thanks to Prof. Daniel Brunner and Prof. Xavier Porte for our collaboration on the (3+1)D printing project.

I am grateful to the members of my thesis committee: Prof. Ileana-Cristina Benea-Chelms, Prof. Romain Fleury, Prof. Aydoğın Özcan, and Prof. Sylvain Gigan. Their time, effort, and insightful comments during my thesis examination have been invaluable.

I extend my thanks to all past and present members of the Laboratory of Optics and Laboratory of Applied Photonics Devices: Ye Pu, Mohammad Hashemi, Navid Borhani, Steven Schenk, Ioakeim Sioutis, Elizabeth Antoine, Pooria Hadikhani, Ahmed Bassam Ayoub, Amirhossein Saba, Kyriakos Skarsoulis, Jorge Madrid Wolff, Qianyi Zhang, Viola Sgarminato, Buse Ünlü, Maria Castano, Felix Wechsler, Victoria Fay, as well as our administrative support, Silke Jan and Sabrina Martone, for their contributions and camaraderie.

Special thanks are extended to Eirini Kakkava, my supervisor during my master's studies, whose guidance in optical experiment setups has been invaluable to my academic journey. I am also grateful to Joowon Lim for his assistance with coding and valuable insights into "Learning Tomography". My gratitude extends to Giulia Panusa, my office neighbor, with whom I shared both work and struggles in additive manufacturing, and to Carlo Gigli, who took over the Italian corner and maintained the spirit of fun in our office. Heartfelt thanks to Leo Jih-Liang Hsieh, a kind and helpful colleague and office mate. Special thanks to Uğur Teğın, whose insightful discussions, both scientific and beyond, have enriched my research experience. Lastly, I owe special thanks to İlker Oğuz and Mustafa Yıldırım, whose close collaboration was not only fruitful but also brought a great deal of fun to our work.

I am grateful to my friends in Lausanne for the unforgettable moments we shared in Switzerland. I would also like to express my appreciation to my former colleagues from the Electrical Engineering Department at ODTÜ: Onur Külahlıođlu, Giray Efe, Ufuk Efe, and Mertcan Erdil. Additionally, I extend my gratitude to my former flatmates in Ankara, Berken Ayebe, Emre Sepici, and Zeynep Uğur, for the invaluable time we spent together.

A heartfelt thank you goes to Şilan Şahan, my partner in crime, for her enduring support and constant presence throughout this journey, always finding ways to bring laughter into my life. I owe her immensely, not just for the love and patience she has shown, but also for her influential role in my life, including her suggestion of the Ursula Le Guin quote that graces the front of my thesis. I also extend my gratitude to our little roommates, our cats, Zen, Ganja, and Gaia, for their conditional, which is cat-minded, support and love.

Finally, I must express my deepest gratitude to my parents, Celalettin Dinç and Fatma Dinç, and my brother, Deniz Dinç. Words cannot fully express my appreciation for their unconditional support and love throughout my life.

Lausanne, December 2023

Niyazi Ulaş Dinç



# Abstract

The optical domain presents potential avenues for enhancing both computing and communication due to its inherent properties of bandwidth, parallelism, and energy efficiency. This research focuses on harnessing 3-Dimensional (3D) diffractive optics for novel interconnect schemes as well as a nonlinear processing technique based on multiple scattering and representation of the input data multiple times.

The initial discussion of this thesis revolves around the importance of 3D techniques for optical circuits. Transformations between 3D and 2D domains, vital in fields like optical tomography, additive manufacturing, and optical memory storage, are elaborated upon with a perspective of 3D optical circuit design. First, we use additive manufacturing at the micro-scale to create multilayered diffractive volume elements. The concept of Learning Tomography, which is a method to reconstruct 3D objects from 2D projections, is introduced as an inverse design approach to calculate these elements. Subsequently, we introduce the (3+1)D printing, a term we coined. This method facilitates the fabrication of graded-index optical devices, such as volume holograms and optical waveguides. A notable aspect of this technique is its capacity to produce volume holograms with a linear diffraction efficiency relation, breaking  $1/M^2$  limit. The research then examines the application of commercial spatial light modulators for constructing reconfigurable interconnect devices at a larger scale. By combining free space diffraction principles with repetitive wavefront shaping, we potentially offer enhanced connectivity between nodes in data center networks. The following section delves into the nonlinear characteristics found in opto-electronic systems where the optical part is solely linear. These nonlinearities are namely phase encoding, data detection, and multiple scattering. A theoretical framework is constructed for computing enabled by these transformations. We conclude by a multilayer diffractive optical network mimicking digital deep neural networks. The research posits that by utilizing multiple scattering with repetitive representation of the input data in the scattering potential, linear and nonlinear transformations can be achieved concurrently, which has significant implications for low-power optical computing.

In summary, this dissertation provides a comprehensive examination of current methodologies, tools, and challenges in the area of optical computing and interconnects, showcasing novel modalities, and suggesting directions for further research and development.

## Keywords

3D optics, optical interconnects, (3+1)D printing, volume holograms, multilayer diffractive optics, optical switch, optical computing, machine learning.





# Résumé

Le domaine de l'optique présente des possibilités d'amélioration des technologies informatiques et de la communication grâce à ses propriétés inhérentes de largeur de bande, de parallélisme et d'efficacité énergétique. Ce travail de recherche se concentre sur l'exploitation de l'optique diffractive tridimensionnelle (3D) pour de nouveaux schémas d'interconnexion ainsi que pour une technique de traitement non linéaire basée sur la diffusion multiple et la représentation des données d'entrée plusieurs fois.

La discussion initiale de cette thèse tourne autour de l'importance des techniques 3D pour les circuits optiques. Les transformations entre les domaines 3D et 2D, vitales dans des domaines tels que la tomographie optique, la fabrication additive et le stockage optique de donnée, sont élaborées dans une perspective de conception de circuits optiques 3D. Tout d'abord, nous utilisons la fabrication additive à micro-échelle pour créer des éléments de volume diffractifs multicouches. Le concept de « Learning Tomography », qui est une méthode de reconstruction d'objets 3D à partir de projections 2D, est présenté comme une approche de conception inverse pour calculer ces éléments. Ensuite, nous présentons l'impression (3+1)D, une technique créée au sein du labo. Cette méthode facilite la fabrication de dispositifs optiques à gradient d'indice, tels que les hologrammes de volume et les guides d'ondes optiques. Un aspect notable de cette technique est sa capacité de produire des hologrammes de volume avec une relation d'efficacité de diffraction linéaire, dépassant la limite de  $1/M^2$ . La recherche examine ensuite l'application des modulateurs spatiaux de lumière commerciaux pour construire des dispositifs d'interconnexion reconfigurables à plus grande échelle. En combinant les principes de diffraction en espace libre avec la mise en forme répétitive du front d'onde, nous pouvons potentiellement offrir une connectivité améliorée entre les nœuds dans les réseaux des centres de données. La section suivante se penche sur les caractéristiques non linéaires trouvées dans les systèmes opto-électroniques où la partie optique est uniquement linéaire. Ces non-linéarités sont notamment le codage de phase, la détection des données et la diffusion multiple. Un cadre théorique est construit pour le calcul rendu possible par ces transformations. Nous concluons par un réseau optique diffractif multicouche imitant les réseaux neuronaux numériques. La recherche postule qu'en utilisant la diffusion multiple avec une représentation répétitive des données d'entrée dans le potentiel de diffusion, les transformations linéaires et non linéaires peuvent être réalisées simultanément, ce qui a des implications significatives pour l'informatique optique à faible puissance.

En résumé, cette thèse fournit un examen complet des méthodologies, outils et défis actuels dans le domaine de l'informatique et des interconnexions optiques, en présentant de nouvelles modalités et en suggérant des orientations pour la poursuite de la recherche et du développement.

## Mots-clés

Optique 3D, interconnexions optiques, impression (3+1)D, hologrammes de volume, optique diffractive multicouche, commutateur optique, informatique optique, machine learning.



# Contents

<b>Acknowledgements</b> .....	<b>i</b>
<b>Abstract</b> .....	<b>iii</b>
<b>Résumé</b> .....	<b>v</b>
<b>List of Figures</b> .....	<b>ix</b>
<b>List of Equations</b> .....	<b>xi</b>
<b>Chapter 1 Introduction</b> .....	<b>13</b>
<b>Chapter 2 A tomographic view on inverse design</b> .....	<b>17</b>
2.1 Introduction.....	17
2.2 Optical tomography.....	18
2.2.1 Optical tomography based on direct inversion.....	19
2.2.2 Machine learning and iterative methods for optical tomography.....	20
2.3 3D optical memories .....	22
2.4 Recent approaches using neural network learning.....	25
2.5 Conclusion and outlook.....	29
<b>Chapter 3 3D printing multilayer optics for multiplexing</b> .....	<b>31</b>
3.1 Introduction.....	31
3.2 Methodology .....	32
3.2.1 Optimization with LT .....	32
3.2.2 Representation error.....	35
3.2.3 Full volume optimization.....	38
3.3 Additive Manufacturing of the 3-Layer Volume Element and Results .....	40
3.4 Conclusions.....	42
<b>Chapter 4 Direct (3+1)D laser writing of graded-index optical elements</b> .....	<b>43</b>
4.1 Introduction.....	43
4.2 Fabrication methodology .....	45
4.3 Characterization of the GRIN profiles.....	45
4.4 GRIN optical elements.....	48

---

4.4.1	Volume holograms.....	48
4.4.2	Photonic waveguides.....	50
4.5	Conclusions.....	52
<b>Chapter 5</b>	<b>Volume holograms with linear diffraction efficiency relation by (3+1)D printing.....</b>	<b>55</b>
5.1	Theoretical and numerical investigations.....	55
5.2	Fabrication and experiment results.....	58
<b>Chapter 6</b>	<b>Reconfigurable multilayer optics for interconnects.....</b>	<b>63</b>
6.1	Introduction.....	63
6.2	Methodology.....	65
6.3	Results.....	66
6.4	Conclusion and outlook.....	69
<b>Chapter 7</b>	<b>Nonlinearities in systems based on linear optics.....</b>	<b>71</b>
7.1	Intensity detection.....	72
7.2	Phase encoding.....	72
7.3	Multiple scattering with data repetition.....	73
<b>Chapter 8</b>	<b>Reconfigurable multilayer optics for nonlinear processing.....</b>	<b>77</b>
8.1	Introduction.....	77
8.2	nPOLO framework.....	78
8.3	Discussion.....	82
8.4	Methods.....	83
8.4.1	Derivation of the nonlinear response in nPOLO.....	83
8.4.2	Digital training.....	84
8.4.3	Experimental setup.....	84
<b>Chapter 9</b>	<b>Conclusions.....</b>	<b>85</b>
<b>Appendix A</b> .....	<b>89</b>	
<b>Appendix B</b> .....	<b>95</b>	
<b>Appendix C</b> .....	<b>105</b>	
<b>Appendix D</b> .....	<b>109</b>	
<b>References</b> .....	<b>113</b>	
<b>Curriculum Vitae</b> .....	<b>121</b>	

# List of Figures

Figure 1:1 – The ideal all-optical pipeline .....	13
Figure 2:1 – Optical Tomography.....	20
Figure 2:2 – 3D optical memory implementations .....	23
Figure 2:3 – Different holographic strategies .....	24
Figure 2:4 – Optical interconnections design.....	25
Figure 2:5 – Different approaches for inverse design of volume optical elements. ....	27
Figure 2:6 – Different modalities for 3D optical circuitry.. ..	28
Figure 3:1 – Optimization scheme of LT utilized in ODT and design of OVEs. ....	34
Figure 3:2 – Representation of the optimization scheme on a single layer.....	35
Figure 3:3 – The scheme of the optimization based on LT. ....	36
Figure 3:4 – The representation error .....	37
Figure 3:5 – The representation error with field distribution examples.....	37
Figure 3:6 – Comparison of layer topographies.....	38
Figure 3:7 – GRIN concept .....	39
Figure 3:8 – Amplitude of the reconstructed fields by GRIN OVE for different angles.....	39
Figure 3:9 – Multilayer multiplexer.....	40
Figure 3:10 – Multiplexing results.....	41
Figure 3:11 – 1 $\mu$ m by 1 $\mu$ m pixels manufactured with high aspect ratio .....	41
Figure 4:1 – Concept of (3+1)D printing.....	44
Figure 4:2 – Exposure calibration.....	46
Figure 4:3 – Volume grating characterization.....	47
Figure 4:4 – Volume hologram with two letters. ....	49
Figure 4:5 – Volume hologram with four fiber modes.....	50
Figure 4:6 – Fabricated waveguides.....	51
Figure 4:7 – Loss and coupling of waveguides .....	52
Figure 5:1 – Logarithmic plot for the simulated diffraction efficiency.....	57
Figure 5:2 – Characterization of single gratings. ....	59
Figure 5:3 – Diffraction efficiency measurements. ....	60
Figure 5:4 – SEM image of stitched blocks fabricated in adjacent field of views .....	61
Figure 6:1 Conceptual schematic of ROSSMi. ....	64
Figure 6:2 Working principle and optimization of ROSSMi.....	65
Figure 6:3 Experimental setup of ROSSMi. ....	66

Figure 6:4 Results of unicast spatial granularity..... 67

Figure 6:5 Results of multicast spatial granularity..... 68

Figure 6:6 Results of spatial-spectral granularity. .... 69

Figure 7:1 - A system based on linear optics.. .... 71

Figure 7:2 – A system based on linear optics and multiple/repetitive data presentation. . 73

Figure 7:3 - Simplified optical system for multiple scattering with data repetition. .... 74

Figure 8:1 - The framework of nPOLO. .... 79

Figure 8:2 - the classification accuracy results ..... 80

Figure 8:3 - Samples of trained layer masks to be displayed on SLM ..... 81

Figure 8:4 - Co-training of optical trainable parameters and digital trainable parameters..81

Figure 9:1 Conceptual schematic of nPOLO at the edge, serving as an accelerator..... 86

# List of Equations

Equation 2:1 - Helmholtz equation. ....	18
Equation 2:2 – Phase accumulation by optical path length difference. ....	19
Equation 2:3 – Wolf transform. ....	19
Equation 2:4 – Loss function for iterative optimization.....	20
Equation 3:1 – Cost function.....	33
Equation 3:2 – Phase to thickness conversion.....	36
Equation 4:1 - Interference of reference and object beams.....	48
Equation 5:1 – Diffraction efficiency relation for volume holograms.....	56
Equation 5:2 – Interference of reference and object beams (re-stated).....	56
Equation 5:3 – Refractive index dynamic range as a summation of sinusoids. ....	56
Equation 5:4 – Modulated sinusoid in 1D.....	56
Equation 5:5 – Proportionality of index dynamic range and number of stored holograms with DC build-up. ....	56
Equation 5:6 – Proportionality of index dynamic range and number of stored holograms without DC build-up.....	56
Equation 5:7 – Diffraction efficiency of single volume grating by coupled wave theory.....	58
Equation 7:1 – Transmission matrix formalism for linear systems. ....	72
Equation 7:2 – Transmission matrix formalism with elements shown explicitly. ....	72
Equation 7:3 – Expression for $\mathbf{o}$ by intensity detection. ....	72
Equation 7:4 – Phase encoding of $\mathbf{d}$ on $\mathbf{i}$ .....	72
Equation 7:5 – Output with phase encoding without the intensity detection. ....	73
Equation 7:6 – Output with phase encoding with the intensity detection.....	73
Equation 7:7 – The system response for Modulation layer N=1.....	74
Equation 7:8 – The system response for Modulation layer N=2.....	75
Equation 7:9 – Output of multiple scattering with the phase encoding and without the intensity detection. ....	75
Equation 7:10 – Output of multiple scattering with the phase encoding and the intensity detection.....	75
Equation 7:11 – Cosine double angle identity .....	76
Equation 7:12 – The outputs for Modulation layer N=3.....	76
Equation 7:13 – Cosine triple angle identity.....	76
Equation 8:1 - The system response for Modulation layer N=1 (re-stated) .....	83
Equation 8:2 – Expression for $\mathbf{o}$ by intensity detection for arbitrary K (N=1).....	83
Equation 8:3 – Expression for $\mathbf{o}$ by intensity detection for arbitrary K and N. ....	83





# Chapter 1 Introduction

“Conventional wisdom says that electrons compute and photons communicate” [1]. The reasoning behind this statement is the strong Coulomb interactions among electrons to perform nonlinear processing (e.g. Boolean logic) in a highly localized manner. In contrast, the absence of a comparable photon-photon interaction allows for the utilization of numerous spatial and spectral channels. This increases the capacity of optical communication with minimal losses. Moreover, the  $1/r^2$  dependence of Coulomb interactions provides compact storage units in the electronic domain whereas it is very challenging to build a competitive optical storage scheme. Nonetheless, prospects of low power consumption and fast computation thanks to not having Ohmic loss and RC time constant attracted scientists to optical computing and storage. On the other hand, improvements in lithography resolution allowed researchers to harness exponential gains under Moore’s law with the miniaturization of transistors and formed the basis of the microelectronics revolution, which caused optics to lag behind. As of 2020s, technology is rooted in three main pillars: electronic computing, electronic storage, and optical communication. Nevertheless, the recent explosion in machine learning applications and the vast amounts of data to be processed, coupled with the impending limits of Moore’s law, challenges the status quo. The existing paradigm, which combines optical communication with electronic computing and storage, necessitates electrical-to-optical and optical-to-electrical conversions. These conversions are not only costly but also introduce latency, a significant impediment for machine learning tasks. Moreover, as it will be explained shortly, machine learning hardware implementation can be inherently well suited for using optics. That is another reason why, optical computing and storage research undergone a resurgence. It is crucial to highlight that beyond the three aforementioned pillars, there is a fourth pillar: data acquisition (such as imaging, spectroscopy, etc.), in which optics plays a dominant role. However, this pillar is not among the topics of this dissertation. With the acquisition, we complete the overall picture as visualized in Figure 1:1.

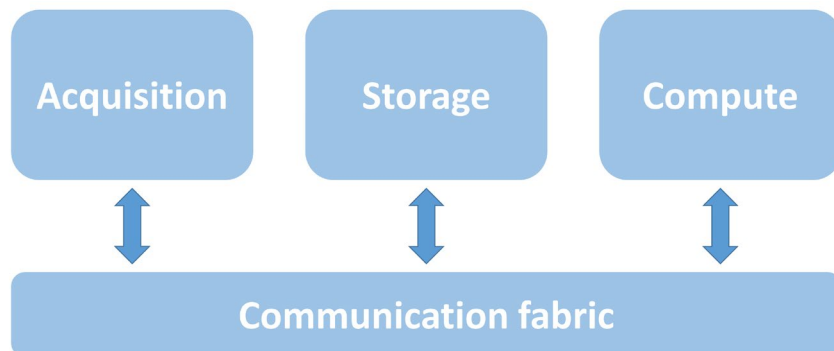


**Figure 1:1 – The ideal all-optical pipeline.**

The ideal all-optical pipeline would consist of opto-electronic devices where an acquisition device gathers optical signal of interest. The optical compute unit would then process this signal. Any necessary prior knowledge for information extraction would be either physically encoded in the compute unit or retrieved from optical storage. An

optical communication fabric consisting of optical interconnects, waveguides, and fibers would connect all these components, ensuring that data remains entirely within the optical domain. For specific applications, such a pipeline could become practical and viable in the future. To contribute to this path, this thesis delves into storage, computation, and interconnect architectures.

Let us begin our discussion with the computation aspect. Despite the historical strengths of electronics, traditional computing algorithms cannot perform well in certain problems such as recognition and generative tasks. Neural network computation, inspired from the brain, emerged to solve such problems where traditional algorithmic approach fails. The brain consists of a very large number of interconnected neurons. A neuron can be modelled as a node with a nonlinear activation function. During the course of computation, each neuron independently accepts the output of its neighbors and, based on the weights of the interconnections, determines its own output. Neural network computation is a collective process: the basic yet concurrent functioning of individual neurons contributes to the advanced overall operation of the neural network. Moreover, this architecture allows information to be encoded in the interconnections rather than in separate memory elements. Each distinct piece of stored information can be represented by a unique pattern of interconnections among neurons [2]. In other words, a neural network consists of a large number of simple processing nodes that are extensively interconnected. Therefore, optics arises as a natural candidate to implement neural network computation. The first optical neural network was pioneered by Farhat et al., in 1985, adapting the Hopfield model into the optical realm using a transmittance mask and an LED array, which received feedback from a photodiode array [3]. This work paved the way for other notable contributions, such as the demonstration of a network based on photorefractive crystals by Psaltis et al. [4]. In recent times, there has been a renewed interest in optical computing research, which spans both integrated and 3D solutions. Prime examples include the deployment of integrated Mach-Zehnder interferometers by Shen et al. [5], the advent of deep diffractive neural networks introduced by Lin et al. [6], random projections that approximates kernels by Saade et al. [7], and opto-electronic diffractive processing units by Zhou et al. [8]. Recent literature has highlighted innovative optical implementations of reservoir computing [9], recurrent networks with reinforcement learning [10], and extreme learning machines [11]. Moreover, metamaterials have sparked considerable interest in the field of analog computing, opening up a range of promising applications [12], [13]. Additionally, computing capabilities are not exclusive to optics; wave phenomena also have potential applications in various fields as demonstrated in [14] for mechanics and analogue electronics as well as acoustics [15].

Optical interconnect topologies have been a subject of study for quite some time, with a foundational paper published in 1984 by Goodman et al. that reviewed potential approaches [16]. Since then, the fundamental principles have remained consistent, but the nuances of implementation strategies have evolved. In the realm of optical data storage, the 1990s witnessed numerous pivotal works, with many concentrating on 3D strategies [17]–[20]. It is worth noting that 3D implementations of optical interconnects and storage share significant similarities. To illustrate, consider a volume hologram. When employed as an optical storage device, an address beam retrieves data stored in the medium, effectively realizing a random access memory. The retrieved data is encoded on the diffracted beam activated by the addressing reference beam. The structure of this reference beam can vary based on the multiplexing mechanism, and consequently, the retrieved beam is also structured due to the encoded data. The relationship between the addressing reference beam and the diffracted, retrieved beam can be interpreted as a weighted interconnection between the spatiotemporal nodes defined within both beams [4]. Thus, by simply altering our perspective on the same phenomenon, it becomes evident that the optical storage medium also functions as an interconnect device. The architectures studied in this thesis also follows this duality.

For the flow of this dissertation, it is imperative to note that this thesis aligns with the perspective that 3D optical implementations are more practical than their 2D integrated counterparts, particularly when considering scalability. One primary reason is the relatively long optical wavelengths, which result in expansive footprints in 2D configurations. Furthermore, the necessity for waveguiding in integrated solutions diminishes optics' most significant advantage: parallelism resulting from the non-interaction in the spatial domain. The loss of spatial degrees of freedom restricts scalability. After considering the aforementioned arguments, we must also recognize the significant

challenges in the design and fabrication of 3D implementations. That said; recent advancements have led to several noteworthy demonstrations, some of which have been previously mentioned. With this in mind, Chapter 2, in a way as a continuation of this introduction chapter, reviews recent work and establishes connections to tomography, a prominent field that focuses on the collection of 3D information using light, thereby addressing issues that share fundamental similarities. This chapter embarks on an exploration of the transition between 3D and 2D dimensions, a topic of growing interest in the context of 3D optical implementations by inverse design. Optical tomography, as a technique, offers insights into this transition. The challenge arises in adapting 2D data channels to these 3D structures. This transition is essential in various fields, such as optical tomography, additive manufacturing, and 3D optical memories. This chapter reviews the methodologies employed to address these transformations, emphasizing iterative techniques and neural networks' roles.

Chapters 3 to 5 focus on micro-scale interconnects and volume holographic storage by utilizing different fabrication approaches by having 2-photon polymerization as a commonality. Chapter 3 delves into the advancement of additive manufacturing or 3D printing, which enables producing multilayered diffractive volume elements at the micro-scale with sufficient resolution for optics. Here, we follow the conventional use of 3D printing as a binary method meaning that a voxel is either printed or left empty resulting in a binary refractive index contrast. We use a novel optimization technique that adapts Learning Tomography, which will be discussed in Chapter 2 as well, to reconstruct 3D structures based on their input-output functionalities. By comparing simulated and experimental results, the chapter showcases how an optical volume element can perform angular multiplexing in a minuscule space. Chapter 4 introduces the novel method of (3+1)D printing, which utilizes light exposure as an extra dimension in three-dimensional (3D) fabrication. This single-step fabrication, employing a commercially available equipment based on 2-photon polymerization, showcases its application in the development of volume holograms and optical step-index and graded-index waveguides. Then in Chapter 5, we use the (3+1)D printing for fabricating volume holograms to experimentally validate that diffraction efficiency can be made linearly dependent on the number of multiplexed holograms when DC buildup is prevented within the available dynamic range of refractive index. This defies the conventional  $1/M^2$  limit seen with traditional methods of distributed optical recording.

In Chapter 6, we shift the focus from micro-scale fixed interconnects to the domain of reconfigurable optical interconnect devices with a centimeter-scale architecture. We explore the commercial spatial light modulators to build such an architecture emulating multilayer optics. As a bridge chapter, it provides a foundation for discussing nonlinear processing devices in Chapter 8 thanks to the architectural commonality. This is a preliminary exploration and further refinements are needed as will be discussed. However, the demand for efficient and scalable interconnects is skyrocketing due to evolving data center needs. That is why we believe that this chapter provides an important starting point for realizing an optical interconnect having efficient multicasting capabilities with spatial-spectral granularity.

As a prelude for Chapter 8, the last chapter before the conclusions, Chapter 7 delves into the potential nonlinear functionalities hidden within traditionally linear optical systems. By dissecting the interactions stemming from intensity detection, phase encoding, and multiple scattering, the chapter posits that linear optical systems are capable of complex computational processes. Such possibilities have implications for various applications, including optical signal processing and computational imaging. Then Chapter 8 introduces a framework we refer to as nPOLO (as an acronym for “nonlinear processing with only linear optics”) for realization of neural networks using a low-power continuous wave laser and diffractive layers. The framework can perform simultaneous linear and nonlinear operations in the optical domain by leveraging the nonlinearity between the scattering potential, where the input data is presented repetitively, and the scattered light. To induce this nonlinear relation of multiple scattering, we repeat the presentation of data multiple times. As an additional effect, data repetition in modulation layers leads to the generation of polynomial expansions and enhanced robustness against noise. Finally, we provide concluding remarks and outlook in Chapter 9.

This dissertation encompasses the primary focus of the author's Ph.D. studies. Additionally, the author has been involved in research examining spatiotemporal characteristics in multimode optical fibers for potential neuromorphic computing applications and in projects using neural networks to predict these characteristics. The author has also contributed to work on printing fiber bundles for imaging purposes. A comprehensive list of publications that the author has contributed is available in the CV section at the end of this document.

# Chapter 2 A tomographic view on inverse design

This chapter is the post-print version of the following review article published in *Nanophotonics*. For the sake of coherence and maintaining thematic focus, the segment titled "Section 3: Volumetric printing" have been excluded. The remainder of the document is adjusted to seamlessly incorporate this exclusion.

**From 3D to 2D and back again** by Niyazi Ulas Dinc<sup>1,2</sup>, Amirhossein Saba<sup>1</sup>, Jorge Madrid-Wolff<sup>2</sup>, Carlo Gigli<sup>1</sup>, Antoine Boniface<sup>2</sup>, Christophe Moser<sup>2</sup> and Demetri Psaltis<sup>1</sup>

<sup>1</sup>Optics Laboratory, École polytechnique fédérale de Lausanne, Switzerland

<sup>2</sup>Laboratory of Applied Photonics Devices, École polytechnique fédérale de Lausanne, Switzerland

*Nanophotonics*, Volume 12, Issue 5 (2023)

<https://doi.org/10.1515/nanoph-2022-0512>

The prospect of massive parallelism of optics enabling fast and low energy cost operations is attracting interest for novel photonic circuits where 3-Dimensional (3D) implementations have a high potential for scalability. Since the technology for data input-output channels is 2-Dimensional (2D), there is an unavoidable need to take 2D-nD transformations into account. Similarly, the 3D-2D and its reverse transformations are also tackled in a variety of fields such as optical tomography, additive manufacturing, and 3D optical memories. Here, we review how these 3D-2D transformations are tackled using iterative techniques and neural networks. This high-level comparison across different, yet related fields could yield a useful perspective for 3D optical design.

## 2.1 Introduction

Optical information processing is an attractive topic for scientists and researchers due to the potential fast and energy-efficient performance guaranteed by the intrinsic physical properties of optics [21]. With the advancements in micro/nano fabrication, nowadays implementing photonic circuitry is becoming more and more a reality. However, the field still stays infant and requires breakthroughs. Along with integrated solutions [5], [22]–[24], one of the promising ways of taking advantage from the parallelism of optics is using 3-Dimensional (3D) implementations, which enable the scalability of the systems [7], [25]–[27]. Nonetheless, the data injection and read-out systems, such as spatial light modulators and detectors are at best 2-Dimensional (2D); hence, it subsists an imperative necessity for transformations between 3D and 2D for both illuminating and collecting information with light. This is also the case for human vision. We live in a 3D world but we rely on a set of 2D sensors (the retinas in our eyes). Therefore, the human neural vision system adapted to perform an incredible job; from only a set of two 2D projections at a slightly different angle, our brain can reconstruct the 3D scene. Following the machinery of evolution,

one would expect artificial neural networks to have a similar role in carrying out these transformations. It is therefore worthy to take a step back to enumerate and understand the problems related to 3D-2D transformations.

In this paper, we first review optical tomography, which is one of the most prominent methods for 3D imaging dealing with the reconstruction of volumetric objects from 2D recordings. The inversion of the scattering problem, at the core of this technique, is severely hampered by the limited number of available projections, at the origin of the so-called “missing cone”, which makes the transformation back to 3D an ill-posed problem, and multiple scattering occurring within the object. Neural networks are frequently employed to unscramble and fill in the missing information using data-driven (statistical) and physics-based approaches with different techniques presented in section 2. In section 3, we review 3D optical memories as an example where the 3D information is retrieved from 2D measurements. In this case, we have 2D input-output planes and a 3D medium that specifies the different mappings between the input-output planes.

Finally, in section 4, we outline the recent approaches using neural networks and other iterative optimization schemes for designing 3D optical circuitry, which unavoidably performs 2D-to-2D mappings using 3D features of optics. We believe that understanding how other fields deal with the fundamental challenges arising from 3D-2D transformations and how neural networks are used in these fields could provide a valuable perspective for optical/photonic circuit design and fabrication. Photonics, in this regard, would be most beneficial for neural network architectures particularly when massive parallelism is required, which establishes interesting positive feedback between two fields.

## 2.2 Optical tomography

Optical tomography is an example of an imaging method that reconstructs the 3D refractive index distribution of the sample using multiple 2D projections. Here, 2D projections correspond to quantitatively measured scattered fields acquired by illuminating the sample from different angles as shown in Figure 2:1.a. The sample, with 3D refractive index distribution  $n(r)$ , is illuminated with a set of plane-waves  $U_m^i = e^{j\vec{k}_m \cdot \vec{r}}$ , and the complex fields,  $U_m^t$ , are measured for each projection,  $m$ . The refractive index of the sample is locally correlated with the mass density, which makes its 3D reconstruction interesting for a variety of biological applications [28], [29].

Conventionally, the 2D projections are measured in an off-axis holography configuration to capture both amplitude and phase information of the scattered field. A standard optical tomography setup is presented in Figure 2:1.b where a coherent and collimated visible source is divided into a signal and reference beams with a beam-splitter. The angle of the signal beam is controlled using a pair of galvo-mirrors, and a 4F system is used to magnify the illumination angle. The illuminated sample is then imaged onto a camera through another 4F system consisting of a microscope objective and a tube lens. The off-axis reference beam and the signal beam are recombined to form the hologram on the detector plane. We can process the holograms in the Fourier domain to retrieve the phase and amplitude of the complex projections.

The optical scattering can be described by the Helmholtz equation in an inhomogeneous medium [30]:

$$\nabla^2 U^s(r) + (k_0 n_0)^2 U^s(r) = -V(r)U(r)$$

Equation 2:1 - Helmholtz equation.

where  $U^s(r)$  is the scattered field,  $k_0$  is the wave number in free space,  $n_0$  is the refractive index of the background medium,  $U(r) = U^s(r) + U^i(r)$  is the total field, and  $V(r) = (k_0 n_0)^2 (n^2(r)/n_0^2 - 1)$  is the scattering potential of the sample. The integral solution of  $U^s(r)$  based on Equation 2:1 - Helmholtz equation is nonlinear with respect to the scattering potential, and as a result, the optical scattering problem cannot be directly inverted to achieve the 3D scattering potential. Additionally, due to the finite number of projections, and limited-numerical aperture (NA) of the imaging system, there is missing information that makes the inverse problem more difficult. In the following, we summarize ray-optics-based and single-scattering approximations that linearize the 3D scattering

potential reconstruction problem, and then we review optimization and machine learning techniques for addressing missing information and multiple-scattering problems.

### 2.2.1 Optical tomography based on direct inversion

Charrière et al. [31], and Choi, et al. [32] reported the first experimental implementation of tomographic refractive index reconstruction for biological cells. Even though optical diffraction tomography was theoretically proposed and elaborated much earlier, the refractive index reconstruction method in [31], [32] is based on the ray-optics approximation. If we assume weakly diffractive objects, the phase of a 2D projection in  $U(r') = U^I(r')e^{j\varphi(r')}$  will be proportional to the integration of  $\delta n(r)$ , the refractive index contrast of the sample with respect to the background medium, along the optical axis [31]:

$$\varphi(x', y', z' = z_0) = \int^{z_0} k_0 \delta n(r') dz'$$

Equation 2:2 – Phase accumulation by optical path length difference.

Equation 2:2 is the line integral of the refractive index contrast along the projection direction, which is known as the Radon transform of  $\delta n$  [33]. This representation clarifies the similarity to computed X-Ray tomography for 3D reconstruction of the absorption using 2D intensity measurements. Having the 2D phase profiles for different illumination angles, an inverse Radon algorithm based on filtered back projection can be used to reconstruct the 3D tomograms of refractive index contrast,  $\delta n(r)$ .

For samples with features comparable to the wavelength, the diffraction of light cannot be neglected. Emil Wolf proposed optical diffraction tomography (ODT) [30] in 1969 using the Born approximation to linearize the integral solution of Equation 2:1. Wolf showed that using the Born approximation, the 3D Fourier transform of the scattering potential can be related to the 2D Fourier transform of each projection according to the incident wave-vector,

$$\mathcal{F}_{2D}\{U_m^S\}(k_x, k_y) = \frac{2\pi j}{k_z} \tilde{V}(k_x - k_x^{in}, k_y - k_y^{in}, k_z - k_z^{in})$$

Equation 2:3 – Wolf transform.

where  $U_m^S$  is the scattered field for projection  $m$ ,  $k_x$  and  $k_y$  are the spatial frequencies,  $k_x^{in}$ ,  $k_y^{in}$ , and  $k_z^{in}$  are the wave vectors of the illumination beam and  $k_z = \sqrt{k^2 - k_x^2 - k_y^2}$ .

We can use Equation 2:3 to fill the 3D Fourier domain of the scattering potential. Devaney proposed using the Rytov approximation for ODT [34] by using  $U^I(r) \log\{U(r)/U^I(r)\}$  instead of  $U^S(r)$  on the left side of Equation 2:3 which can be justified with the first-order Taylor expansion. Sung et al. [35] presented the first experimental results on diffraction tomography using the Rytov approximation. Later, many groups thoroughly studied different aspects of ODT such as illumination beam rotation [36], sample rotation [37], temporally incoherent ODT [38], wavelength scanning [39], and polarization-sensitive ODT [40]. In Figure 2:1.d, a 3D refractive index reconstruction of hepatocyte cells is shown using Wolf's method with the Rytov approximation [41]. The ill-posed nature of the direct inversion of the scattering problem causes missing frequencies in the Fourier domain of the reconstructed scattering potential. The missing spatial frequencies make the 3D refractive index reconstruction underestimated and elongated along the optical axis. To solve this issue, iterative methods for optical tomography have been investigated.

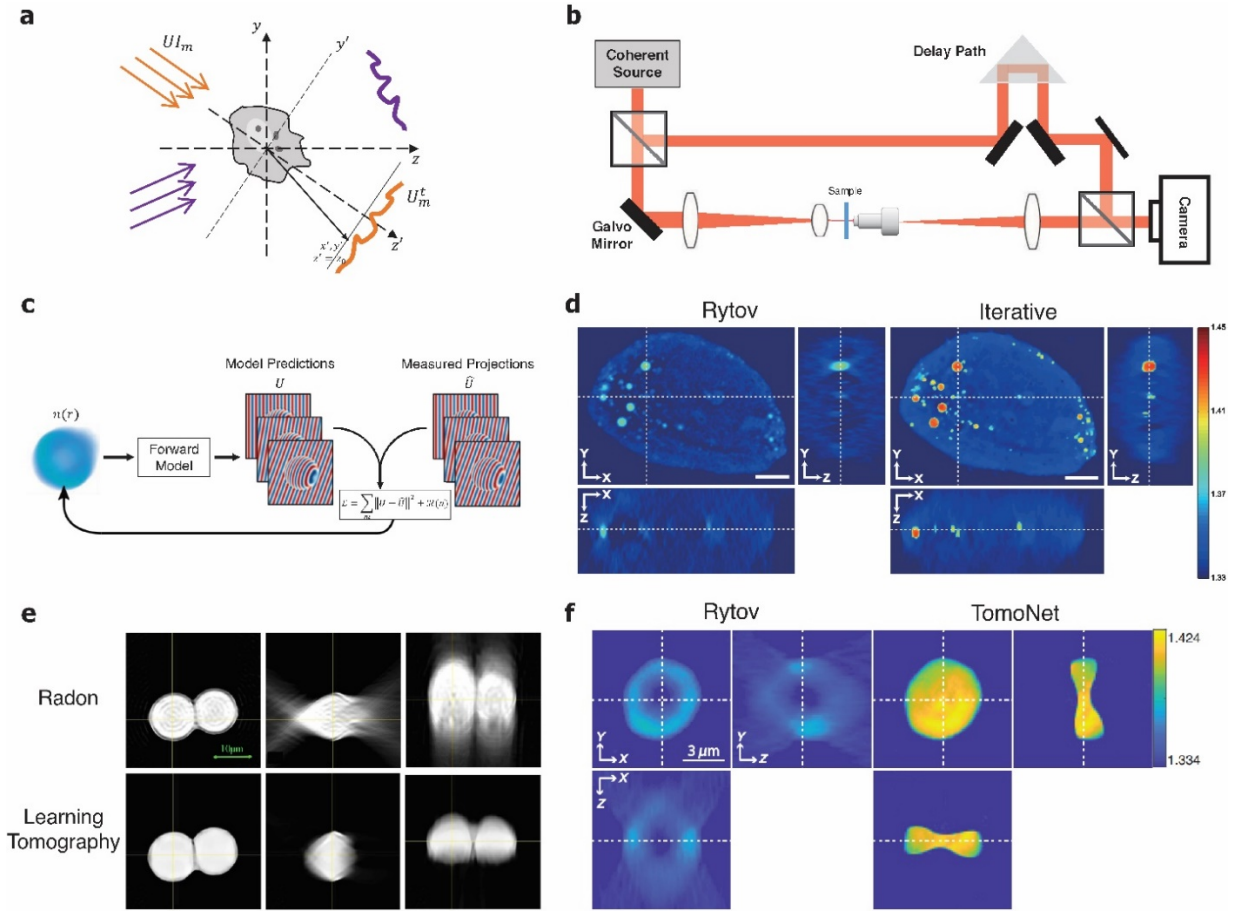


**Figure 2:1 – Optical Tomography.** **a.** An overview of the optical tomography problem. A 3D object is illuminated with different plane waves, and 2D quantitative phase projections are measured for each illumination angle. **b.** A standard off-axis holography setup for refractive index tomography. The illumination angle can be controlled using a pair of galvo mirrors. **c.** Iterative optical diffraction tomography (ODT): A forward model (such as single-scattering [41] or beam propagation method [42]) computes the 2D projections for each illumination angle. By comparing this field to the measurements, a loss function is calculated, which is minimized by improving the reconstruction of the 3D refractive index iteratively. **d.** Comparison of ODT reconstruction results for a hepatocyte cell using the Rytov approximation and iterative ODT with edge-preserving regularization (Adapted from [41] Copyright OPTICA). The scale bar is 5  $\mu\text{m}$ . **e.** Tomographic results of two 10  $\mu\text{m}$  polystyrene beads immersed in oil with  $n_0=1.516$  based on inverse Radon transform and Learning Tomography (Adapted from [42], Copyright OPTICA). **f.** 3D reconstruction of a red blood cell using TomoNet. (Adapted from [46] Copyright SPIE). Figures (e) and (f) show that Learning Tomography and TomoNet solve underestimation and elongation of the reconstructions

## 2.2.2 Machine learning and iterative methods for optical tomography

To consider a more accurate forward scattering model rather than Born or Rytov approximations, and solve the missing frequencies problem, several iterative optimization schemes have been proposed for optical tomography. The main idea of iterative tomography, shown in Figure 2:1.c is finding the 3D refractive index distribution by minimization of a loss function, which includes the difference between the field calculated by a forward model and the measured projections, plus a regularization term based on some prior information about the sample,

$$\mathcal{L} = \sum_m \|U_m^{model}(V) - \hat{U}_m^{projection}\|^2 + \mathcal{R}_{prior}(V)$$

Equation 2:4 – Loss function for iterative optimization.

where  $U_m^{model}(V)$  is the 2D projection calculated for the estimated scattering potential in that iteration using a forward model,  $\hat{U}_m^{projection}$  is the measured projection, and  $\mathcal{R}_{prior}(V)$  is a regularization term based on prior knowledge of the 3D scattering potential. The iterative optimization for the reconstruction of the refractive index



has been presented for ray-optics tomography [32]. For ODT, different regularizers are compared in [41] using a single-scattering forward model. Their results in Figure 2:1.d show significant improvement in the underestimation and elongation of the sample, using an edge-preserving regularization term.

A more accurate forward model for the calculation of  $U_m^{model}$  is used in [42] based on the beam propagation method. This approach, known as Learning Tomography, accounts for the multiple scattering and provides a decent 3D reconstruction of the refractive index, as shown in Figure 2:1.e. This idea was further investigated to achieve 3D reconstructions using a few projections [43], or intensity measurements [44]. Additionally, Tian and Waller demonstrated that LED illumination could be used for tomographic reconstruction with a multi-slice forward model to overcome laser fluctuations and speckle artifacts [45].

Recently, several groups studied machine-learning techniques for ODT. Lim et al. [46] presented a deep neural network, TomoNet, which maps the Rytov-based low axial resolution 3D tomograms to the improved 3D refractive index tomograms. They have generated a dataset of red blood cell phantoms with different sizes, refractive indices, and orientations. Then, they calculated synthetic projections for 40 illumination angles for each phantom by discrete-dipole approximation and calculated Rytov-based reconstruction using these synthetic projections. In such a manner, a dataset of red blood cells with their corresponding Rytov reconstructions can be achieved to train a deep neural network with a U-Net structure. This network, which is trained on synthetic data, can provide 3D tomograms with a reconstruction error two orders of magnitude smaller than Rytov, and it can be also used for experimental projections. In Figure 2:1.f, the 3D reconstruction of the refractive index of a mouse red blood cell is shown using TomoNet in comparison with the Rytov approximation. Recently, SILACT, a machine learning technique for the 3D reconstruction of the refractive index was presented [47], which is based on a deep neural network that converts a single frame hologram with angle-multiplexing illumination to the 3D refractive index tomogram. In this method, a dataset of input/output pairs is generated as follows: each sample is illuminated with a single frame of angle-multiplexed illumination with four angles, and a raw hologram is measured using off-axis holography. Raw holograms are considered as the input of the network. Then, the sample is illuminated with 49 projections, each from a single angle, and a 3D reconstruction of the sample is calculated using Learning Tomography based on these projections. This 3D reconstruction is considered as the output of the network. The deep neural network is trained on these input/output pairs. Using the trained deep neural network, a 3D reconstruction of the sample can be achieved with an angle-multiplexed single hologram. Another deep learning method for 3D tomography was recently investigated using a physics-informed neural network, MaxwellNet, as the forward model in Equation 2:4 – Loss function for iterative optimization. Equation 2:4 [48]. MaxwellNet minimizes a physics-informed loss function (such as Maxwell equations) and it was originally proposed for an inverse design problem [49]. In contrast to the conventional data-driven neural networks that require a huge dataset, MaxwellNet exploits physical laws to suggest a fast solution to the forward and inverse scattering problems.

Iterative solutions of ODT [41]–[44], [48] provide better 3D reconstructions at the cost of computation time. Direct ODT approaches such as Wolf’s method [30] are relatively fast since they require a few operations such as multiplication and Fast Fourier Transform (FFT) per projection or an additional phase-unwrapping step for each projection in the case of Rytov approximation. However, reconstructing the 3D refractive index tomogram with an iterative optimization method requires performing the forward model for all the projections in each iteration. As a result, depending on the complexity of the forward model and the number of iterations, iterative optical tomography methods are time-consuming. Ref [43] compares Beam Propagation Method (BPM) and Split-Step Non-Paraxial (SSNP) method as forward models for the iterative reconstruction where one iteration (running on a graphics card) takes approximately 3 to 13 seconds for BPM depending on the computation volume and 50% more time required for the SSNP version. Note that the required iterations are in the order of a few hundred. More sophisticated forward models such as Lippmann-Schwinger [50], [51], are also used to show high-fidelity reconstructions when the complexity of the data is high at the expense of more computational power. Hence, the time per iteration may differ by an order of magnitude when such models are employed. Moreover, the applied regularization method is

also an important factor in the computation time per iteration, which can make a difference by an order of magnitude as shown in Ref. [41]. On the other hand, deep neural networks such as TomoNet [46] and SILACT [47] present tomographic 3D reconstructions of a specific class of samples with a fast inference time, which goes below a second for the whole process of 3D reconstruction of a sample.

Iterative approaches using prior knowledge, accurate forward models such as BPM, and statistical information accomplished by machine learning frameworks can help to achieve a better 3D refractive index reconstruction in the ill-posed optical tomography problem.

## 2.3 3D optical memories

A well-known way for going back from 2D to 3D is through 3D optical memories. Here, the goal is to define a 3D distribution to store many 2D data pages or mappings by modifying the optical properties of the media. Unlike volumetric printing, here the idea is to satisfy a 2D-2D mapping rather than the geometric fidelity. Establishing particular 2D-2D mappings is also the goal of photonic circuits or networks, as we will investigate more in the next section. Moreover, it is conceivable to expect an optical memory for fast computation rather than having the memory in electronics. Before moving on to that, we propose to first revisit the “classical” techniques to obtain 3D optical memories.

The motivation behind the benefit of using 3D volumes to store 2D data is quite intuitive: the extra degree of freedom provided by the third dimension entails an increase in the storing capacity as compared to 2D layouts. On the other hand, one has to simultaneously deal with cross-talk limitations emerging in tomography and additive manufacturing, i.e. one must be able to access and record data in an isolated way. We can separate 3D optical memories into two main groups concerning the way the data recording and read-out are handled to address this issue: holographic access techniques and two-photon access techniques [52]. In the holographic methods, one piece (analog or discrete) of data is distributed throughout the whole volume whereas one bit of data is stored in a localized spot in two-photon methods. For the sake of completeness, it is worth mentioning that there are other proposals such as persistent spectral hole burning yielding a response in temporal frequency domain [53], [54], but we will limit ourselves to the spatial domain approaches hereafter. Although we referred to holographic data storage as a distributed way of storing data since gratings are recorded in the whole encoding volume, it must be noticed that this process just consists of localizing the data in the spatial frequency domain instead of real space. In Figure 2:2.a, we show this phenomenon by using Ewald’s sphere representation. Ewald’s sphere is a conceptual construction of a sphere whose radius is equal to the momentum of light. When we place the  $k$ -vector (momentum) of incident light between the center and the surface of the sphere, the grating vector must connect the tip of the incident  $k$ -vector onto the sphere to satisfy the conservation of momentum. In Figure 2:2.a, we show the grating vector as a well-defined (or localized) vector, which would satisfy the Bragg condition only for a specific angle with a given wavelength. The amplitude of the sinusoidal grating would store an analog value, which can be read out with the reference beam as shown in Figure 2:2.a. The conventional way to obtain such gratings is by optical interference of two plane waves. The obtained hologram is thus transferred to the photosensitive recording material as the 3D variation of the intensity generates a similar variation in some optical properties such as absorption or refractive index [17].

In the case of a two-photon technique, the interaction volume is localized using two-photon absorption that scales with the square of the intensity. On top of that, crossing two orthogonal beams, as shown in Figure 2:2.b, to satisfy the required intensity to initiate two-photon absorption further narrows the focus volume in comparison with a single beam that has an ellipsoidal point spread function elongated in the optical axis [18], [19]. The local modification obtained by two-photon absorption serves as a written bit of data. During the read-out, the address beam, which could be a light sheet, excites a specific page in the volume and the fluorescence signal modulated with respect to the recorded data is subsequently detected. Selecting a specific volume for recording and read-out provides parallel access and prevents inter-layer interference of different data pages at the same time. We also note

that optically induced dielectric breakdown of glass could serve as a localized way of recording and reading data in 3D [20].

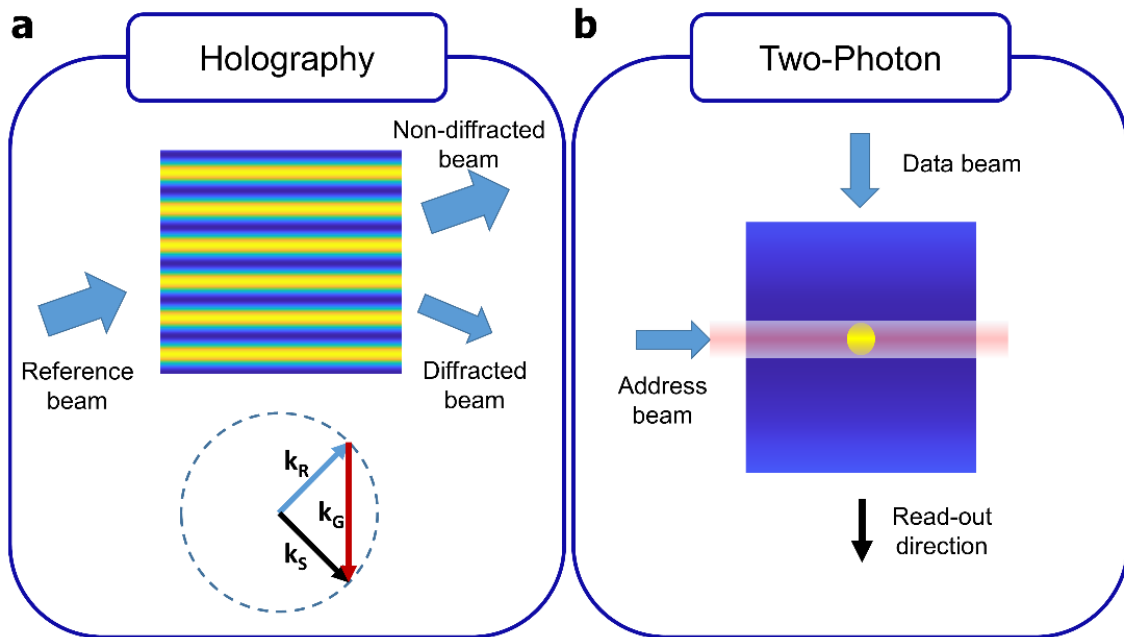


**Figure 2:2 – 3D optical memory implementations.** **a.** Diffraction from a sinusoidal grating according to Bragg matching condition. On Ewald's sphere representation,  $k_R$ ,  $k_S$ , and  $k_G$  refer to the wave vectors of the reference, signal, and recorded grating re-spectively. The reference beam simply addresses and reads out the data stored in the grating. **b.** Simple sketch of recording and read-out for a two-photon technique. Here, the address beam (analog of the reference beam in the case of holography) is depicted as a light sheet accessing a layer of the volume and the data beam encodes the information. During the read-out, the address beam selects the target layer to excite a fluorescence signal that would be modulated with respect to the recorded data (following the description in [18]).

To record many data pages in the two-photon system, one should consider the two-photon absorption cross-section and the intensities of the address and data beams to decide on the distance of adjacent spots of data. One should also consider dynamic focus optics synchronized with the address beam to increase the signal-to-noise ratio in the read-out as the emitted photons would undergo some scattering in the media. For holographic access, we should understand how Bragg selectivity works. When many gratings are superimposed, based on the incidence angle, only the Bragg-matched grating would yield strong diffraction towards a designated area whereas all the rest of the refractive index modulation would scatter the light mainly in the direction of the non-diffracted beam. For instance, having the reference and data beams orthogonal to each other, would yield clean read-outs as shown in Figure 2:3.a. An infinitely large grating would have a well-defined (or ideally localized) grating vector. However, a finite volume grating would have a so-called grating cloud, which is simply due to the convolution of its Fourier transform by a 3D sinc function because of bounded volume [55]. To record many gratings for multiple pages of data, grating clouds should be well separated to prevent cross-talk as depicted Figure 2:3.b. The bandwidth of the data in the recorded page would broaden the recording along Ewald's sphere. This can be understood simply by considering the angular spectrum, meaning that all the individual spatial frequencies in the data page would launch a plane wave with different angles, which would record different gratings with the corresponding reference beam mapped onto Ewald's sphere. Changing the angle (polar to spherical coordinate) of the reference beam generates another Ewald sphere with the same radius but shifted (as shown in Figure 2:3.b), thus separating the data pages thanks to Bragg selectivity. This method is called angular multiplexing [56]. If we change the wavelength, then of course the radius of Ewald's sphere will change, yielding wavelength multiplexing. If the data page could form a  $4\pi$  distribution, then the Bragg method would fill all the  $k$ -space. However, having a data page forming a  $4\pi$  distribution is practically impossible. Hence, one can change the azimuthal angle of the reference beam such that the new

position is farther apart by the bandwidth of the recorded pages to fill the k-space. In this case, the data pages multiplexed along the azimuthal direction would all be Bragg-matched (imagine having a fixed Ewald's sphere in Figure 2:3.b and rotating it along the z-axis) but they will simply form the reconstructions along different directions. Having a fixed detector with the numerical aperture matched with the bandwidth of the signals would prevent cross-talk. This approach is called peristrophic multiplexing [57].

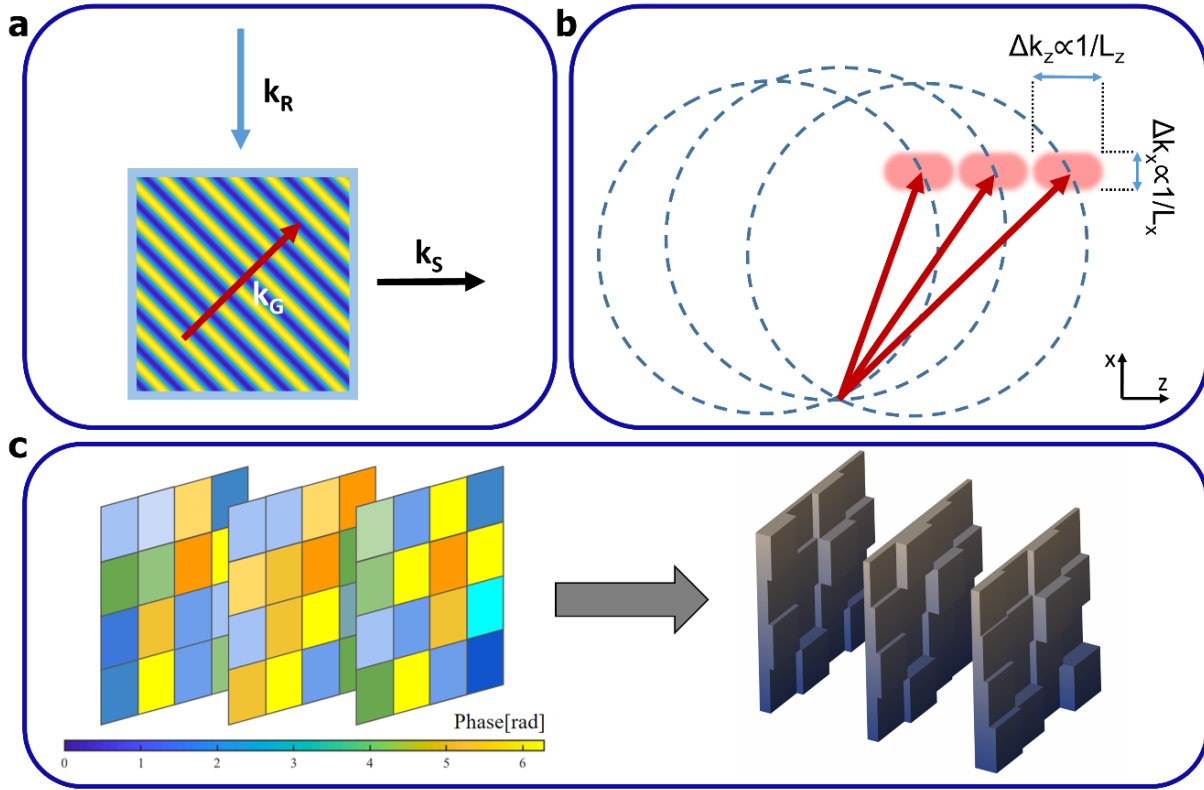


**Figure 2:3 – Different holographic strategies.** **a.** 90° geometry decoupling the non-diffracted beam and modulated diffracted beam.  $k_R$ ,  $k_S$ , and  $k_G$  refer to the wave vectors of the reference, signal, and recorded grating respectively. **b.** Bragg-selectivity in k-space separates the different pages of data by mapping them on different Ewald's spheres due to the different carrier frequencies. The vector clouds are designated by the shaded regions where the size of the cloud inversely depends on the dimensions of the volume hologram,  $L_x$  and  $L_z$ , as shown. The same argument applies to the y-direction as well. **c.** Schematic for a phase mask stack. The stacked phase masks exhibit volumetric properties when the separation between them is large enough for Fresnel propagation to take place. The varying phase can be encoded as varying thicknesses, which enables the fabrication with a binary-index approach.

When we fill the k-space with different gratings that are modulated by data envelopes, we can also display a different pattern rather than a reference beam to access the recorded data. Depending on the spatial and angular distribution of the displayed pattern, the superimposed modulated gratings would diffract some portion of the incoming beam, which turns the volume hologram into a correlator with respect to the recorded data in it [58]–[60]. Moreover, the recording phase of the volume hologram could be arranged in a way that the volume hologram satisfies independent linear connections between the input and output plane, which would resemble the linear weights of a neural network architecture [4]. Hence, a volume hologram becomes a natural candidate for a part of photonic circuitry. One bottleneck is the efficiency of individual reconstructions as they decrease with respect to the square of the number of recorded data pages with the explained conventional way of recording [61]. In [62], recording localized holograms in doubly doped  $\text{LiNbO}_3:\text{Fe},\text{Mn}$  demonstrated a linear efficiency relation. This method can be seen as a hybrid way of recording a 3D memory using holographic and two-photon access at the same time enabling also selective erasure [63].

Another approach to increase efficiency is multilayered systems such as multilayer of phase masks. A phase mask is a 2D variance of phase delay, which gives a shift-invariant response with respect to the excitation angle. By

stacking multiple planes, one can destroy shift invariance and introduce multiplexing schemes. With recent advances in additive manufacturing such as two-photon polymerization [64], [65], it has become possible by expressing the phase masks in terms of topography variation, as exemplified in Figure 2:3.c, and fabricating the stack [66]. As we will delve into the details in the next section, the calculation for such a stack does not have a direct solution and requires iterative methods since the relation of phase modulation with the output field is nonlinear even though the 3D structure provides a linear transform between input and output fields.

## 2.4 Recent approaches using neural network learning

In Section 2 we discussed how, given an unknown 3D object, it is possible to extract its geometrical and electromagnetic properties by collecting several 2D projections under different excitation conditions. The methods developed with this diagnostic approach, in which the object under study is fixed and we have free control over the excitation source and collection channel, pave the way to the design of photonic devices where the question is reversed: given a fixed source or a set of input channels, how should I shape matter and choose its electromagnetic properties to obtain the desired output? The answer to this question is at the very essence of many devices such as optical interconnections, multiplexers, couplers, optical filters, spatial and time modulators, optical computers, and so on. We review in the following the main approaches adopted for the design problem sketched in Figure 2:4: we assume to have one or multiple input channels described by the input electric field distribution  $\mathbf{E}_i(\mathbf{r})$  on a 2D plane, and we have to determine the electric permittivity distribution  $\varepsilon(\mathbf{r})$  that gives the target output  $\mathbf{E}_o(\mathbf{r})$  at another 2D plane.

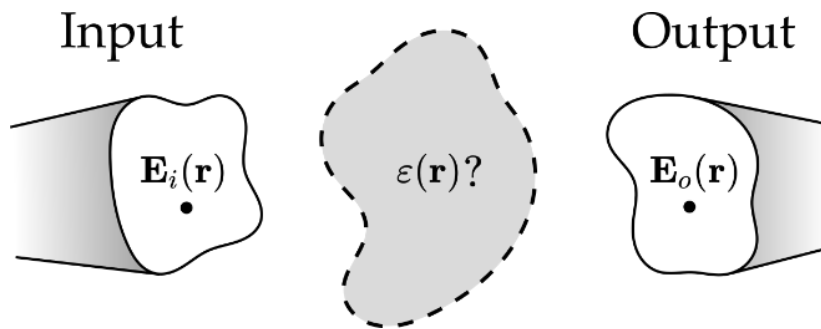


**Figure 2:4 – Optical interconnections design.** The goal is the determination of geometrical and material properties of the central grey volume that maps input  $\mathbf{E}_i(\mathbf{r})$  to output  $\mathbf{E}_o(\mathbf{r})$  electric fields with maximal efficiency and minimal cross talk.

For instance, the input may be associated with the modes of an incoming fiber, which should be mapped to or combined with the modes of another fiber. Realizing such an optical interconnect represents an archetypal problem since exploiting free propagating light instead of electrical wiring would result in lower energy consumption, faster communication, and larger parallelizability. The analysis presented in this section holds not only for data transfer and processing but also for optical memories presented in the previous section. In addition, we restrict the problem here to electric fields and currents, but one can straightforwardly extend it to magnetic materials.

The goal of the design problem shown in Figure 2:4 is to provide the maximal coupling efficiency between a large number of input and output channels within the smallest volume. To make a comparison with biology, the optical interconnect plays the same role as a synapse in a neuron [4]. In this sense, the 3D structure of Optical Volume Elements (OVEs) is promising to overcome electronic implementations as the added degrees of freedom enable maximization of the number of optical modes that can be multiplexed [67], [68]. Here, we stress the term OVE to make it clear that the mentioned optical element has transmission and reflection properties that strongly depend on the spatial and spectral shape of the input field because of the volumetric nature of the optical element.

The first fabrication option, as we investigated in the previous section, is to optically record the volume hologram given by the interference of the input field  $\mathbf{E}_i$  and the complex conjugate of the objective field at the output  $\mathbf{E}_o$ , see Figure 2:5. The technique is usually implemented with photosensitive polymers or photorefractive crystals [69]

and the number of exposures required to couple  $N$  input with  $N$  output channels is of the order of  $N^2$ . The total number of recorded hologram scales as  $V/\lambda^3$  where  $V$  is the crystal volume and  $\lambda$  the recording wavelength. Increasing  $N$  the cross-talk among different channels due to undesired diffraction orders represents the main bottleneck of the method [70].

Optically recorded devices can be outperformed by computer-generated holograms (CGHs) in terms of efficiency. Iterative approaches developed for 2D CGHs can be extended to volume holograms. In Ref. [71] the authors propose a method similar to the Gerchberg–Saxton algorithm where, instead of iteratively going from a 2D near to a 2D far field, they go from the 3D direct scattering potential to the inverse space and fill the Ewald’s sphere under Born approximation. As introduced in the previous section, multiple phase masks can be stacked to have multiplexing or a correlator that can separate different features as an alternative to continuous volumetric approaches. Another way of thinking about this is distributing the memory in multiple planes, where the diffraction between the planes yields volumetric optical properties as demonstrated using spatial light modulators (SLMs) where the layers are optimized by a general version of the Gerchberg–Saxton iterative optimization algorithm [72].

The analogy between ODT and OVE design is intriguing as one can imagine this latter process as the 3D reconstruction of an unknown object of which we know just the 2D projections (the desired output fields  $\mathbf{E}_o$ ) for given incident conditions (the known input fields  $\mathbf{E}_i$ ). Similar to ODT, the efficiency of iterative algorithms strongly depends on the physical model used to simulate wave propagation. As discussed in Section 2, whenever the refractive index contrast is low and Fresnel reflections are negligible, the split-step beam propagation method (BPM) represents a convenient computational tool. Learning tomography was demonstrated as a design algorithm to be combined with additive manufacturing [66] so that the multilayer approach is realized without active devices such as SLMs. The OVE is discretized as a stratified medium where every voxel in each layer provides a phase delay proportional to its refractive index. The output field  $\mathbf{E}_o$  computed with BPM is compared with the target  $\bar{\mathbf{E}}_o$  for all excitation conditions and the error is backpropagated to update the value of the refractive index in each voxel. In this case, unlike from ODT where any prior knowledge on the sample is added through a regularizer term, the designed element is updated at each iteration according to the fabrication constraints. Two-photon polymerization is used in a conventional binary way (either polymerized or not polymerized) that yields a binary index structure, forcing the design into a multilayer element as shown in Figure 2:6.a. Moreover, having BPM as the forward model enables us to directly optimize the topography rather than the 2D phase masks. Hence, multiple scattering is also captured during the optimization, which further increases the fidelity. In this framework, additive manufacturing through two-photon polymerization was proven as a critical technological step forward, which is compliant with in-plane sub-wavelength resolutions. By using this platform 3D waveguide interconnects have been experimentally demonstrated [73], [74] (see Figure 2:6.b).

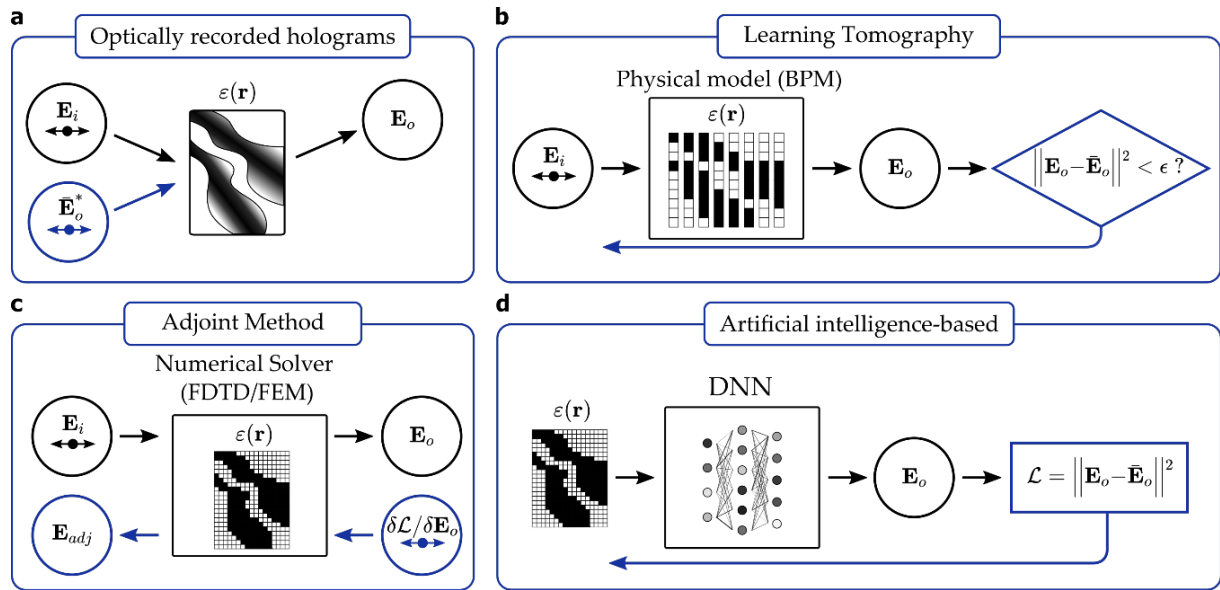


**Figure 2:5 – Different approaches for inverse design of volume optical elements.** **a.** Optically recorded holograms obtained from the interference of incident field  $E_i$  (black) and the conjugated objective field  $\bar{E}_o^*$  (blue). **b.** Learning tomography. The input field is propagated through the guess structure by BPM (black). The predicted output  $E_o$  is compared with the target field  $\bar{E}_o^*$  and the error is backpropagated to iteratively update the structure (blue). **c.** Adjoint variable method: the gradients of the objective function with respect to design parameters are computed through two simulations. The forward one (black) and the adjoint in which the source depends on the original fields and objective function and the corresponding time-reversed simulation (blue). **d.** AI-based methods: a DNN maps the relationship between permittivity and output fields (black). The loss is computed as in (b) and backpropagated through the network (blue).

Being able to backpropagate light using the time-reversal scheme in Fresnel formulation yields a striking resemblance with the error backpropagation algorithms used in neural networks [42]. Lin et al. [6] introduced diffractive deep neural networks (see Figure 2:6.c) by using many examples from a large dataset and back-propagating the error using machine learning algorithms and Fresnel propagation as the forward model. The linear transform performed by multiple layers combined with the absolute square nonlinearity of the detector produced very competitive accuracy results. This method is also applied to different areas from pulse shaping [75] to computational imaging [76]. Following a similar approach, Zhou et al. [8] demonstrated the diffractive processing unit that consists of a digital Micromirror device (DMD), an SLM, and a detector. In the unit, data is injected via DMD and bias terms are introduced via SLM, where the free space propagation relays the modulated field to the detector that reads the intensity. Cascading this unit by feeding the detected signal back into DMD, the authors demonstrated a recurrent implementation to perform human action recognition. Other interesting applications where the optical implementations solve algorithmic problems include phase recovery [77] and increasing the resolution of displays [78] using diffractive layers.

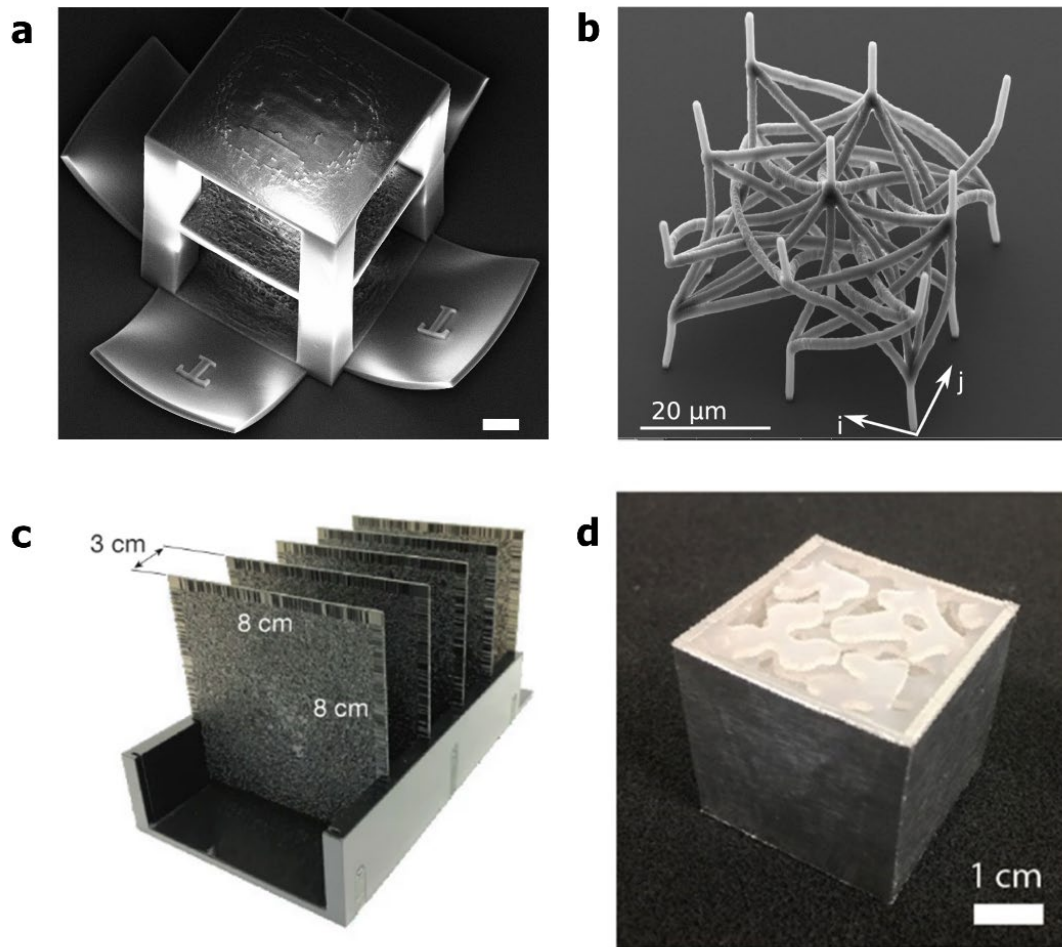


**Figure 2:6 – Different modalities for 3D optical circuitry.** **a.** Multilayer computer-generated optical volume element as an interconnect working in the optical domain printed by two-photon polymerization. The scale bar measures 20  $\mu\text{m}$ . (Taken from [64], Copyright De Gruyter) **b.** Waveguide interconnects with complex 3D routing to perform image-processing filters (Taken from [72], Copyright Optica). **c.** Diffractive deep neural network for various classification tasks experimentally demonstrated in the THz regime (Taken from [6], Copyright AAAS). **d.** Volumetric element optimized by adjoint method for wavelength and polarization sorting experimentally demonstrated in the THz regime (Taken from [80], Copyright Optica).

For complex structures for which BPM fails, more accurate numerical models, such as finite differences and finite elements, are needed. However, the nonlinear numerical solvers rely on matrix inversions that are not differentiable. In turn, the calculation of objective function gradients with respect to the design parameters is not straightforward as for BPM and it would require a numerical simulation for each derivative of the objective function with respect to a single parameter, e.g. the refractive index value in a voxel. The workaround for topology optimization is represented by the adjoint method [79], [80]. By exploiting Lorentz reciprocity, the gradient with respect to all the input variables can be computed through two successive simulations: a forward one, and an adjoint in which the source term is proportional to the gradient of the objective function with respect to the original fields. Once the derivatives have been computed locally, gradient descent is adopted as in LT for the search of local minima/maxima. The method, largely applied in the nanophotonics community [81], was recently implemented for the optimization of wavelength and polarization splitting OVEs [82] (see Figure 2:6.d). The most delicate operation of this approach is the derivation of the adjoint variable formalism. It was recently demonstrated that this step can be also combined or replaced by the same auto-differentiation algorithms developed in machine learning [83].

The similarity of the adjoint variable method and LT scheme with deep neural networks brings us directly to the fourth option for the inverse design of OVE shown in Figure 2:5. The highly non-linear relationship between dielectric constant and electric field can be mapped with a digital neural network. In the early stages this was done by



collecting a large amount of input-output pairs through numerical simulations, and successively training the network through a direct data-driven approach [84]. Deep enough networks trained with a massive dataset can in this case replace physics-based optimizations for the fast computation of gradients through backpropagation. Recently, different approaches have been proposed to overcome the burden of data collection. Lim et al. [49] proposed to replace the data-driven loss with a physics-based metric by numerically evaluating the residual of Maxwell's equations on the predicted field from the network. Such indirect training allows for avoiding numerical simulations. Importantly, it also provides a quantitative evaluation of the capability of the network in returning fields that satisfy Maxwell's equations, instead of just creating an interpolation between input and output images. Although the training remains the most time-expensive process and it requires scanning a large space of parameters before the network is able to generalize to unseen distributions, inference time and gradient computation are an order of magnitude faster than the adjoint method or LT.

As an alternative, Deep Neural Networks (DNNs) have been proposed for the solution of partial differential equations [85], [86]. In this case, the input is not the permittivity distribution but independent variables, such as time and spatial coordinates, and backpropagation is used to rapidly compute the derivatives of the output fields with respect to these latter ones and construct a physics-based loss. Chen et al. [87] demonstrated such physics-informed neural networks for the inverse design of cloaking metamaterials. In contrast with the previous implementation, the network is trained for satisfying Maxwell's equations and minimizing the difference between output and target fields for a single permittivity distribution and the training has to be performed from scratch for every design task. In both cases, the ability of DNN in mapping deeply nonlinear functions in high dimensional spaces embodies a key ingredient for the realization of 3D optical devices with complex functionalities. Another key concept that makes employing neural networks in the design process is the ability to express high dimensional computational volumes (one can assume the number of voxels as the number of dimensions in the optimization problem) in smaller dimensions, or in other words in latent space representation [49], [88]. This paves the way to optimize large objects that require a heavy computational cost for even a single-pass simulation with the finite difference or finite element methods.

## 2.5 Conclusion and outlook

Neural networks are emerging as an effective tool for the design of photonic circuits. Tomography, on the other hand, has a longer history and tackled some of the problems already. Therefore, photonic circuit design has a lot to learn from tomography. Another interesting relation arises with tomography when we consider the transmission matrix approach [89]. One can probe the response of a 3D medium by using different inputs (illuminations) and construct the transmission matrix mapping input to output patterns, enabling to structure illumination for a desired response [90]. Once the transmission matrix is obtained, one can use tomography algorithms to figure out the 3D distribution since the required projections can be extracted from the matrix. This equals to say that one can design a transmission matrix providing the desired mapping and use tomography tools to obtain the 3D media. This clarifies the strong connection of tomography with the 3D photonic circuit design.

On the other hand, these circuits can be used to alleviate the heavy digital computations. It was recently demonstrated, for instance, phase recovery [77] by optically implemented networks, which can provide some portion of the required information for optical tomography. Phase recovery, unwrapping, and combining different streams of data from different projections yield a computational burden, which is quite heavy considering that the given problem is, in addition, ill-posed and nonlinear. Optical networks can accelerate the computation by pre-processing the data, which would not require an additional Electrical-to-Optical conversion as the data is already in the optical domain.

The design of 3D circuits can be often cumbersome and subjected to strong technological constraints. Here, additive manufacturing techniques come to the rescue for the fabrication of complex 3D shapes. Considering the resolution, two-photon polymerization appears to be the needed tool since features comparable to optical wavelengths can be printed. Moreover, graded-index optical elements are also demonstrated using two-photon polymerization [91],

[92], which increases the degrees of freedom by introducing the refractive index variance on top of the geometrical degrees of freedom. However, the point-scanning nature of two-photon polymerization yields long fabrication times, making commercial-grade manufacturing challenging. To speed up the fabrication combining one-photon and two-photon techniques is also proposed [93]. From the fabrication time aspect, volumetric additive manufacturing lays a very promising route. The Radon transform-based inverse tomographic approach already provided sub 100- $\mu\text{m}$  resolution, which is striking considering the centimeter scale of the printed objects. Employing tomographic algorithms that incorporate the effects of diffraction might further increase the resolution while maintaining the fast fabrication scheme of volumetric printing, making it a future-candidate fast approach for the fabrication of photonic circuits.

Lastly, we reviewed the recent studies on 3D optics for functional mappings considering the various design approaches and algorithms, namely starting from optical interference for 3D optical memories to adjoint optimization, learning tomography, data-driven error backpropagation through a physical forward model and physics-inspired deep neural network implementation.

Considering the computational difficulty of the classical numerical tools, neural networks are becoming an attractive tool for the 3D optics and photonic circuit design as they have already become for tomography to solve the fundamental challenges of 3D-2D transformations. The fact that improvements in the photonic circuitry would yield accelerated and power-efficient neural network architectures tends to remove the boundary between these two disciplines.

# Chapter 3 3D printing multilayer optics for multiplexing

This chapter is the post-print version of the following article published in *Nanophotonics*.

**Computer generated optical volume elements by additive manufacturing** by Niyazi Ulas Dinc<sup>1,2</sup>, Joowon Lim<sup>1</sup>, Eirini Kakkava<sup>1</sup>, Christophe Moser<sup>2</sup> and Demetri Psaltis<sup>1</sup>

<sup>1</sup>Optics Laboratory, École polytechnique fédérale de Lausanne, Switzerland

<sup>2</sup>Laboratory of Applied Photonics Devices, École polytechnique fédérale de Lausanne, Switzerland

*Nanophotonics*, Volume 9, Issue 13 (2020)

<https://doi.org/10.1515/nanoph-2020-0196>

Computer generated optical volume elements have been investigated for information storage, spectral filtering, and imaging applications. Advancements in additive manufacturing (3D printing) allow the fabrication of multilayered diffractive volume elements in the micro-scale. For a micro-scale multilayer design, an optimization scheme is needed to calculate the layers. The conventional way is to optimize a stack of 2D phase distributions and implement them by translating the phase into thickness variation. Optimizing directly in 3D can improve field reconstruction accuracy. Here we propose an optimization method by inverting the intended use of Learning Tomography, which is a method to reconstruct 3D phase objects from experimental recordings of 2D projections of the 3D object. The forward model in the optimization is the beam propagation method (BPM). The iterative error reduction scheme and the multilayer structure of the BPM are similar to neural networks. Therefore, this method is referred to as Learning Tomography. Here, instead of imaging an object, we reconstruct the 3D structure that performs the desired task as defined by its input-output functionality. We present the optimization methodology, the comparison by simulation work and the experimental verification of the approach. We demonstrate an optical volume element that performs angular multiplexing of two plane waves to yield two linearly polarized fiber modes in a total volume of  $128\mu\text{m}$  by  $128\mu\text{m}$  by  $170\mu\text{m}$ .

## 3.1 Introduction

Optical volume elements (OVEs) can be defined as media whose transmission or reflection properties strongly depend on the spatial or spectral shape of the incident beam. Examples to OVEs consist of fiber Bragg gratings, volume holograms, photonic crystals, photonic lanterns and multiple layers in stratified fashion. Volume holographic elements in particular have been investigated for information storage and processing applications [56], [58], [94]. For example, multiple pages of information (i.e. two-dimensional spatial signal, analog or digital) or holograms can be stored or multiplexed in a volume element, and they can be accessed selectively either by utilizing

different angles, wavelengths or phase distributions. Periodic structures in 3D media are widely used as optical filters in telecommunications and other applications [95].

The fabrication of such volume elements is done either by optical means (e.g. volume holography) or by lithographic deposition. In this paper, we present an approach to computationally design an OVE and fabricate it via additive manufacturing. Advancements in additive manufacturing based on two-photon polymerization (TPP) have made it practical to produce multilayered diffractive elements. TPP is a layer-by-layer technique and it offers great advantages in fabricating optically transparent arbitrary 3D micro/nanostructures [65].

There have been some studies to investigate the multilayer configuration of computer generated volume elements. Initially, computer generated 2-layer binary diffractive elements have been demonstrated experimentally with angular multiplexing for different diffraction patterns of letters [96]. Later, multilayer configurations have been shown for wavelength multiplexing of different letters [97], [98] and for spatial multiplexing of fiber modes [99]. Furthermore, a dynamic multilayer implementation utilizing a Spatial Light Modulator (SLM) has been shown for angular and wavelength multiplexing [72]. For the design process, an optimization scheme must be adopted. The above-mentioned studies used variants of generalized Gerchberg–Saxton algorithms [100]. Recently, algorithms that utilize the error backpropagation concept of deep neural networks have been used to calculate multi-layered diffractive elements to carry out different tasks including classification [6], [101]. The output of such algorithms is a stack of phase masks that should satisfy the thin element approach. These phase mask layers are physically implemented by thickness variations. Hence, there is a fundamental limit for the compactness of these designs, since the maximum thickness variation in each layer should be negligible when compared to the layer separation. Otherwise, there is a degradation in diffraction efficiency since the phase retardation that should be introduced by the mask and its representation by thickness variation start to differ significantly. We define this degradation as representation error, whose effect is shown in subsequent sections. To prevent representation error, the thickness variation of the layers should be taken into account during the optimization. In other words, the algorithm should optimize the thickness variation directly to realize a desired functionality of the 3D structure. Learning tomography (LT), which is a method to reconstruct 3D phase objects from experimental recordings of 2D projections of the 3D object [42], [43] is adapted by inverting its intended use to calculate the 3D index distribution of the OVE from examples of desired input-output pairs.

## 3.2 Methodology

A commercial Direct Laser Writing (DLW) system (Nanoscribe Photonic Professional GT) is used to fabricate a micro-scale optical element. This printer utilizes TPP, initiated by a laser beam highly focused into the volume of the photosensitive resin, yielding solidification. After the writing process of the desired structures inside the resin, the development step (washing out of the non-illuminated regions) follows, which yields the final polymerized material in the written 3D form. This binary nature of TPP constrains the design accordingly. In other words, the available refractive index values to achieve modulation are only  $n_{polymer}$  and  $n_{background}$ . If the structure is not immersed in another material, the  $n_{background}$  simply becomes the refractive index (RI) of air. We implement modulation by varying the thickness of the polymer layers due to the same reason.

### 3.2.1 Optimization with LT

LT is a nonlinear optimization algorithm for optical diffraction tomography (ODT), which provides 3D RI distributions of transparent objects. The principle of ODT is to combine multiple 2D projections measured at different illumination angles to provide 3D distributions of RI [30]. In order to do so, the relationship between the 3D index distribution of a sample and the field scattered by the sample should be properly modeled. Unlike conventional reconstructions algorithms based on the first order approximations, LT is able to capture high orders of scattering by utilizing models such as the beam propagation method (BPM) [42] or split-step non-paraxial method (SSNP) [43]. The overall scheme of LT is to utilize one of such methods as the forward model in an iterative reconstruction

scheme along with an intermediate step of regularization to impose our prior knowledge. This method has been referred to as *Learning Tomography* due to the multi-layer structure in the forward models, and depending on which model is used for the forward model, it can be further differentiated as LT-BPM or LT-SSNP. It has been shown [43] that LT-SSNP is the more accurate version of the mentioned methods. However, for small angles (i.e. multiplexing angles in OVE design and illumination angles for ODT) accuracy of LT-BPM and LT-SSNP are similar. In addition, LT-SSNP takes longer time for computation. Because of these reasons, we used LT-BPM in this work. In case of OVE design that utilizes high angles, LT-SSNP would be a better choice. This will be investigated in future work.

In this study, instead of experimental measurements obtained from ODT, LT is fed by the desired output field patterns. On the input side, these desired patterns have the plane wave illuminating fields at the corresponding incidence angles to establish angular multiplexing. Since 3D printing is a layer-by-layer technique, the computation volume is constrained to have RI change in a layer-by-layer fashion. The multilayer volume element and angular multiplexing schemes are demonstrated in the bottom part of Figure 3:1 for two input-two output case with three layers. For the desired fields, we arbitrarily decided to use linearly polarized (*LP*) fiber modes. Among them  $LP_{02}$  and  $LP_{21}$  are chosen arbitrarily. Both the typical use of LT for ODT and how we change its use to design OVEs in this work are depicted in Figure 3:1.

Here, the most fundamental difference between our adapted use and typical use of LT is that for the volume element optimization, we are not looking for a unique solution. Any RI distribution that gives the desired output fields as intended is equally acceptable. We used the following cost function in LT to design OVE:

$$\operatorname{argmin}_x \frac{1}{2L} \sum_{l=1}^L \left\| y_K^{(l)} - S_K^{(l)}(x) \right\|_2^2$$

Equation 3:1 – Cost function.

The above expression, consists of only the data fidelity term that calculates the difference between the desired output  $y_K^{(l)}$  and current prediction of the forward model  $S_K^{(l)}(x)$  for each multiplexing angle ( $l$ ).  $x$  is the current solution (3D RI distribution),  $L$  is the total number of angles and  $K$  stands for the last slice of the forward model. In ODT, there is also 3D total variation (TV) regularization term [102] in the cost function to impose edge sparsity, which introduces prior knowledge about object characteristics. In this work, we discard the regularization term and implement hard constraints to satisfy multilayer binary index structure.

To design a multilayer OVE, the algorithm is initiated with layers of uniform thickness. Alternatively it can be initiated with any initial guess. Conversion of the optimized phase masks into varying thicknesses as initial guess can speed up the process if the phase masks are available. Each layer consists of many thin slices in BPM. The last slices of each layer consist of active voxels. They are active in the sense that the refractive indices of these voxels are allowed to change according to the error reduction scheme. When the refractive indices reach the upper or lower limits (i.e. the RI of the 3D printed polymer or the background medium), the active voxels are elongated forward or backward respectively. This approach is demonstrated in Figure 3:2. For simplicity, a representative sketch of one layer is shown. At the end of the iterations, we have a multilayer structure of varying thicknesses as shown previously in Figure 3:1. Note that optimization is not carried out in a binary manner since it prevents convergence of the algorithm.

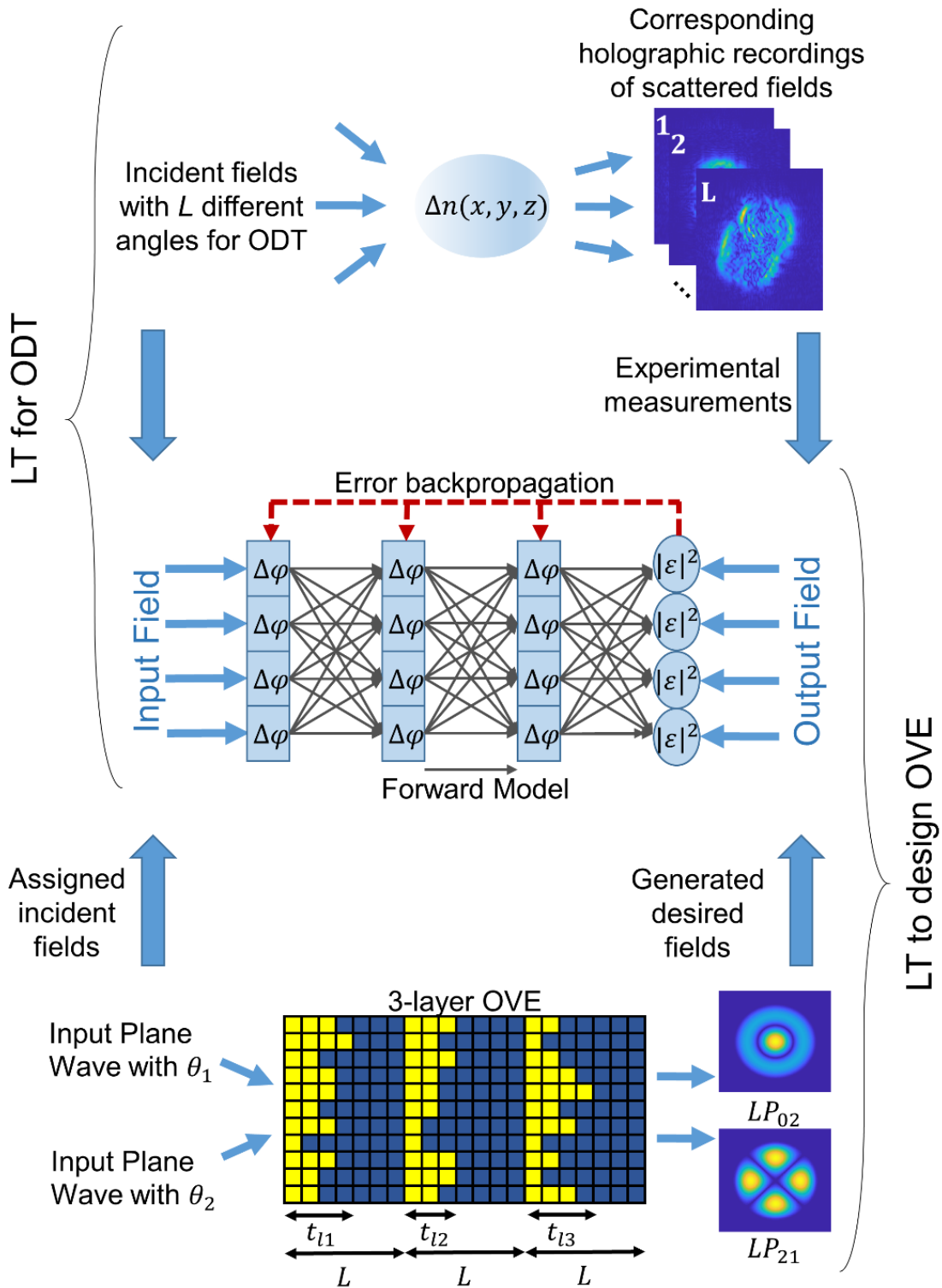


**Figure 3:1 – Optimization scheme of LT utilized in ODT and design of OVEs.**  $\Delta\varphi$  is the phase modulation of a voxel and  $|\varepsilon|^2$  is the mean squared error between the reconstructed field of the computational model and the desired output field. Even though the voxels are drawn separated to make room to indicate the forward model, they are physically adjacent. A representative sketch of a 3-layer computer generated OVE is shown in the bottom part.  $t_{l1}$ ,  $t_{l2}$ ,  $t_{l3}$  are layer thicknesses and  $L$  is the layer separation. For  $LP_{02}$  and  $LP_{21}$ , the amplitude maps are provided.

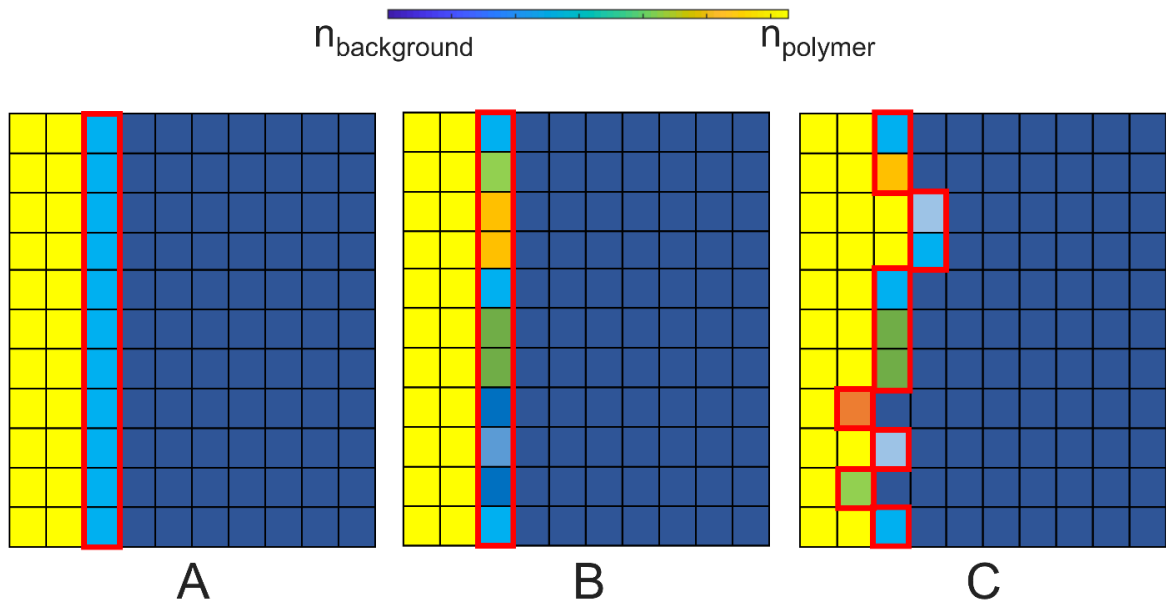


**Figure 3:2 – Representation of the optimization scheme on a single layer.** (A) Initialization step with a uniform layer and active voxels (shown with red boundaries). (B)  $n^{\text{th}}$  iteration where we observe changes of refractive index in active voxels. (C)  $m^{\text{th}}$  iteration where we observe the elongation of active voxels. Provided that:  $m > n > 1$ .

The resolution of the simulation and the manufacturing are important parameters to consider. For an accurate simulation, the necessary resolution is higher than the chosen 3D printing method. With Nanoscribe, a pixel size of  $2\mu\text{m}$  by  $2\mu\text{m}$  is the standard for diffractive optical element applications where smaller pixel sizes suffer from edges, which start to dominate as we decrease the size further. However, there is no constraint in axial direction except the resolution limit of the printer. For the forward model, we observed that a safe value for sampling interval is a quarter of the wavelength ( $\lambda/4$ ), which implies that for a  $2\mu\text{m}$  by  $2\mu\text{m}$  lateral size in 3D printing, approximately 64 voxels are necessary in one axial slice of BPM (when  $\lambda=1.03\mu\text{m}$ ). In our case, voxels of each slice are averaged in each iteration to take into account this lateral size limitation. In other words, the volume element is oversampled in the optimization process. The overall optimization scheme is summarized in Figure 3:3.

Another fundamental difference between the adapted version and the conventional version of LT is updating the RI. In conventional LT, the whole computation volume is updated whereas we update specific voxels (i.e. active voxels) to construct layer-by-layer volume elements. Another important difference to note is the synthetic generation of input-output pairs to establish the desired task. On the contrary, the output fields are experimentally recorded in tomography applications as depicted in Figure 3:1. Moreover, thickness limitations can be imposed on each layer if necessary.

### 3.2.2 Representation error

Representation error is the degradation of the fidelity in the reconstructed output fields after a multilayer OVE when the implemented layers do not satisfy the thin element approximation. To prevent representation error, topography (i.e. thickness variation) of the layers should be taken into account. BPM and SSNP are forward models that can account for the effects introduced by the topography of the layers since they represent these layers by having many sub-slices in the computation. We compare the performance obtained with and without LT in the propagation through the topographically encoded phase masks.

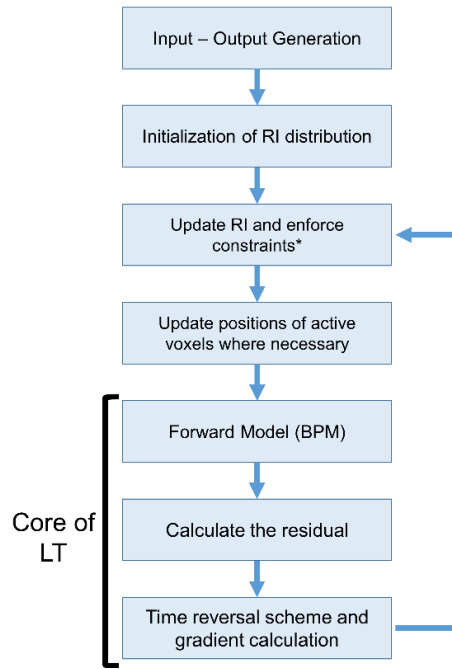


**Figure 3:3 – The scheme of the optimization based on LT.** \*Possible constraints are voxel averaging, RI limitations and thickness limitations.

If we do not elongate the active voxels and allow the RI to vary continuously, then our approach reduces to a phase mask optimization approach. In each layer, the active voxels are kept on a plane (the last BPM slice of each layer) and RI (or equivalently the phase modulation) is updated in each step, which yields a phase mask at the end. If we consider the optimization steps in Figure 3:2, the phase mask optimization is equivalent to carry out the iterations as shown in Figure 3:2.B and not carrying out the step shown in Figure 3:2.C. A stack of phase masks can be converted to thickness variation simply by the following equation:

$$t = \frac{\Delta\varphi}{2\pi(n_{polymer} - n_{background})} \lambda + t_{offset}$$

Equation 3:2 – Phase to thickness conversion.

In Equation 3:2,  $\Delta\varphi$  is the optimized phase of the corresponding pixel,  $t$  is the thickness that represents this optimized phase and  $t_{offset}$  prevents negative values. Let us call the maximum value of  $t$  within a layer as  $t_l$ , which can be seen as overall thickness variation of a layer. For simplicity, we set equal separation between layers, denoted as  $L$  in Figure 3:1. To demonstrate the effect of representation error, we conducted the simulation in two approaches. First, we imposed a constraint on  $t_l$  to keep it fixed. Also, we kept  $\Delta n = n_{polymer} - n_{background}$  fixed as 0.2. By varying  $L$ , different phase mask stacks are optimized. These phase mask stacks are converted to thickness varying elements by Equation 3:2. Then, we optimized the voxel elements with LT under the same constraints. We compared all these structures with structural similarity index metric [103] comparing the magnitudes of the obtained output with the desired output amplitudes. In Figure 3:4, the effect of representation error is shown by comparing structural similarity index between the calculated outputs and the desired outputs with respect to the ratio of layer thickness ( $t_l$ ) to the layer separation ( $L$ ) for a 3-layer volume element as depicted in Figure 3:1. Note that these volume elements are obtained via optimizing three layers to multiplex two incident plane waves with  $+3^\circ$  and  $-3^\circ$  incidence angles to yield  $LP_{02}$  and  $LP_{21}$  modes at the output plane. Second, we kept  $L$  fixed and varied  $\Delta n$  to obtain different  $t_l$  values via Equation 3:2. This creates a different scenario, but still shows the effect of LT optimization on the representation error. The obtained results are given in Figure 3:4.B.



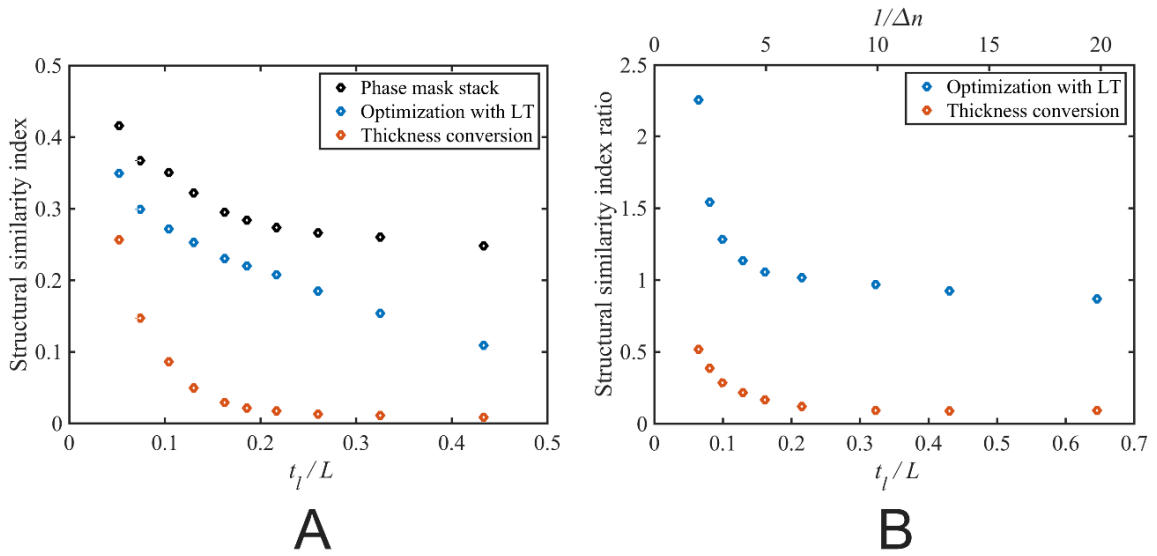


**Figure 3:4 – The representation error.** (A) Averaged structural similarity index of output fields  $LP_{02}$  and  $LP_{21}$  vs  $t_l/L$  (thickness variation/layer separation). (B) Averaged structural similarity index of output fields  $LP_{02}$  and  $LP_{21}$  divided by the average structural similarity index of corresponding discretized phase mask stack vs  $t_l/L$  and equivalently  $1/\Delta n$  for this scenario. See Section 1 and 2 of the Supplementary Material (Appendix A) for more details. Decreasing trend with increasing  $t_l/L$  demonstrates the effect of representation error.

As seen from Figure 3:4, optimization with LT provides a better performance. Moreover, in Figure 3:5, one can compare the target field, the output obtained by phase mask stack, to the output obtained by thickness conversion element with  $t_l/L = 7.5\%$  and the output obtained by direct optimization of the varying thickness by LT. The layers have  $80\mu\text{m}$  separation, which results in a volume element of approximately  $128\mu\text{m}$  by  $128\mu\text{m}$  by  $170\mu\text{m}$ . The improvement obtained by our method can be seen by comparing Figure 3:5.C and Figure 3:5.D.

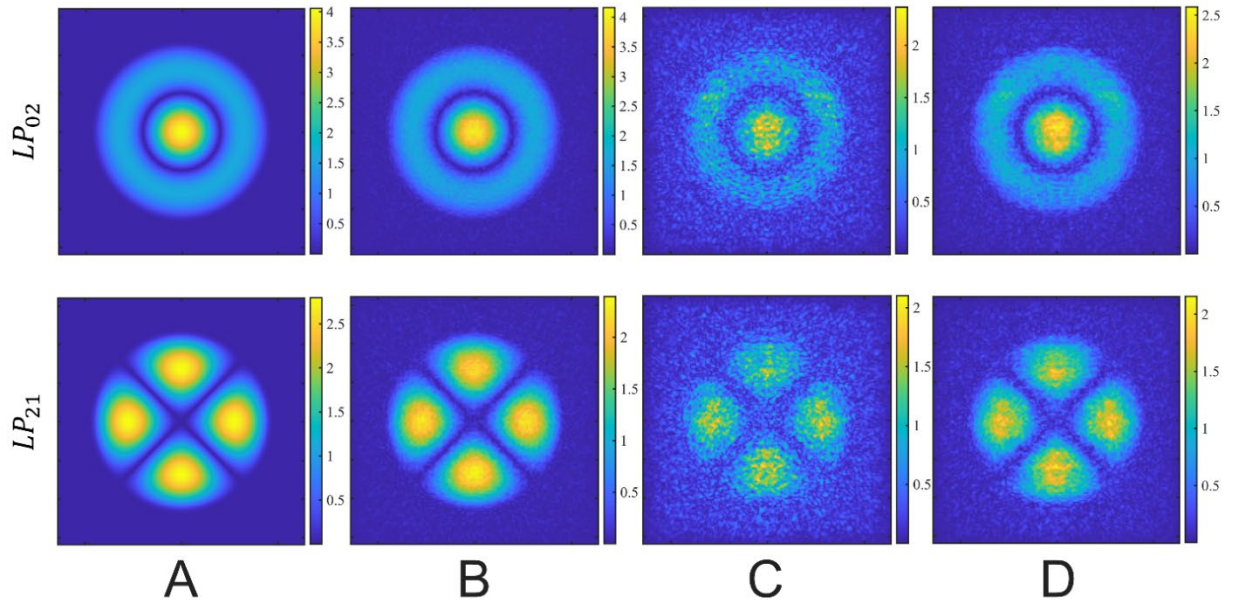


**Figure 3:5 – The representation error with field distribution examples.** (A) The amplitude of the desired output fields, (B) the amplitude of outputs simulated through phase masks stack volume element, (C) the amplitude of outputs simulated through thickness varying ( $t_l/L=7.5\%$ ) multilayer volume element, (D) the amplitude of outputs simulated through the result of varying thickness optimization by LT. All windows are  $128\mu\text{m}$  by  $128\mu\text{m}$ .

In Figure 3:6.A, the optimized phase distribution of the layers is provided, which is the volume element yielding the output fields in Figure 3:5.B. In addition, the thickness conversion from these phase masks is provided in terms of the thickness map in Figure 3:6.B, which gives the output fields in Figure 3:5.C. Finally, we see the thickness map of volume element optimized by LT in Figure 3:6.C, which gives the output fields in Figure 3:5.D. For comparison, difference of thickness distributions of simply converted volume element and LT-optimized volume element are given in Figure 3:6.D.

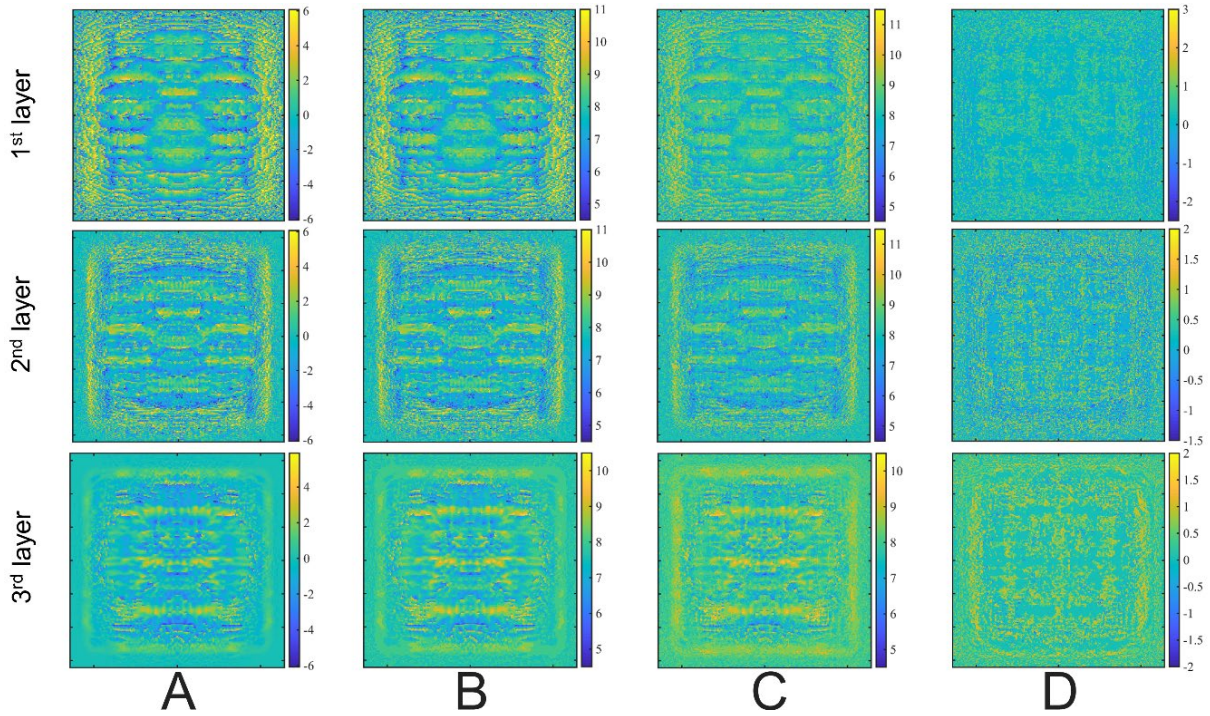


**Figure 3:6 – Comparison of layer topographies.** (A) The phase distribution of each layer of the 3-layer phase mask stack (colorbar represents phase in radians). (B) Direct thickness conversion from phase masks. (C) Optimization on thickness distribution by LT, (D) the difference between B and C. Colorbars for B, C, D show thickness in micrometers and all windows are  $128\mu\text{m}$ .

### 3.2.3 Full volume optimization

By changing writing parameters, it is possible to tune the RI to yield graded index (GRIN) materials with TPP [104]. However, the RI variation is quite low. Moreover, controllability and repeatability of the process are still challenging. If writing GRIN structures become more mature, then the true power of this optimization method can be further manifested for manufacturing of volume elements since the most significant advantage of this method is having access to all gradient values throughout the computation volume. By using GRIN writing, these volume elements become voxel-by-voxel encoded volume holograms, which should have higher diffraction efficiency in comparison with volume holograms that are recorded with optical means [105]. As a showcase, a volume of  $64\mu\text{m}$  by  $64\mu\text{m}$  by  $120\mu\text{m}$  is optimized to multiplex eight modes with RI variation of 0.15. Figure 3:7 depicts this GRIN element. The simulation results are given in Figure 3:8 in terms of amplitude of the output fields. Since our method optimizes with respect to electric field, we optimize both phase and amplitude. Section 3.1 of the Supplementary Material (Appendix A) provides both phase and amplitude of reconstructed fields and desired fields. The inputs are plane waves with different incidence angles as indicated in Figure 3:8.

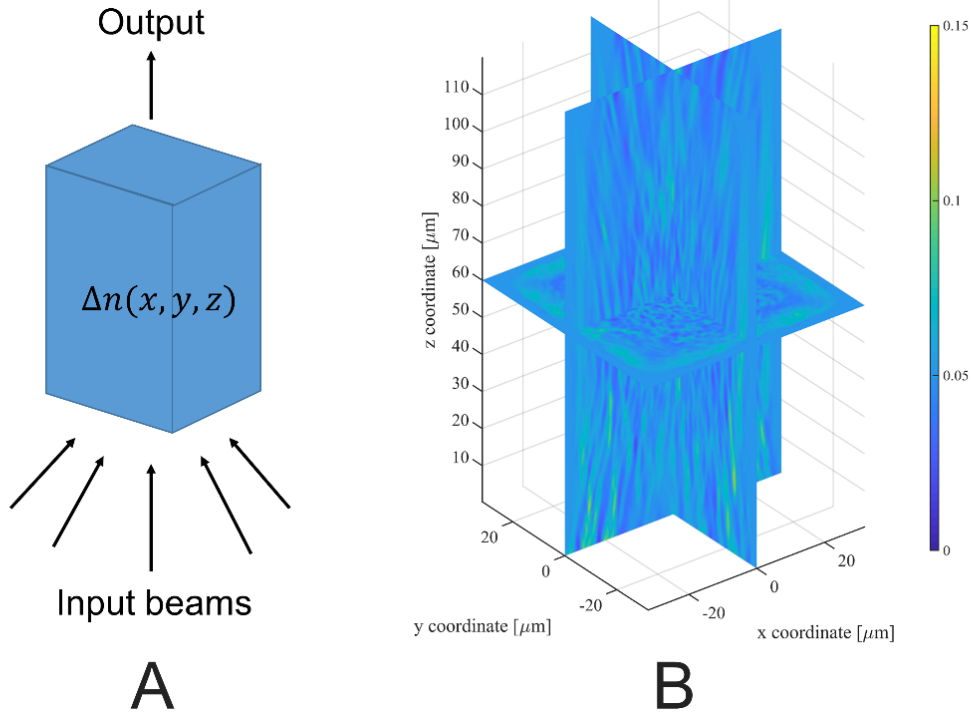


**Figure 3:7 – GRIN concept.** (A) Multiplexing scheme with GRIN volume element where  $\Delta n(x, y, z)$  stands for RI variation. (B) XY, YZ and XZ cut planes of the optimized volume by LT. Colorbar shows RI variation.

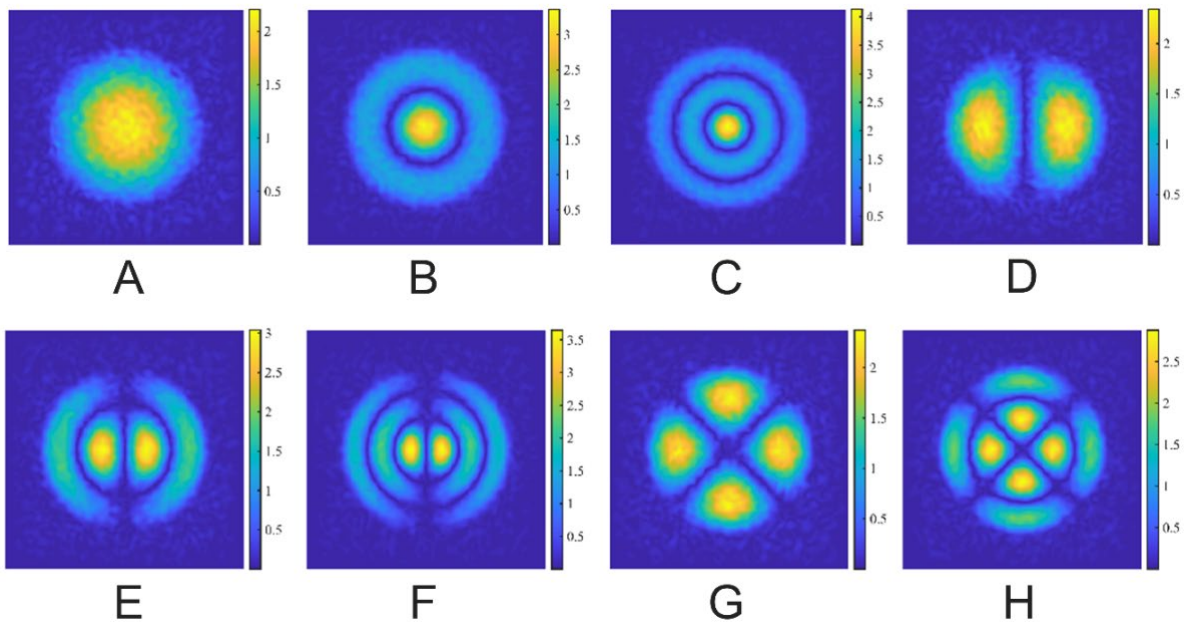


**Figure 3:8 – Amplitude of the reconstructed fields by GRIN OVE for different input angles.** (A)  $LP_{01}$  mode for  $\theta_x = -3^\circ, \theta_y = -3^\circ$  (B)  $LP_{02}$  mode for  $\theta_x = -3^\circ, \theta_y = 3^\circ$  (C)  $LP_{03}$  mode for  $\theta_x = 3^\circ, \theta_y = -3^\circ$  (D)  $LP_{11}$  mode for  $\theta_x = 3^\circ, \theta_y = 3^\circ$  (E)  $LP_{12}$  mode for  $\theta_x = 0, \theta_y = -5^\circ$  (F)  $LP_{13}$  mode for  $\theta_x = 0, \theta_y = 5^\circ$  (G)  $LP_{21}$  mode for  $\theta_x = -5^\circ, \theta_y = 0$  (H)  $LP_{22}$  mode for  $\theta_x = 5^\circ, \theta_y = 0$ . All windows are  $64\mu\text{m}$  by  $64\mu\text{m}$ .

Even though the relation between the RI and the output fields is nonlinear, the relation between input and output fields is linear. A lossless linear optical system that is designed to produce a specified pattern for a given illumination field (e.g angle of incidence of a plane wave) can also work in reverse producing the illumination field in re-

sponse to the specified pattern. In other words, the OVE designed for angular multiplexing can also act as demultiplexer. Moreover, the OVE acts as a correlator. This correlation manifests itself as the strengths of the resulted plane waves with specific angles. With LT, it is possible to design an OVE that learns how to correlate variants of classes such as handwritten digits provided that it is trained with many examples (See Section 3.2 of Appendix A).

### 3.3 Additive Manufacturing of the 3-Layer Volume Element and Results

The 3-layer volume element for multiplexing two incident plane waves with  $+3^\circ$  and  $-3^\circ$  incidence angles to yield  $LP_{02}$  and  $LP_{21}$  is fabricated by DLW.  $t_l/L$  ratio for this structure is 7.5%, which arises as a result of optimization when it converged. In other words, limitations on thickness have not been imposed. Nanoscribe photoresist IP-Dip is used with 63x objective. The optimized structure is given in Figure 3:9 with CAD rendering and Scanning Electron Microscope (SEM) images. There are four additional base layers with letter “T” as can be seen from Figure 3:9.B. These layers are useful for better adhesion of the volume element to the glass substrate and alignment in optical setup. We see that they slightly lifted of due to the development process after 3D printing.

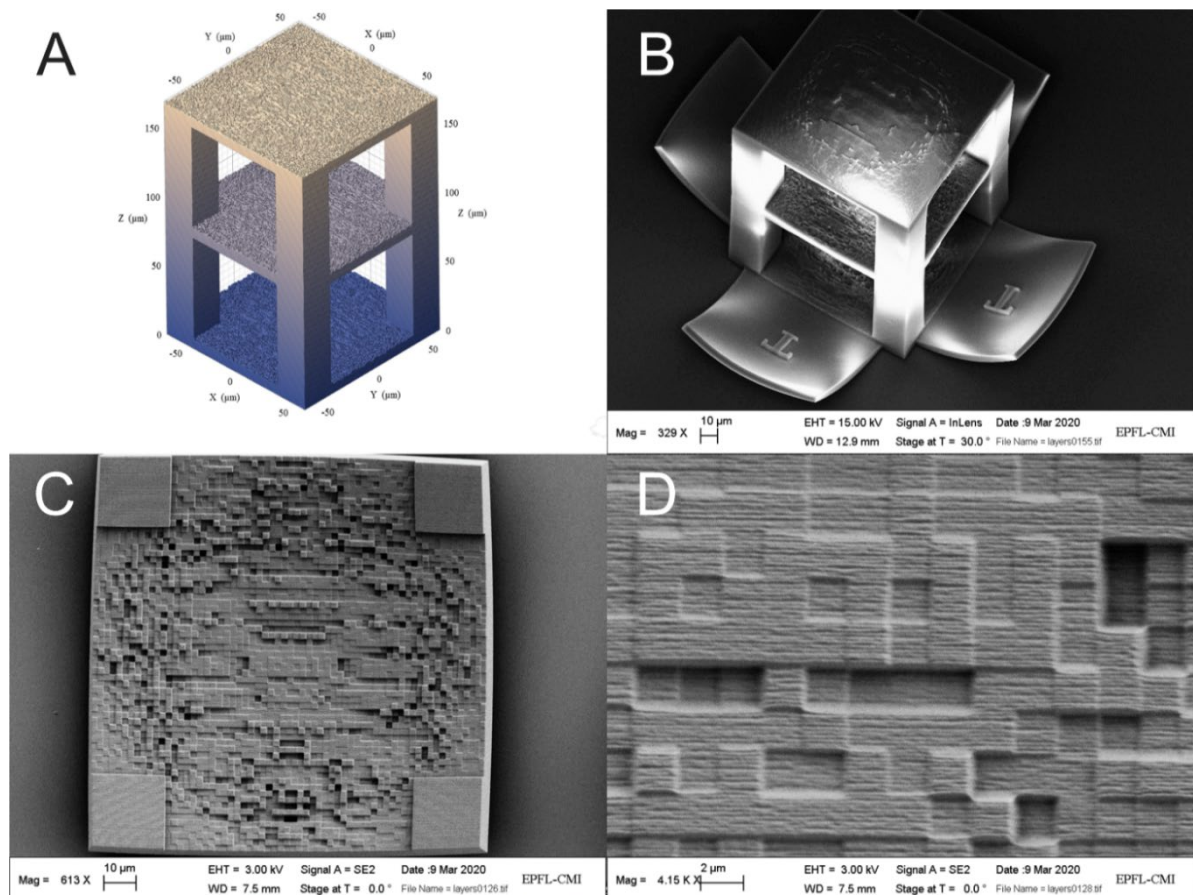


**Figure 3:9 – Multilayer multiplexer.** (A) CAD rendering of 3-layer volume element. (B) Scanning Electron Microscope image of the volume element with four additional bases on sides. (C) One layer of the Volume element. (D) Zoomed in version to show  $2\mu\text{m}$  by  $2\mu\text{m}$  lateral size of voxels.

The experiments for testing the multiplexing capabilities of the printed structure were performed by using an optical setup in which a spatial light modulator (SLM, Pluto-NIR2, Holoeye) is used to change the angle of incidence beam to the volume element. As the light source, Amplitude Laser - Satsuma generating pulses at 1030nm is used. After the volume element, a 4f imaging system is used to record the output field. In the experiments, we observed an increase in the high-frequency noise compared to simulations. One source of error is 3D printing in terms of the

shrinkage of the polymer after development, edge effects and slight RI deviation. The effect of shrinkage can be observed in Figure 3:9.C and Figure 3:9.D. In Figure 3:9.C, we see that the sides of the given layer are curved, which implies that the structure shrunk. In addition, size of the structure is less than the design value of  $128\mu\text{m}$ . In Figure 3:9.D, we can see that transverse dimensions of the voxels are slightly less than the design value of  $2\mu\text{m}$  for this sample. Another source of error is the optical setup in terms of the non-ideal illumination beam shape and slight misalignments. To prevent high-frequency noise, we put an iris in the Fourier plane of the imaging  $4f$  system to block the high frequencies. The output intensity measurements corresponding both specified illumination angles are given in Figure 3:10.

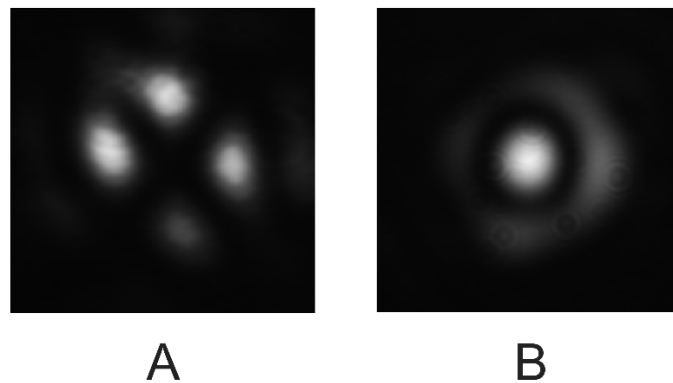


**Figure 3:10 – Multiplexing results.** The experimental output intensity of the volume element for (A)  $+3^\circ$  incidence angle to yield  $LP_{21}$  and (B)  $-3^\circ$  incidence angle to yield  $LP_{02}$

We have tried oversampling for both  $2\mu\text{m}$  by  $2\mu\text{m}$  and  $1\mu\text{m}$  by  $1\mu\text{m}$  lateral dimensions. Having a smaller voxel size is advantageous since it increases degrees of freedom in a fixed volume and enables modulating higher frequencies. However, the disadvantage is degradation due to edge effects which is depicted in Figure 3:11 with high aspect ratio pillars (i.e. high  $t_l$ ) whose lateral dimensions are  $1\mu\text{m}$  by  $1\mu\text{m}$ . In our experiments, we have not observed a significant difference between the two configurations. Probably, observed noise is dominated by other factors.

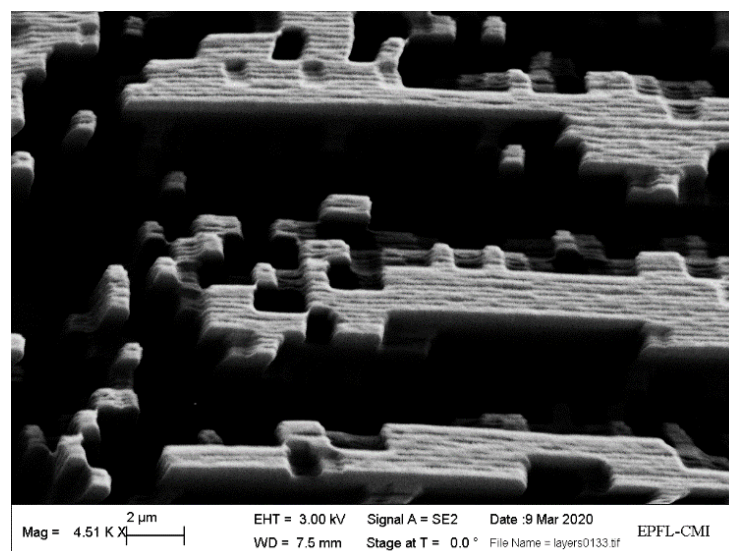


**Figure 3:11 –  $1\mu\text{m}$  by  $1\mu\text{m}$  pixels manufactured with high aspect ratio,** which demonstrates the degradation in 3D printing quality on edges more dramatically.

## 3.4 Conclusions

In this study, we have proposed a new optimization scheme to calculate OVEs and investigated angular multiplexing property. Practical constraints enforce a multilayer volume element with the binary RI. Our proposed method can adapt to these constraints and optimize an OVE directly in 3D. In other words, there is no intermediate step of optimizing the stack of phase masks and converting the phase values to corresponding thickness values for physical implementation. We showed that this approach improves the performance especially when the layer separation becomes comparable with the thickness variation of each layer. Moreover, our proposed method can reconstruct a continuous RI variation in the whole volume to yield a computer generated, voxel-by-voxel encoded volume hologram, which might show improved efficiency and storage capacity per volume. Additive manufacturing allows reaching every voxel individually in the printing process, which means that we can translate the degrees of freedom that we have computationally to physical implementation if the printed RI values are varied in a manageable manner. Further investigation for ways of manufacturing such an element is planned, using GRIN that shows more promising results.

For multilayer configuration, we used additive manufacturing, specifically TPP, to experimentally verify our method. We observed that the OVE perform angular multiplexing and reconstruct the desired output fields as intended. However, we see more high-frequency noise than what we have in our simulations, which can be due to additive manufacturing imperfections and optical setup imperfections as mentioned. In our optical setup, high-frequency noise is filtered in the Fourier plane so that satisfactory outputs are recorded at the expense of high-frequency information. Another factor is that our forward model (BPM) does not count for reflections and this can create a discrepancy. More accurate forward models are computationally too heavy as soon as the computation volume becomes larger than  $(20\mu m)^3$ . This is another aspect of the follow-up work. In this study, the dimensions of experimentally verified structure are approximately  $128\mu m$  by  $128\mu m$  by  $170\mu m$ , which succeeds to multiplex two different input beams and reconstruct two different output patterns in such a small volume.

# Chapter 4 Direct (3+1)D laser writing of graded-index optical elements

This section is the post-print version of the following article published in *Optica*.

**Direct (3+1)D laser writing of graded-index optical elements** by Xavier Porte<sup>1,†</sup>, Niyazi Ulas Dinc<sup>2,3,†</sup>, Johnny Moughames<sup>1</sup>, Giulia Panusa<sup>2</sup>, Caroline Juliano<sup>2</sup>, Muamer Kadic<sup>1</sup>, Christophe Moser<sup>3</sup>, Daniel Brunner<sup>1</sup>, and Demetri Psaltis<sup>2</sup>

†Equally contributing authors

N.U.D. led the design, fabrication, and characterization of the volume gratings and volume holograms whereas X.P. led the design, fabrication, and characterization of waveguides.

<sup>1</sup> Institut FEMTO-ST, Université Bourgogne Franche-Comté, CNRS UMR 6174, Besançon, France

<sup>2</sup> Optics Laboratory, École Polytechnique Fédérale de Lausanne, Lausanne, Switzerland

<sup>3</sup> Laboratory of Applied Photonics Devices, École Polytechnique Fédérale de Lausanne, Lausanne, Switzerland

*Optica*, Volume 8, No 10 (2021), <https://doi.org/10.1364/OPTICA.433475>

We propose a single-step fabrication of graded-index optical elements by introducing the light exposure as the additional dimension to three-dimensional (3D) laser writing, hence (3+1)D writing. We use a commercial printer and photoresist to realize the proposed single step fabrication method that can be swiftly adopted for research and engineering. After presenting the characterization of the graded-index profiles via basic structures, we demonstrate two different optical devices: volume holograms that are superimposed using angular and peristrophic multiplexing, and optical waveguides with well-defined refractive index profiles. In the latter, we precisely control the propagating modes via tuning the (3+1)D-printed waveguide parameters and report step-index and graded-index core-cladding transitions.

## 4.1 Introduction

Additive manufacturing by two-photon polymerization (TPP) is rapidly becoming an important hybridization tool among various photonic integrated platforms due to its high versatility. Neither photo-masks nor etchings are required for additive manufacturing, and intricate dielectric photonic structures can accommodate a wide range of host platforms, for example quantum systems [106], silicon photonics [23] or the tip of fibers [107]. Crucially, this fabrication technology is largely agnostic to particularities of such host platforms. Sub-wavelength feature sizes, i.e. beyond diffraction limit resolution, makes TPP highly attractive for meta-optics [108], high density photonic integration [73], [74] as well as for functionalization via free-form optical components [109], [110] and multilayer

diffractive elements [66]. These applications often require intricate designs, and the precise control of analogue 3D refractive index distributions in 3D additive manufacturing is highly desirable. Besides the binary index approaches mentioned above, there are multi material approaches to have additional degrees of freedom on top of geometry. Sequentially introducing different photoresists through microfluidic channels have been reported [111], [112]. Two-component photopolymers are reported as high dynamic range alternatives [113]–[115] and multiple patterning on these materials for even more dynamic range has been demonstrated [116]. Recently, graded-index (GRIN) lenses have been demonstrated, relying on varying polymerization inside a porous host material [92]. In addition, fabrication of a cell phantom via TPP that has multiple refractive index values by varying polymerization has been reported [117]. In this work, we also rely only on a single polymer to obtain GRIN optical volume elements in a single step with a 3D printing machine by having the exposure as the fourth variable in the writing process; hence establishing (3+1)D printing to access and modify each voxel's refractive index independently. For that purpose, we rely on the exposure-dependent refractive index of broadly utilized commercial photoresists [104], [118]–[120], dynamically modifying the exposure during the printing process to construct optical waveguides and volume holograms with single-step, single-material, and fully commercially available process.

The waveguide is a principal component of integrated photonics, as evidenced through applications like photonic wire bonding [121], [122], on-fiber direct laser writing [107], [123] and in the context of scalable photonic interconnects [73], [74]. Core-cladding 3D-laser printed structures guide light with a refractive index of the core moderately larger than that of the cladding. Such waveguides are currently the subject of intense study, and basic photonic tools like single-mode low-loss waveguides [124] or multimode light splitters [125] are being demonstrated. However, those either require direct inscription into a bulk material [92], intricate 3D photonic crystal fiber structures [126], or a multi-step process relying on different materials to provide the required refractive index difference between core and cladding [23], [127]. Our approach based on (3+1)D printing requires a single fabrication step only and enables precise control of the refractive index's profile.

Another fundamental and highly relevant 3D structure is the volume hologram [56], [58], [94]. A stack of 2D images can be multiplexed in a volume hologram and each of these images can be retrieved individually by employing different angles, wavelengths or phase distributions. In a volume hologram, each 2D data corresponds to an individual hologram to be multiplexed with several others. Its high resolution makes TPP suitable for fabricating such volume holograms. Crucially, since TPP provides independent access to each voxel in the fabrication volume, a hologram can be designed digitally without considering a recording schedule and avoiding the crosstalk between the individual recording sequences.

Figure 4:1 illustrates our GRIN printing concept for the two applications discussed here: volume holograms (Figure 4:1(a)) and photonic waveguides (Figure 4:1(b)). Leveraging such (3+1)D, or gray-tone lithography, our technique elegantly capitalizes on available and established 3D TPP materials and equipment and can be widely adopted without delay.

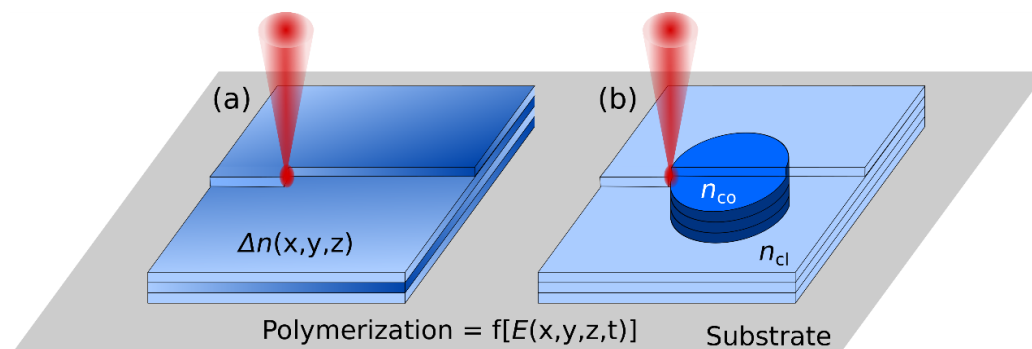


**Figure 4:1 – Concept of (3+1)D printing:** the refractive index ( $\Delta n$ ) is controlled by dynamically changing the laser power during the printing process ( $E(x,y,z,t)$ ). Illustration of this concept in a (a) volume grating used for holography and a (b) photonic waveguide with a step-transition between refractive indices of the central core ( $n_{co}$ ) and the surrounding cladding ( $n_{cl}$ ), printed with respective laser beam field amplitudes  $E_{co} > E_{cl}$ .



## 4.2 Fabrication methodology

The Clausius–Mossotti relation states that the refractive index of a material depends on the number of molecules per unit volume. Many photo-resins yield greater density in the polymer phase than in the resin phase, and the degree of polymerization depends on the polymerization kinetics which is driven by light intensity and exposure time. Thus, the refractive index can be modulated by changing the light exposure [104], [118], [120], [128]. We use this physical mechanism to demonstrate GRIN structures printed with the (3+1)D principle. We used commercial direct-laser writing systems from Nanoscribe GmbH (Photonic Professional GT+) and the negative tone photoresist "IP-Dip".

The (3+1)D printing process can be dissected in the following steps: the photoresist is dropped on a fused silica glass substrate ( $25 \times 25 \times 0.7 \text{ mm}^3$ ) and is photo-polymerized via TPP with a 780 nm femtosecond pulsed laser, focused by a 63X (1.4 NA) microscope objective. The printing process was realized in consecutive horizontal layers as schematically illustrated in Figure 4:1, and the laser power was dynamically modified for each voxel to produce the desired 3D refractive index distribution. The vertical (slicing) and the horizontal (hatching) sampling resolution is  $0.3 \text{ }\mu\text{m}$  and  $0.1 \text{ }\mu\text{m}$ , respectively. For volume holograms, the scan speed of the writing beam was chosen to be  $7 \text{ mm/s}$  and the laser power range is set to be 28-42% of the maximum average power that is  $20 \text{ mW}$ , while for photonic waveguides, scanning speed was chosen to be  $10 \text{ mm/s}$  and the laser power range was set to be 35-58% of the maximum average power. Therefore, the utilized laser fluences ( $\text{J/cm}^2$ ) per unit volume are comparable for both applications, once normalized with respect to the scan speed. The particular values are the result of a careful optimization, balancing the refractive index uniformity and mechanical stability. Very low degrees of polymerization result in unstable structures that do not hold the intended shape, while very high degrees of polymerization are unavailable due to burning and micro-explosions occurring during writing. We used an off-axis digital holographic interferometry (DHI) setup for the principle identification of conditions resulting in good structure-refractive index fidelity (see Appendix B.1 for further details). After printing and during the development process the non-polymerized leftover resin is washed away for the fabrication of the waveguides. The development process results in a low degree of structural shrinkage, where in particular volumes of relatively lower degrees of polymerization are affected. As waveguides are embedded in a comparably large surrounding volume, the vital part of core stability is inherently given and shrinkage is no issue. However, the development step is skipped for volume gratings and holograms so that shrinkage that is occurring due to development is avoided and that the liquid resin serves as an index matching liquid. For high exposure values, the polymerization yield is complete and the material is mechanically stable [129].

## 4.3 Characterization of the GRIN profiles

To calibrate the laser power vs refractive index relation, a rectangular prism is printed with the power increasing linearly along one transverse dimension. The phase accumulation through this structure is measured by DHI. Knowing the thickness, the measured phase is converted to a refractive index difference with respect to the background, which is the not polymerized resin. The obtained index difference is given in Figure 4:2(a). An exponential curve is fitted on the experimental data, which we use for mapping a desired refractive index to writing power. This is particularly crucial for writing gratings and holograms since an accurate refractive index distribution is essential for maximum diffraction efficiency. Hence, the laser power is adjusted according to the target refractive index value at each voxel position.

In Figure 4:2(b), we provide the mean and standard deviation of this measurement obtained from five different samples fabricated with the same writing scheme and parameters. This averaged measurement results in relatively large error bars, especially towards the low index difference. The first reason, which applies to all the data points, is the noise level in the digital interferometry setup for the phase measurements. The second reason are small sample to sample variations in the laser writing caused by allocation of the sample interface. Optical resolution limits the accuracy of allocating this interface to a few tens of nanometers, which in turn leads to different phase

accumulation along the thickness of the sample and hence a systematic offset variation for each sample. On top of that, slightly different focusing in DHI for different samples contributes to sample-to-sample differences. These effects become relatively higher for the regions where the refractive index change is small (see Appendix B.2 for further details). Since the relative index change within a sample is more meaningful, we stick with the calibration curve and following power adjustment obtained from a single sample. Nonetheless, we provide the result by averaging over different samples as a general reference as it reports relevant information about the fabrication process. The significant effect of the nonlinear power vs refractive index relationship is shown in Figure 4:2(c), where phase extractions are given from sinusoidal gratings that are printed assuming linear power dependence assumption and the exponential fit to experimental data. The arrows in the zoom-in panels of Figure 4:2(c) highlight distortions on the sine wave due to the saturation of refractive index (or polymerization) at high power caused by the linear approximation.

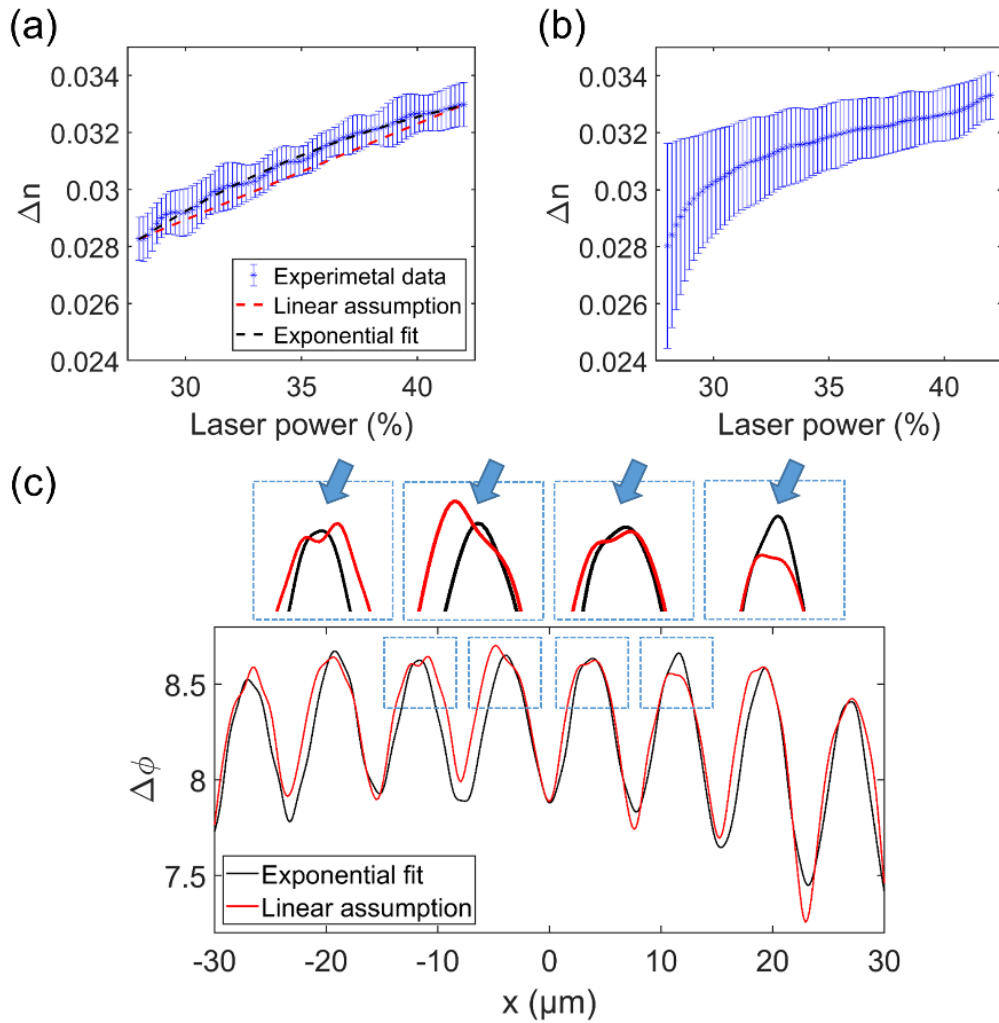


**Figure 4:2 – Exposure calibration.** (a) Refractive index difference of the polymerized part with respect to the monomer resin vs laser power from a sample. (b) Refractive index difference of the polymerized part with respect to the monomer resin vs laser power obtained from five samples. (c) Phase extractions from the 20- $\mu\text{m}$  thick sinusoidal gratings printed with linear power dependence assumption and the exponential fit where the arrows highlight the effect of saturation.

To cross-validate the obtained results from DHI experiments, we printed several volume gratings. A volume grating is a sinusoidal refractive index distribution in any orientation. Therefore, any arbitrary distribution can be represented by a superposition of volume gratings, which makes it the fundamental 3D building block of GRIN volume elements. We printed unslanted volume gratings with a 6  $\mu\text{m}$  period, which yields approximately 3.2° Bragg angle at 1.03  $\mu\text{m}$  wavelength in 1.52 refractive index. The transverse dimension is (120  $\mu\text{m}$ )<sup>2</sup> and the thickness is varied from 30  $\mu\text{m}$  to 120  $\mu\text{m}$  in 30  $\mu\text{m}$  steps. High dynamic range and sample thickness lead to over-modulated gratings

where the diffraction efficiency at the Bragg condition decreases and the energy goes to the lateral lobes in the angular spectrum [130]. Gratings thicker than  $120\ \mu\text{m}$  are not investigated to keep the samples in the under-modulated regime. The calibration curve shown in Figure 4:2(a) is utilized to fabricate the sinusoidal GRIN profile as depicted in Figure 4:3(a), where all the volume is polymerized with different degrees of polymerization by (3+1)D printing and targeting a dynamic range of  $\Delta n = 5 \cdot 10^{-3}$ . Figure 4:3(a) shows the  $90\text{-}\mu\text{m}$  thick grating where the  $z$ -axis is the optical axis. All the volume gratings are printed on the same substrate with  $250\text{-}\mu\text{m}$  center-to-center separation. The first,  $30\text{-}\mu\text{m}$  thick grating takes 40 minutes to fabricate, which is the same for uniform exposure of an equivalent structure in terms of size, sampling, scanning speed; varying exposure does therefore not impact fabrication time, and fabrication time only scales linearly with the printed volume.

A collimated beam with a dimension that is comparable to the transverse area of a single volume grating is used as the input beam. This input beam illuminated each volume grating one by one, and the transmitted beam is recorded while the input angle is varied to measure Bragg selectivity. The efficiency vs thickness curve is given in Figure 4:3(b). By using the coupled wave theory pioneered by Kogelnik [55], [131],  $\sin^2$  curve fitting is performed. From the argument of the  $\sin^2$  fit,  $\Delta n$  is found to be  $5.1 \cdot 10^{-3}$ , which is in excellent agreement with the targeted dynamic range and hence an independent confirmation of the rectangular prism-based calibration via DHI. The angles of the input plane waves are swept around the Bragg angle for all samples of different height, and the efficiency relation by [55], [131] is employed for curve fitting as exemplified in Figure 4:3(c) for the  $90\ \mu\text{m}$  thick grating. The first null is labeled as  $(\Delta\theta)_B$  referring to Bragg selectivity. Figure 4:3(d) shows the Bragg selectivity for all thickness values along with the theoretical curve that is numerically calculated for  $\Delta n = 5.1 \cdot 10^{-3}$ , where we observe a good match with the experimental results (see Appendix B.3 for further details).

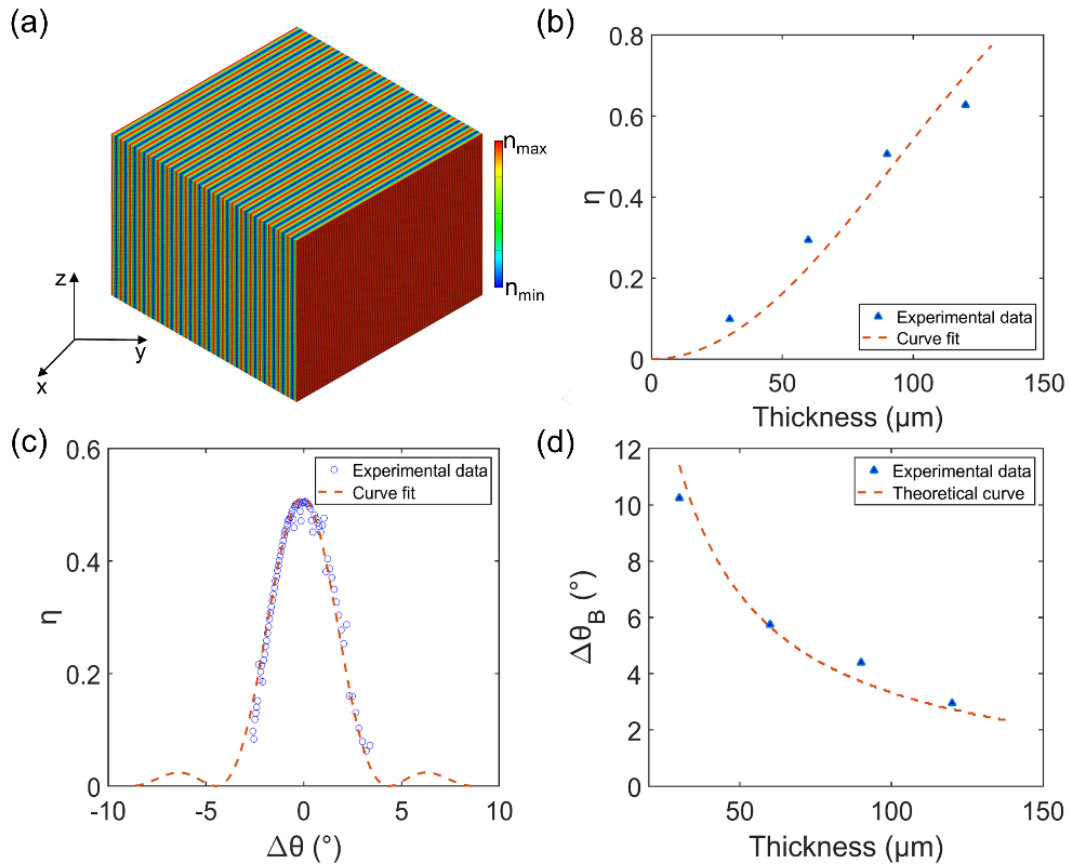


**Figure 4:3 – Volume grating characterization.** (a) Visualization of the printed volume gratings, (b) the efficiency vs the structure thickness plot, (c) the Bragg selectivity measurement around the Bragg angle for the grating of  $90\text{-}\mu\text{m}$  thickness, (d) the Bragg selectivity vs the structure thickness plot of the experimental data along with the numerically calculated theoretical curve.

Finally, the optical response of (3+1)D printed samples does not significantly change over time, indicating that there is negligible aging effect, which is in accordance with the results reported in [119], while the final density of the material can be subject to small changes due to diffusion of monomers and post-polymerization. In Appendix B.4, we provide DHI measurements of the same phase grating on various days after fabrication, where we do not observe any difference larger than experimental error range. The same finding was confirmed independently based on our waveguides, which did not experience modifications over a time-span exceeding one year.

## 4.4 GRIN optical elements

### 4.4.1 Volume holograms

Volume holograms have been of great interest for parallel optical interconnects [25], data storage [61] and optical mode multiplexing and demultiplexing [66], [132]. TPP has also been identified as a candidate technique for optical data storage [18]. When a hologram is optically recorded in a photosensitive medium by interfering a reference ( $E_{\text{ref}}$ ) and object ( $E_{\text{obj}}$ ) beam, the recorded hologram is given by:

$$|E_{\text{ref}} + E_{\text{obj}}|^2 = E_{\text{ref}}E_{\text{ref}}^* + E_{\text{obj}}E_{\text{obj}}^* + E_{\text{ref}}E_{\text{obj}}^* + E_{\text{ref}}^*E_{\text{obj}}$$

Equation 4:1 - Interference of reference and object beams.

The last term in Equation 4:1 provides the reconstruction of the object beam upon illumination with the reference. The first two terms constitute the DC component and the third term is the conjugate of the reconstruction term. For a linear and reciprocal polymer media, the refractive index modulation follows Equation 4:1. As a result, we can state that the object beam is a signal that is modulated by a carrier generated by the reference beam. To multiplex  $M$  holograms, we can use  $M$  different object beams and slightly different carrier frequencies, which are sufficient to be individually retrieved in a volume hologram by taking advantage of the angular Bragg selectivity. When  $M$  holograms are stored, the efficiency of an individual hologram is inversely proportional with  $M$  squared, which is a well-established rule for both photorefractive and photopolymer media [133]–[136]. For a photopolymer, while multiplexing many holograms, the DC terms build up within the dynamic range of the material, leaving only a fraction to the signal terms. This phenomenon decreases the diffraction efficiency of the holograms since the diffraction efficiency of each hologram is related to its share from the available dynamic range. When the refractive index change in a recording media is not bipolar, the DC build-up cannot be removed.

However, unlike classical optical recording, additive manufacturing enables updating the index value of a single voxel in the media without affecting the others. Hence, we can design an index distribution digitally and fabricate it thanks to voxel by voxel (3+1)D printing. On a computer, we can superimpose holograms by eliminating the DC terms as if negative intensity values and bipolar responses were available. The obtained refractive index distribution can then be scaled to match the dynamic range of the material, allowing fabrication via TPP leveraging only monotonic index change using physical (non-negative) intensity values, while importantly preventing the DC build-up.

To demonstrate this approach as a proof of concept, the initials of the Optics Laboratory, O and L, are chosen to be peristrophically multiplexed in a  $(50 \mu\text{m})^3$  volume as presented in Figure 4:4(a). The images of the letters are propagated digitally by the Beam Propagation Method (BPM) and the diffracted fields are phase-conjugated and superimposed with two plane waves tilted at  $6.5^\circ$  in  $x$  and  $y$  axis for each letter, eliminating the DC terms. In Figure 4:4(a), the refractive index distributions of the first (at  $z=0$ ), middle (at  $z=25 \mu\text{m}$ ) and last (at  $z=50 \mu\text{m}$ ) layers are demonstrated, where the target refractive index dynamic range is  $5 \cdot 10^{-3}$ . A bright field microscope image of the sample is given in Figure 4:4(b). The obtained experimental reconstructions are given in Figure 4:4(c-d) where the volume hologram is illuminated with the assigned plane wave.

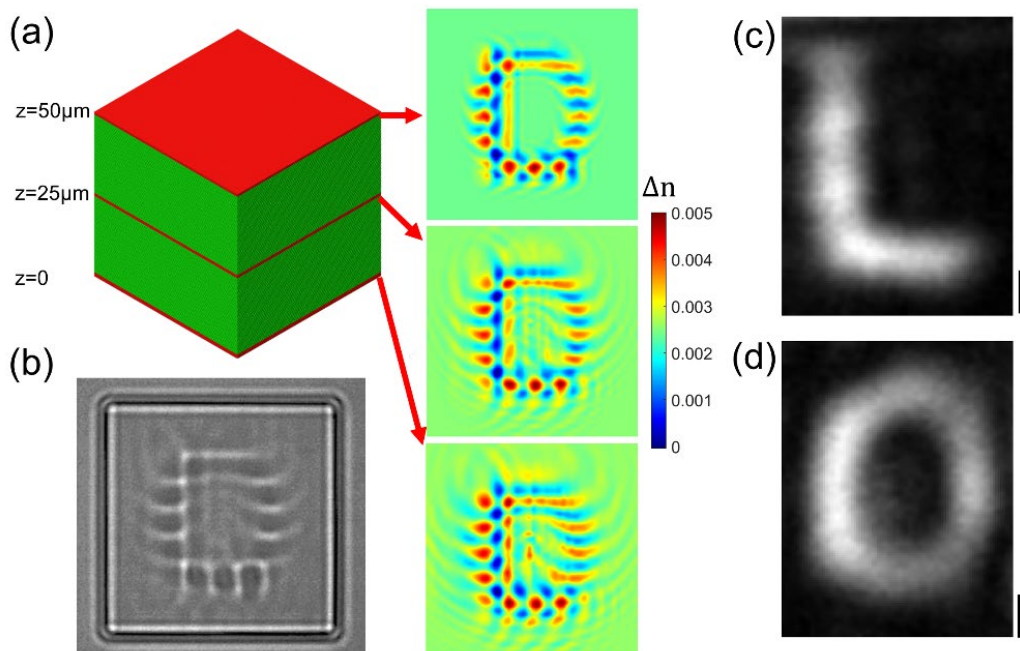


**Figure 4:4 – Volume hologram with two letters.** (a) The target index distribution of the angular-peristropic hologram, (b) bright field microscope image of the fabricated hologram whose transverse dimensions is  $50 \times 50 \mu\text{m}^2$ , (c-f) reconstructed images corresponding to  $LP_{21}$ ,  $LP_{12}$ ,  $LP_{11}$ , and  $LP_{31}$  respectively. The index distribution is up sampled for better visualization.

To demonstrate angular multiplexing as well, four arbitrarily chosen linearly polarized (LP) modes of a multimode fiber ( $LP_{21}$ ,  $LP_{12}$ ,  $LP_{11}$ , and  $LP_{31}$ ) are multiplexed in a volume of  $50 \times 50 \times 60 \mu\text{m}^3$  following similar steps. Four carriers were chosen corresponding to  $7^\circ$  and  $13^\circ$  in both x and y-axes. The diffraction of the chosen LP modes can be neglected for  $60 \mu\text{m}$  propagation distance since their spatial distributions have low frequency components. Hence, the z-variation is kept uniform for this hologram. The target XY refractive index variation is given in Figure 4:5(a), the bright field microscope image of the sample is given in Figure 4:5(b), and the obtained experimental intensity reconstructions are given in Figure 4:5(c-f). The fabrication times for both holograms are roughly 150 minutes where it is 13 minutes for uniform exposure of an equivalent structure in terms of size, sampling, scanning speed. The reason for this discrepancy is software-related. For the volume gratings, we do not observe this discrepancy since the varying laser power is expressed with a simple formula, which is not possible for the holograms. An array should store the power values for each voxel, however, the DeScribe printing software does not allow for an array structure. Thus, power values are stored via thousands of if-else statements, which slows down the execution by control software considerably.

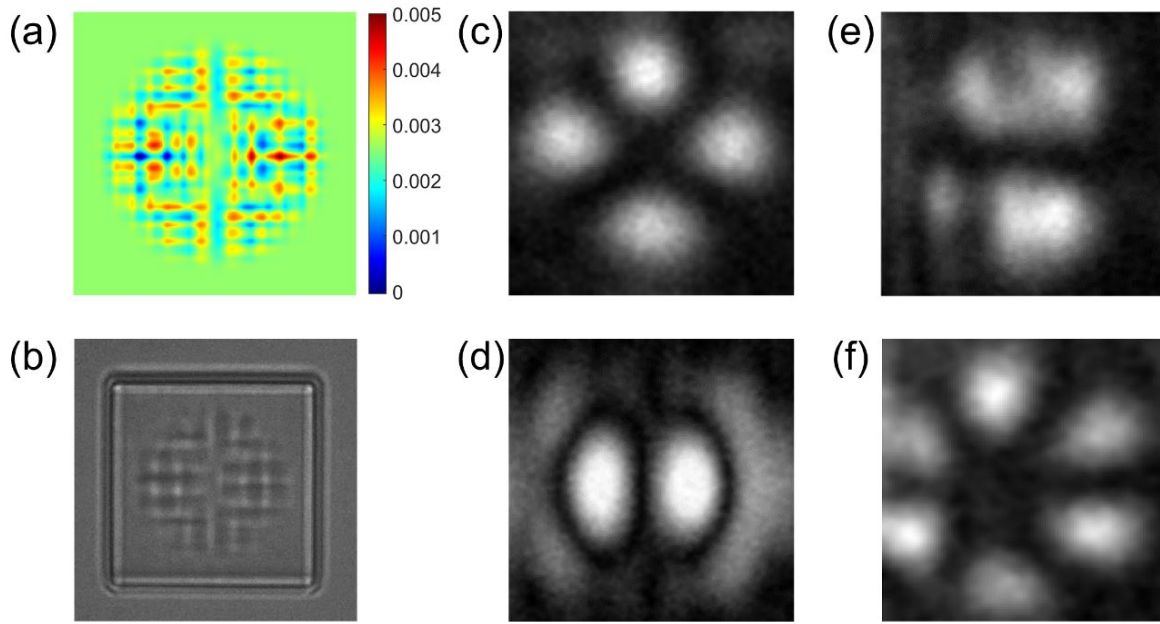


**Figure 4:5 – Volume hologram with four fiber modes.** (a) The target index distribution of the angular-peristropic hologram, (b) bright field microscope image of the fabricated hologram whose transverse dimensions is  $50 \times 50 \mu\text{m}^2$ , (c-f) reconstructed images corresponding to  $\text{LP}_{21}$ ,  $\text{LP}_{12}$ ,  $\text{LP}_{11}$ , and  $\text{LP}_{31}$  respectively. The index distribution is up sampled for better visualization.

#### 4.4.2 Photonic waveguides

We (3+1)D-printed photonic waveguides with both, step-index (STIN) and graded-index (GRIN) refractive index profiles. As schematically illustrated in Figure 4:1(b), the waveguide's core printed with high laser power is surrounded by a cladding printed with a lower laser power. We used writing powers of 58% (11.6 mW) and 35% (7 mW) for the highest and lowest refractive index, respectively. STIN waveguides result from a constant laser writing power all across their core, while for the core of GRIN waveguides writing power changes from high to low along a parabolic profile. We printed 25 STIN waveguides with diameters  $D \in [1 \dots 20] \mu\text{m}$ , and 13 GRIN waveguides with diameters  $D \in [5 \dots 10] \mu\text{m}$ , all embedded in cuboids of  $300 \mu\text{m}$  height. The scanning electron microscopy micrograph of Figure 4:6(a) depicts an exemplary cuboid accommodating 20 printed STIN waveguides. The fabrication time for such a large structure is  $\sim 180$  minutes. By printing waveguides with different diameters  $D$ , we effectively scan their normalized frequency  $V = \frac{\pi}{\lambda_0} D \cdot \text{NA}$ , where  $\text{NA} = \sqrt{n_1^2 - n_2^2}$  is the numerical aperture,  $\lambda_0 \approx 660 \text{ nm}$  is the wavelength of the illumination laser and  $n_1$  ( $n_2$ ) are the refractive indices of core (cladding).

We extract the waveguide's relevant parameters by fitting the experimental output intensities for diameters below the cut-off condition of the second propagating mode. Figure 4:6(b) depicts the fit of  $\text{LP}_{01}$  to the normalized output of a STIN waveguide with radius  $R = 3 \mu\text{m}$ , where the intensity profile of the  $\text{LP}_{01}$  mode is given by  $J_0^2\left(u \frac{r}{R}\right)$  for  $|r| \leq R$  and  $K_0^2\left(v \frac{r}{R}\right)$  for  $|r| \geq R$ . The output of a GRIN waveguide with same radius ( $3 \mu\text{m}$ ) is shown in Figure 4:6(c). The normalized experimental intensity is fitted with  $\exp\left(-\frac{1}{2} V \frac{r^2}{R^2}\right)$ , which corresponds to the intensity distribution of the fundamental mode of a GRIN fiber with an infinite parabolic refractive index profile [137]. From the fit parameters we extract the corresponding NAs (see Appendix B.5 for further details). Using  $n_1 = 1.547$  as the refractive index of IP-Dip at saturation [112], we obtain an averaged numerical aperture of  $\text{NA} = 0.08 \pm 0.01$  (i.e.  $n_1 = n_2 + 2.4 \cdot 10^{-3}$ ) for STIN and of  $\text{NA} = 0.18 \pm 0.02$  for GRIN. Comparing the intensity profiles and the averaged NAs of single-mode GRIN and STIN waveguides we evidence that the core-confinement of the former is significantly higher, which offers a crucial advantage for photonic integration schemes [73], [74].

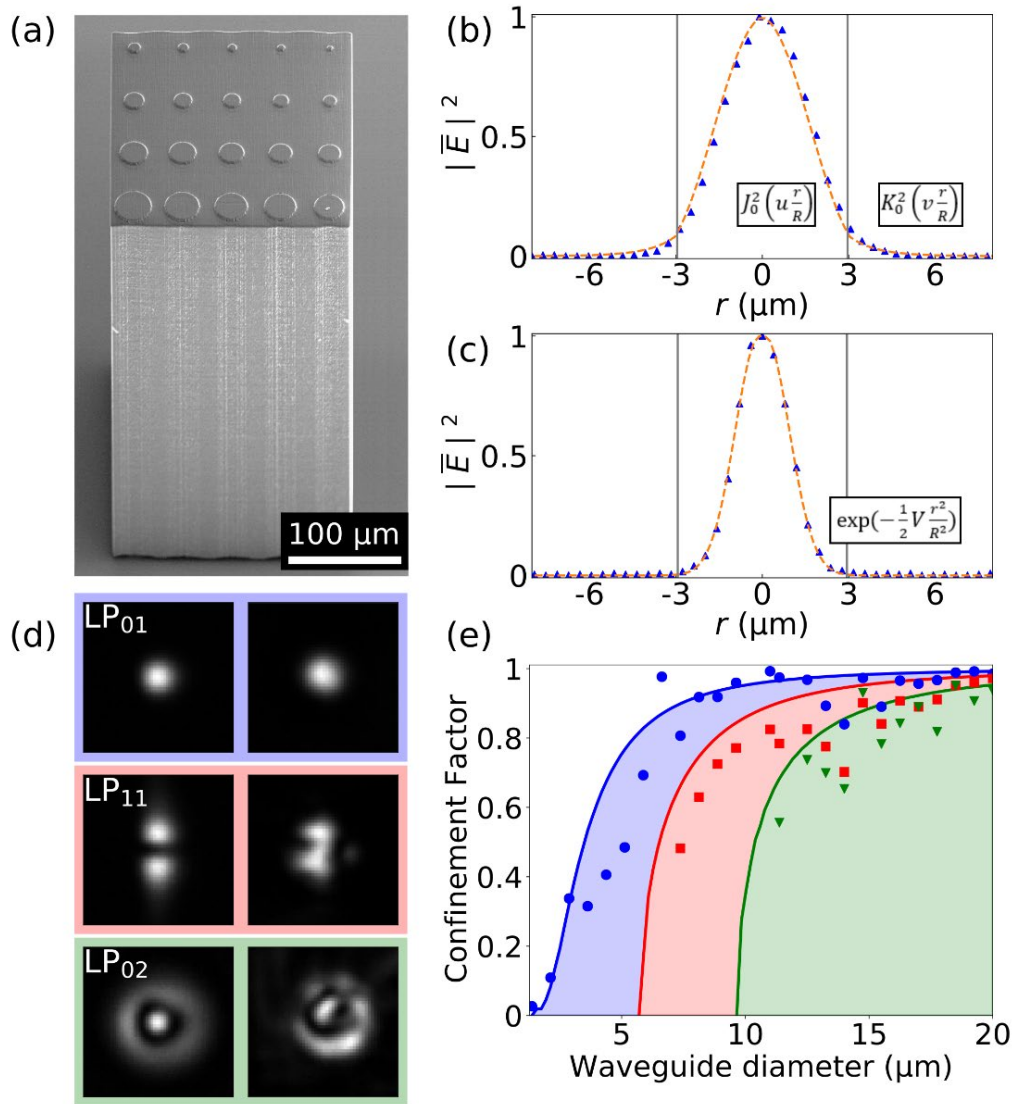


**Figure 4:6 – Fabricated waveguides.** (a) SEM image of a cuboid with 20 printed STIN waveguides. Panels (b) and (c) depict the output intensities (triangles) and fundamental mode fits (dashed lines) of a 6  $\mu\text{m}$  diameter STIN and a GRIN waveguides, respectively. (d) Exemplary intensity profiles of injected LP modes (left) and their outputs after propagation through STIN waveguides of different diameters (right). We depict the first waveguide with confinement factor above 0.8 for each respective mode. (e) Theoretical confinement factor as function of the STIN waveguides diameter  $\Gamma(D)$ . Symbols are experimental and lines are theoretical curves for each mode LP<sub>01</sub> (blue), LP<sub>11</sub> (red), LP<sub>02</sub> (green).

In order to investigate the modal propagation properties, we used a spatial-light modulator (Santec LCOS SLM-200) to generate a set of LP modes, which we injected into the waveguides under close to NA-matched conditions (see Appendix B.6 for detailed description of the experimental setup). Figure 4:6(d) shows injected LP modes (left panels) and exemplary waveguide outputs (corresponding right panels). For each printed waveguide, we calculated the confinement factor  $\Gamma(D)$  defined as the fractional optical power confined to the core. The experimentally measured confinement factors  $\Gamma(D)$  for STIN waveguides are plotted in Figure 4:6(e), together with the theoretically calculated curves for each mode. Experimental  $\Gamma(D)$  follows the theoretical predictions with a small systematic vertical offset that we attribute to a systematic offset in the waveguides' diameter due to the non-negligible voxel dimensions.

We furthermore investigate the propagation-length dependent losses and the maximum waveguide packing density. Propagation losses primarily depend on scattering, host-material absorption and insufficient mode confinement. We determined the global losses of the LP<sub>01</sub> mode after propagating through the waveguides with lengths ranging from 50  $\mu\text{m}$  to 300  $\mu\text{m}$ . We chose STIN waveguides with five different diameters between 5 and 7  $\mu\text{m}$ ,

which provide high enough  $LP_{01}$  confinement while remaining single mode. After propagation, we fitted the output intensity to a Gaussian and discarded the background. Figure 4:7(a) depicts the propagation losses for an injection NA of  $\approx 0.12$ . We linearly fit the average losses of all diameters for every length value and the resulting dependency has a slope of  $-6.2$  dB/mm. Noteworthy, Figure 4:7(a) includes injection losses of  $\sim 0.5$  dB. Total losses for STIN and GRIN waveguides are very similar within  $\sim 1$  dB difference. For the waveguides depicted in Figure 4:6(b) and Figure 4:6(c), the latter one has an excess loss of 0.7 dB with respect to the STIN waveguide combining both in coupling as well as propagation losses. While low for a first proof of concept demonstration, losses are around one order of magnitude above the material's bulk absorption [92], but a factor of 3 lower than for 3D printed waveguides [73].

Figure 4:7(b) shows the evanescent coupling rate between neighboring waveguides. For our characterization we printed pairs of  $300 \mu\text{m}$ -length and  $7 \mu\text{m}$ -diameter waveguides with separations ranging from  $0.5 \mu\text{m}$  up to  $6 \mu\text{m}$ . Optical crosstalk between adjacent waveguides is based on the overlap of their respective evanescent fields, which decay exponentially over distance. Our evanescent coupling rate follows the expected exponential dependency, and the coupling rate reduces as  $-1.32 \mu\text{m}^{-1}$  with waveguide separation. STIN waveguides in direct contact couple at a rate of  $3 \text{ mm}^{-1}$ , while this coupling strongly reduces to  $0.02 \text{ mm}^{-1}$  for an intra-waveguide distance of  $6 \mu\text{m}$ . The rapidly decaying evanescent coupling therefore allows a high integration density, supporting circuits with  $\sim 6000$  waveguides per  $\text{mm}^2$ .

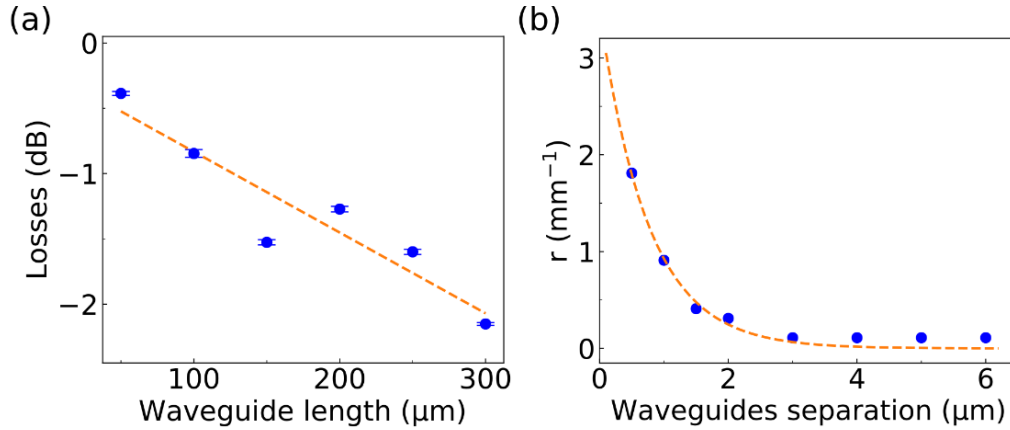


**Figure 4:7 – Loss and coupling of waveguides.** (a) Propagation losses. (b) Evanescent-coupling rate between waveguide pairs as a function of waveguides separation. The optical injection NA is  $\approx 0.12$ . The corresponding linear and exponential fits are depicted as dashed lines in both panels

## 4.5 Conclusions

In summary, we have introduced a single-step process to manufacture photonic GRIN elements based on a commercial laser writing system. We first carried out different fundamental characterizations that independently confirmed the high level of control over a complex 3D refractive index distribution. Comparing these independent measurements (rectangular prisms with volume gratings) reveals, a very small  $\Delta n$  deviation of 2% only ( $\Delta n = 5 \cdot 10^{-3}$  compared to  $\Delta n = 5.1 \cdot 10^{-3}$ , respectively). This shows the excellent spatial and refractive index resolution of our technique. We then demonstrated (3+1)D printed GRIN volume holograms, as well photonic waveguides with a controlled number of propagating modes.

For the STIN and GRIN photonic waveguides, we determined the waveguides' NA by carefully fitting their propagation parameters under single-mode condition, characterized propagation losses and the evanescent coupling rates between neighboring waveguides. We find higher NA and mode confinement for GRIN waveguides. Moreover, significantly larger NAs should be achievable in the future, as the investigated and other commercial resins allow for larger refractive index modifications [119]. Further future efforts should reduce propagation losses in order to bring them closer to this of integrated silicon photonics. For the volume holograms, the results demonstrate printing an index distribution arbitrarily varying in 3D. Since currently the printed volumes are small, a small number of holograms is supported, and the fabrication of greater volumes to store more information is an important future objective.



The currently employed printing technique would require stitching of different blocks to reach larger volumes since the field of view of the writing objective is limited. Any shift due to a stitching error would make different parts of the hologram out of phase. Thus, a thorough optimization of the fabrication process for stitching is necessary to approach mm sizes. One of the main goals of the future study is to fabricate a volume where many holograms are multiplexed and compare the diffraction efficiency with optically recorded counterparts. Moreover, over-modulated volume gratings fabricated by (3+1)D printing is another interesting avenue to explore, which requires a careful inspection [138]. For the characterization and calibration process, more recent and sensitive techniques can be adopted for high sensitivity demanding applications [139].

In general, the additive nature of our approach is a crucial asset. It makes the process less dependent on the working distance of microscope objectives, and just recently millimeter-sized photonic components utilizing the same TPP process have been demonstrated [109]. Furthermore, (3+1)D additive photonic fabrication has the potential functionalize integrated photonic or electronic circuits, for example by adding scalable photonic interconnects [73], [74] to bring large scale parallel communication to classical photonic or electronic chips. (3+1)D direct laser writing hence provides a highly versatile addition to the photonics toolbox.



# Chapter 5 Volume holograms with linear diffraction efficiency relation by (3+1)D printing

This chapter is the pre-print version of the following article accepted in *Optics Letters*. The pre-print is available in *arXiv*.

**Volume holograms with linear diffraction efficiency relation by (3+1)D printing** by Niyazi Ulas Dinc<sup>1,2</sup>, Christophe Moser<sup>1</sup> and Demetri Psaltis<sup>2</sup>

<sup>1</sup>Laboratory of Applied Photonics Devices, École polytechnique fédérale de Lausanne, Switzerland

<sup>2</sup>Optics Laboratory, École polytechnique fédérale de Lausanne, Switzerland

*Optics Letters*, ahead of print, <https://doi.org/10.1364/OL.508097>

Available in arXiv (2023), <https://doi.org/10.48550/arXiv.2310.06350>

We demonstrate the fabrication of volume holograms using 2-Photon polymerization with dynamic control of light exposure. We refer to our method as (3+1)D printing. Volume holograms that are recorded by interfering reference and signal beams have a diffraction efficiency relation that is inversely proportional with the square of the number of superimposed holograms. By using (3+1)D printing for fabrication, the refractive index of each voxel is created independently and thus by, digitally filtering the undesired interference terms, the diffraction efficiency is now inversely proportional to the number of multiplexed gratings. We experimentally demonstrated this linear dependence by recording  $M=50$  volume gratings. To the best of our knowledge, this is the first experimental demonstration of distributed volume holograms that overcome the  $1/M^2$  limit.

## 5.1 Theoretical and numerical investigations

The utilization of volume holograms has garnered significant attention in various applications such as optical interconnects [4], data storage [19], [56], optical correlators [59], [60] and mode multiplexing/demultiplexing [67]. The rationale behind harnessing 3-Dimensional (3D) volumes to store and process information is inherently intuitive: the introduction of an additional dimension offers an expanded storage capacity when compared to 2D optical layouts [25], [140]. However, a major challenge for volume holograms is the diffraction efficiency, defined as the fraction of the light power diffracted by the hologram to the incident power, which falls inversely with the square of the number of multiplexed holograms when the holograms are recorded with optical interference [133]:

$$\eta = \frac{(M\#)^2}{M^2}$$

Equation 5:1 – Diffraction efficiency relation for volume holograms.

where  $\eta$  is diffraction efficiency,  $M$  is the number of multiplexed holograms and  $(M\#)$  is the system metric to quantify the medium's storage capacity, which depends on the dynamic range of the refractive index (RI) and the thickness of the medium [141]. The dependence on the square of the number of holograms arises from the undesired terms that are included in the interference between the reference ( $E_R$ ) and signal ( $E_S$ ) beams during optical recording:

$$|E_R + E_S|^2 = E_R E_R^* + E_S E_S^* + E_R^* E_S + E_R E_S^*$$

Equation 5:2 – Interference of reference and object beams (re-stated).

The RI of the medium is modulated by the 3D intensity pattern given in Equation 5:2. For the read-out, the reference beam illuminates the medium. The first term is usually a DC term since the reference beam is typically a plane wave. The second term contributes to noise by scattering the light in an undesired manner. The third term is the reconstruction term of the signal beam whereas the last term is the conjugate of the reconstruction term.

We can analyze the recording of multiple holograms by considering the summation of modulated sinusoids in 1D without loss of generality. We express the RI as:

$$\Delta n(x) = \sum_{m=1}^M A_m(x)$$

Equation 5:3 – Refractive index dynamic range as a summation of sinusoids.

where  $A_m$  is the index modulation due to a single recording, which can be expressed by a DC term and an AC term modulated by a data envelope ( $f_m$ ) with oscillation frequency ( $\omega_m$ ), resulting from the angle between the reference and the signal:

$$A_m = c_{DC} + c_{AC} \sin(\omega_m x + \varphi_m) \times f_m(x)$$

Equation 5:4 – Modulated sinusoid in 1D.

When we substitute Equation 5:4 into Equation 5:3, we find that the DC term grows linearly with  $M$  whereas the signal term only grows as the square root of  $M$  for large  $M$ :

$$\Delta n \propto M + \sqrt{M}$$

Equation 5:5 – Proportionality of index dynamic range and number of stored holograms with DC build-up.

For large  $M$ , we can simply neglect  $\sqrt{M}$ . With this further simplification, Equation 5:5 simply states that each modulated sinusoid has an amplitude proportional to  $1/M$ . Note that the diffraction efficiency for the intensity of each sinusoidal grating is proportional to the square of its share of the dynamic range of  $\Delta n$ , yielding the  $1/M^2$  trend. If we are somehow able to equate  $c_{DC}$  to zero to prevent the DC buildup, then Equation 5:5 becomes:

$$\Delta n \propto \sqrt{M}$$

Equation 5:6 – Proportionality of index dynamic range and number of stored holograms without DC build-up

Equation 5:6 implies that each modulated sinusoid would have an amplitude proportional to  $1/\sqrt{M}$ , consequently yielding a diffraction efficiency relation with  $1/M$  trend. This phenomenon was verified previously by recording localized holograms in separate slices of a doubly doped lithium niobate crystal, which were locally photosensitized prior to holographic recording [62]. However, for fully distributed holograms, DC buildup is unavoidable with optical distributed means of recording. We have previously demonstrated voxel-by-voxel arbitrary RI writing by using 2-photon polymerization, which we refer to as (3+1)D printing [91]. Here, we use this method with a commercially

available Nanoscribe 2-photon printer to demonstrate that it is achievable to obtain a linear diffraction efficiency relation for non-localized (distributed) volume holograms as well. First, we compute digitally the index distribution  $\Delta n(x, y, z)$  for volume holograms that consist of only the superimposed volume gratings without the first two terms of Equation 5:2. Note that we need to keep the conjugate of the reconstruction term to obtain real-valued index distribution. Using the Beam Propagation Method (BPM), we simulated the wave propagation [142] and verified in simulation the linear trend as shown in Figure 5:1 for 200  $\mu\text{m}$  and 400  $\mu\text{m}$  thick holograms in transmission geometry (see Appendix C Section 1 for more details). In Figure 5:1, we clearly observe the expected linear dependence. For reference, we also plot  $1/M$  and  $1/M^2$  lines. Note that doubling the thickness of the material roughly doubles the  $M\#$  as theoretically expected, which is obtained by a linear fit to the data points for  $M > 10$ .

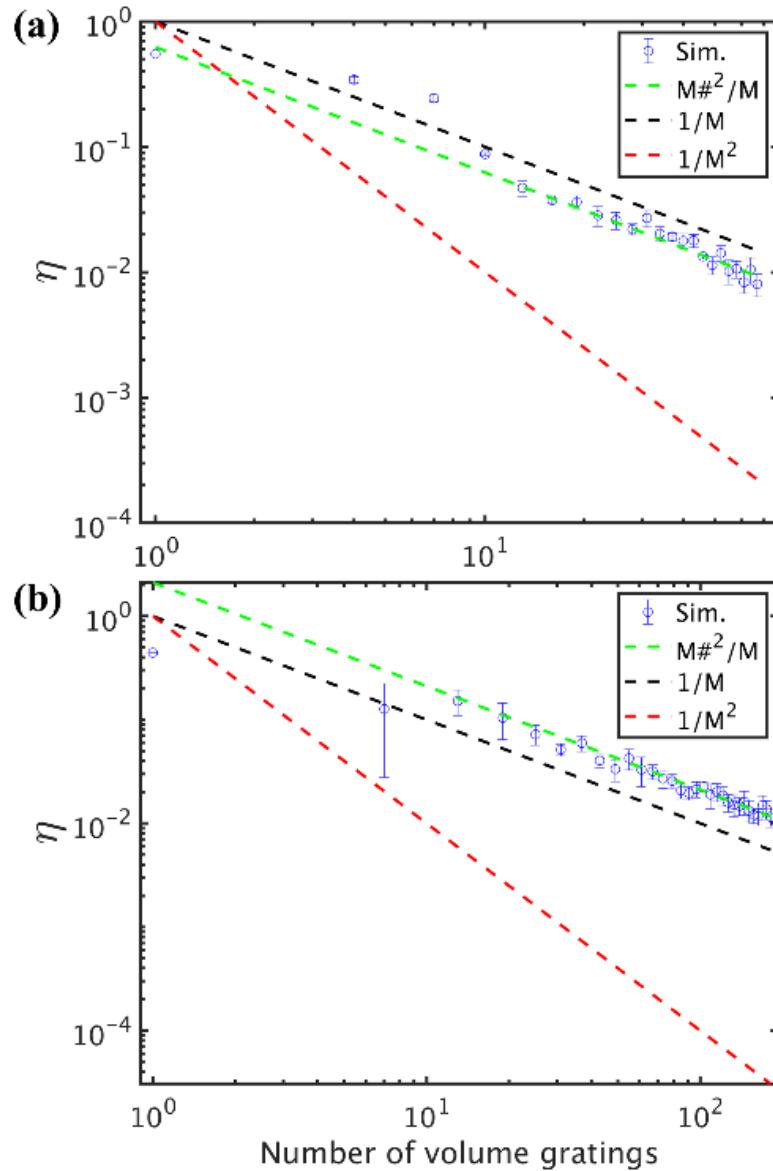


**Figure 5:1 – Logarithmic plot for the simulated diffraction efficiency** (y-axis) versus number of multiplexed volume gratings (x-axis) for (a) 200  $\mu\text{m}$  thickness with  $\sim 70$  volume gratings superimposed and (b) 400  $\mu\text{m}$  thickness with  $\sim 200$  volume gratings superimposed. Y-intercept of the plots correspond to  $M\#^2$ .

## 5.2 Fabrication and experiment results

Thanks to (3+1)D printing, we can directly fabricate these digitally calculated holograms. Instead of the IP-Dip resin, we used earlier [91]; we use IP-S, which has a smoother polymerization curve [119] enabling calibration-free fabrication by assuming near-linear dependence of RI vs. power. It is worthwhile to note that IP-Dip and IP-S resins have been used to fabricate various optical structures as reported in literature [66], [93], [106], [143]–[145]. Here, we used 10 mm/s scanning speed as a fixed parameter and we varied the laser beam power to vary the polymerization exposure, which goes from 15% to 75% of the maximum power of the Nanoscribe system (when power scale is set to one), corresponding to an average power range from 3 mW to 15 mW. IP-S is photo-polymerized with a 780 nm femtosecond pulsed laser built-in in the Nanoscribe printer, focused by a 25x microscope objective. Hatching (lateral spacing between the centers of two voxels) and slicing (vertical spacing between the centers of two voxels) distances are 0.4  $\mu\text{m}$  and 1  $\mu\text{m}$  respectively. Hatching and slicing distances are important parameters, as they maintain a delicate balance between two key factors: structural stability and resolution on one hand, and printing speed on the other. Since we work in transmission geometry for holograms, the hatching distance is more critical as it sets the more demanding lateral resolution. A hatching distance of 0.4  $\mu\text{m}$  is chosen as a good balance as we did not observe significant differences in diffraction orders when hatching is reduced (see Appendix C Section 2) suggesting that we become restricted by the polymerization process and diffusion.

We started the experimental characterization by printing, unslanted sinusoidal volume gratings and sweeping the grating period. In Figure 5:2(a-c) we provide Scanning Electron Microscope (SEM) images with three different periods. Since the voxel volume increases with the exposure, there is a surface relief pattern that forms and it is picked up by the electron microscope. This explains why the topography qualitatively shows the exposure map of the printed structure. In Figure 5:2(d), we also provide a SEM image of a slanted volume grating, which clearly shows the slanted lines from the side. We decided to set  $\Lambda=2 \mu\text{m}$  as the minimum lateral period for this study since below this value, high index voxels merge together. This  $\Lambda$  value corresponds to a maximum incidence angle of approximately  $13^\circ$  for a wavelength  $\lambda=681 \text{ nm}$  and average RI of the medium as 1.51. To find the dynamic range of RI with the given printing parameters, we printed unslanted volume gratings of different thicknesses of 110, 140, 170, and 200  $\mu\text{m}$  with  $6^\circ$  Bragg angle and obtained the diffraction efficiency plot given in Figure 5:2(e). To prevent additional diffraction from the air-polymer interface, an additional 5- $\mu\text{m}$  thick homogeneous layer is printed on top. Using coupled wave theory [55], [131] we extracted the RI variance  $\Delta n= 1.7 \times 10^{-3}$  using Equation 5:7 :

$$\eta = \sin^2 \left( \frac{\pi n_1 L}{\lambda \cos \theta} \right)$$

Equation 5:7 – Diffraction efficiency of single volume grating by coupled wave theory.

where the amplitude of index variation is  $n_1 = \Delta n/2$ ,  $L$  is the thickness, and  $\theta$  is the Bragg angle.

We printed the holograms as cubes with volume of  $(200 \mu\text{m})^3$  in accordance with the field of view and the working distance in the printing configuration. We can directly deduce the M# from the last data point in Figure 5:2(e), which corresponds to 200  $\mu\text{m}$  thickness. Hence, the M# of our holograms is the square root of 0.5, resulting in roughly 0.7 for the given Bragg angle.

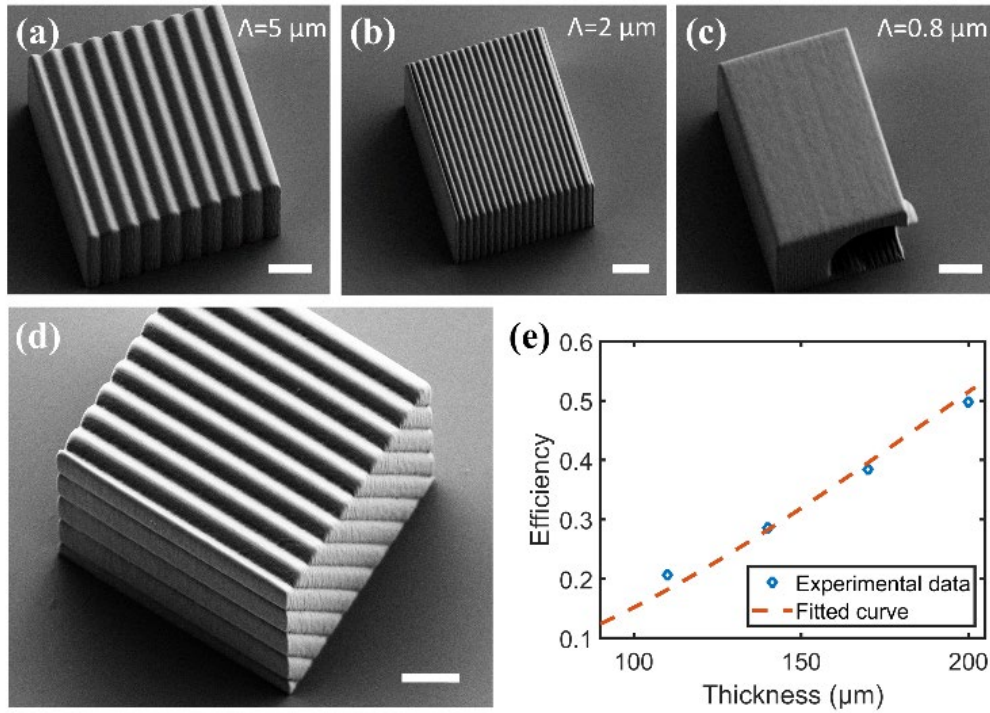


**Figure 5:2 – Characterization of single gratings.** (a-c) SEM images of unslanted sinusoidal volume gratings with periods  $5 \mu\text{m}$ ,  $2 \mu\text{m}$ , and  $0.8 \mu\text{m}$  respectively. (d) SEM image of a slanted volume grating. Scale bars measure  $10 \mu\text{m}$ . (e) Diffraction efficiency of single gratings of different thicknesses along with  $\sin^2$  curve fitting yielding the dynamic range of RI.

As well as RI, the voxel size varies with the optical power. Larger voxel size effectively decreases the resolution. For higher carrier frequencies, this inevitably results in a smoothing effect. Since the higher carrier frequencies are distorted, we see a frequency response in diffraction efficiency measurements. To probe this effect, we fabricated a hologram by multiplexing five gratings with equal strengths that were designed to be Bragg-matched to the same signal beam (designed to be in the same direction) at five different reference beam angles. Since diffraction is a linear phenomenon, we built a reciprocal experimental setup where the illumination is such that it excites all the recorded gratings simultaneously. In this way, we can read-out all five gratings at the same time with a single beam illumination (see Appendix C Section 2). We schematically show this reciprocity in Figure 5:3(a) using k-vectors of incident and diffracted beams and the gratings within the Ewald's sphere representation. In Figure 5:3(b), we show the camera capture where we see all the five diffracted beams. We observe that the diffracted power decrease as the carrier frequency or the corresponding angle increases. We simulated the beam propagation in the calculated hologram to mimic the experiment. As theoretically expected, all the diffracted signals have equal strengths as shown on the cut line plot in Figure 5:3(c). We hypothesize that the decrease of diffraction efficiency is caused by the smoothing of the sinusoidal grating during fabrication due to the voxel size dependence on optical power. To test this hypothesis, we model the smoothing by convolving the index distribution of each grating with a 2D Gaussian smoothing kernel on each slice of the calculated hologram. As we vary the standard deviation ( $\sigma$ ) of the Gaussian kernel, we observed decreasing diffracted signal power as the angle increases mimicking our experimental observation. In Figure 5:3(c), we provide the cutline plot of the simulated diffraction pattern with no Gaussian filtering, along with cutline plots obtained with filtered holograms for  $\sigma=1$  and  $\sigma=2.1$  and the experimentally recorded data points. We note that the smoothed hologram with  $\sigma=2.1$  roughly corresponds to the decreasing power trend experimentally measured.

In order to perform diffraction efficiency measurements as a function of the number of recorded gratings independently of the frequency response, we printed three  $(200 \mu\text{m})^3$  cubes with 10, 30, and 50 multiplexed gratings and we measured the diffraction efficiency of the ones with the same spatial frequency. This is approximately  $7.2^\circ$  between the reference and the signal beams (see Appendix C Section 2). In Figure 5:3(d), we show the experimentally measured diffraction efficiencies in log-log scale. We applied a linear curve fit and constrained y-intercept to

be less than 0.5 as we know that the baseline efficiency should be smaller than the one we found using single grating with  $6^\circ$  Bragg angle because of the frequency response. In Figure 5:3(d), we also provide the fitting curve, which yields a slope of -1.097 and y-intercept of 0.38 ( $M\#=0.62$ ). For reference, we also plot the lines with slopes -1 and -2, having the same  $M\#$ .

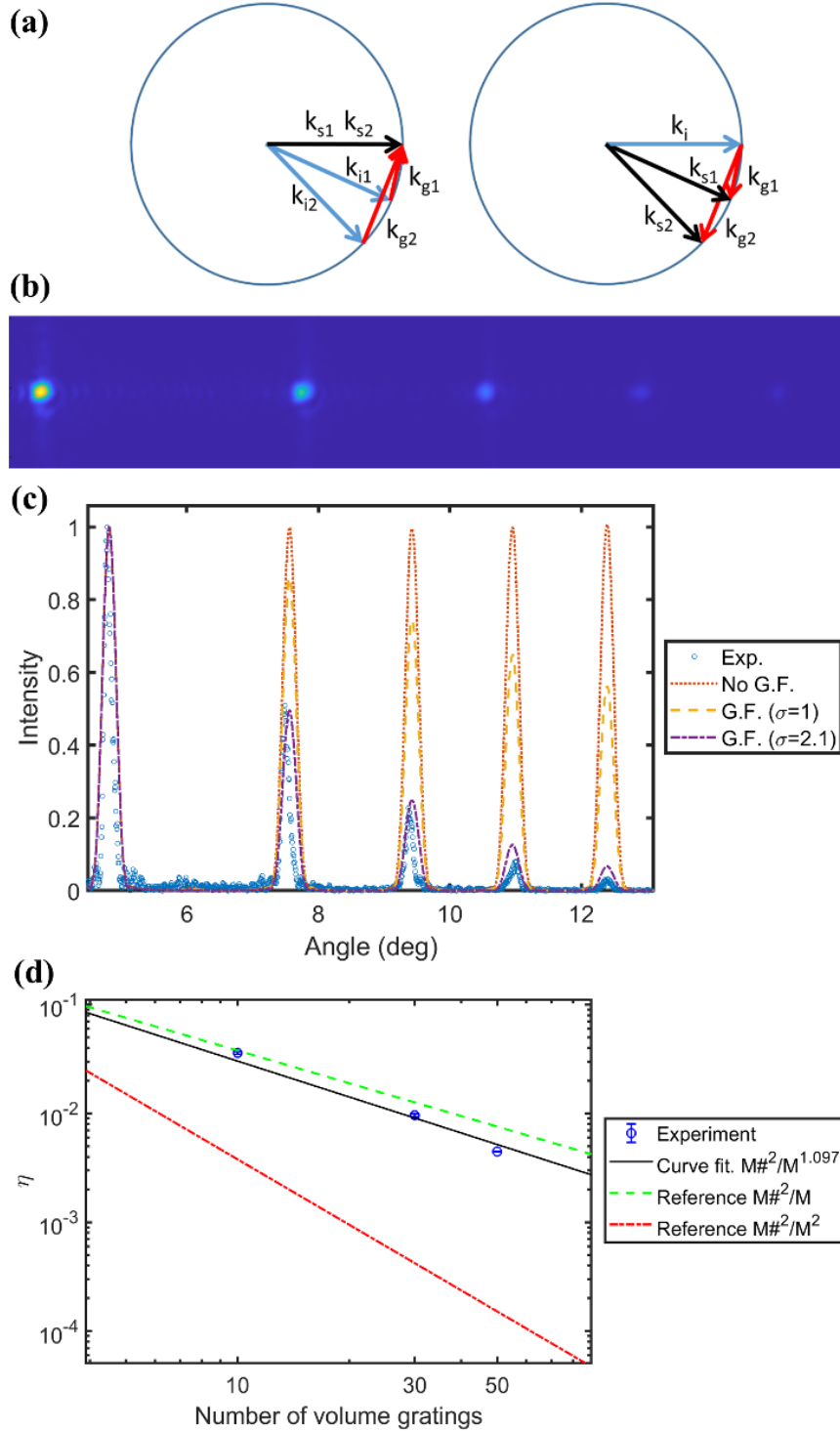


**Figure 5:3 – Diffraction efficiency measurements.** (a) Ewald sphere representation, highlighting momentum matching for two different incidence beams in forward pass through a transmission hologram on the left. On the right, the reciprocal excitation of all the recorded gratings. (b) Camera capture of diffracted signals from the printed hologram. (c) Cut line plot showing the experimental data along with simulation data where G.F. stands for Gaussian-Filtered. (d) Experiment results showing near-linear diffraction efficiency trend along with reference lines of  $M\#^2/M$  and  $M\#^2/M^2$ .



Although (3+1)D printing paves way for digital optimization of the RI design, having a photoresist that has a frequency response because of the varying voxel size hampers the diffraction efficiency for higher carrier frequencies. We argue that this effect might also be responsible for the discrepancy of the experimental finding from the exact linear relation, although this argument requires more investigation as a future work. A photoresist whose RI varies without a significant change of voxel size is desired. However, we acknowledge that achieving such a chemistry is very challenging. Moreover, scaling the volume of the printed structures is crucial to reach higher storage capacities. Because of the limited working distance and field of view in photo polymerization, this can be achieved by employing stitching of different blocks. The risk of stitching is having a phase difference in different blocks, which would yield a distorted reconstruction. We have performed a preliminary study to show that stitching is feasible by observing SEM images showing slanted grating periods in phase among different blocks (see Figure 5:4). This is achieved when the printing is performed layer by layer for all the structure instead of block by block, which is consistent with our previous study [144].

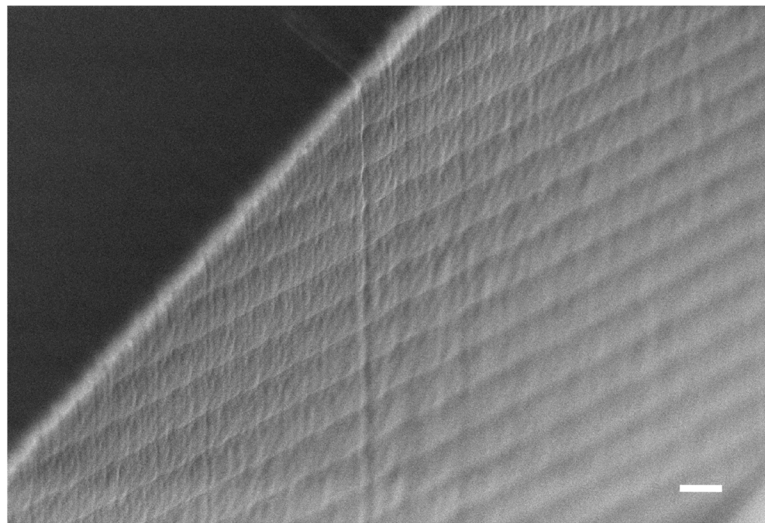


**Figure 5:4 – SEM image of stitched blocks fabricated in adjacent field of views of the printing system.** Block boundary is visible by the vertical line. The grating lines are visibly in-phase. The scale bar measures 2  $\mu\text{m}$ .

Scaling is still challenging with respect to fabrication time since 2-photon-polymerization is a point-scanning technique. Another technical difficulty arises from the fact that we need to have all the voxels to be printed stored in the memory of the printing computer with assigned coordinates and dynamic laser power values, which becomes demanding for volumes greater than  $(200 \mu\text{m})^3$  for the 8 GB memory that is available in the facility. Nonetheless this issue can be solved by optimizing the printing protocols for (3+1)D printing.

Overall, this study reports on an important milestone for optical data storage, which is the experimental demonstration that the diffraction efficiency of M holograms is inversely related to M rather than  $M^2$ . This has been achieved by writing the computed holograms voxel by voxel using 2-photon printing.



# Chapter 6 Reconfigurable multilayer optics for interconnects

Up to this point, our discussions have centered on innovative approaches to micro-scale fixed interconnects, created using high-resolution 2-photon printing. This chapter pivots to explore the use of commercial spatial light modulators in constructing reconfigurable interconnect devices on a centimeter-scale. Notably, the architecture introduced in this chapter also functions as a nonlinear processing device, a topic we will delve into in Chapter 8. Therefore, this chapter acts as a bridge between topics. It is essential to highlight that while the results in this chapter offer a proof-of-concept, further refinement and characterization will be discussed in the conclusion and outlook section.

We believe that this is a timely investigation since the demand for efficient, scalable, and high capacity interconnects has surged in the rapidly evolving landscape of data center networks. While the current optical interconnect technologies offer benefits over electrical interconnects, they fall short in providing efficient multicasting capabilities, a crucial aspect for emerging applications. In this chapter, we introduce a novel reconfigurable optical interconnect device, termed as ROSSMi (Reconfigurable Optical Space-Spectrum Multicast interconnect). The ROSSMi device stands distinct as it harnesses the principles of free space diffraction coupled with programmable spatial light modulation techniques. By doing so, it can efficiently offer bidirectional and selective multicast connectivity between nodes with space-spectrum granularity. This innovative combination paves the way for designing more compact, energy-efficient, and low-latency network architectures that are imperative for the computational demands of the future.

## 6.1 Introduction

Over the past few decades, large-scale data centers have been instrumental in the development of global Internet services. As machine learning has gained importance, the need for large-scale, distributed computing capabilities in data centers has increased. Data center networking enables interconnectivity to carry out the workloads required for these services. While industrial practices have relied on electrical packet switching with fiber optic cables between nodes for data routing, the incorporation of multifunctional optical interconnects into the network architecture has the potential to recast network design. The emergence of Software-Defined Networking (SDN) roughly a decade ago enabled the separation of the data and the control planes in networks [146], which lifted the requirement to detect the signal in a network switch. This led to a plethora of studies within the last decade to implement an optical switch to reduce hardware complexity and increase performance and efficiency. Optical interconnects have several benefits over electrical ones, including independence from data rate resulting in interoperability with different generations of electronic devices, low latency, and energy efficiency. Integrating optical interconnects

with bandwidth-intensive and latency-sensitive applications, such as machine learning, can significantly improve latency, and bandwidth efficiency with lower costs [147].

One of the existing optical interconnect technologies is based on optical circuit switches with MEMS mirrors [148]. While these switches can provide energy-efficient optical routing, they cannot multicast single input to many output channels. This arises from the ray-optic characteristics when using millimeter-sized, two-axis continuously rotating mirrors or the binary modulation characteristics when utilizing digital Micromirror devices. Moreover, the former systems are not wavelength sensitive, only satisfying space granulatiy [149], [150]. Another solution, Wavelength-selective switches (WSSs) are devices capable of redirecting optical signals to different output ports based on their wavelengths. These switches typically consist of a one-dimensional (1D) diffraction grating and a beam-steering mechanism. The diffraction grating disperses the optical signals into their constituent wavelengths, while the beam-steering mechanism directs them to specific output ports based on their wavelengths. In many WSSs, Liquid-Crystal-on-Silicon (LCoS) spatial light modulators are commonly utilized as the beam-steering device [151], [152]. However, a limitation of WSSs is that they can only redirect one input signal to one output port at a time. Consequently, WSSs are also unsuitable for multicasting. Moreover, 1D input/output configuration also hampers the scalability of WSSs unless it is combined by MEMS-based re-routing at the cost of increased complexity [152].

To have multicast in the optical domain, a common approach involves adding a separate passive splitter to switches [153]–[155]. By combining the splitter with an optical switch, the system can re-route an input to multiple output channels, enabling multicasting. However, this solution has its drawbacks, primarily due to the drastic power drop caused by the passive splitters, which limits the scalability of the overall switching fabric.

To address these limitations, we present a reconfigurable optical interconnect with multicasting capability. Our method leverages spatial light modulation on multiple planes to enable on-demand reconfiguration of optical paths and multicast capabilities. The conceptual schematic of ROSSMi is shown in Figure 6:1. Input beams traverse the spatial light modulator (SLM) multiple times, while wavefront shaping arranges the optical paths corresponding to each input. For instance, in Figure 6:1(a), the spatial-only (broadband response in wavelength) interconnect is illustrated, where different inputs experience both unicast and multicast scenarios. In Figure 6:1(b), we showcase unicast and multicast for wavelength channels entering from the same input position/space. In this configuration, the channels are mapped to distinct spatial positions based on their respective wavelengths as desired.

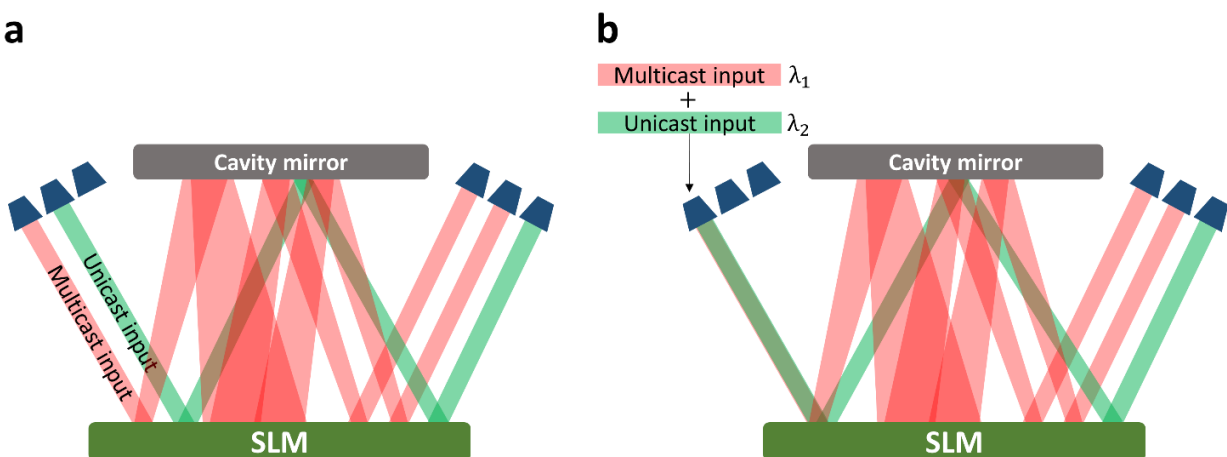


**Figure 6:1 Conceptual schematic of ROSSMi.** (a) The connectivity with spatial granularity. (b) The connectivity with spatial-spectral granularity.

## 6.2 Methodology

The ROSSMi technique's foundation is based on using multiple evenly spaced phase-only modulation planes as schematically depicted in Figure 6:2. The Beam Propagation Method (BPM) helps determine the phase patterns displayed on the SLM, serving as the forward model in our optimization. We utilize LT-based error backpropagation, detailed in Chapters 2 and 3, optimizing the input as ports that produce the incidence beam and desired outputs as the target outputs. To achieve spectral granularity, we execute the forward model for each wavelength, adjusting the pixel phase based on the aggregated backpropagated error signals. Notably, comparable arrangements with fixed printed diffractive surfaces are documented in existing literature [156].

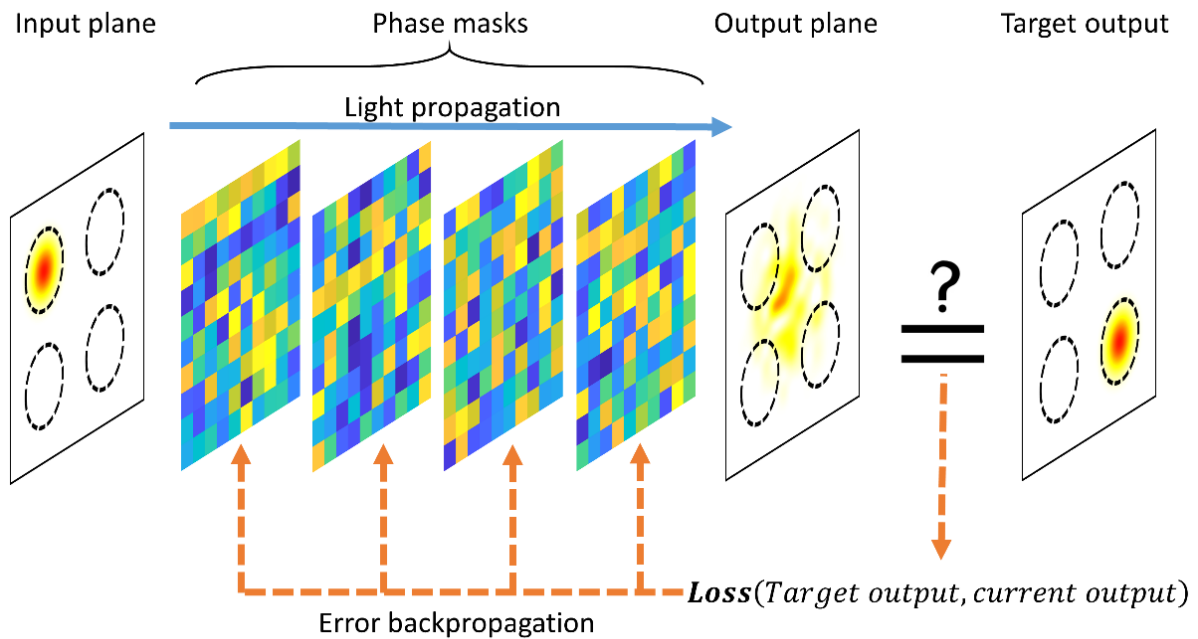


**Figure 6:2 Working principle and optimization of ROSSMi.** For simplicity, only four spatial input and output ports are depicted. The light propagation and modulation by phase masks are calculated using BPM. Depending on the phase values of the masks (indicated by the color code), an output field is obtained. This output field is compared with the target output pattern to generate a loss function, which initiates the error backpropagation to update the phase values of the masks.

The physical realization of ROSSMi combines a liquid crystal Spatial Light Modulator (SLM) with a folding mirror positioned across the SLM display. This arrangement permits the concurrent display of multiple modulation planes on a singular SLM device, creating a multi-bounce single-pass cavity. Within this setup, each plane acts as a thin modulating element, altering the phase of light as it moves successively between planes. Figure 6:3 displays a photograph of our optical setup. For our tests, a continuous wave Solstis M2 laser was employed. The selected mirror, measuring 11.6 mm in width, accommodates the four reflections. To channel the beam to the SLM, 4F imaging was applied, relaying the beam that was reflected off a digital micromirror device (DMD). This DMD acts to simulate the input grid by activating specific sub-regions. For the modulation layers, we designated patches of 300 by 300 pixels on the SLM. The SLM used in our arrangement has a pixel pitch of  $\Lambda=8 \mu\text{m}$ . To establish the multi-bounce cavity, we integrated a Holoeye Pluto Spatial Light Modulator (SLM) and set the mirror 15.2 mm away from the SLM screen. This spacing ensures that the diffraction from one layer's corner pixel can reach the opposite corner of the subsequent layer, facilitating comprehensive pixel connectivity. The setup facilitates four mirror reflections of the input beam. Following the fourth reflection, the beam is magnified 1.2 times, with the resultant output intensity captured by a CMOS camera.

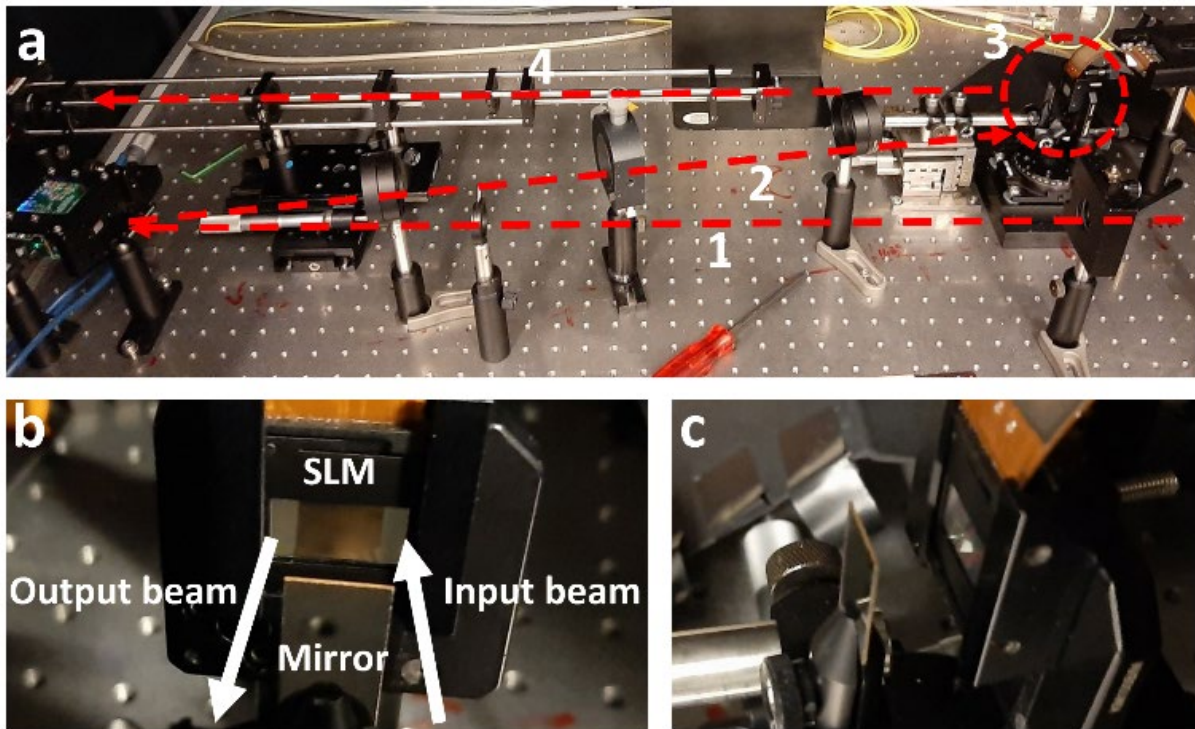


**Figure 6:3 Experimental setup of ROSSMi.** (a) The experimental setup. 1-collimated laser beam path, 2-a Digital Micromirror Device (DMD) emulates input aperture and a 4F imaging system relays the light into multi-bounce cavity, 3-multi-bounce cavity, 4-another 4F imaging system relays the output of the multi-bounce cavity on a camera. (b) Front-view of the multi-bounce cavity in the setup (c) side-view of the multi-bounce cavity.

### 6.3 Results

In this section, we provide three examples for different connectivity modalities. First, we start by numerical and experimental study on unicast connections by employing four modulation layers that interconnect 25 input ports to 25 output ports that are positioned as a 5 by 5 grid. Figure 6:4 shows four phase masks obtained via employed optimization scheme. The operating wavelength is 850 nm and the output grid is simply recorded on a CMOS camera. Simulations show that for such a 25 by 25 unicast, broadband (meaning that spectral granularity is not utilized) device, we achieve 75% efficiency in connectivity (equivalent to -1.25 dB insertion loss) with a 5% standard deviation across different nodes for different connectivity maps with a mean cross-talk of -24 dB. In Figure 6:4(b), we also provide some examples of obtained outputs. In the last row of Figure 6:4, we provide the obtained transmission matrix where rows represent the input nodes and columns represent the output nodes (up to 25 for inputs and outputs in this example) meaning that the diagonal entries highlight optical power in correct mappings and off-diagonal entries indicate the cross-talk. We have not measured the transmission matrix experimentally as additional work is required to minimize the discrepancy between simulation and experiment.

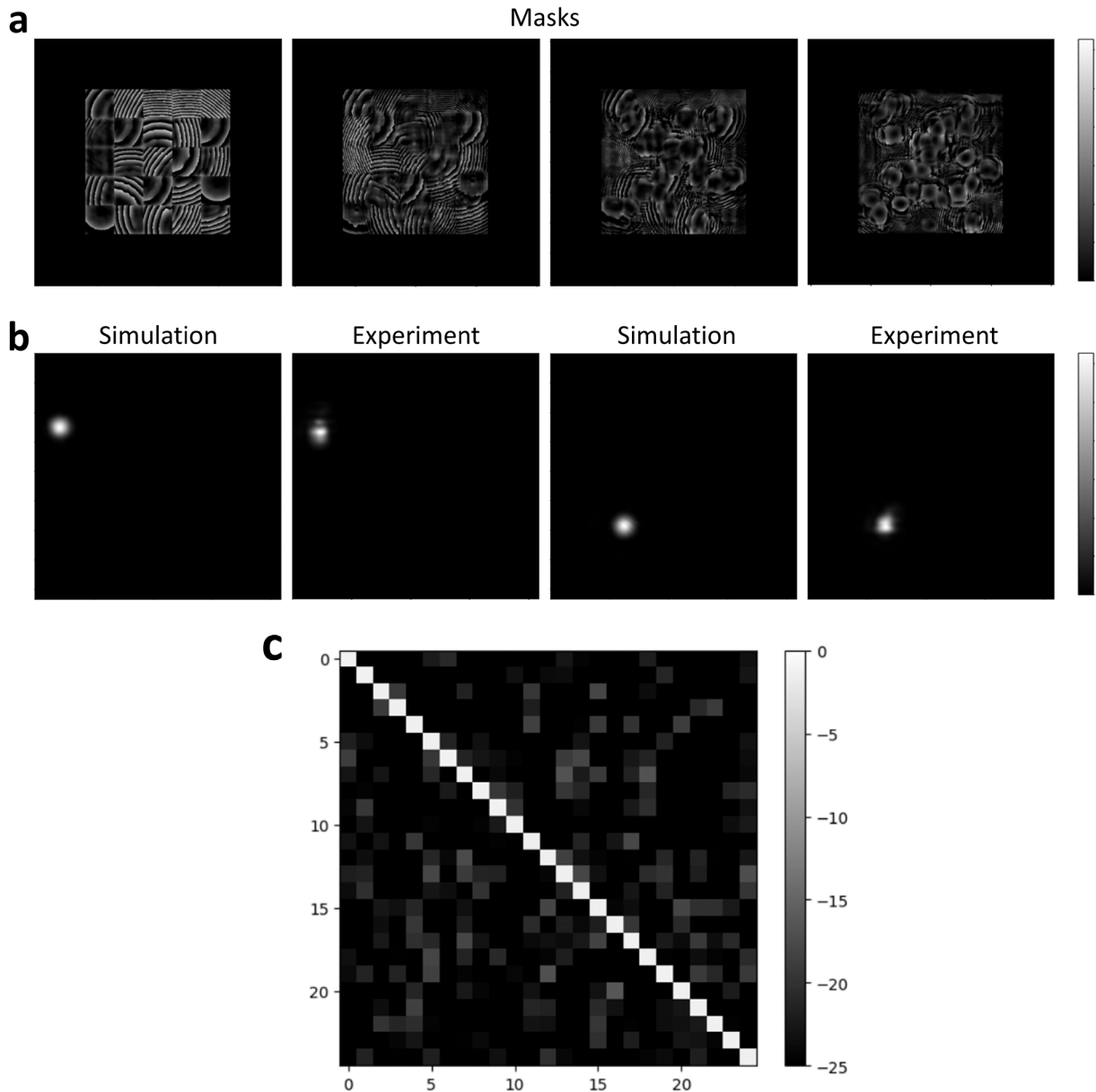


**Figure 6:4 Results of unicast spatial granularity.** (a) Optimized phase masks. The color bar shows the phase from 0 to  $2\pi$ . The inner squares where we observe the phase modulation are 2.4 mm by 2.4 mm. (b) two different examples of simulated outputs that correctly coincide with the target position and corresponding experimental results. The color bar shows the normalized intensity for each recording and simulation. (c) Simulated transmission matrix. The color bar spans from 0 to -25 dB.

Figure 6:5 shows an example of masks and results of a device with four modulation layers that interconnect 25 input ports to 25 output ports that are positioned as a 5 by 5 grid similar to the above-mentioned example. This time, five input ports are multicasting their signal to three, four, five, six, and seven different output ports respectively, populating all the output ports. Again, spectral granularity is not utilized in this example. In Figure 6:5(b), we show two examples, 1-to-3 and 1-to-7 multicasting respectively by providing simulated output planes that correctly coincide with the target position and corresponding experimental results. Note that, in this example, the positions of the input ports are also visible by checking the first modulation mask since there is a phase response only when there is input light on the modulation layer. With this multicast configuration, there is no significant change in connectivity efficiency and cross-talk in the simulations. Since it is not straightforward to provide a simple transmission matrix for the case of multicasting, we do not provide it here to avoid confusion.

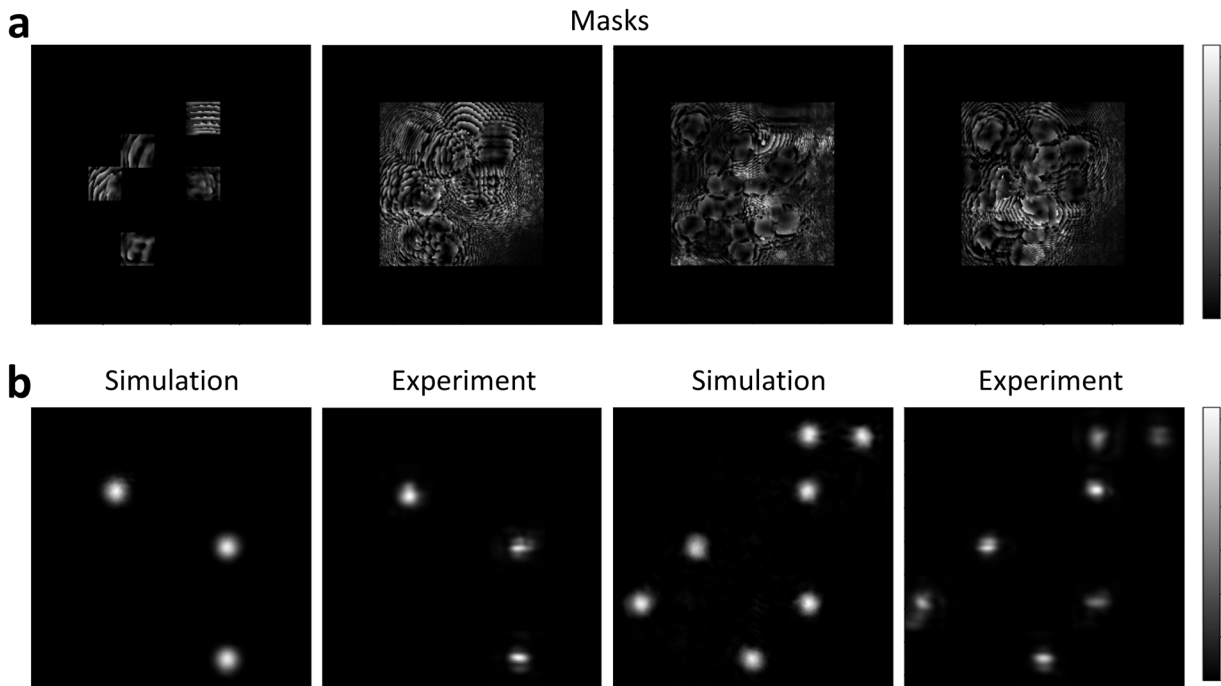


**Figure 6:5 Results of multicast spatial granularity.** (a) Optimized phase masks. The color bar shows the phase from 0 to  $2\pi$ . The inner squares where we observe the phase modulation are 2.4 mm by 2.4 mm. (b) two different examples of simulated outputs that correctly coincide with the target position and corresponding experimental results for 1-to-3 and 1-to-7 multicasting respectively. The color bar shows the normalized intensity for each recording and simulation.

To demonstrate space-spectrum granularity, we made a numerical investigation. Figure 6:6 shows six optimized phase masks and results of a device with six modulation layers that interconnect 9 spatial input ports to 9 spatial output ports that are positioned as a 3 by 3 grid where three different wavelengths are also incorporated in each channel (830 nm, 850 nm, and 870 nm respectively). In other words, this example demonstrates space-spectrum granularity by arbitrarily interconnecting 27 spatial-spectral input ports to 27 spatial-spectral output ports. Different wavelengths are routed to their assigned port by repetitive wavefront shaping. Simulations show that for such a configuration, we achieve 65% efficiency in connectivity (equivalent to -1.9 dB insertion loss) with a 10% standard deviation across different nodes for different connectivity maps with a mean cross-talk of -14 dB. In the last row of Fig. 10, we provide an example of transmission matrices for each wavelength where rows represent the input nodes and columns represent the output nodes. The combination of three matrices naturally constitutes 27 spatial-spectral input/output nodes.



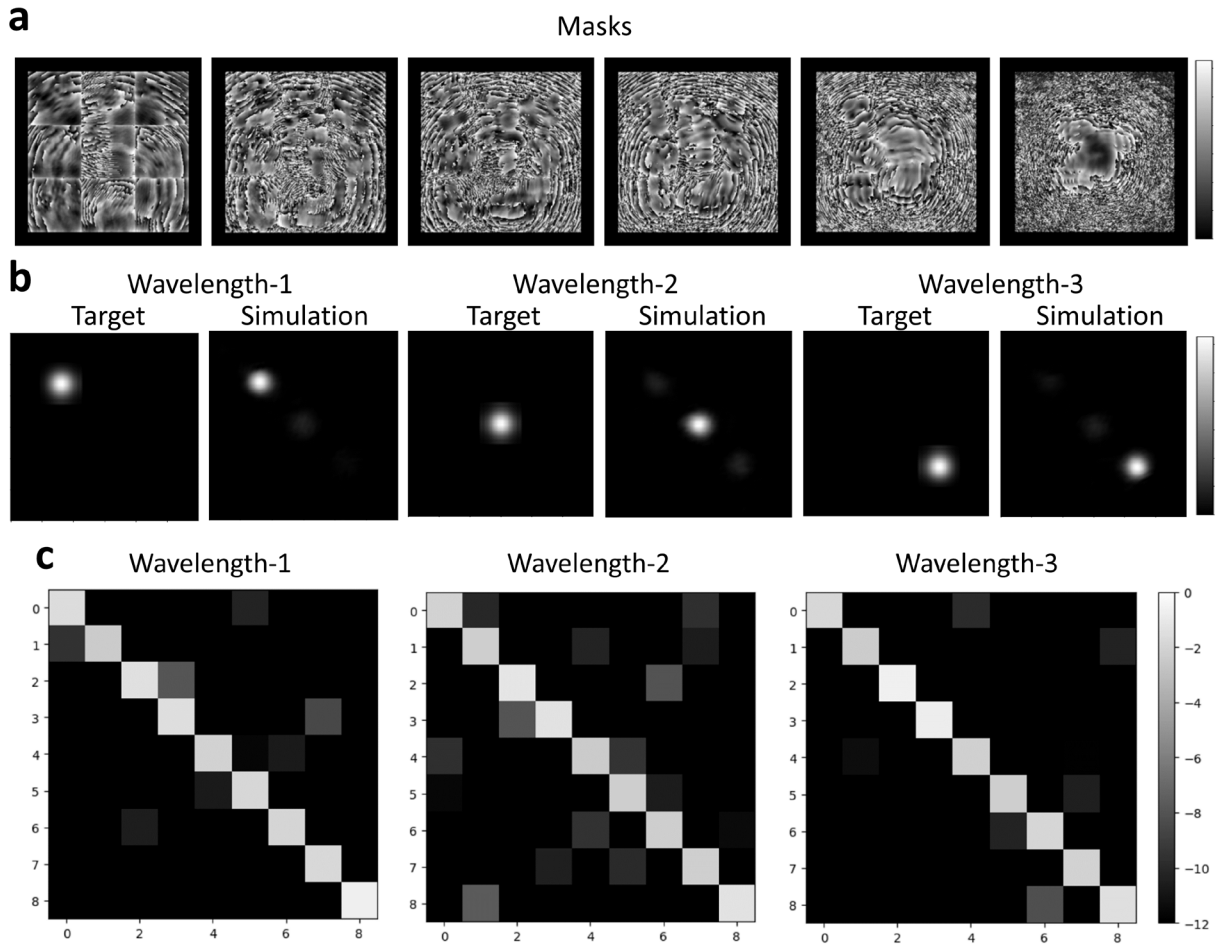


**Figure 6:6 Results of spatial-spectral granularity.** (a) Optimized phase masks. The color bar shows the phase from 0 to  $2\pi$ . The inner squares where we observe the phase modulation are 2.4 mm by 2.4 mm. (b) three different examples of simulated outputs that correctly coincide with the target for three different wavelengths. The color bar shows the normalized intensity for each simulation. (c) Simulated transmission matrices for each wavelength. The color bar spans from 0 to -12 dB.

## 6.4 Conclusion and outlook

Our study details how ROSSMi employs the principles of free space diffraction combined with programmable spatial light modulation techniques. Distinctively, this method differs from traditional methods that often depend on singular paths. Instead, the use of spatial light modulation across multiple planes allows ROSSMi to introduce a paradigm of on-demand reconfiguration for optical paths, inclusive of its inherent multicasting capabilities.

Numerical studies have yielded promising efficiency values. It is noted that free-space techniques inherently present potential efficiency, a notable advantage over integrated solutions where factors like waveguide loss and coupling losses can affect performance. Comparable architectures have been documented in the literature for multiplexing/demultiplexing fiber modes [157] along with Chapter 3 of this thesis, suggesting versatility in domains like varied mode domains and input/output grid geometries. With ROSSMi, the efficiency for multicasting remains consistent, offering a potential solution to the longstanding multicasting challenges in conventional optical systems. Our research also demonstrates the capacity to manage both space and spectrum in the interconnect through trials with three distinct wavelengths, indicating a potential shift in optical interconnect approaches. This not only enhances the reconfigurability of optical paths but also broadens the spectrum of wavelengths and spatial inputs that can be managed. It is important to note, however, that while the preliminary findings for ROSSMi are encouraging,

the technique is still evolving. Discrepancies between simulation and experimental results exist, highlighting the importance of further refinement. A potential advancement might involve utilizing the optical signal from the experiment to compute the loss, which would then digitally back-propagate, as exemplified in [14].

To sum up, the ROSSMi device offers a new perspective in network design, potentially bridging the efficiency gap in multicasting present in today's optical interconnect technologies.

# Chapter 7 Nonlinearities in systems based on linear optics

This is a prelude chapter to introduce the nonlinear transformations that can be obtained in systems relying on linear optics. One group of nonlinear relationships arise from the way data is injected and read-out since these systems are inevitably hybrid and interfaced with electronics. We will particularly delve into the nonlinearity arising from introducing the input data by phase encoding using modulators and read read-out by cameras that detect the intensity of light given that there is a linear optical system in between input plane and output plane (see Figure 7:1). Note that we have a 3D perspective in the analysis, but the conclusions remain valid when the dimensionality is reduced to 2D, making it applicable to integrated solutions.

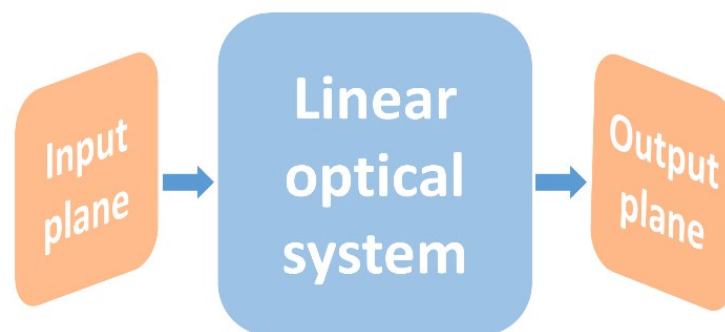


**Figure 7:1 - A system based on linear optics.** Each block may have opto-electronic components.

The linear optical system can be free-space [158], random scattering medium [7], [159], structured scattering medium [6], [160] or a multimode fiber [27], [161]. In this section, we do not analyze the nonlinearities arising from light-matter interaction, which can introduce additional enrichment of the nonlinear transform in any of the mentioned arrangements (except, of course, the free-space). Lastly, we will establish the theoretical framework of nonlinearity arising from multiple scattering [162]–[164], which is employed in the next chapter to perform classification tasks typically undertaken by digital neural networks. In Chapter 2, we explained in detail the highly nonlinear relationship between the output field and the scattering potential given that multiple scattering occurs. This is the reason why iterative optimization schemes are employed in optical diffraction tomography and inverse design of linear optical elements aiming for multiplexing or interconnection tasks. In this chapter, we will introduce the theoretical background of using this nonlinear relationship for computing based on the architecture introduced in the previous chapter for reconfigurable multilayer interconnects without loss of generality. In the next chapter, we will provide the examples of applications of classification tasks.

## 7.1 Intensity detection

We start by the simplest mechanism that yields a nonlinear transformation, the intensity detection. Here, we explain how intensity detection plays a vital role than simply applying elementwise absolute square on the field when there is a linear system that couples the pixelated pieces of information presented in the input plane. A linear system can be modeled by its transmission matrix [89], which can be expressed as follows:

$$\mathbf{o} = \mathbf{A}\mathbf{i}$$

Equation 7:1 – Transmission matrix formalism for linear systems.

Without loss of generality, let us assume that we have an optical system that has an input aperture and output aperture that are discretized/sampled by the same number of  $K$  pixels. Hence, in Equation 7:1,  $\mathbf{o}$  stands for the output vector (Electric field) with dimensions  $K \times 1$ , and  $\mathbf{i}$  stands for the input vector (Electric field) with dimensions  $K \times 1$ . Thus,  $\mathbf{A}$  stands for the transmission matrix of the system with dimensions  $K \times K$ . For simplicity, let us assume  $K = 2$ . Note that this assumption does not prevent generalization to an arbitrary number of  $K$ . In this case, Equation 7:1 can be written as:

$$\begin{bmatrix} o_1 \\ o_2 \end{bmatrix} = \begin{bmatrix} A_{11} & A_{12} \\ A_{21} & A_{22} \end{bmatrix} \begin{bmatrix} i_1 \\ i_2 \end{bmatrix}$$

$$\begin{bmatrix} o_1 \\ o_2 \end{bmatrix} = \begin{bmatrix} A_{11}i_1 + A_{12}i_2 \\ A_{21}i_1 + A_{22}i_2 \end{bmatrix}$$

Equation 7:2 – Transmission matrix formalism with elements shown explicitly.

Intensity detection transforms  $\mathbf{o}$  by:

$$\begin{bmatrix} |o_1|^2 \\ |o_2|^2 \end{bmatrix} = \begin{bmatrix} |A_{11}i_1|^2 + A_{11}i_1A_{12}^*i_2^* + A_{12}i_2A_{11}^*i_1^* + |A_{12}i_2|^2 \\ |A_{21}i_1|^2 + A_{21}i_1A_{22}^*i_2^* + A_{22}i_2A_{21}^*i_1^* + |A_{22}i_2|^2 \end{bmatrix}$$

Equation 7:3 – Expression for  $\mathbf{o}$  by intensity detection.

Note that \* stands for complex conjugate. When we take a look at Equation 7:3, we see that multiplicative cross-terms of elements of  $\mathbf{i}$  emerged by the absolute square of the output field that is a scrambled version of the input field by the transmission matrix  $\mathbf{A}$ . If we did not have off-diagonal elements of  $\mathbf{A}$ , these cross-terms would not have emerged. It is important to note that generation of these cross-terms is very important for computing as they might represent useful features for certain tasks. This is the reason why intensity detection can be very powerful given that there is a linear optical system with non-zero off-diagonal terms in its transmission matrix. It is important to note that this result is independent of how the data is encoded on  $\mathbf{i}$ .

## 7.2 Phase encoding

In this section, we demonstrate that encoding data onto the phase of light is not merely an exponentiation operation, but rather establishes a more complex nonlinear relationship. Let us continue our discussion from Equation 7:2 without going into intensity detection. This time, we will consider a data vector  $\mathbf{d}$ , which is encoded on  $\mathbf{i}$  as the phase term, meaning that:

$$\begin{bmatrix} i_1 \\ i_2 \end{bmatrix} = \begin{bmatrix} e^{jd_1} \\ e^{jd_2} \end{bmatrix}$$

Equation 7:4 – Phase encoding of  $\mathbf{d}$  on  $\mathbf{i}$ .

Plugging Equation 7:4 into Equation 7:2 yields:

$$\begin{bmatrix} o_1 \\ o_2 \end{bmatrix} = \begin{bmatrix} A_{11}e^{jd_1} + A_{12}e^{jd_2} \\ A_{21}e^{jd_1} + A_{22}e^{jd_2} \end{bmatrix}$$

Equation 7:5 – Output with phase encoding without the intensity detection.

Equation 7:5 provides a weighted summation of the exponentiated data terms, which is a rich nonlinear representation. Let us also take a look at this expression with the intensity detection:

$$\begin{bmatrix} |o_1|^2 \\ |o_2|^2 \end{bmatrix} = \begin{bmatrix} |A_{11}|^2 + A_{11}A_{12}^*e^{j(d_1-d_2)} + A_{12}A_{11}^*e^{-j(d_1-d_2)} + |A_{12}|^2 \\ |A_{21}|^2 + A_{21}A_{22}^*e^{j(d_1-d_2)} + A_{22}A_{21}^*e^{-j(d_1-d_2)} + |A_{22}|^2 \end{bmatrix}$$

Equation 7:6 – Output with phase encoding with the intensity detection.

Equation 1:6 provides a weighted summation of the exponentiated data terms after subtraction, with bias terms emerging from the transmission matrix. Contrary to what one might assume, these bias terms don't necessarily hinder the signal; in fact, they can be thought of as a threshold-like mechanism. Nonetheless, determining which expression, whether from Equation 1:5 or Equation 1:6, is more useful is challenging. Such assessments largely depend on the data and the optimization algorithm, and the ideal choice is typically found empirically.

### 7.3 Multiple scattering with data repetition

Here we will investigate how we can utilize the highly nonlinear relationship between the scattering potential and the output field beyond Born approximation (or single scattering in other words) that we have discussed in Chapters 2 and 3. Our analysis will be based on the architecture we introduced in the previous chapter with reconfigurable multilayer approach meaning that now we explicitly define the linear optical system where the input data is repetitively presented in the multiple layers. In a way, this can be represented as cascading linear systems as depicted in Figure 7:2. However, the conclusions are valid for all the previously mentioned optical systems.

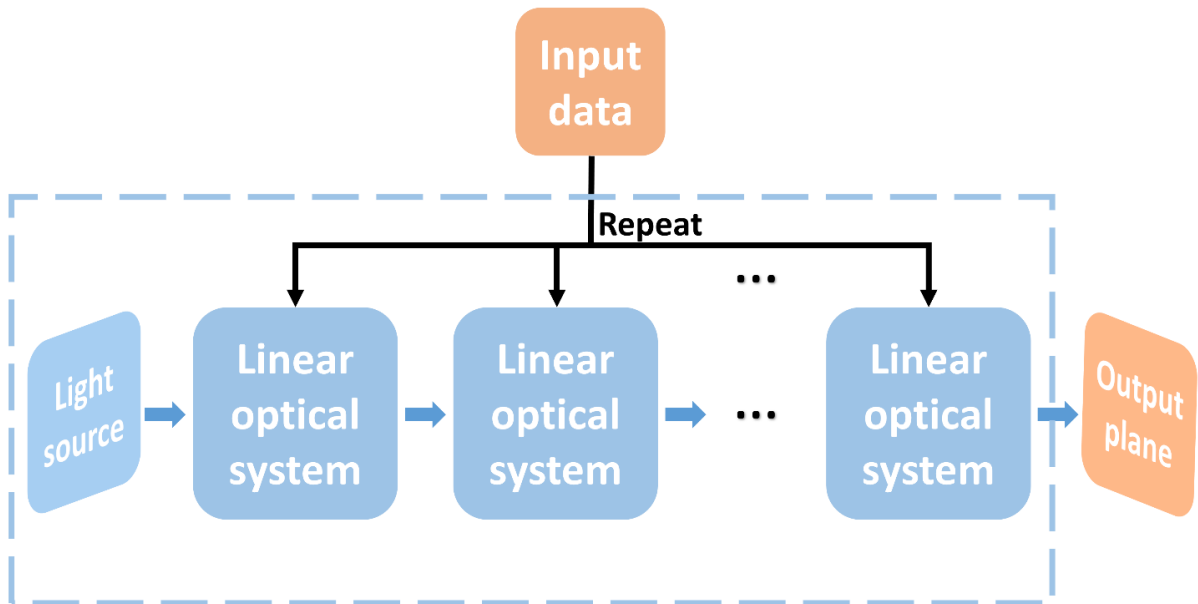
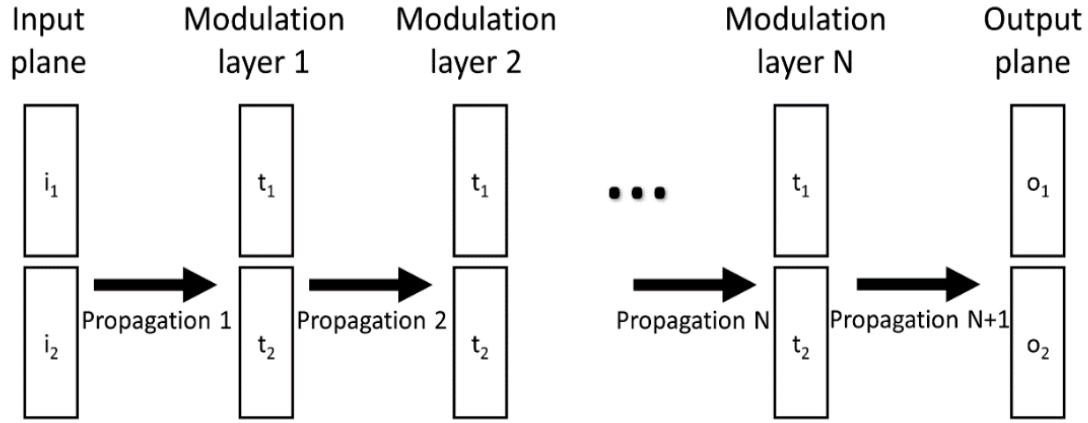


Figure 7:2 – A system based on linear optics and multiple/repetitive data presentation.

We acknowledge that the derivation for this section is adopted from the supplementary information of the preprint version of the article “Nonlinear Processing with Linear Optics” by Dinc, Yildirim, Oguz, Psaltis, and Moser available in arXiv [164]. We present an analysis of a simplified optical system where each plane/layer consists of two pixels (see Figure 7:3) and a propagation step whose system response is expressed by a matrix with linear

coefficients. The generalization of this analysis to an arbitrary number of pixels in each layer is straightforward. We provide the investigation for Modulation layer number  $N=1$ ,  $N=2$ , and  $N=3$  for ease of explanation and the conclusions are valid for arbitrary  $N$  by inductive reasoning.



**Figure 7:3 - Simplified optical system for multiple scattering with data repetition** where each plane/layer consists of two pixels.

The system response for Modulation layer  $N=1$  is the following:

$$\mathbf{o} = \mathbf{P}_2 \mathbf{T} \mathbf{P}_1 \mathbf{i}$$

Equation 7:7 – The system response for Modulation layer  $N=1$

Where  $\mathbf{P}_1$  is the propagation matrix 1,  $\mathbf{P}_2$  is the propagation matrix 2, and  $\mathbf{T}$  is the modulation matrix. For  $\mathbf{P}_1$ , we assume zero propagation for simplicity without losing generality and for  $\mathbf{P}_2$  we use a Toeplitz matrix to represent diffraction for an arbitrary distance. For a two-pixel per layer system we simply have the following:

$$\mathbf{P}_1 = \begin{bmatrix} 1 & 0 \\ 0 & 1 \end{bmatrix}$$

$$\mathbf{P}_2 = \begin{bmatrix} h_{11} & h_{12} \\ h_{21} & h_{22} \end{bmatrix}$$

$$\mathbf{T} = \begin{bmatrix} t_1 & 0 \\ 0 & t_2 \end{bmatrix}$$

Hence:

$$\begin{bmatrix} o_1 \\ o_2 \end{bmatrix} = \begin{bmatrix} h_{11} & h_{12} \\ h_{21} & h_{22} \end{bmatrix} \begin{bmatrix} t_1 & 0 \\ 0 & t_2 \end{bmatrix} \begin{bmatrix} i_1 \\ i_2 \end{bmatrix}$$

And we have:

$$\begin{bmatrix} o_1 \\ o_2 \end{bmatrix} = \begin{bmatrix} h_{11}t_1i_1 + h_{12}t_2i_2 \\ h_{21}t_1i_1 + h_{22}t_2i_2 \end{bmatrix}$$

Following similar steps for Modulation layer N=2 (assuming  $\mathbf{P}_3 = \mathbf{P}_2$  without loss of generality). Note that the data in layer N=2 is the same as layer N=1.

$$\begin{aligned} \begin{bmatrix} o_1 \\ o_2 \end{bmatrix} &= \begin{bmatrix} h_{11} & h_{12} \\ h_{21} & h_{22} \end{bmatrix} \begin{bmatrix} t_1 & 0 \\ 0 & t_2 \end{bmatrix} \begin{bmatrix} h_{11}t_1i_1 + h_{12}t_2i_2 \\ h_{21}t_1i_1 + h_{22}t_2i_2 \end{bmatrix} \\ \begin{bmatrix} o_1 \\ o_2 \end{bmatrix} &= \begin{bmatrix} h_{11}^2t_1^2i_1 + h_{11}h_{12}t_2t_1i_2 + h_{12}h_{21}t_1t_2i_1 + h_{12}h_{22}t_2^2i_2 \\ h_{21}h_{11}t_1^2i_1 + h_{21}h_{12}t_2t_1i_2 + h_{22}h_{21}t_1t_2i_1 + h_{22}^2t_2^2i_2 \end{bmatrix} \end{aligned}$$

Equation 7:8 – The system response for Modulation layer N=2

Hence, we reach a nonlinear relationship between the output field  $o_1, o_2$  and the data plane  $t_1, t_2$ . When intensity detection is employed as the acquisition method, the obtained output will be the absolute square of the field, providing a 4th order polynomial of the parameters inserted in the modulation layers for the specific case of 2 layers (N=2). Clearly, when data is introduced in the modulation layers, we obtain a nonlinear processing of the data at the output plane either by detecting the field (by a holographic recording) and/or the intensity (by a simple detector, which can be CMOS, CCD, etc.). The input field  $i$  can be a programming parameter to change the effective transform. For simplicity, we will continue with a plane wave input without loss of generality:

$$\begin{bmatrix} i_1 \\ i_2 \end{bmatrix} = \begin{bmatrix} 1 \\ 1 \end{bmatrix}$$

For a phase-only modulation, we have the following relation for the modulation terms:

$$t_i = e^{j\phi_i}$$

In this case, the data becomes  $\phi_i$ . Then we have:

$$\begin{bmatrix} o_1 \\ o_2 \end{bmatrix} = \begin{bmatrix} h_{11}^2e^{j2\phi_1} + h_{11}h_{12}e^{j(\phi_1+\phi_2)} + h_{12}h_{21}e^{j(\phi_1+\phi_2)} + h_{12}h_{22}e^{j2\phi_2} \\ h_{21}h_{11}e^{j2\phi_1} + h_{21}h_{12}e^{j(\phi_1+\phi_2)} + h_{22}h_{21}e^{j(\phi_1+\phi_2)} + h_{22}^2e^{j2\phi_2} \end{bmatrix}$$

Equation 7:9 – Output of multiple scattering with the phase encoding and without the intensity detection.

In the above expression, there is no polynomial order of the data at the output electric field, although the relation is nonlinear due to the summation of exponentials. When we detect the intensity, we obtain the following:

$$\begin{aligned} \begin{bmatrix} I_1 \\ I_2 \end{bmatrix} &= \begin{bmatrix} |o_1|^2 \\ |o_2|^2 \end{bmatrix} = \begin{bmatrix} \left| h_{11}^2e^{j2\phi_1} + h_{11}h_{12}e^{j(\phi_1+\phi_2)} + h_{12}h_{21}e^{j(\phi_1+\phi_2)} + h_{12}h_{22}e^{j2\phi_2} \right|^2 \\ \left| h_{21}h_{11}e^{j2\phi_1} + h_{21}h_{12}e^{j(\phi_1+\phi_2)} + h_{22}h_{21}e^{j(\phi_1+\phi_2)} + h_{22}^2e^{j2\phi_2} \right|^2 \end{bmatrix} \\ &= \begin{bmatrix} DC + C_1 \cos(\phi_1 - \phi_2 + \theta_1) + C_2 \cos(2(\phi_1 - \phi_2 + \theta_2)) \\ DC + C_3 \cos(\phi_1 - \phi_2 + \theta_3) + C_4 \cos(2(\phi_1 - \phi_2 + \theta_4)) \end{bmatrix} \end{aligned}$$

Equation 7:10 – Output of multiple scattering with the phase encoding and the intensity detection.

In the above expression, the DC term refers to the grouping of the terms that do not depend on the SLM phase pattern  $\phi_i$ . The constant terms  $C_i$  represent the electric field amplitude resulting from light propagation between

layers.  $\theta_i$  is the additional phase bias of the constants arriving from propagation matrix. The elements of the propagation matrix are complex valued. Note that the intensity detection yields cosine terms. The integer multiplier (the factor 2) in the second cosine term comes from the fact that there are two modulation layers. Note that this term has a polynomial orders:

$$\cos(2\theta) = 2\cos^2(\theta) - 1$$

Equation 7:11 – Cosine double angle identity

Hence, intensity detection provides the nonlinearity (cosine) and where the multiple modulation layers provide the polynomial orders of the cosine term. Similarly, when adding a third modulation layer N=3, we have:

$$\begin{bmatrix} o_1 \\ o_2 \end{bmatrix} = \begin{bmatrix} h_{11}^3 t_1^3 + (h_{11}^2 h_{12} + 2h_{12} h_{21} h_{11}) t_2 t_1^2 + (h_{11} h_{12} h_{22} + h_{12}^2 h_{21} + h_{12} h_{21} h_{22}) t_1 t_2^2 + h_{12} h_{22}^2 t_2^3 \\ h_{21} h_{11}^2 t_1^3 + (h_{21} h_{11} h_{12} + h_{21}^2 h_{12} + h_{11} h_{21} h_{22}) t_2 t_1^2 + (h_{22}^2 h_{21} + 2h_{12} h_{21} h_{22}) t_1 t_2^2 + h_{22}^3 t_2^3 \end{bmatrix}$$

$$\begin{bmatrix} I_1 \\ I_2 \end{bmatrix} = \begin{bmatrix} DC + C_1 \cos(\phi_1 - \phi_2 + \theta_1) + C_2 \cos(2(\phi_1 - \phi_2 + \theta_2)) + C_3 \cos(3(\phi_1 - \phi_2 + \theta_3)) \\ DC + C_4 \cos(\phi_1 - \phi_2 + \theta_4) + C_5 \cos(2(\phi_1 - \phi_2 + \theta_5)) + C_6 \cos(3(\phi_1 - \phi_2 + \theta_6)) \end{bmatrix}$$

Equation 7:12 – The outputs for Modulation layer N=3

Noting that:

$$\cos(3\theta) = 4\cos^3(\theta) - 3\cos(\theta)$$

Equation 7:13 – Cosine triple angle identity

By induction, it is obvious that the polynomial orders increases with the number of modulation layers N. In summary, complex modulation (amplitude and/or phase) or with only amplitude modulation in the different layers yield a nonlinear relationship between the output field and the modulation parameters. The intensity detection performed along with phase only modulation results in nonlinear relationship via polynomial orders of sinusoidal terms induced by intensity detection.



# Chapter 8 Reconfigurable multilayer optics for nonlinear processing

This chapter is the pre-print version of the following article available in *arXiv*.

**Nonlinear Processing with Linear Optics** by Mustafa Yildirim<sup>1,2,†</sup>, Niyazi Ulas Dinc<sup>1,2,†</sup>, Ilker Oguz<sup>1,2</sup>, Demetri Psaltis<sup>2</sup> and Christophe Moser<sup>1</sup>

† Equally contributing authors

N.U.D., M.Y., D.P., and C.M. conceived and initiated the project. N.U.D. provided the first version of numerical training module. N.U.D. and M.Y. modified the training scheme according to the needs of this project. N.U.D., M.Y., and I.O. worked on the experimental setup and used datasets.

<sup>1</sup> Laboratory of Applied Photonics Devices, Ecole Polytechnique Fédérale de Lausanne (EPFL), Switzerland

<sup>2</sup> Optics Laboratory, Ecole Polytechnique Fédérale de Lausanne (EPFL), Switzerland

Available in arXiv (2023)

<https://doi.org/10.48550/arXiv.2307.08533>

Deep neural networks have achieved remarkable breakthroughs by leveraging multiple layers of data processing to extract hidden representations, albeit at the cost of large electronic computing power. To enhance energy efficiency and speed, the optical implementation of neural networks aims to harness the advantages of optical bandwidth and the energy efficiency of optical interconnections. In the absence of low-power optical nonlinearities, the challenge in the implementation of multilayer optical networks lies in realizing multiple optical layers without resorting to electronic components. In this study, we present a novel framework that uses multiple scattering that is capable of synthesizing programmable linear and nonlinear transformations concurrently at low optical power by leveraging the nonlinear relationship between the scattering potential, represented by data, and the scattered field. Theoretical and experimental investigations show that repeating the data by multiple scattering enables nonlinear optical computing at low power continuous wave light.

## 8.1 Introduction

Optical computing has reemerged as an alternative to electronics for performing computations and handling information, particularly in the context of artificial intelligence applications. Optical neural networks (ONNs) hold promise in terms of speed and energy efficiency compared to traditional electronic computing [165]. However, the development of fully optical ONNs has proven to be a challenging task due to the need for incorporating both linear and nonlinear computations within the optical domain [21]. While several approaches have demonstrated efficient

optical computing hardware for linear calculations [3], [5], [6], [23], [166], effectively integrating these capabilities with nonlinear computations remains a significant obstacle for a complete realization of ONNs. Researchers have explored nonlinear light-matter interactions in the context of reservoir computing [26], [167], [168], employing high intensity pulsed lasers for nonlinear data processing [14], [27], [169], [170]. This approach is distinct because nonlinear light-matter interactions require high-power lasers, whereas low-power continuous wave lasers have been employed for linear computations. Platforms like integrated meshes of Mach Zehnder Interferometers [5], diffractive neural networks [6], [8], [171], micro-ring resonators [166], [172], and free space linear systems [3], [173], [174] have facilitated linear calculations. However, for nonlinear computations, optoelectronic nonlinearity or electronic computation has been relied upon, resulting in limitations such as non-programable optoelectronic nonlinearity and high energy consumption. Therefore, there is a need to find a low power flexible solution to implement non-linear operations in the optical domain in order to fully harness the low power computing potential offered inherently by linear optics.

The Ozcan group has introduced an approach to ONNs through the utilization of successive spatially engineered transmissive diffractive layers, employing additive manufacturing techniques [171]. These deep learning-enabled multi-layer diffractive processors enable computation by facilitating the propagation of free-space light through a sequence of structured passive scattering surfaces. This optical processing technique leverages the three-dimensional connectivity between nodes in consecutive layers, achieved via diffraction, thereby providing a path to scalability [140]. However, one limitation of this approach is that the nonlinearity is limited to the square law detection at the output which limits the realization of complex ONNs.

Another avenue that can be explored is the relationship between the scattering potential and the scattered light. While at low intensity levels, the propagation of light through a scattering medium exhibits linearity in terms of the relation between input and output light field, the output light can have a nonlinear dependence on the data encoded in the scattering potential. This form of nonlinearity is referred to as structural nonlinearity, and it has been investigated by a separate research group through the use of multiple scatterings within an integrating sphere [162].

In this paper, we present a programmable framework called nonlinear Processing with only Linear Optics (nPOLO) for the all-optical realization of neural networks using a low-power continuous wave laser and diffractive layers. The nPOLO framework enables simultaneous linear and nonlinear operations within the optical domain. In this way, nPOLO unifies multi-layer light modulation and structural nonlinearity such that the collective impact of data modulated layers on propagating light generates high order nonlinear transform of the data. Data is repetitively embedded into the modulation layers, combined with trainable parameters that enable the desired relationship (linear and nonlinear) between the data and the output field. Our results demonstrate that increasing the number of layers and data repetitions leads to the generation of higher-order nonlinearities, such as polynomial orders, which include cross-terms among the different elements of the input data. To illustrate the effectiveness of data repetition, we conducted a comparative analysis of the performance obtained between repeating the data in each modulation layer and presenting the data only once. Our results demonstrate that, when both systems have an equal number of degrees of freedom in terms of the displayed pixels in modulation layers, the data repetition approach consistently achieves higher accuracy scores and exhibits improved robustness against experimental imperfections and simulated noise. Overall, our findings showcase the ability of the nPOLO framework to synthesize a learnable both linear and non-linear data transform in a hybrid optical-digital neural network using only low power continuous wave light.

## 8.2 nPOLO framework

The core of the nPOLO technique involves utilizing multiple data planes that are evenly spaced apart. The physical implementation of nPOLO includes a liquid crystal Spatial Light Modulator (SLM) and a mirror positioned opposite to it [72], allowing the simultaneous display of multiple modulation planes on a single SLM device. This configuration forms a multi-bounce single pass cavity, where each plane serves as a thin element that modulates the phase

of light as it propagates progressively from one plane to the next. Figure 8:1 provides a visual representation of nPOLO. We introduce trainable parameters to program the transformation for executing specific tasks. These trainable parameters, in the form of scaling and bias, are applied to each pixel value of the data presented on the modulation layers. These parameters are trained digitally via a computer model (see Methods). Once the desired nonlinear transformation is achieved in the computer, the parameters are applied to the multiple layers (adjacent planes on the SLM) in the experimental setup, resulting in an intensity pattern that is recorded by a camera. Subsequently, a compact representation of the recorded camera pattern is obtained through average pooling, resulting in a 2D matrix of values such as a 4-by-4 or an 8-by-8 grid. This compact representation is then fed into a digital linear classifier, which processes the data via a single fully connected linear layer, thereby producing the final classification results.

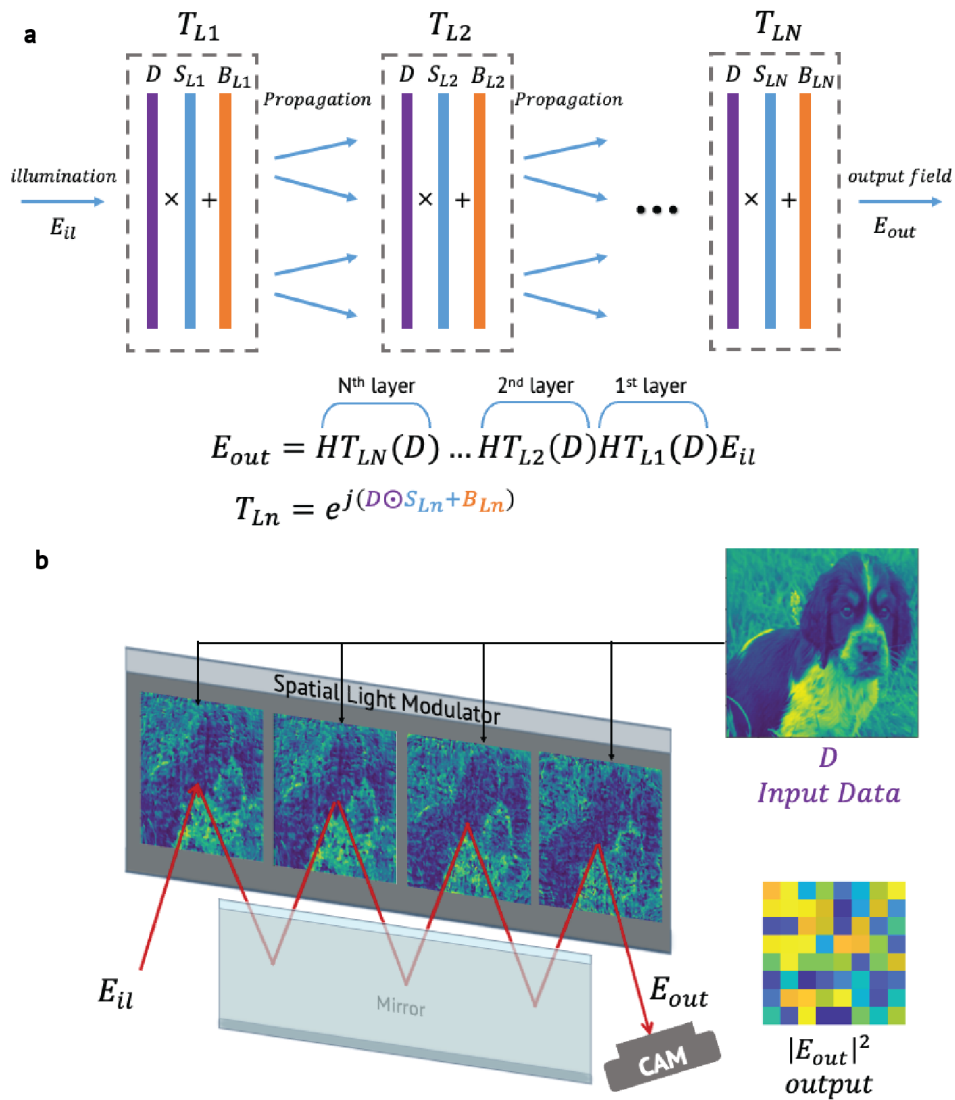


**Figure 8:1 - The framework of nPOLO** a) The computation scheme is depicted, showcasing multiple modulation layers ( $T_{Ln}$ ) within the framework. The data ( $D$ ) is presented on these layers, accompanied by trainable scaling ( $S_{Ln}$ ) and bias ( $B_{Ln}$ ) parameters to optimize the transformation. Propagation is represented by  $H$  (Toeplitz matrix) b) The physical implementation nPOLO, featuring a single pass multi-bounce cavity configuration. This implementation consists of a Spatial Light Modulator (SLM) and a mirror, positioned in a way that enables the realization of consecutive layers on the SLM side by side. The propagation distance is determined by the reflection from the mirror, allowing the light to propagate between the layers. Output light is captured with a camera.

By increasing the number of layers i.e. adjacent planes on the SLM, one can assess the impact of the polynomial orders resulting from structural nonlinearity. However, the increase in the number of layers also leads to an increase in the system's degrees of freedom and space-bandwidth product. Therefore, we devised an alternative comparison experiment to mitigate these effects. In our experiments, we maintained the same number of layers and pixels but modified the data allocation. Specifically, we initially incorporated the data only in the first layer, while the subsequent layers consisted exclusively of trainable bias parameters without any data or scaling parameters. To evaluate the performance of the nPOLO framework, we conducted experiments using the Imagenette, Fashion MNIST and Digit MNIST datasets [175]–[177]. The obtained numerical and experimental results are provided in Figure 8:2.

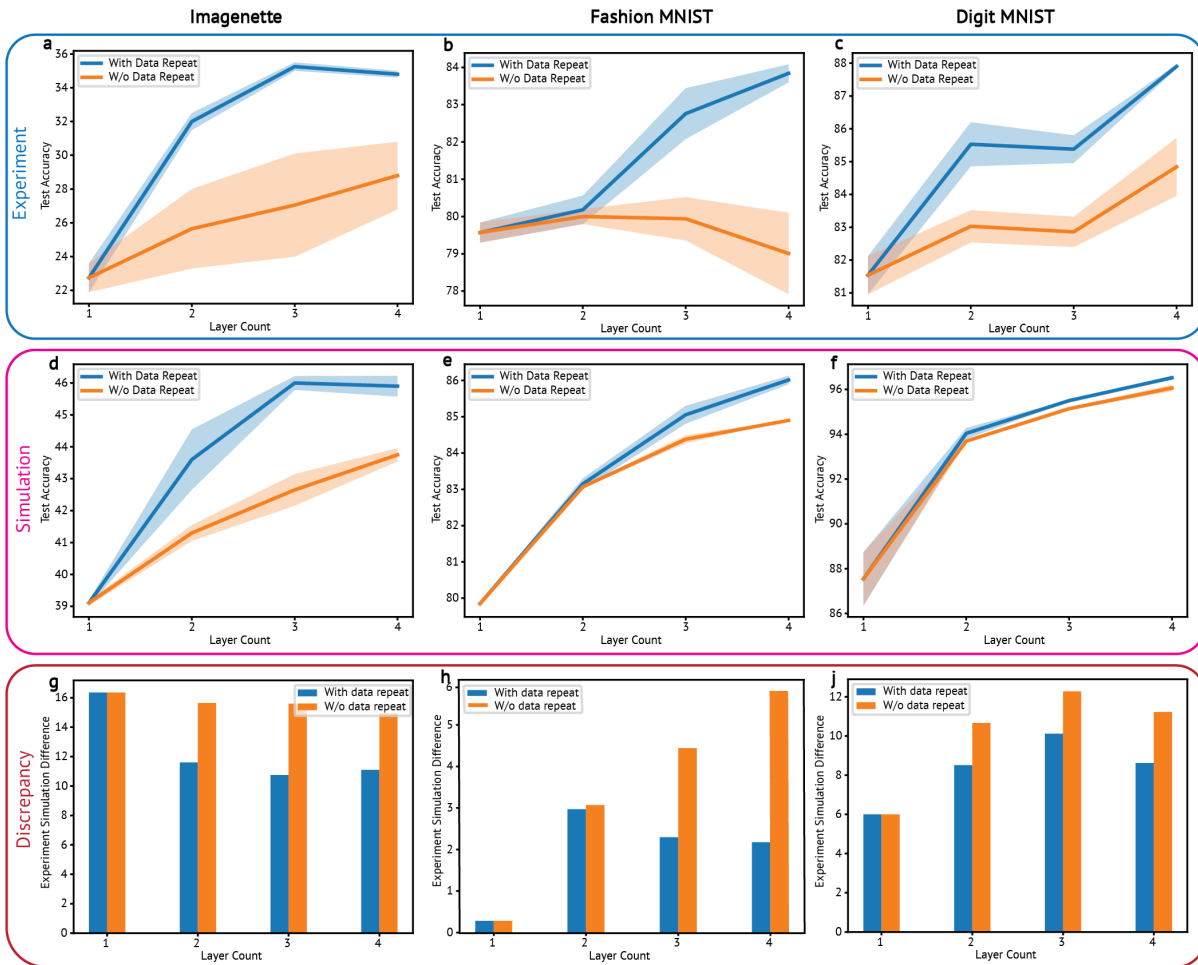


**Figure 8:2 - the classification accuracy results** obtained for the Imagenette (a,d,g), Fashion MNIST (b,e,h) and Digit MNIST (c,f,j) datasets, comparing two different schemas: one with "data repeat" and one without. The layer count ( $N$ ) is varied from one to four for both schemas. Each configuration is trained independently, resulting in layer masks that are applied to the Spatial Light Modulator (SLM) as phase masks. a, b, c) The experimentally obtained test accuracies for all datasets are displayed, representing the performance with and without structural nonlinearity. d, e, f) Test accuracies of corresponding simulations are plotted for both schemas likewise in experiments. g, h, j) The accuracy difference between experimental and simulated results are shown as bar plot for varying layer number with and without data repeat.

For clarity, we provide examples of the displayed masks in Figure 8:3 "with data repeat" and "without data repeat" configurations using an example from the Fashion MNIST and Imagenette datasets with four modulation layers. Also see Appendix D for the comparative depiction of parameter allocation. The trainable parameters were optimized by computer simulation, wherein the physical light propagation was modeled using the Beam Propagation Method (BPM).

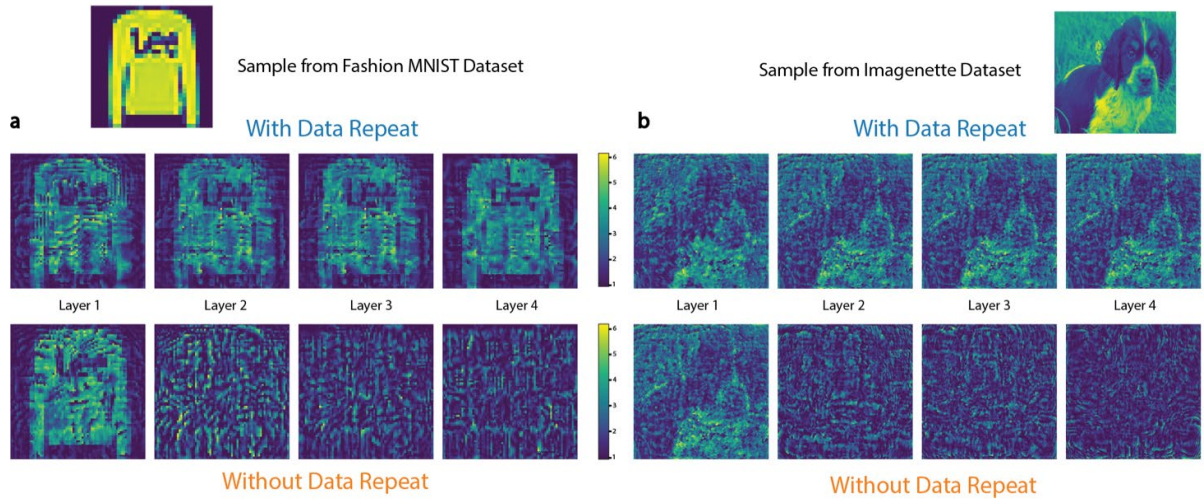


**Figure 8:3 - Samples of trained layer masks to be displayed on SLM for Fashion MNIST and Imagenette.** (a) Presents an example sample from the Fashion MNIST dataset alongside its corresponding layer masks, combined with trainable parameters, according to both schemas. The color code utilized represents the phase modulation ranging from 0 to  $2\pi$ . Similarly, panel (b) showcases an example sample from the Imagenette dataset and its corresponding layer masks combined with trainable parameters for both schemas.

Since BPM consists of differentiable calculation steps, the error can be backpropagated to the trainable parameters, and they are optimized using stochastic gradient descent. In Figure 8:4, we present the training scheme used, in which the digital model of the optical system and the digital classifier were co-trained for the classification tasks. By following this co-training approach, we obtained scaling and bias masks for different layer configurations, ranging from layer  $N=1$  to layer  $N=4$ , both with and without data repetition. It is important to note that in the case of a single layer ( $N=1$ ), both data repetition options are equivalent, as we only had a single layer available to introduce the data.

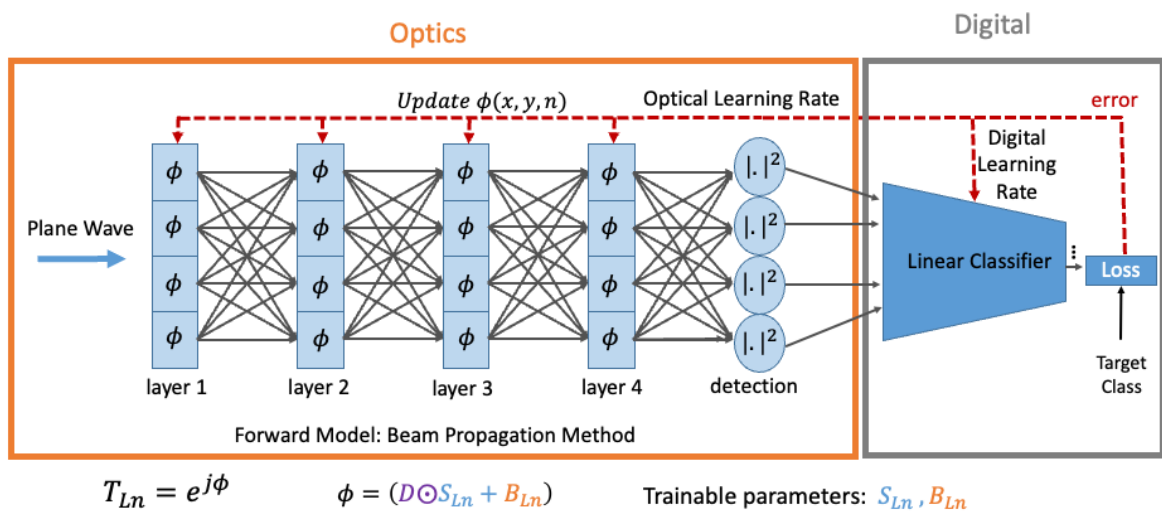


**Figure 8:4 - Co-training of optical trainable parameters and digital trainable parameters.** Simulation model of four-layer system based is built by beam propagation method, where layers are composed of trainable parameters ( $S_{Ln}$  and  $B_{Ln}$ ). Training of optical layers and linear classifier is performed simultaneously using separate learning rates.

Our experimental findings in Figure 8:2-a, b and c consistently demonstrated that when data was repeated across multiple layers, we achieved higher classification accuracy compared to configurations without data repetition. Moreover, increasing the number of layers also contributed to improved accuracy. We also observed that when

the number of layers was held constant, eliminating data repetition led to a reduction in accuracy. These results highlight the contribution of both higher order optical nonlinearities generated via data repetition and the number of layers in maximizing the classification task performance. We observed a similar trend in our simulations while calculating the trainable parameters (see Figure 8:2-d,e,f). Both experimental and simulated results validate the contribution of the nPOLO framework. However, it is worth mentioning that the experimental accuracies were lower than the simulated ones. Figure 8:2-g,h,j illustrate the accuracy difference between simulations and experiments in all three datasets. The decrease in accuracy is less pronounced in cases involving data repetition compared to those without. We attribute this discrepancy to imperfections between the simulated model and the physical implementation, such as the non-ideal phase response of the SLM and beam tilt, among others. As a preliminary study to assess digital counterpart of the nPOLO for these tasks, we trained simple convolutional neural networks and obtained comparable performance, see Appendix D.

### 8.3 Discussion

As described in the Methods section, the fixed and complex connectivity provided by free space propagation between each layer does not guarantee the extraction of useful representations. To address this limitation, we introduced trainable scaling and bias parameters for the pixel values of the displayed samples. It is important to note that this approach serves as a simple scheme for tuning the transformation. Future studies could explore alternative approaches, such as using convolutional kernels or eigenmodes of the optical system as trainable parameters, similar to investigations conducted for fiber-based optical learning machines [161]. During the final stage of this work, we became aware of an independent and different approach to perform passive optical non-linearity, exploiting reflections inside a disordered cavity [163]. By investigating these methods, we may further exploit the effects of higher-order nonlinearities.

Furthermore, we observed that the contribution of structural nonlinearity became more pronounced when dealing with more challenging classification tasks. The impact of using repeated data versus not using repeated data was more significant for Imagenette compared to Digit MNIST. This disparity arises because Digit MNIST represents an easier task, and the structural nonlinearity becomes redundant in the presence of detection nonlinearity.

Another notable observation is the increased robustness of data repetition across multiple layers against experimental imperfections. We initially noticed this phenomenon during experiments conducted on different datasets and layer configurations. To further investigate this, we introduced phase noise in BPM simulations to emulate experimental imperfections while keeping the trained masks fixed (see Appendix D.1). Gradually increasing the simulated noise level, we observed that the configurations with data repetition exhibited greater robustness compared to the configurations without data repetition. The latter experienced a more rapid drop in accuracy, consistent with the experimental results. This finding strengthens the argument for the noise robustness of the data repetition scheme, as we have empirical data from both experiments and simulations. One possible explanation for this phenomenon is that by introducing the data multiple times, we create multiple paths from the input data to the output plane, resulting in not only higher polynomial orders but also cross-terms that couple with different optical paths and reach the detector plane. The existence of multiple routes for highlighting useful features in the output plane may make the data repetition scheme less susceptible to noise.

Overall, the nPOLO framework presents a novel approach for generating optical nonlinearity using low-power optical devices, eliminating the need for electronic components to achieve higher orders of nonlinearity. Furthermore, the introduction of data repetition to generate polynomial nonlinearities enhances robustness against noise. Note that, this framework is applicable to the cascade of any optical linear system such as integrated waveguide Mach-Zehnder interferometers [5]. These characteristics make nPOLO a promising platform for realizing optical neural networks.

## 8.4 Methods

### 8.4.1 Derivation of the nonlinear response in nPOLO

Without loss of generality, let us assume that we have an optical system that has an input aperture and output aperture that are discretized/sampled by the same number of  $K$  pixels where this optical system comprises of  $N$  modulation layers that are equally spaced from each other. The system response for a single modulation layer is the following:

$$\mathbf{o} = \mathbf{P}_2 \mathbf{T} \mathbf{P}_1 \mathbf{i}$$

Equation 8:1 - The system response for Modulation layer  $N=1$  (re-stated)

Where  $\mathbf{o}$  is the  $K \times 1$  output vector (Electric field),  $\mathbf{i}$  is the  $K \times 1$  input vector (Electric field),  $\mathbf{P}_1$  is the propagation matrix representing the diffraction from the input aperture to the modulation layer,  $\mathbf{P}_2$  is the propagation matrix representing the diffraction from the modulation layer to the output aperture, and  $\mathbf{T}$  is the modulation matrix. Assuming the same number of  $K$  pixels in the modulation layer as in the input/output apertures,  $\mathbf{T}$  becomes a diagonal matrix with size  $K \times K$ . We use a Toeplitz matrix to represent diffraction for an arbitrary distance<sup>16</sup>. For simplicity, we assume that the modulation layer coincides with the input aperture, which makes  $\mathbf{P}_1$  a unity matrix and the input field is a plane wave, which makes  $\mathbf{i}$  a vector of ones. For the subsequent propagation matrices, we will assume them to be the same and denote as  $\mathbf{H}$ . Then, for a single modulation layer for the explained configuration, we have:

$$\begin{bmatrix} o_1 \\ \vdots \\ o_K \end{bmatrix} = \begin{bmatrix} \sum_{k=1}^K h_{1k} t_k \\ \vdots \\ \sum_{k=1}^K h_{Kk} t_k \end{bmatrix}$$

Equation 8:2 – Expression for  $\mathbf{o}$  by intensity detection for arbitrary  $K$  ( $N=1$ ).

Where  $h_{ij}$  are coefficients of the propagation matrix  $\mathbf{H}$ . If we repeat this process  $N$  times for  $N$  modulation layers, we have:

$$\begin{bmatrix} o_1 \\ \vdots \\ o_K \end{bmatrix} = \begin{bmatrix} \prod_{n=1}^N \left( \sum_{k=1}^K h_{1k} t_k \right) \\ \vdots \\ \prod_{n=1}^N \left( \sum_{k=1}^K h_{Kk} t_k \right) \end{bmatrix}$$

Equation 8:3 – Expression for  $\mathbf{o}$  by intensity detection for arbitrary  $K$  and  $N$ .

From this relationship, we can see that repeating the modulation layers with the same coefficients yields cross-terms and polynomial orders of the coefficients belonging to the modulation layer. Hence, when the data is introduced in the modulation layers, we end up with the nonlinear relationship along with the generated cross-terms that yield additional features. In Appendix D, we further analyze the outcomes when the modulation layer provides complex modulation or phase-only modulation along with the difference between field detection and intensity

detection. When we have phase-only modulation, the multiplicative nature of the repetition causes a linear relationship between the modulation layers and the output field. Hence intensity detection is required to establish a nonlinear response that results in polynomial orders of the sinusoidal terms further enriching the nonlinear mixing of the introduced data in multiple modulation layers (recall Chapter 7).

## 8.4.2 Digital training

Optimization methods are already demonstrated to reconstruct 3D phase objects from experimental recordings of 2D projections[42], [45]. In the ref. [42], the forward model in the optimization is the beam propagation method (BPM). The iterative error reduction scheme and the multilayer structure of the BPM resembles a multilayer neural network. Therefore, this method is referred to as Learning Tomography. We showed that instead of imaging an object, we can reconstruct the 3D structure that performs the desired task as defined by its input-output functionality [66]. To establish the target functionality, the 3D phase modulation, either through a continuous medium or multiple planes, and the scattered field caused by the phase modulation must be accurately modeled. Unlike conventional reconstruction algorithms that rely on first-order approximations, LT incorporates higher-order scattering effects by employing BPM. The LT algorithm involves an iterative reconstruction process using the forward model, along with the constraints arising from experimental considerations such as the pixel pitch of the SLM. In this study, we adapted this approach presented in the ref<sup>30</sup>, where additional details can be found, to generate scaling and bias parameters for demonstrated classification tasks. The output intensity pattern of the forward model is average pooled to yield a 4-by-4 matrix for each sample of Fashion MNIST dataset and an 8-by-8 matrix for each sample of the Imagenette dataset. These matrices are flattened to act as an input layer of a digital classifier that has 10 output neurons for each class of the datasets without any hidden layer and nonlinear activation function. The trainable parameters employed in the BPM model and digital classifier are co-trained by a continuous error backpropagation where different learning rates are assigned to digital weights (i.e.,  $10^{-4}$ ) and optical scaling and bias parameters (i.e.,  $10^{-3}$ ) using categorical cross entropy as the loss function. We used batch learning with a batch size of 20 and a random shuffle in every batch. PyTorch libraries are used for the whole training process.

Note that, as explained in the experimental setup section, we use 300 by 300 pixels on SLM for each modulation layer whereas the Fashion MNIST and the Digit MNIST dataset samples contain 28 by 28 pixels and Imagenette dataset samples contain 320 by 320 pixels. For the Fashion MNIST and the Digit MNIST datasets, we used 4 by 4 superpixels on SLM, yielding 75 by 75 pixels for accepting and assigning trainable parameters, which means that we assign 11250 parameters (scaling and bias) per modulation layer. We accordingly linearly up-sampled the samples of those datasets to 75 by 75. For the Imagenette dataset, we linearly down-sampled the samples to 300 by 300 and did not use any superpixels on SLM meaning that we used 300 by 300 pixels for accepting and assigning trainable parameters, which means that we assign 180000 parameters (scaling and bias) per modulation layer.

## 8.4.3 Experimental setup

The experimental setup is the same as the one introduced in Chapter 6. The output beam in the camera occupies an area of 834 by 834 pixels. During image acquisition, we applied average pooling to resize the obtained images to either 4 by 4 or 8 by 8 dimensions. For the Imagenette dataset, we used the whole training and test samples as originally prepared. For the Digit and Fashion MNIST datasets, we used the whole training set (60000 samples) for the simulations however we used the first 10000 samples for the re-training of digital weights after the experiments and we used the first 2500 samples of the test set for blind testing of the experimental results.



# Chapter 9 Conclusions

The foundational premise that “electrons compute and photons communicate” set the backdrop for much of the twentieth and early twenty-first century’s technological progress. However, as illuminated in this dissertation, the crossroads between the insatiable demand for computational power, primarily for machine learning tasks, and the impending barriers of Moore’s law have reignited interest in optical computing and storage. The envisioned all-optical pipeline, with the interplay of acquisition, computation, storage, and communication, promises transformative enhancements, particularly in circumventing latencies and high power use introduced by electro-optical conversions. In this final chapter, we first summarize the conclusions of the body chapters and then discuss future directions.

In Chapter 2, we descend into the specifics of 3D photonic device design in literature, emphasizing the integral connection between fabrication techniques and design. The interplay between tomography and neural networks offers an exciting dimension to the field. Using tomographic algorithms in the design process can potentially enable more precise and intricate optical devices, integrating the insights from both disciplines. The notion of a transmission matrix, mapping input to output patterns, emphasizes the deep synergy between tomography and 3D photonic circuit design. As the field of photonic device design rapidly evolves, it is poised at a juncture where traditional methods, neural networks, and tomographic techniques are converging. These integrated approaches are set to catalyze breakthroughs in optical interconnections, multiplexers, and other optical devices, driving the next wave of advancements in optical computing and communication. The challenges remain, but the potential is vast, and the horizon looks promising for the realization of more efficient, intricate, and versatile photonic devices.

The thesis through Chapters 3 to 5 delved into the promising world of 3D printing and its applications in photonics. The adaptability of Learning Tomography to optimize multilayer optics, as discussed in Chapter 3, stands as a testament to the power of such interdisciplinary approaches. Learning Tomography, in its original form, reconstructs 3D refractive index (RI) distributions of transparent objects using multiple 2D projections. The chapter adapts this method for optical volume element design, feeding it with desired output patterns and using plane waves at different incidence angles as inputs. Then we introduced (3+1)D printing approach offering high degree of control over refractive index distributions, as discussed in Chapter 4, enabling the fabrication of graded-index volume holograms and photonic waveguides. Chapter 5 adds depth to this discourse by introducing the potential of linear diffraction efficiency in volume holograms, despite recognizing inherent challenges such as the unintended consequence of a frequency response in diffraction efficiency due to varying voxel size. Addressing this requires an overall engineering of printing optics with photoresist chemistry that can vary the RI without altering the voxel size.

Chapters 6 shifted the focus towards adaptability and reconfigurability in interconnects. Chapter 6’s analysis of the multi-plane spatial light modulation approach offers an alternative route for optical network designs, providing, flexible reconfigurability in optical paths for interconnecting spatiotemporal nodes, coupled with inherent multicasting capabilities. The efficiencies obtained in our numerical studies are encouraging, especially when compared to integrated solutions that are susceptible to losses like waveguide and coupling losses. Notably, the multicasting efficiency remains consistent, suggesting a solution to the age-old challenges inherent in standard optical systems.

Finally, in Chapter 7, we have analyzed sources of nonlinearities that naturally arise in systems based on linear optics by either from interfacing input/output planes and/or data repetition in the scattering potential that leads to a nonlinear transform when output scattered light is considered. In Chapter 8, we used these principles to introduce the nPOLO framework, showcasing a method for realizing neural networks with nonlinear transformation in the optical domain without light-matter interaction. From this aspect, the nPOLO framework opens a new frontier.

In conclusion, this dissertation presents multiple directions of optics research concerning strage, interconnection, and computation. While we have obtained considerable outcomes with proof-of-concept demonstrations, the journey is, of course, far from over. The all-optical pipeline discussed in Chapter 1 remains a vision for the distant future in terms of generalizable large-scale computations. However, there are promising prospects for implementing such a pipeline at the edge, serving as an accelerator. This could become feasible in the near future, especially for energy and latency-sensitive applications, such as autonomous navigation platforms. To illustrate this point, we include a conceptual schematic in Figure 9:1. Here, the nPOLO framework, in conjunction with the acquisition, functions as an accelerator. This setup minimizes the load on electronic back-end processing, leading to increased energy efficiency and reduced latency in the recognition-to-decision-making process.

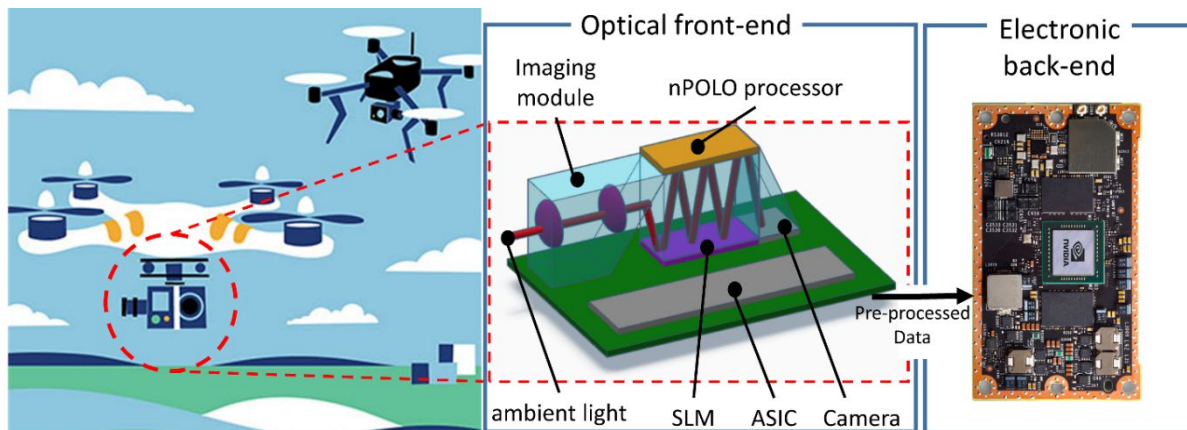


**Figure 9:1 Conceptual schematic of nPOLO at the edge, serving as an accelerator.**

Considering the challenges faced while realizing the presented work in this thesis, we identify three key future directions that will further enable the progress of optical pipeline:

### 1. Algorithms

Training digital neural networks and physical computing hardware (in our case, training an optical neural network or using the training methodologies for inverse design) requires different considerations, given the unique attributes of each domain. While digital training algorithms provide a solid foundation, they must be adapted to accommodate the unique constraints of physical computing systems, which is currently not exactly the case. The demonstrations in this thesis rely on variants of mean squared error and variants of stochastic gradient descent (if a forward model is available), which is also the case mostly in the literature. One of the fundamental distinctions is the energy conservation constraint in physical systems without a gain mechanism. For instance, a digital weight exceeding one, which would indicate gain, does not have a straightforward analog in the optical domain. Such disparities can hamper convergence during optimization, possibly preventing the attainment of a global minimum or a more desirable local minimum. As highlighted by research on digital neural networks, the choice of optimization algorithm can profoundly influence performance, sometimes even more so than the number of parameters or the system's capacity. We acknowledge that there are recent works to address these issues such as equilibrium propagation algorithm in the context of energy-based models [178]. Moreover, precision levels and noise mechanisms

are drastically different between digital and physical systems and must be taken into account as well as the regularization to ensure that the trained models are robust to the inherent variabilities in physical systems if one thinks of a commercial product that would have many copies with slight differences due to fabrication.

## **2. Fabrication**

In this thesis, the primary fabrication method used for the presented structures is 2-photon polymerization. This method is groundbreaking due to its ability to fabricate 3D structures with sub-micron resolution. However, its point-scanning nature results in prolonged fabrication times. The time-intensive nature of this method favors multilayer binary index structures. This is because they require significantly less printed volume than polymerized graded-index volumes, given an equivalent effective modulation power. The advantage of multilayer structures is the high index difference between the polymerized structure and a background medium, such as air. In contrast, graded-index structures face challenges due to a small refractive index dynamic range when the overall volume is constrained to micro-scale due to fabrication time. However, it is worth noting that multilayer structures tend to be more vulnerable to errors arising from fabrication imperfections. On the other hand, localized flaws generally less impact the reconstructed beam from a graded-index volumetric structure, since the encoding is distributed throughout the volume. In conclusion, there is a clear need for faster, more reproducible methods with high resolution, capable of effortlessly fabricating intricate 3D structures. Volumetric additive manufacturing may offer a solution to these time constraints, but the achievable resolution, while impressive at sub-100  $\mu\text{m}$  for centimeter-scale structures crafted in mere minutes [179], still falls short for applications like optical data storage. However, it provides a promising future direction.

## **3. Modulators**

This thesis emphasizes 3D structures, and as such, we spotlight spatial modulators that leverage spatial degrees of freedom. These modulators are pivotal, as devices will inevitably be opto-electronic, reflecting the complementary foundations of optics and electronics. For efficient data injection with minimal energy, modulators that facilitate opto-electronic conversion are sought after. The most direct strategy is to enhance the modulation rate without incurring a significant rise in energy expenditure. Importantly, increasing the modulation rate will not drastically affect the energy efficiency of the rest of the optical system. By doing so, the overall energy cost per operation can be significantly reduced. Current modalities, such as Liquid Crystal on Silicon, lag in offering rapid modulation rates. Even Digital Micromirror devices, which boast kHz modulation rates, might fall short for cutting-edge optical systems unless their spatial degrees are meticulously engineered. That said, there are promising developments in the field. For example, Panuski et al. showcased a 64-pixel device with a modulation rate exceeding 100 GHz [180]. As pixel counts increase, such innovations could profoundly influence the viability of 3D optical technologies.



# Appendix A

This is the edited post-print version of the *Supplementary Information* of the following article published in *Nanophotonics*.

## Computer generated optical volume elements by additive manufacturing

Niyazi Ulas Dinc<sup>1,2</sup>, Joowon Lim<sup>1</sup>, Eirini Kakkava<sup>1</sup>, Christophe Moser<sup>2</sup> and Demetri Psaltis<sup>1</sup>

<sup>1</sup>Optics Laboratory, École polytechnique fédérale de Lausanne, Switzerland

<sup>2</sup>Laboratory of Applied Photonics Devices, École polytechnique fédérale de Lausanne, Switzerland

Nanophotonics, Volume 9, Issue 13 (2020)

<https://doi.org/10.1515/nanoph-2020-0196>

## Computer Generated Optical Volume Elements by Additive Manufacturing: Supplementary Material

For a more detailed view of Learning Tomography algorithm, the reader could check the references [42], [43], [181]. We implemented the algorithms by using custom scripts in MATLAB R2018a (MathWorks Inc., Natick, MA, USA) on a desktop computer.

### Discussion on design parameters in varying layer separation scenario

In the Section “2.2 Representation Error” of the main text, two scenarios are investigated. The first scenario is imposing a constraint on  $t_l$  to keep it fixed and keeping  $\Delta n = n_{polymer} - n_{background}$  fixed as 0.2. This scenario provided the Figure 4A of the main text. Note that the first observation is that higher layer separation provides higher performance in terms of structural similarity index in all cases. Please note that phase-to-thickness converted elements and LT optimized elements have the fixed thickness variation. Therefore, the only changing parameter is the layer separation. For the phase mask stacks, the masks are taken as thin planes whose transmittance function is the following:

$$t(x, y) = \exp(j\Delta\varphi(x, y)) \quad (A.1)$$

Where  $j = \sqrt{-1}$  and  $\Delta\varphi$  is the phase modulation of given pixel. Since the layers are modeled as phase objects as mentioned, increased reconstruction accuracy with increased layer separation is an expected result. Modulated light has more room to diffract and interact with more voxels. This result is in agreement with the discussion provided in [72]. It is important to note that equation (A.1) does not perfectly govern the layered volume elements

when the phase modulation is implemented by varying thickness. It can provide a good approximation if the thickness variation is negligible compared to layer separation and if the thickness variation is not too large than the wavelength as well.

Another important aspect is the pixel pitch or transverse voxel dimensions in the case of volume elements. Each layer can be thought as superposition of many gratings. Since the strength of a grating is inversely proportional to its period, higher transverse voxel dimensions have less capability to modulate light. Moreover, for a fixed overall size, increasing the voxel dimensions reduces the number of different voxels and hence the degrees of freedom. Different voxel dimensions (obtained by averaging) are implemented and its effect on reconstruction is investigated by keeping other parameters the same. Figure 4A provides the results for transverse voxel dimensions of  $(0.5 \mu\text{m})^2$ . In the Figure A.1, we provide the same plots for different voxel dimensions under the same constraints with the structures investigated in Figure 4A. Figure A.1 confirms the expectations. Note that in Figure A.1D, we see that the effect of reducing the degrees of freedom starts to dominate the error in reconstruction rather than the representation error since we observe that the expected trend between Phase mask stack, Optimization with LT and Thickness conversion does not hold for all data points.

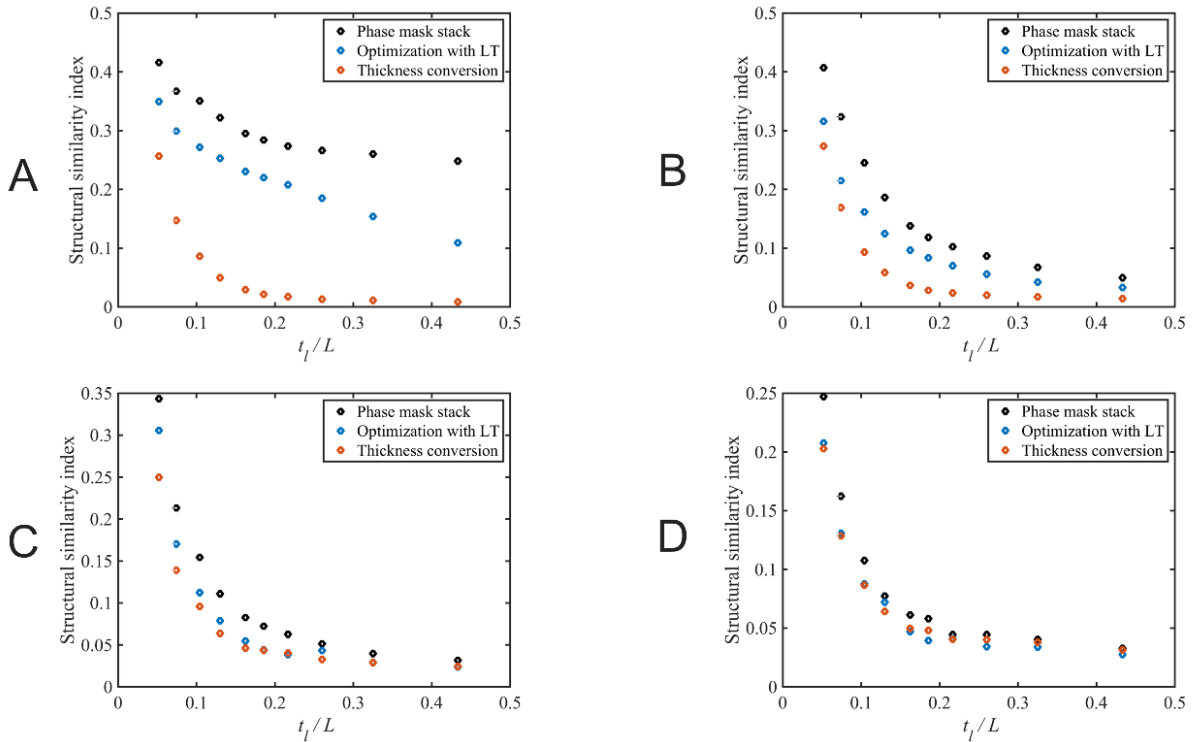
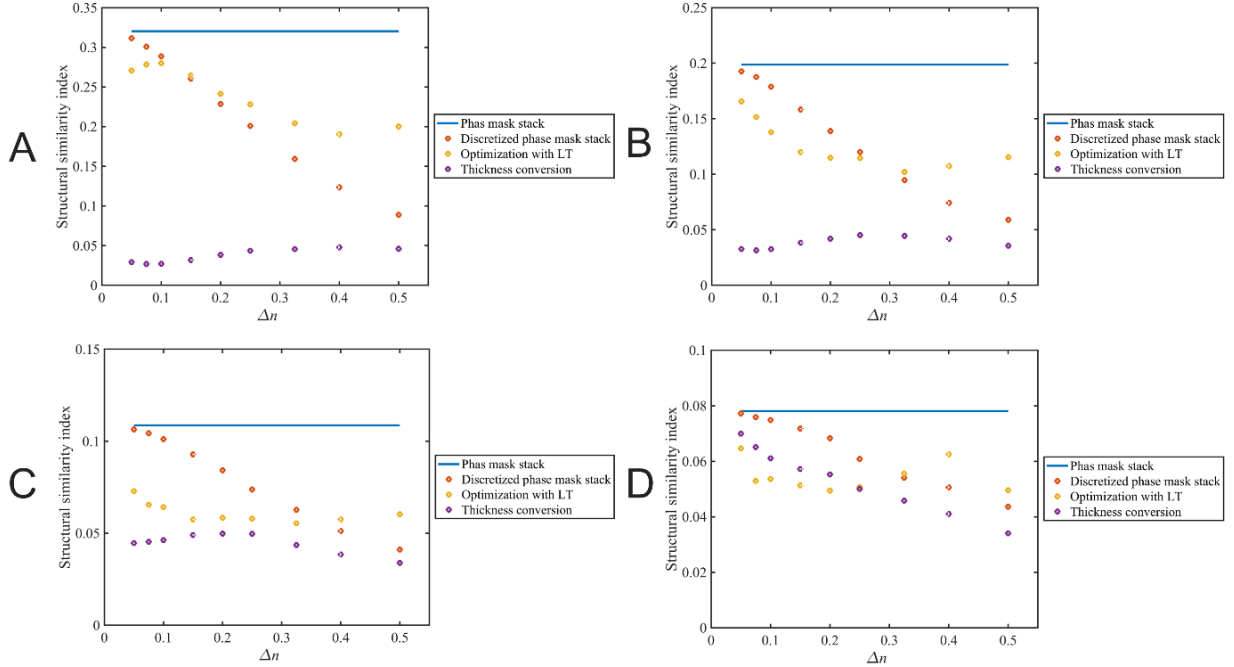


**Figure A.1:** Structural similarity index plots for different transverse voxel dimensions. (A)  $0.5 \mu\text{m} \times 0.5 \mu\text{m}$ , (B)  $1 \mu\text{m} \times 1 \mu\text{m}$ , (C)  $2 \mu\text{m} \times 2 \mu\text{m}$  (D)  $4 \mu\text{m} \times 4 \mu\text{m}$ . Note that (A) is the same plot with the Figure 4A in the main text.

### Discussion on design parameters in varying index scenario

In this part, we kept  $L$  fixed and varied  $\Delta n$  to obtain different  $t_l$  values via Equation (2) of the main text. Obtained plots are given in Figure A.2 for different transverse voxel dimensions. Note that the optimized phase mask stack has continuous RI values and sets the upper limit. Plots in Figure A.2 show that LT performs better to suppress representation error except Figure A.2D. Again, in Figure A.2D, we see that the effect of reducing the degrees of freedom starts to dominate the error in reconstruction rather than the representation error. Note that Figure 4B of the main text is obtained from Figure A.2A. To get Figure 4B, results of LT optimized structure and thickness conversion structure are divided by corresponding results of discretized phase mask stack to eliminate the effect of discretization error and yield only the effect of representation error. Needless to say, x axis of Figure 4B of the main text is  $1/\Delta n$  to make it coherent with Figure 4A where in Figure A.2, the x axis is  $\Delta n$ . Another interesting note

is that, LT outperforms discretized phase mask stack when the discretization is very coarse due to high index contrast, which results in less discrete thickness steps for a fixed resolution. This happens because LT optimizes according to given structural constraints including the thickness discretization. In the previous scenario where layer separation is varied, the difference between the phase mask stack and its discretized version is insignificant since



we have 50 steps (corresponding to 50 thickness steps for the chosen resolution) to discretize the phase masks (Recall that  $t_l$  is fixed for all  $L$ ). Hence, they are not differentiated in Figure A.1.

**Figure A.2:** Structural similarity index plots for different transverse voxel dimensions. (A)  $0.5\mu\text{m} \times 0.5\mu\text{m}$ , (B)  $1\mu\text{m} \times 1\mu\text{m}$ , (C)  $2\mu\text{m} \times 2\mu\text{m}$  (D)  $4\mu\text{m} \times 4\mu\text{m}$ .

### Full Volume Optimization: Angular Multiplexing of More Modes

Amplitudes of reconstructed fields from the GRIN OVE that is designed to multiplex eight  $LP$  modes are provided in Figure 8 of the main text. In Figure A.3, phase profiles of the reconstructed fields are given. In addition, amplitudes and phase profiles of the desired fields are provided for comparison as well.

### Full Volume Optimization: Classification of MNIST Digits

As stated in the main text, LT can learn how to correlate variants of classes. To demonstrate this, we conducted a classification task by using MNIST dataset. The GRIN volume element is trained by randomly selected 10000 images from the MNIST database. The obtained OVE is tested by randomly selected 2000 images that the OVE has not seen during the training. The optimization was initiated with a uniform RI equal to 1.5. After training with the optical OVE using the LT algorithm as previously described we obtained 81.3% accuracy on the test set. The results are summarized in Figure A.4. Figure A.4A depicts how the classification works with GRIN OVE. A Fourier transform lens is virtually placed to map the output angles into spatial domain. Corresponding areas for each angle/digit are also provided. Figure A.4B provides the obtained OVE and Figure A.4C provides the confusion matrix.

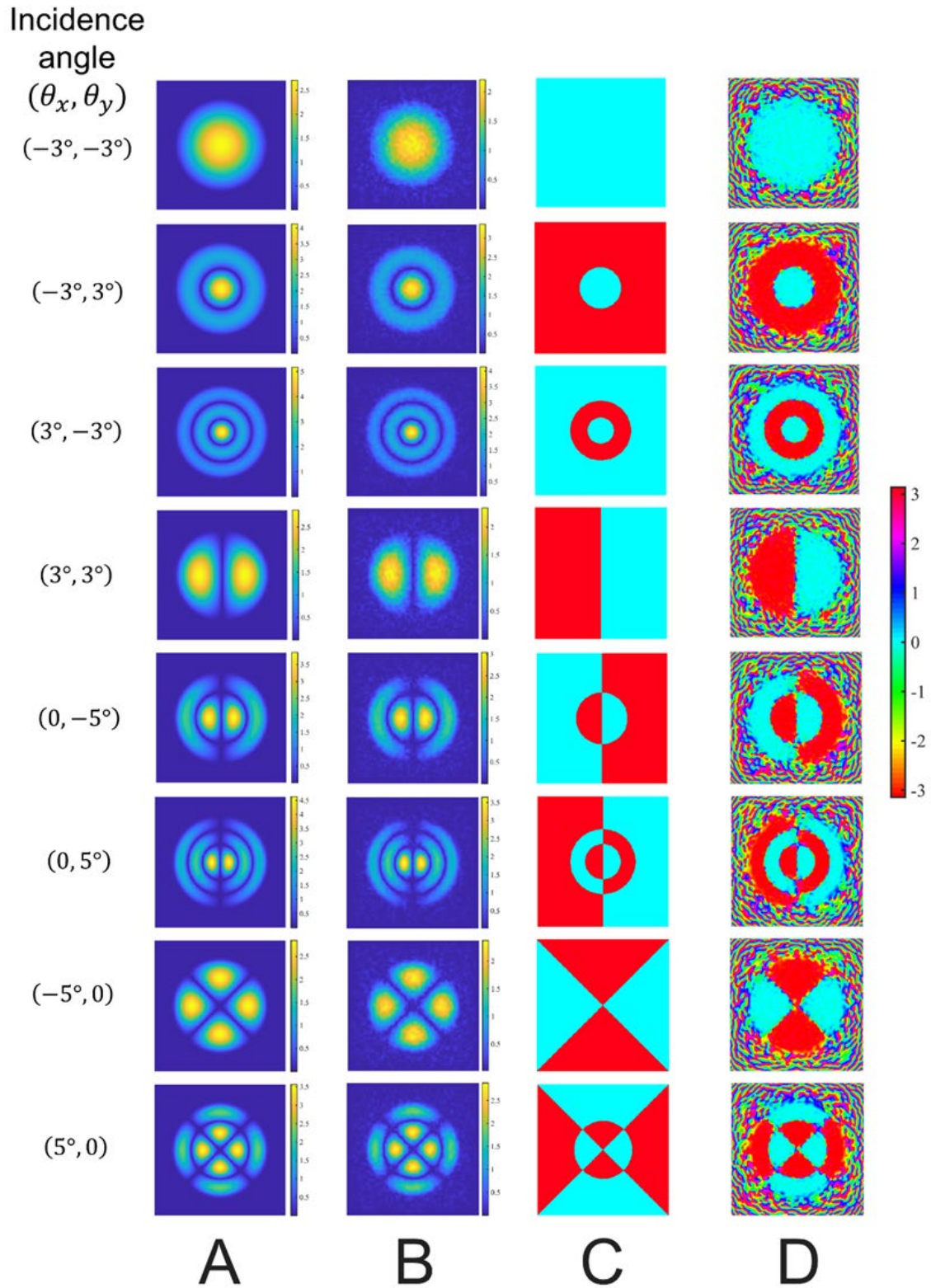


**Figure A.3:** Simulation results of GRIN volume element for multiplexing eight  $LP$  modes. (A) The amplitude of the desired output fields. (B) The amplitude of the output fields reconstructed by the volume element. (C) The desired phase distributions of the output fields. (D) The phase distribution of the reconstructed field by the volume element. All the phase plots share the same Colorbar in radians on the right. All windows are  $64\mu\text{m}$  by  $64\mu\text{m}$ .



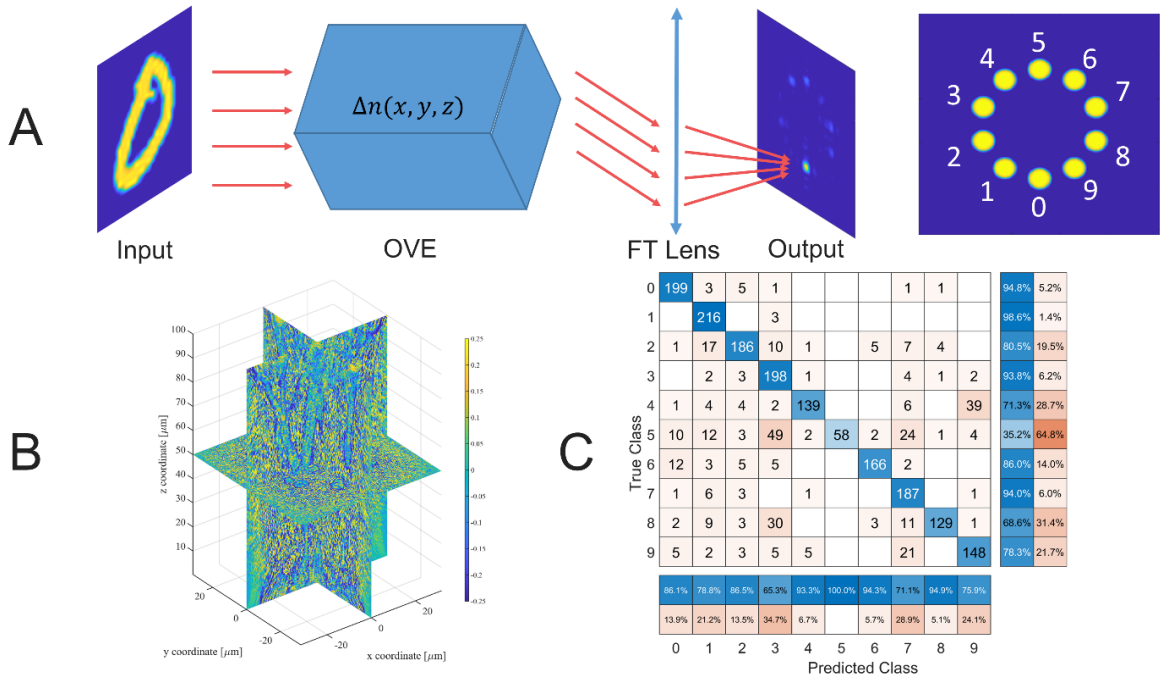


**Figure A.4:** Simulation results of GRIN volume element for classification task. (A) GRIN OVE classifies the digits by resulting output beams in different angles. FT Lens is the Fourier transform lens that maps the angles to corresponding points on the detector plane. (B) XY, YZ and XZ cut planes of the optimized volume by LT. Colorbar shows RI variation. (C) The confusion matrix after the test with 2000 examples.

## Experimental Setup

The experiments performed by using an optical setup in which a spatial light modulator (SLM, Pluto-NIR2, Holoeye) is used to change the angle of incidence beam to the volume element. As the light source, Amplitude Laser - Satsuma generating pulses at 1030nm is used. First, the output of the SLM is imaged on the input plane of the 3-layer OVE to scan different angles. After the volume element, another 4f imaging system is used to relay the output field to detector plane. The sketch of experimental setup is given in Figure A.5.

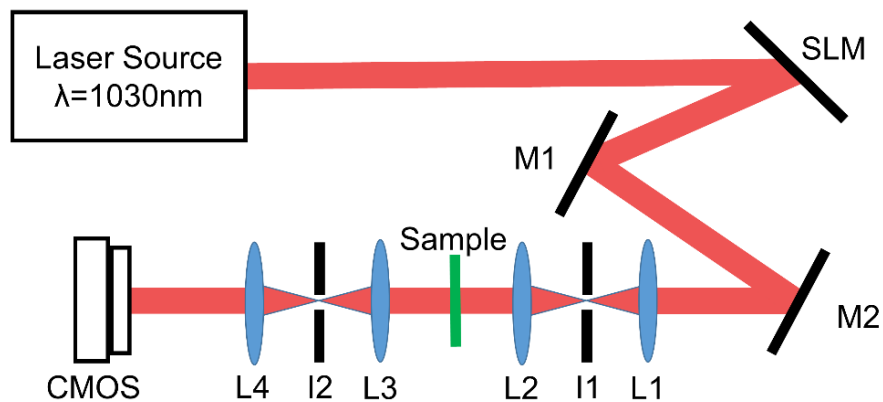


**Figure A.5:** Sketch of the experimental setup for characterization of the manufactured volume element. M1 and M2 stand for Mirror 1 and Mirror 2. L1 and L2 stand for the lenses of the 4f imaging system for the input to the volume element and I1 stands for Iris 1 to block zero order reflection from the SLM. L3 and L4 stand for the lenses of the 4f imaging system for the output of the volume element and I2 stands for Iris 2 to block high frequency noise.



# Appendix B

This is the edited post-print version of the *Supplementary Information* of the following article published in *Optica*.

## **Direct (3+1)D laser writing of graded-index optical elements**

Xavier Porte<sup>1,†</sup>, Niyazi Ulas Dinc<sup>2,3,†</sup>, Johnny Moughames<sup>1</sup>, Giulia Panusa<sup>2</sup>, Caroline Juliano<sup>2</sup>, Muamer Kadic<sup>1</sup>, Christophe Moser<sup>3</sup>, Daniel Brunner<sup>1</sup>, and Demetri Psaltis<sup>2</sup>

†Equally contributing authors

<sup>1</sup>Institut FEMTO-ST, Université Bourgogne Franche-Comté, CNRS UMR 6174, Besançon, France

<sup>2</sup>Optics Laboratory, École Polytechnique Fédérale de Lausanne, Lausanne, Switzerland

<sup>3</sup>Laboratory of Applied Photonics Devices, École Polytechnique Fédérale de Lausanne, Lausanne, Switzerland

*Optica*, Volume 8, No 10 (2021)

Supplement DOI: <https://doi.org/10.6084/m9.figshare.16566735>

Parent Article DOI: <https://doi.org/10.1364/OPTICA.433475>

## **Direct (3+1)D laser writing of graded-index optical elements: supplementary material**

### **Supplementary Discussion 1: The structure-refractive index fidelity**

To have a high dynamic range of refractive index, exposure parameters should scan the extreme values to have high difference in degree of polymerization. In theory, degree of polymerization can be varied from 0% to 100%. However, practically, this is not the case. Very low degree of polymerization yield unstable structures that do not hold the intended shape, and very high degree of polymerization cannot be obtained due to burning and micro-explosions happening while laser writing. Hence, there exists a trade-off relation between high dynamic range of refractive index and the material's fidelity. Compromise between the two should be made case by case. Moreover, it is observed that the refractive index saturates as we increase the exposure dose even before reaching the burning regime. We used a Digital Holographic Interferometry (DHI) setup given in Figure B.1 to retrieve the accumulated phase through the structures for the calibration.

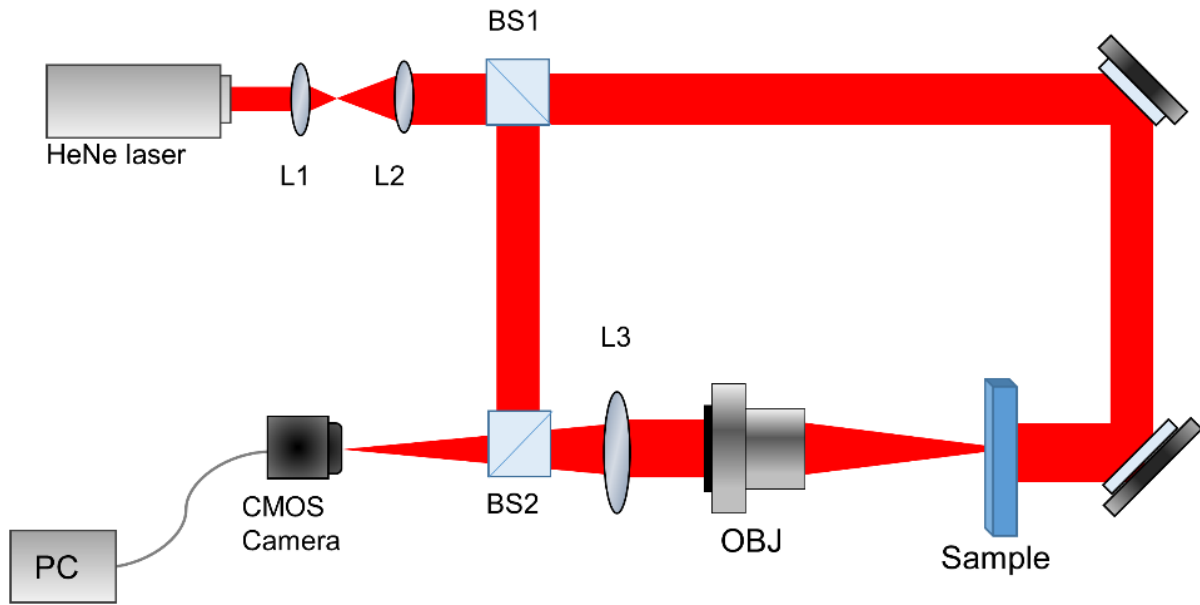


**Figure B.1:** Off-axis Digital Holographic Interferometry (DHI) setup to measure the complex field and extract the accumulated phase through the structures.

To check the effect of degree of polymerization on the structural fidelity, we printed a rectangular prism with a constant slope on one side to ease phase unwrapping on the recorded complex field, as depicted in Supplementary Figure B.2(a). In addition, there is a cross on top to ease focusing. This structure is printed homogeneously in terms of exposure. The printing parameters are 34% laser power and 17 mm/s scanning speed where the hatching and slicing distances are  $0.1\ \mu\text{m}$  and  $0.3\ \mu\text{m}$  respectively. After the printing, the remaining resin is not removed to bypass the development phase and the polymerized structures within the surrounding monomer resin sandwiched between two cover slips as shown in Supplementary Figure B.2(b). The hologram of the sample (see Supplementary Figure B.2(c)) is recorded by using the DHI setup where the wavelength is 633nm obtained from a He-Ne laser, which does not correspond to polymerization wavelength of IP-Dip besides the low power. Then Fast Fourier Transform (FFT) algorithm is applied. A circular unit low pass filter filters the first order in the spectrum corresponding to the object beam. The size of the filter is equal to the Numerical Aperture (NA) of the DHI setup. Upon centering the object beam, inverse FFT is applied to retrieve the wrapped phase (see Supplementary Figure B.2(d-f)). To obtain the phase accumulation through the sample, PUMA phase unwrapping algorithm is used [182] to get the 2D phase map shown in Supplementary Figure B.2(g). Having 2D map of extracted phase provides the information of how well the extracted phase resembles the intended geometry. We label the example given in Supplementary Figure B.2 as unsatisfactory as it does not resemble well the intended structure as seen from the cutline given in Supplementary Figure B.2(h).

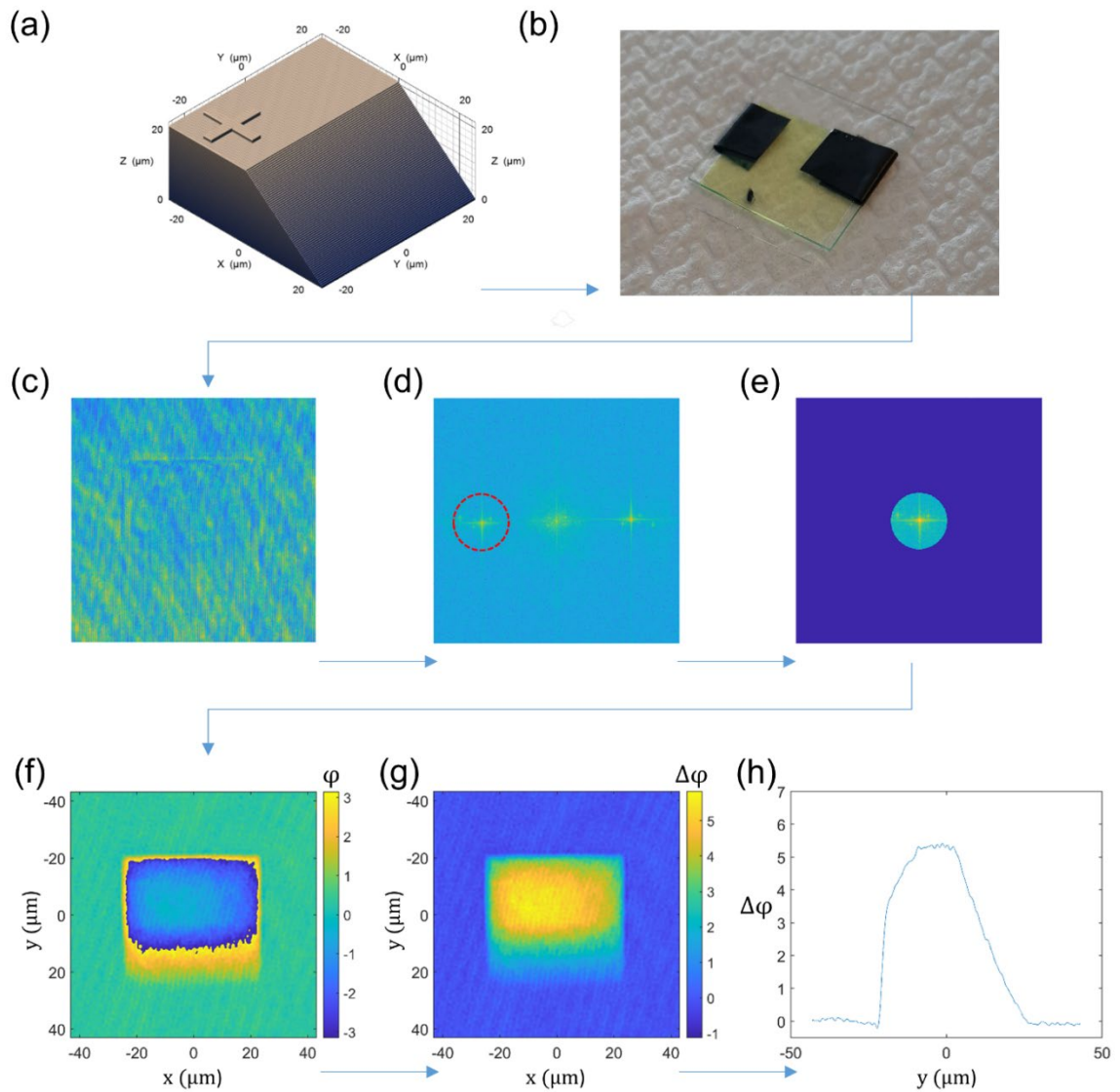


**Figure B.2 :** Pre-calibration experiment workflow. (a) 3D rendering of the printed structure. (b) The picture of the sample as it is sandwiched between two cover slips. The yellowish liquid is the monomer resin. (c) The hologram recorded via DHI setup. (d) FFT of the recorded hologram where the encircled part corresponds to the object beam passing through the structure. (e) The object beam is centered and the parts of the spectrum that lies outside of the NA of the DHI setup are filtered out. (f) Inverse FFT result to retrieve wrapped phase of the object beam. (g) Resulting 2D unwrapped phase map. (h) The central cutline, averaged over a stripe of  $15\ \mu\text{m}$ .

We kept hatching and slicing distances as  $0.1\ \mu\text{m}$  and  $0.3\ \mu\text{m}$  respectively and the exposure parameters are swept to construct an array of these structures. Besides the unsatisfactory example given in Supplementary Figure B.2, we provide a satisfactory example in Supplementary Figure B.3. Supplementary Figure B.3(a-b). shows the extracted phase for 38% laser power and  $8\ \text{mm/s}$  scanning speed and  $y$ -axis cutline averaged over a  $15\ \mu\text{m}$  stripe, which demonstrates that the extracted phase hence the structure well resembles the intended geometry. For convenient comparison, we provide the graphs in Supplementary Figure B.2(g-h) side by side in Supplementary Figure B.3(c-d). Upon the pre-calibration study, we arrived at the printing parameters given in the main text as a good balance between high dynamic range and structure-refractive index fidelity.

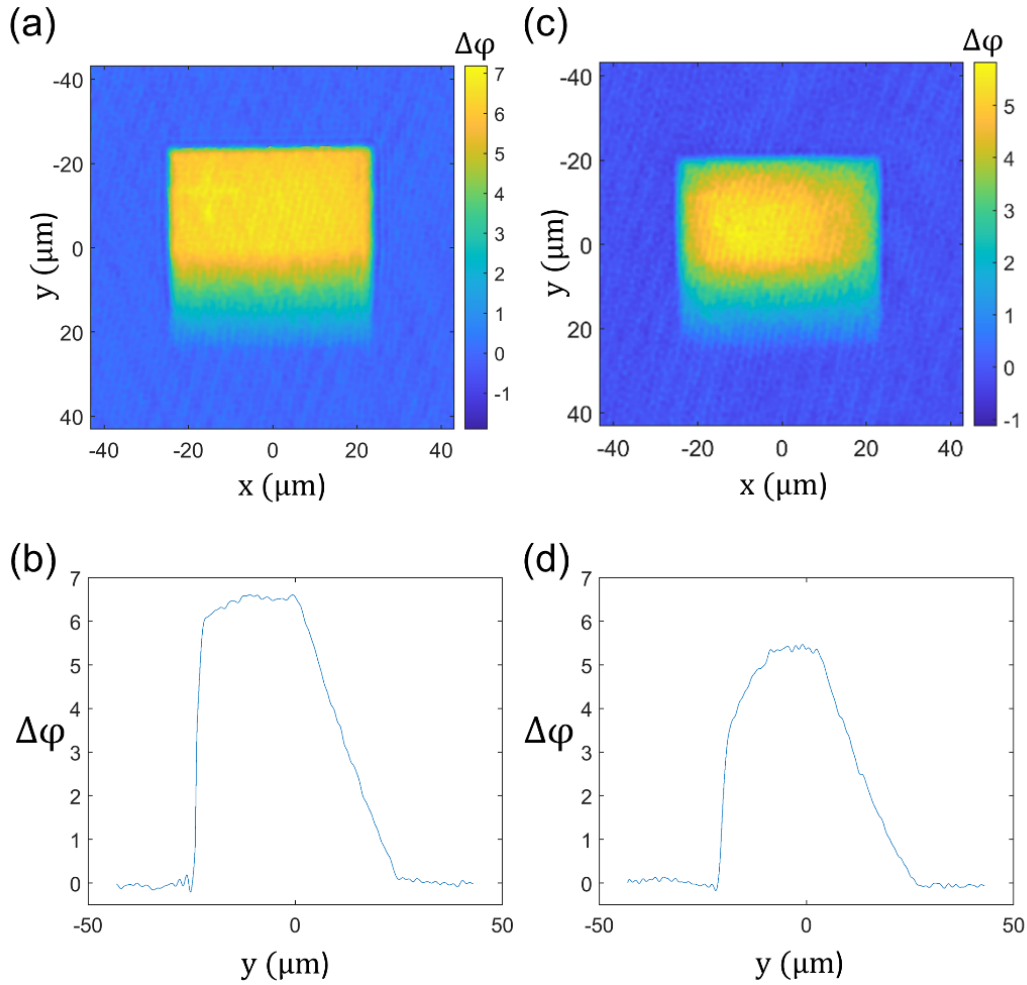


**Figure B.3 :** Pre-calibration experiment results. (a) 2D phase extraction of the structure with 38% laser power and 8 mm/s scanning speed. (b) The y-axis cutline of the phase plot given in a, (c) 2D phase extraction of the structure with 34% laser power and 17 mm/s scanning speed, (d) the y-axis cutline of the phase plot given in c.

### Supplementary Discussion 2: GRIN measurements and calibration

As stated in the main text, five rectangular samples are printed by linearly increasing the laser power in one axis and the refractive index distribution is measured by DHI. In Supplementary Figure B.4(a), the obtained 2D phase maps of all the samples are provided. When we take a single cutline in the middle from sample 1, the plot given in Supplementary Figure B.4(b) is obtained. When we average over many cutlines that create a 20- $\mu\text{m}$  wide stripe, we obtain the plot given in Supplementary Figure B.4(c). When we average five central single cutlines from all the samples, we obtain the plot given in Supplementary Figure B.4(c). When we average over 20- $\mu\text{m}$  wide stripes of all the samples, we obtain the Supplementary Figure B.4(d). Comparing the plots, we can deduce that high error bars occur due to inter-sample differences both in fabrication and in measurement. Note that Supplementary Figure B.4(c) and 4(e) are also provided in the main text in Figure 2.

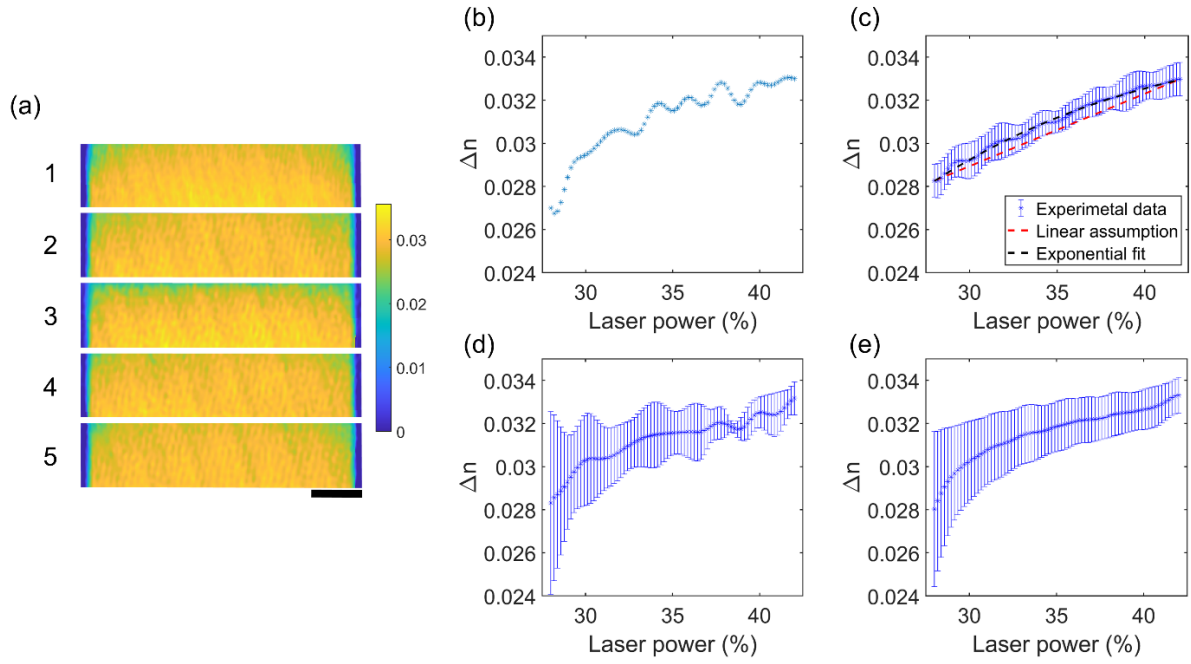


**Figure B.4 :** (a) Extracted phase maps of the calibration samples. Colorbar represents the refractive index difference with respect to the monomer resin background. Scale bar is 10  $\mu\text{m}$ . (b) Central single-pixel cutline from sample 1. (c) Mean and standard deviation obtained from the cutlines within a 20- $\mu\text{m}$  wide central stripe from sample 1. (d) Mean and standard deviation obtained from the central single-pixel cutlines from all the samples. (e) Mean and standard deviation obtained from the cutlines within 20- $\mu\text{m}$  wide central stripes from all the samples.

Due to the saturation trend of the refractive index as the exposure increases, we choose the following form for curve fitting:

$$\frac{c_1}{1 + c_2 e^{c_3 x}} \quad (B.1)$$

We used “lsqcurvefit” solver (nonlinear curve fitting in least-squares sense) of MATLAB R2019b (MathWorks Inc., Natick, MA, USA) on a desktop computer to find  $c_1$ ,  $c_2$  and  $c_3$ . The obtained curve is given in the main text in Figure 2(a) and Supplementary Figure B.4(c). For the laser power adjustment for (3+1)D printing the target refractive index, we simply use the following equation, which is the inverse of Equation B.1:

$$\text{Laser Power}(\%) = \frac{\ln\left[\left(\frac{c_1}{n_{\text{target}}} - 1\right)/c_2\right]}{c_3} \quad (B.2)$$

Note that the curve fit is performed on the refractive index vs laser power percentage of the maximum average power value of the printer. Hence, Equation B.2, directly gives the necessary percentage value that goes in the printer software.

### Supplementary Discussion 3: Characterization of volume gratings and holograms

Volume gratings can be characterized by the Bragg selectivity and the efficiency of diffracted order in the Bragg condition. We use the coupled wave theory pioneered by Kogelnik [55], [131] The Bragg angle is given by:

$$\sin \theta_B = \pm \frac{\lambda}{2\Lambda} \quad (B.3)$$

The relation for the diffraction efficiency is:

$$\eta = \frac{\left( \sin \left( \Phi \sqrt{1 + \chi^2 / \Phi^2} \right) \right)}{1 + \chi^2 / \Phi^2} \quad (B.4)$$

Where,

$$\Phi = \frac{\pi n_1 L}{\lambda \cos \theta} \quad (B.5)$$

$$\chi = \frac{\pi L}{\Lambda \cos \theta} \left[ \Delta \theta \cos(\theta - \psi) - \frac{\Delta \lambda}{2\Lambda} \right] \quad (B.6)$$

Here  $\lambda$  is the wavelength in the medium,  $\Lambda$  is the period of the grating,  $\theta_B$  is the Bragg angle,  $L$  is the thickness of the volume grating,  $\eta$  is the efficiency,  $n_1$  is the peak to mean index modulation ( $n_1 = \Delta n / 2$ , where  $\Delta n$  is the dynamic range),  $\theta$  is the input angle, and  $\psi$  is the slant angle of the grating.  $\Delta \lambda$  stands for the wavelength mismatch.  $\Delta \theta$  is the angular mismatch term. In our analysis the gratings are unslanted, which means  $\psi = 0$ . We also assume  $\Delta \lambda = 0$ . So, at the Bragg condition,  $\chi$  becomes zero, which gives the diffraction efficiency at the Bragg angle as:

$$\eta_B = (\sin \Phi)^2 \quad (B.7)$$

Again, “lsqcurvefit” solver of MATLAB is used to fit a  $\sin^2$  function on the data displayed in the main text Figure 3(b) and  $\Delta n$  is extracted from the argument having other parameters known. For the Bragg selectivity, Eq. B.4 is used to perform a fit on the obtained experimental diffraction efficiencies around the Bragg angle.

The experiments performed by using an intensity only setup where a spatial light modulator (SLM, Pluto-NIR2, Holoeye) is used to change the angle of incidence beam to the volume gratings and holograms. As the light source, Amplitude Laser - Satsuma generating pulses at 1030nm is used. First, the output of the SLM is imaged on the input plane of the volume gratings and holograms by a 4F system to scan different angles. Zero order and higher orders from the SLM are spatially filtered out before the collimated beam from the first order forms onto the sample. After the volume elements, another 4F system is used to relay the output field to the CMOS camera. Similarly as in [66], high frequency light is filtered out in the Fourier plane to get rid of the non-diffracted light from the volume elements. Since the non-diffracted light has a tilt angle, it is mapped to an off-axis point in the Fourier plane, where an iris is used to block it. Note that the diffracted patterns from the holograms are designed to propagate on-axis so that they are not filtered out. The sketch of the experimental setup is depicted in Supplementary Figure B.5.

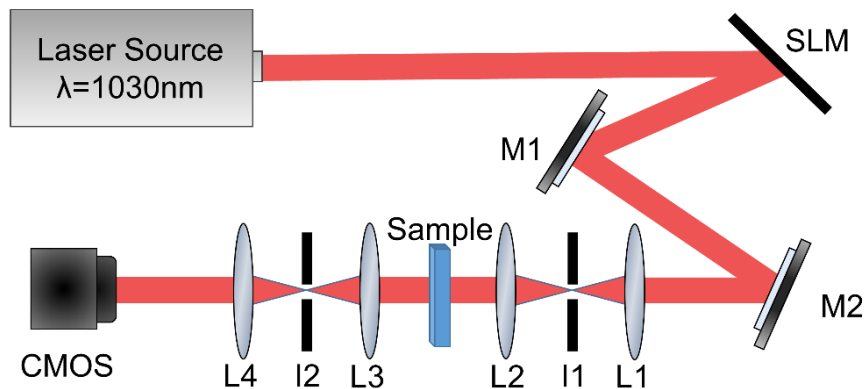


**Figure B.5:** Sketch of the experimental setup for characterization of the volume gratings and imaging the outputs of the volume holograms. M1 and M2 stand for Mirror 1 and Mirror 2. L1 and L2 stand for the lenses of the input



4F imaging system. I1 stands for Iris 1 to block zero order reflection and higher order diffractions from the SLM. L3 and L4 stand for the lenses of the 4F imaging system for the output intensity patterns and I2 stands for Iris 2 to block non-diffracted light after the sample.

#### Supplementary Discussion 4: Aging measurements

A 30- $\mu\text{m}$  thick phase grating is fabricated to check the aging effect. Day 0 measurement is performed 1 hour after the fabrication. Day 1 and Day 2 measurements are performed after 24 and 48 hours respectively. During the whole period, the sample is kept on the DHI setup in the dark. It is illuminated with the He-Ne laser when the holograms are recorded. Mean and standard deviation obtained from the cutlines within 20- $\mu\text{m}$  wide central stripes from all the measurements. In Supplementary Figure B.6(a), the mean values are plotted whereas in Supplementary Figure B.6(b), error bars for Day 0 measurement is provided to highlight that the changes over time do not exceed the error range. To keep the visibility of the graph, error bars of other measurements are not plotted since they follow a similar trend. The measured phase differences are normalized with respect to Day 0 data.

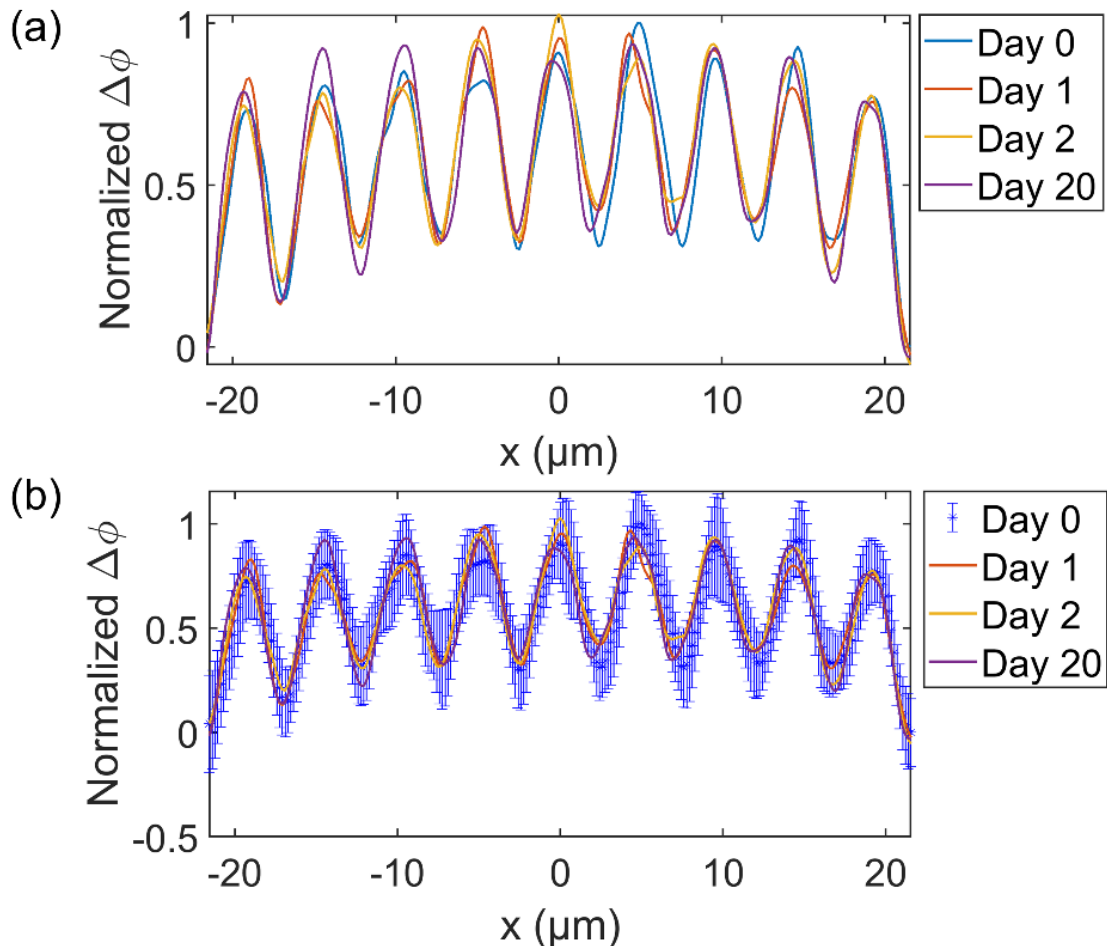


**Figure B.6:** (a) Mean values of the phase measurements (b) same plot given in a except that the error bars for Day 0 measurements are also provided.

#### Supplementary Discussion 5: Determination of the photonic waveguide's parameters

We extracted the waveguide's relevant parameters by fitting the experimental output intensities for radius  $r$  below the cut-off condition of the second propagating mode. For that, we used the intensity functions of the fundamental

modes. In step-index (STIN) waveguides, the fundamental mode ( $LP_{01}$ ) intensity is given by  $J_0^2\left(u\frac{r}{R}\right)$  for  $|r| \leq R$  and  $K_0^2\left(v\frac{r}{R}\right)$  for  $|r| \geq R$ , where  $R$  is the waveguide radius. For fitting our parabolic graded-index (GRIN) waveguides, we use the analytic solution for an infinitely parabolic refractive index profile, given by  $\exp\left(-\frac{1}{2}V\frac{r^2}{R^2}\right)$ , which is a close approximation to our defined refractive index profile in the vicinity of the printed radius [137]. Supplementary Figure B.7(a) shows the normalized frequency obtained from the fits of the STIN waveguides (red dots) and of the GRIN waveguides (blue dots) versus the waveguide radius. The corresponding dashed lines depict the linear fit for each data set, highlighting the expected dependence between the normalized frequency and the waveguide radius  $V = \frac{2\pi R}{\lambda_0}\sqrt{n_1^2 - n_2^2}$ . From  $V$  we extracted the numerical aperture as a function of the waveguide radius, where the numerical aperture of a waveguide with core and cladding refractive indices  $n_1$  and  $n_2$  is defined as  $NA = \sqrt{n_1^2 - n_2^2}$ . The resulting NAs are shown in Supplementary Figure B.7(b) as red (blue) dots for STIN (GRIN) waveguides. In this case, the dashed lines indicate the average NA for each type of waveguide:  $\langle NA_{STIN} \rangle = 0.08 \pm 0.01$  and  $\langle NA_{GRIN} \rangle = 0.18 \pm 0.02$ .

In Figure 5(e) of the main text the confinement factor  $\Gamma$  obtained from integration of the relative intensity in the waveguide cores is compared to the prediction from theory. The latter is straightforwardly calculated after fitting the output intensities as described in the previous paragraph. Once  $u$ ,  $v$  and  $V$  are known, the confinement factor of a given mode  $LP_{mn}$  is given by the expression  $\Gamma_{mn} = \frac{v^2}{V^2} + \frac{u^2}{V^2} \left( \frac{K_m^2(v)}{K_{m-1}(v)K_{m+1}(v)} \right)$ , where  $K_m$  are modified Bessel functions of the second kind [4].

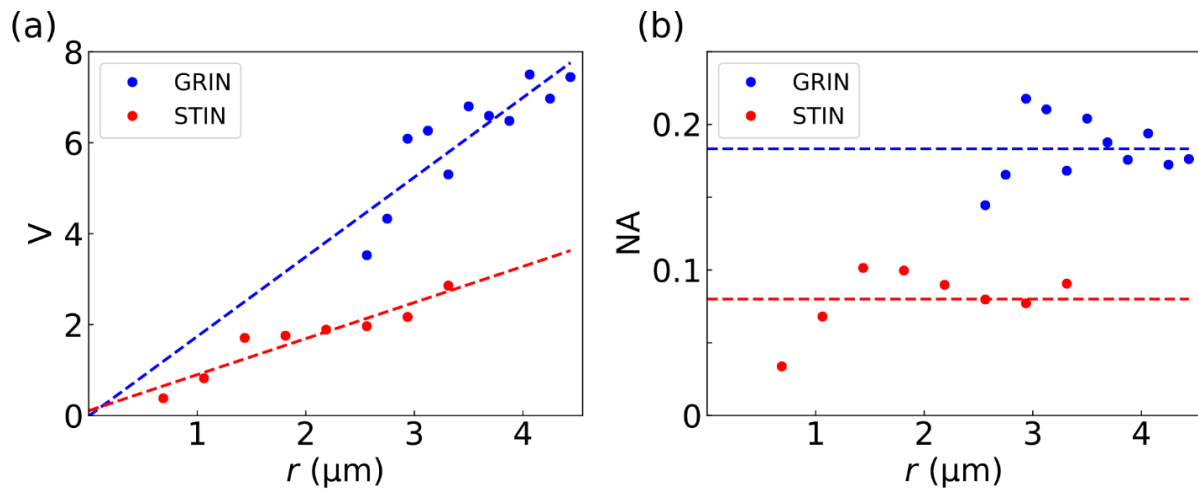


**Figure B.7:** (a) Normalized frequency  $V$  obtained from the fits of the STIN waveguides (red dots) and of the GRIN waveguides (blue dots) versus the waveguide radius. The dashed lines indicate the linear regression of the experimental fits. (b) Calculated values of the numerical aperture NA versus the waveguide radius. The dashed lines indicate the average  $\langle NA \rangle$  for each type of waveguide.

### Supplementary Discussion 6: Experimental setup for optical characterization of 3D-printed photonic waveguides

We optically characterized the 3D-printed waveguides at  $\lambda = 660\text{nm}$ . Supplementary Figure B.8 schematically depicts the optical characterization setup. The single mode Gaussian-like output of a fiber-pigtailed laser diode (LD) was collimated by a microscope objective ( $MO_1$ ; *Olympus PLN10x*). The collimated beam was reflected at a spatial-light modulator (SLM; *Santec SLM-200*) operated in phase-modulation mode. A linear polarizer and a  $\lambda/2$  waveplate (Pol) were used to align the laser's to the SLM's polarization axis. Different phase masks were loaded on the SLM

to generate  $LP_{01}$ ,  $LP_{11}$  and  $LP_{02}$  modes for injection into the waveguides. Modes  $LP_{mn}$  were imaged onto the waveguide's input facets by  $MO_2$ , a 10X microscope objective with  $NA = 0.30$  (*Nikon CFI Plan Achromat 10X*). The waveguide's optical output was collected by  $MO_3$ , a 10X microscope objective with  $NA=0.30$  (*Olympus PLN10x*), and imaging using an achromatic lens (Thorlabs AC254-100-B-ML) with 100 mm focal length resulted in an optical magnification of 5.6 on the transmission camera  $CAM_T$ . The sample's input side was imaged in reflection onto a camera ( $CAM_R$ ) using an identical 100mm lens. We used the same CMOS cameras (iDS U3-3482LE, pixel size  $2.2 \mu\text{m}$ ) for our reflection and transmission experiments. A red LED (635 nm) creates a broad field of incoherent illumination for overall monitoring of the sample, whose position was precisely controlled with a piezo system (Thorlabs 3-Axis Nanomax stage). We aligned each waveguide relative to the injection-laser spot by maximizing the back-reflection off the input waveguide's top-facet via the reflection camera ( $CAM_R$ ). This created reproducible optical injection conditions, ensuring that we characterized each waveguide's generic optical properties.

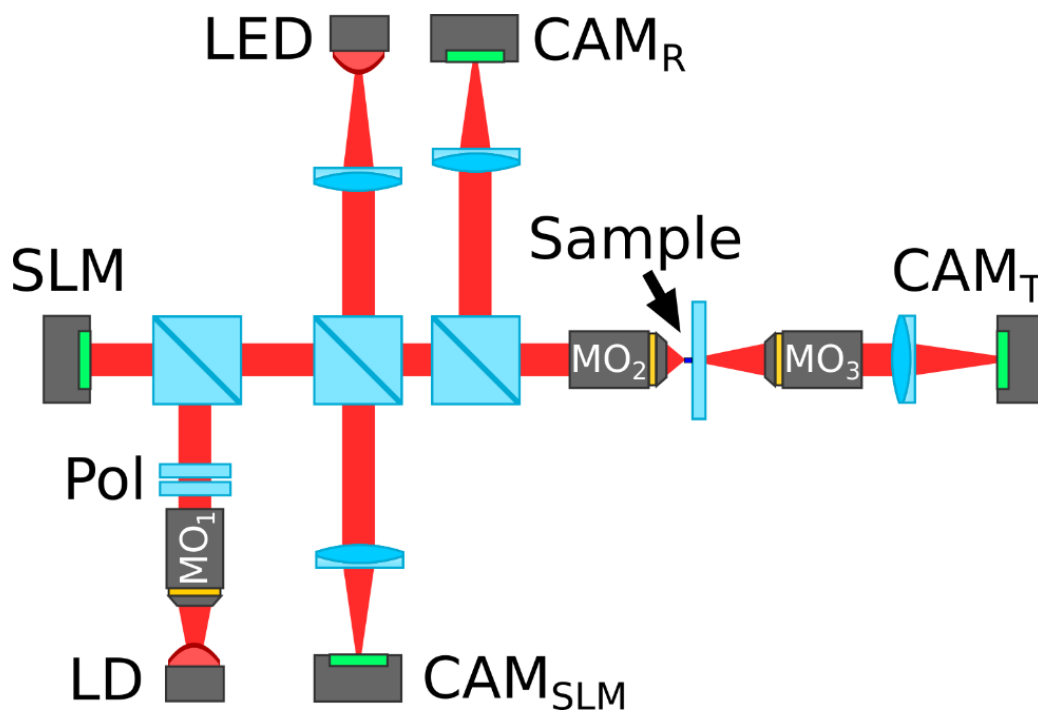


**Figure B.8** : Experimental setup for optical characterization. A 635 nm LED was used as broad field illumination source for coarse positioning of the sample with a piezo-stage (not illustrated). A fiber-coupled laser diode (LD) with 660 nm was collimated by a microscope objective ( $MO_1$ ) and reflected by a spatial-light modulator (SLM) used to generate different  $LP_{mn}$  modes for injection into the waveguides. Polarization optics (Pol; a linear polarizer and a  $\lambda/2$  waveplate) were used to align the input polarization and the SLM to encode the phase patterns. Two 10X microscope objectives were used to inject and collect light from the waveguides. Finally, three CMOS cameras respectively imaged the SLM output ( $CAM_{SLM}$ ), the waveguide's input ( $CAM_R$ ) and the waveguide's output ( $CAM_T$ ).



# Appendix C

This is the edited pre-print version of the *Supplementary Information* of the following article available in arXiv.

## Volume holograms with linear diffraction efficiency relation by (3+1)D printing

Niyazi Ulas Dinc<sup>1,2</sup>, Christophe Moser<sup>1</sup> and Demetri Psaltis<sup>2</sup>

<sup>1</sup>Laboratory of Applied Photonics Devices, École polytechnique fédérale de Lausanne, Switzerland

<sup>2</sup>Optics Laboratory, École polytechnique fédérale de Lausanne, Switzerland

Available in arXiv (2023)

<https://doi.org/10.48550/arXiv.2310.06350>

## Supplementary Information for “Volume holograms with linear diffraction efficiency relation by (3+1)D printing”

### Section 1: Numerical investigations

All the numerical studies are performed on MATLAB using Beam Propagation Method. To compute the index distribution of volume holograms, we simply generate the reference beam and signal beam in the input aperture and let them propagate within the volume of interest. Then we record the 3D field distribution of both beams and compute the filtered interference by simply calculating:

$$E_{filtered,i}(x, y, z) = E_{R,i}^*(x, y, z)E_{S,i}(x, y, z) + E_{R,i}(x, y, z)E_{S,i}^*(x, y, z) \quad (C.1)$$

Where  $i$  denotes the individual hologram. This way we get a real valued  $E_{filtered,i}(x, y, z)$  without undesired DC and noise terms. Then, we simply add up all the computed filtered interferences and scale them according to the dynamic range of refractive index available. Since the reference and signal fields are generated with equal strengths, each hologram approximately shares an equal portion of the dynamic range. To compute the angle of the reference beams, we first compute the available carrier frequencies using Bragg selectivity curves computed for the given volume, background index and the wavelength. The carrier frequencies are computed iteratively by placing the peak of the subsequent one on the first zero crossing of Bragg selectivity curve of the preceding one. This is necessary as we work on small angles for a small volume that yields significant changes in the Bragg selectivity curves. For 200- $\mu\text{m}$  thickness, we have computed 68 gratings to be stored by angular and peristrophic multiplexing. Among which we sampled these holograms with a step of 3 ( $M=1, 4, 7 \dots$ ) and performed beam propagation on each hologram by scanning input angle and recorded the maxima intensities of the diffracted orders to calculate

the mean and standard deviation of the diffraction efficiency. For 400- $\mu\text{m}$  thickness, we have computed 183 gratings to be stored by angular and peristrophic multiplexing. Among which we sampled these holograms with a step of 6 ( $M=1, 7, 13 \dots$ ). We used a RI dynamic range of  $2 \times 10^{-3}$ , wavelength  $\lambda=681 \text{ nm}$  and average RI of the medium as 1.51. The angular sampling is 0.025 degrees for 200- $\mu\text{m}$  thickness and 0.015 degrees for 400- $\mu\text{m}$  thickness.

The  $1/M$  trend assumes statistically independent phase relationship among recorded holograms for a large number of  $M$  so that the summation scales with  $\sqrt{M}$ . If this is not the case, the summation will simply generate beat frequencies in which all the peaks will add up and scale with  $M$  instead of  $\sqrt{M}$ , which would yield  $1/M^2$  diffraction efficiency relation. We introduced a random phase bias to each recording to prevent this phenomenon. Hence, we were able to see the  $1/M$  trend in the simulations even though there is a small oscillation in the mean and standard deviation values. For larger  $M$  than we used, we expect a more stable linear trend. Moreover, since the index distribution is calculated digitally, one can minimize or eliminate the generation of beat frequencies using various methods. A naïve and straightforward approach is sweeping initialized random phases or apply clipping without significantly distorting stored holograms. In our numerical analysis, we did not apply any further restrictions or iterations since the resulting trend was already satisfactory.

## Section 2: Experiments and characterizations

To remove the remaining monomer after the printing, development in PGMEA and IPA is performed for 10 minutes and 4 minutes respectively. In Figure C.1 we provide some snapshots of the excited orders for different holograms we studied during the preliminary phase where we see the desired orders and not the conjugates of those, which is a sanity check showing we indeed multiplexed volume gratings. The number of multiplexed gratings are indicated on the top left corner of each image.

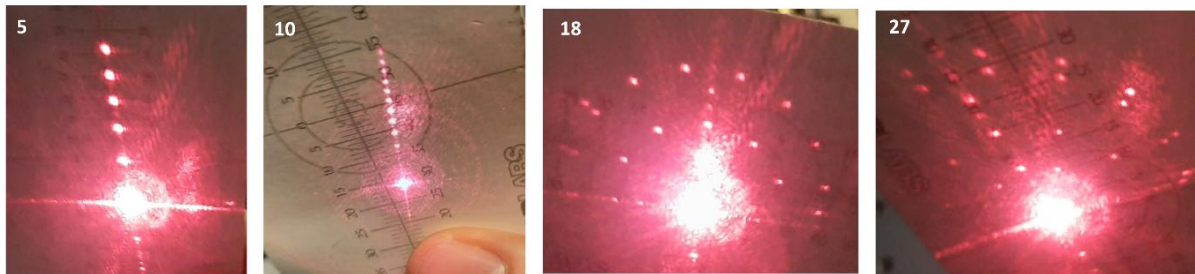


**Figure C.1:** Various snapshots during the preliminary study phase: the diffracted orders obtained when the hologram is flipped and illuminated.

For quantitative measurements, we have characterized the holograms by using the experimental setup whose schematic is given in Figure C.2. We also provide two photographs of the experimental setup in Figure C.3. We used the 4F system indicated to bring the holograms in the center of the illumination beam. Then we flip the front lens of the 4F imaging system and put a camera to realize the setup depicted in Figure C.2. We used the SLM to change the angle of the illumination beam to match the tilt angle of the cover slip, which serves as the substrate of the holograms printed on of it. By doing so, we illuminate the holograms with the perpendicular incidence angle, which maximizes the power in the diffracted orders.

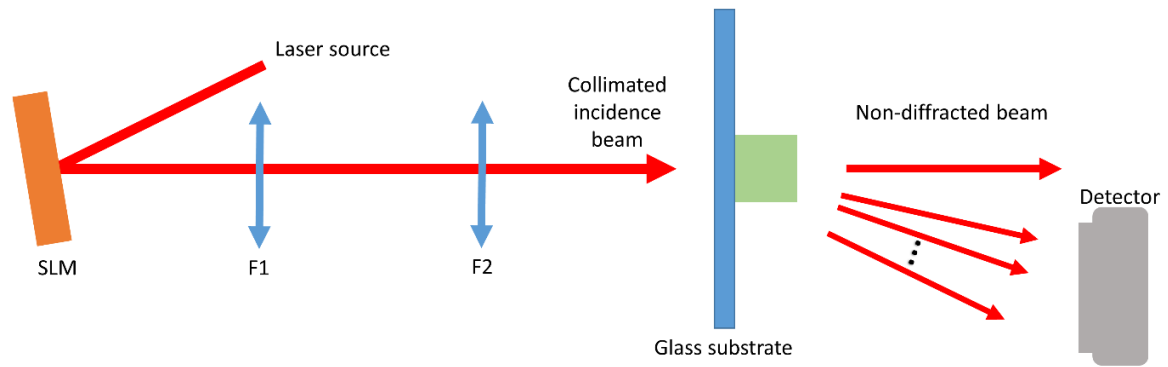


**Figure C.2:** Schematic of the experimental setup for diffraction efficiency measurements.

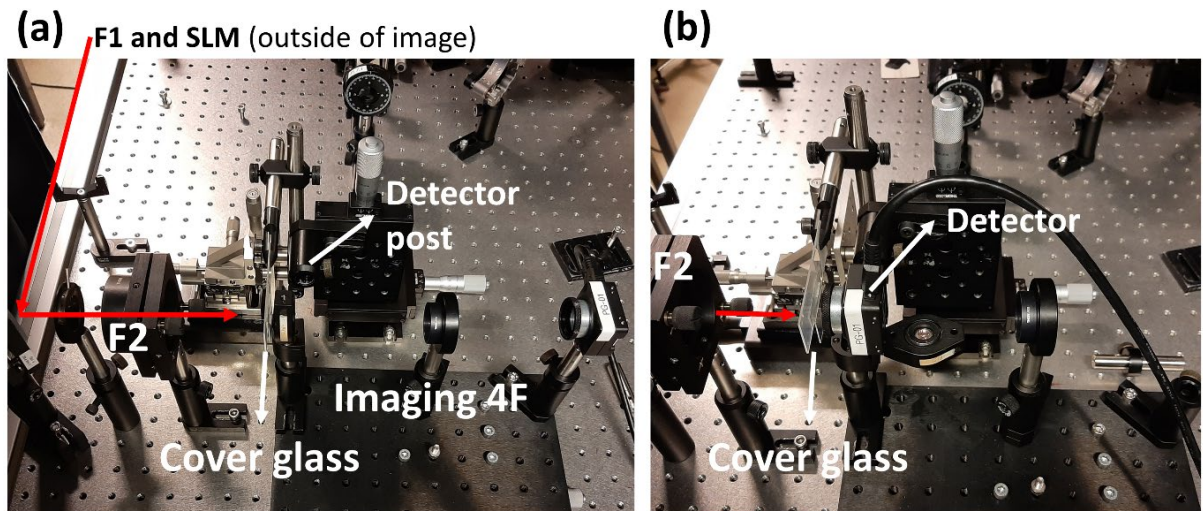


**Figure C.3:** Photographs of the experimental setup for diffraction efficiency measurements. (a) 4F imaging condition where there is a 4F system after the cover glass to align the samples with respect to illumination beam. (b) Configuration for capturing diffraction orders where we place the detector after the cover glass (notice that the front mirror of the imaging 4F is flipped to make room for the detector).

As mentioned in the main text we fabricated a volume hologram that consists five volume gratings. In order to probe if the chosen hatching distance parameter is appropriate, meaning that it provides sufficient sampling, we printed this hologram with different hatching parameters (i.e. different XY sampling of the printer beam trajectory). We provide the results in Figure C.3 showing that there is no significant change in the plots, especially for high angles or large carrier frequencies. This is to say that we are restricted by polymerization chemistry rather than the sampling of the trajectory of the printing beam. Note that to model the smoothing (as in the plots shown in Fig. 3 of the main text) we used “imgaussfilt” function of MATLAB where the standard deviation is set by the “sigma” argument of this function.

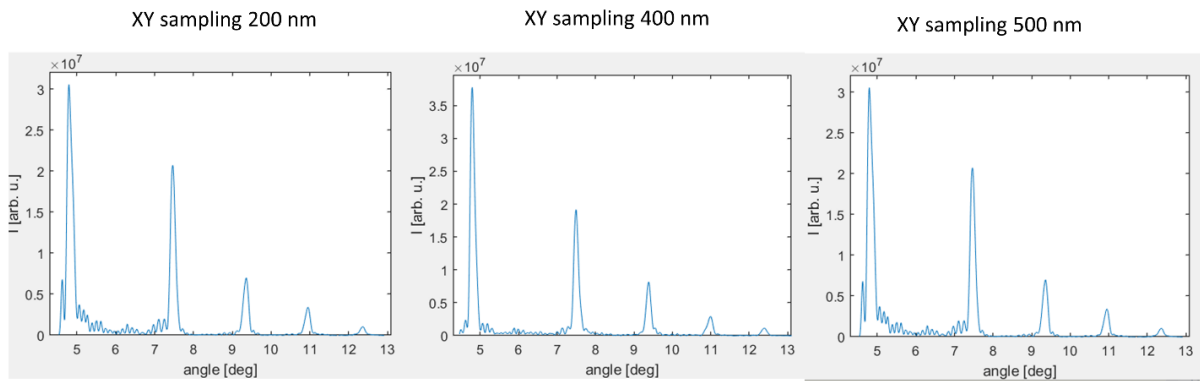


**Figure C.4:** Cut line plot showing the experimental data of diffracted orders corresponding to five volume gratings superimposed. From left to right, the hatching distances (or XY sampling of the trajectory of the printing beam) of the holograms are 200 nm, 400 nm and 500 nm respectively.

In Figure C.5, we show the Fourier transform of the refractive index distribution of middle z-slice of each hologram generated by multiplexing 10, 30, and 50 volume gratings respectively from left to right. Hence the axes represent spatial frequencies in X and Y. Since we just take a slice in z from each hologram, we see the orders and the conjugate terms. Recall that the 3D nature prevents the excitation of conjugate terms. We also indicate the orders, which correspond to approximately  $7.2^\circ$  in polar direction, used to calculate diffraction efficiency by red arrows.

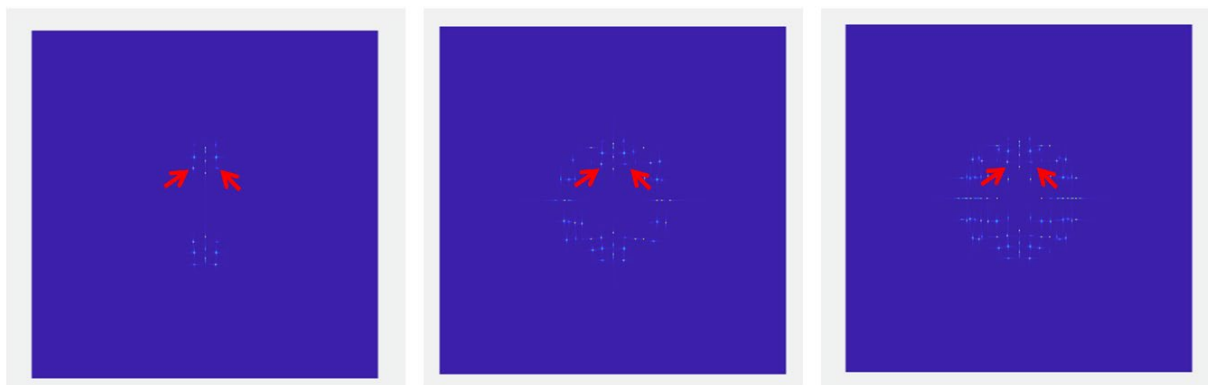


**Figure C.5:** Fourier transforms of the refractive index distribution of mid-z plane of each hologram generated by multiplexing 10, 30, and 50 volume gratings respectively from left to right. Red arrows indicate the orders with the same magnitude of spatial frequency used to compare the diffraction efficiencies of different holograms.



# Appendix D

This is the edited pre-print version of the *Supplementary Information* of the following article available in arXiv.

## Nonlinear Processing with Linear Optics

Mustafa Yildirim<sup>1,2,†</sup>, Niyazi Ulas Dinc<sup>1,2,†</sup>, Ilker Oguz<sup>1,2</sup>, Demetri Psaltis<sup>2</sup> and Christophe Moser<sup>1</sup>

† Equally contributing authors

<sup>1</sup> Laboratory of Applied Photonics Devices, Ecole Polytechnique Fédérale de Lausanne (EPFL), Switzerland

<sup>2</sup> Optics Laboratory, Ecole Polytechnique Fédérale de Lausanne (EPFL), Switzerland

Available in arXiv (2023)

<https://doi.org/10.48550/arXiv.2307.08533>

## Supplementary Material of Nonlinear Processing with Linear Optics

The supplementary material, accessible via the provided DOI above, includes a photograph of the experimental setup and a derivation of the nonlinear response for 2-pixel layers, both of which are omitted from this section. The former can be found in "Chapter 6: Reconfigurable Multilayer Optics for Interconnects," as the physical setup for both the interconnect and nPOLO is identical. The latter has already been detailed in "Chapter 7: Non-linearities in Systems Based on Linear Optics."

### Section 1: Training details

The nPOLO training is designed to determine the optical scaling and bias parameters displayed on the spatial light modulator, in conjunction with the data and the digital weights of the linear classifier post-optics. Figure D.1 illustrates the combination of scaling and bias parameters with the data. This figure also highlights our implementation of the "without data repeat" approach. In Figure D.2, we present examples showcasing the progression of validation accuracies over 20 epochs, both with and without data repeat, utilizing the Imagenette and Fashion MNIST datasets. Given that Imagenette presents a more challenging task, the impact of structural nonlinearity becomes more pronounced when comparing the two plots.

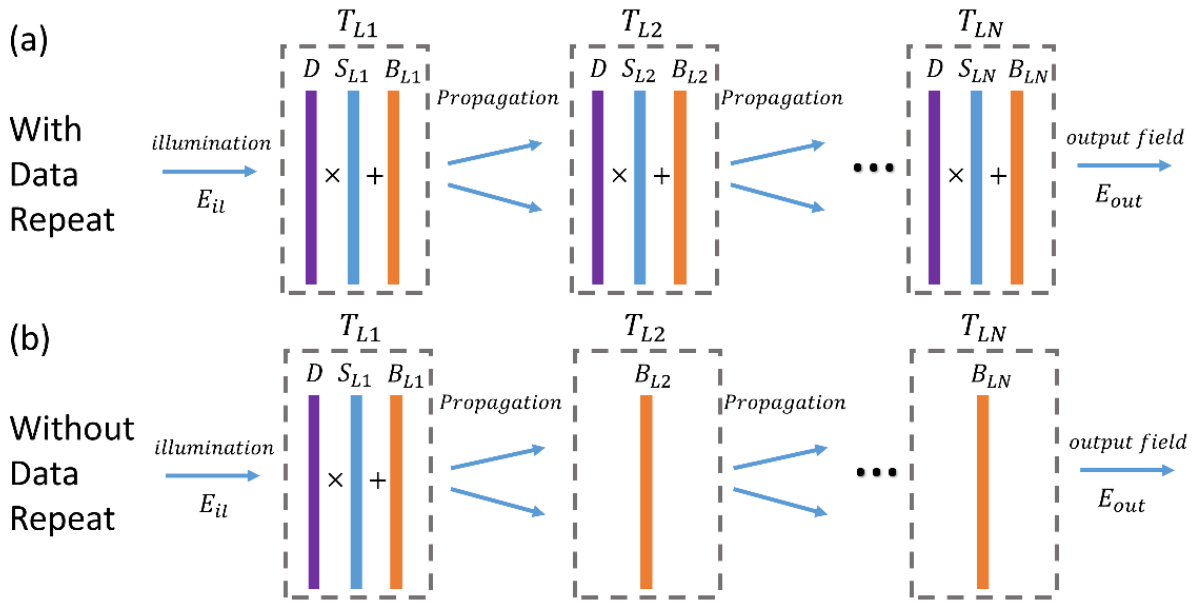


**Figure D.1:** Comparison scheme to observe the effect of structural nonlinearity with equivalent systems in terms of space-bandwidth product. a) Cascaded modulation layers where each layer comprises the input data as given in Figure 1a as well. b) Cascaded modulation layers where only the first layer comprises the input data and the consecutive layers contain trainable bias parameters.

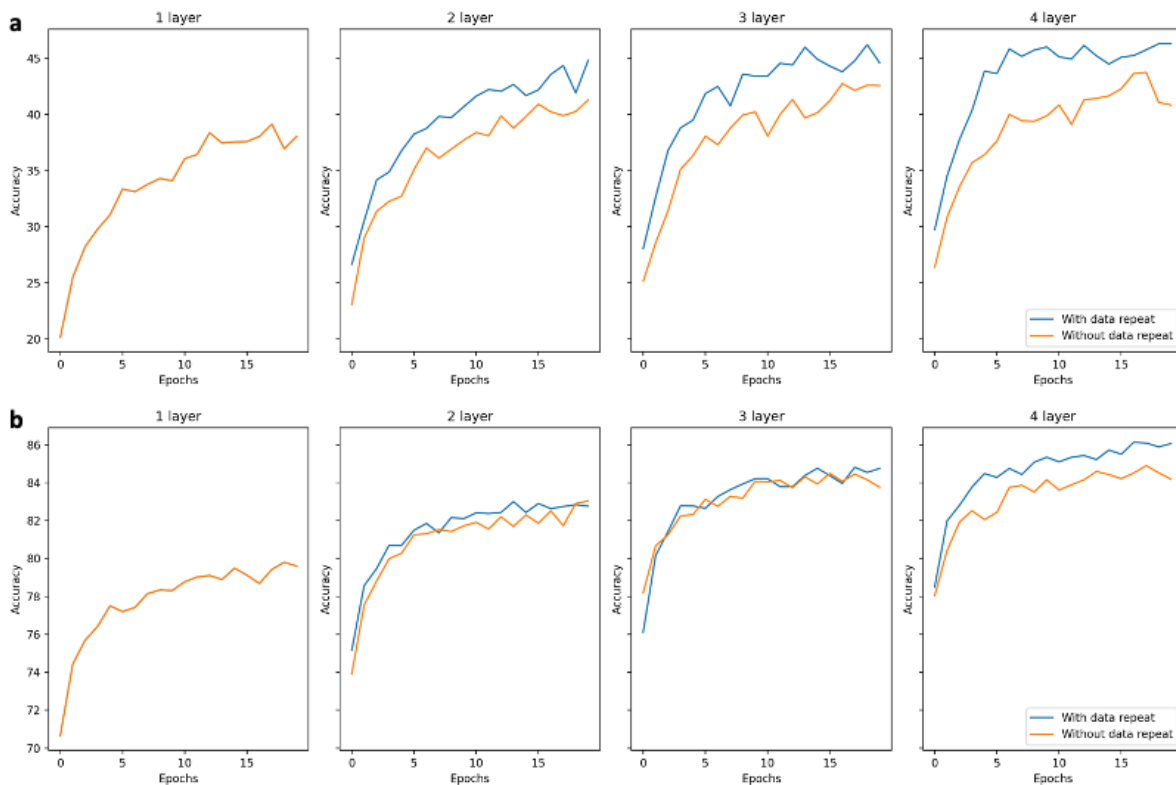


**Figure D.2:** demonstration of the test accuracy results obtained during training of the Imagenette (a) and Fashion MNIST (b) datasets on two different schemas: one with "data repeat" and one without. Note that, one layer corresponds to same configuration for both schemas. Each configuration is trained for 20 epochs.

## Section 2: Numerical study to probe noise robustness

To investigate the influence of discrepancies due to various imperfections in the experimental realization numerically, we conducted simulations by introducing random additive phase noise on the calculated masks. We applied the forward model to all three datasets for various levels of phase noise. The noise was randomly generated from a normal distribution and applied to every pixel of the four layers, meaning that every pixel received a different additive noise value. Subsequently, we determined the output accuracy based on the simulated outputs affected by the introduced noise. To observe the affect of noise, the accuracy of noise-free simulation is normalized to 100% for each dataset studied. Figure D.3 demonstrates that as the strength of the noise increases, the accuracy drop of “without data repetition” occurs more rapidly. This numerical analysis corroborates the findings from our experimental observations.

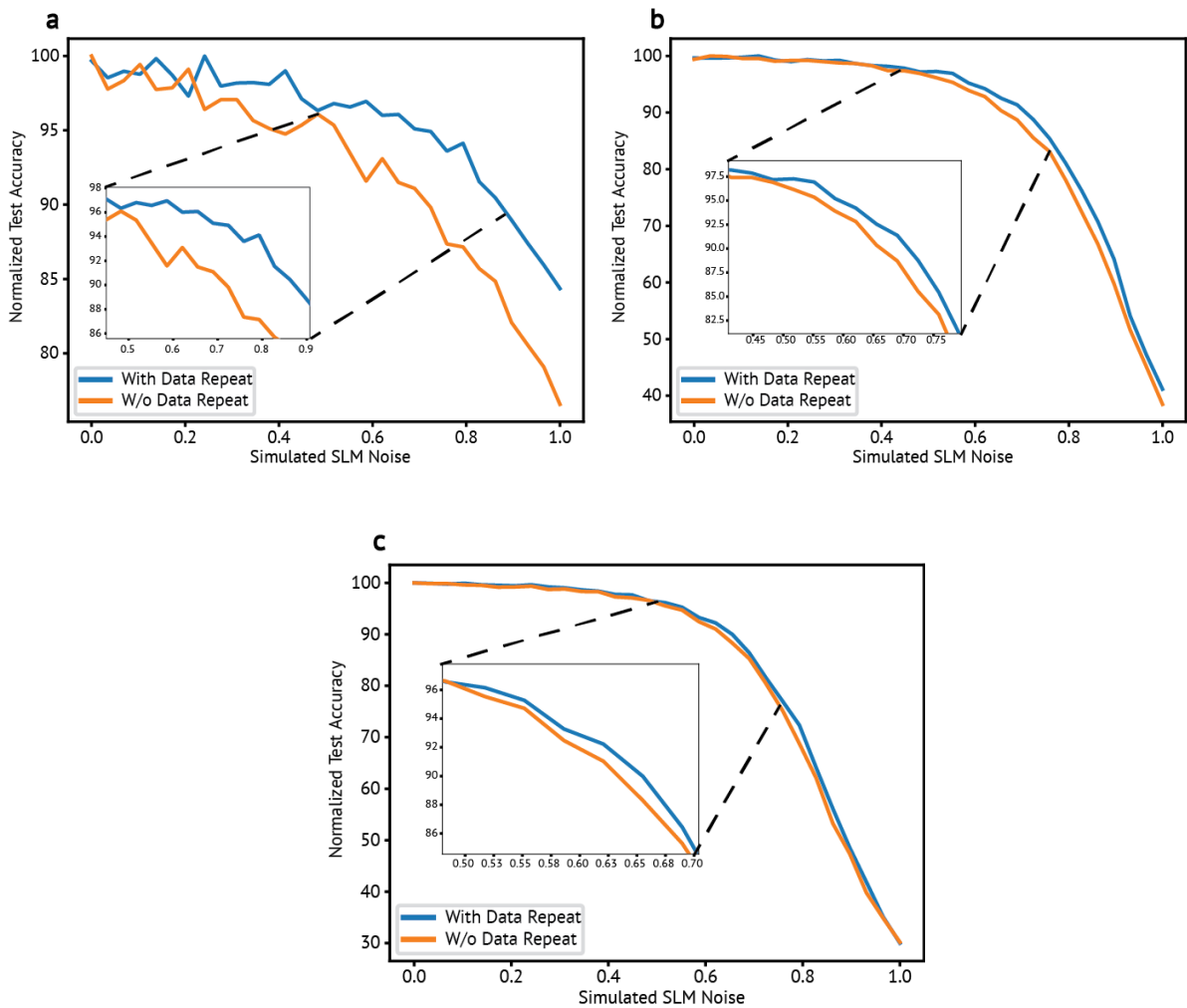


**Figure D.3:** Illustration of the effect of phase noise on pixels. The plots depict the test accuracy drop as the phase noise on the Spatial Light Modulator (SLM) is incrementally increased from zero to one (corresponding to  $2\pi$ ), both for the cases with data repetition and without data repetition. The obtained test accuracies are normalized with respect to the scenario where the phase noise is zero so that accuracies start from 100%. Panels a, b, and c correspond to the datasets: Imagenette, Fashion MNIST, and Digit MNIST, respectively. The insets provide a zoomed view of the difference between the cases with data repetition and without data repetition.

### Section 3: Comparison with Convolutional Neural Networks (CNNs)

We trained convolutional neural networks (CNN) that can provide close performances to nPOLO accuracies obtained in simulations. The results are tabulated in Table D.1 and neural network details are provided for each dataset below.

**Imagenette:** Original dataset consists of 320 by 320 RGB images. Since in nPOLO we use grayscale images we have converted RGB to grayscale. Additionally, the size of images are rescaled to 128 by 128 because of memory considerations for digital networks. The same CNN architecture as LeNet-5 [183] is used but fully connected layers differ in hidden unit size due to the input image size. In this way, hidden unit sizes are 13456, 1024 and 256. For the light CNN, 3 and 6 filters are used in first and second layers of convolutions, respectively. Corresponding hidden unit sizes are: 5046, 256 and 64.

**Fashion and Digit MNIST:** LeNet 5 is initially designed for the input size of 28 by 28. Since Fashion and Digit MNIST already use the same size, we did not change any hidden units of original LeNet 5. For the light CNN, convolutions filter numbers of 3 and 6 are used in the first and second layers. Consequently, hidden unit sizes are: 96, 64 and 42, respectively.

**Table D.1:** The accuracy comparison of nPOLO framework with digital convolutional neural networks.

Network Type	Imagenette	Fashion MNIST	Digit MNIST
LeNet 5 (1st Layer: 6 filters, 2nd Layer: 16 filters)	51.06	89.36	98.98
Light CNN (1st Layer: 3 filters, 2nd Layer: 6 filters)	45.7	88.28	98.5
nPOLO	46.3	86.13	96.43

# References

- [1] R. Athale and D. Psaltis, "Optical Computing: Past and Future," *Optics & Photonics News*, vol. 27, no. 6, p. 32, Jun. 2016, doi: 10.1364/OPN.27.6.000032.
- [2] Y. S. Abu-Mostafa and D. Psaltis, "Optical neural computers," *Scientific American*, vol. 256, no. 3, pp. 88–95, 1987, doi: 10.1038/scientificamerican0387-88.
- [3] N. H. Farhat, D. Psaltis, A. Prata, and E. Paek, "Optical implementation of the Hopfield model," *Appl. Opt., AO*, vol. 24, no. 10, pp. 1469–1475, May 1985, doi: 10.1364/AO.24.001469.
- [4] D. Psaltis, D. Brady, X.-G. Gu, and S. Lin, "Holography in artificial neural networks," vol. 343, p. 6, 1990.
- [5] Y. Shen *et al.*, "Deep learning with coherent nanophotonic circuits," *Nature Photon*, vol. 11, no. 7, pp. 441–446, Jul. 2017, doi: 10.1038/nphoton.2017.93.
- [6] X. Lin *et al.*, "All-optical machine learning using diffractive deep neural networks," *Science*, vol. 361, no. 6406, pp. 1004–1008, Sep. 2018, doi: 10.1126/science.aat8084.
- [7] A. Saade *et al.*, "Random projections through multiple optical scattering: Approximating Kernels at the speed of light," in *2016 IEEE International Conference on Acoustics, Speech and Signal Processing (ICASSP)*, Shanghai: IEEE, Mar. 2016, pp. 6215–6219. doi: 10.1109/ICASSP.2016.7472872.
- [8] T. Zhou *et al.*, "Large-scale neuromorphic optoelectronic computing with a reconfigurable diffractive processing unit," *Nat. Photonics*, vol. 15, no. 5, pp. 367–373, May 2021, doi: 10.1038/s41566-021-00796-w.
- [9] L. Larger *et al.*, "Photonic information processing beyond Turing: an optoelectronic implementation of reservoir computing," *Opt. Express, OE*, vol. 20, no. 3, pp. 3241–3249, Jan. 2012, doi: 10.1364/OE.20.003241.
- [10] J. Bueno *et al.*, "Reinforcement learning in a large-scale photonic recurrent neural network," *Optica, OPTICA*, vol. 5, no. 6, pp. 756–760, Jun. 2018, doi: 10.1364/OPTICA.5.000756.
- [11] D. Pierangeli, G. Marcucci, and C. Conti, "Photonic extreme learning machine by free-space optical propagation," *Photon. Res., PRJ*, vol. 9, no. 8, pp. 1446–1454, Aug. 2021, doi: 10.1364/PRJ.423531.
- [12] F. Zangeneh-Nejad and R. Fleury, "Topological analog signal processing," *Nat Commun*, vol. 10, no. 1, Art. no. 1, May 2019, doi: 10.1038/s41467-019-10086-3.
- [13] F. Zangeneh-Nejad, D. L. Sounas, A. Alù, and R. Fleury, "Analogue computing with metamaterials," *Nat Rev Mater*, vol. 6, no. 3, Art. no. 3, Mar. 2021, doi: 10.1038/s41578-020-00243-2.
- [14] L. G. Wright *et al.*, "Deep physical neural networks trained with backpropagation," *Nature*, vol. 601, no. 7894, Art. no. 7894, Jan. 2022, doi: 10.1038/s41586-021-04223-6.
- [15] A. Momeni, X. Guo, H. Lissek, and R. Fleury, "Physics-inspired Neuroacoustic Computing Based on Tunable Nonlinear Multiple-scattering." arXiv, Apr. 17, 2023. doi: 10.48550/arXiv.2304.08380.
- [16] J. W. Goodman, F. I. Leonberger, S. Y. Kung, and R. A. Athale, "Optical Interconnections for VLSI Systems," *PROC IEEE*, vol. 72, no. 7, pp. 850–866, Jul. 1984, doi: 10.1109/PROC.1984.12943.
- [17] H. J. Coufal, D. Psaltis, and G. T. Sincerbox, *Holographic Data Storage*. 2000.
- [18] S. Hunter, F. Kiamilev, S. Esener, D. A. Parthenopoulos, and P. M. Rentzepis, "Potentials of two-photon based 3-D optical memories for high performance computing," *Appl. Opt.*, vol. 29, no. 14, p. 2058, May 1990, doi: 10.1364/AO.29.002058.
- [19] D. A. Parthenopoulos and P. M. Rentzepis, "Three-Dimensional Optical Storage Memory," *Science*, vol. 245, no. 4920, pp. 843–845, Aug. 1989, doi: 10.1126/science.245.4920.843.
- [20] S. Juodkazis, A. V. Rode, E. G. Gamaly, S. Matsuo, and H. Misawa, "Recording and reading of three-dimensional optical memory in glasses," *Applied Physics B: Lasers and Optics*, vol. 77, no. 2–3, pp. 361–368, Sep. 2003, doi: 10.1007/s00340-003-1224-5.
- [21] G. Wetzstein *et al.*, "Inference in artificial intelligence with deep optics and photonics," *Nature*, vol. 588, no. 7836, pp. 39–47, Dec. 2020, doi: 10.1038/s41586-020-2973-6.
- [22] W. Bogaerts *et al.*, "Programmable photonic circuits," *Nature*, vol. 586, no. 7828, pp. 207–216, Oct. 2020, doi: 10.1038/s41586-020-2764-0.
- [23] J. Feldmann *et al.*, "Parallel convolutional processing using an integrated photonic tensor core," *Nature*, vol. 589, no. 7840, pp. 52–58, Jan. 2021, doi: 10.1038/s41586-020-03070-1.
- [24] X. Xu *et al.*, "Self-calibrating programmable photonic integrated circuits," *Nat. Photon.*, vol. 16, no. 8, pp. 595–602, Aug. 2022, doi: 10.1038/s41566-022-01020-z.
- [25] N. U. Dinc, D. Psaltis, and D. Brunner, "Optical neural networks: The 3D connection," *Photoniques*, no. 104, pp. 34–38, Sep. 2020, doi: 10.1051/photon/202010434.
- [26] G. Van der Sande, D. Brunner, and M. C. Soriano, "Advances in photonic reservoir computing," *Nanophotonics*, vol. 6, no. 3, pp. 561–576, May 2017, doi: 10.1515/nanoph-2016-0132.

- [27] U. Teğin, M. Yıldırım, İ. Oğuz, C. Moser, and D. Psaltis, "Scalable optical learning operator," *Nat Comput Sci*, vol. 1, no. 8, pp. 542–549, Aug. 2021, doi: 10.1038/s43588-021-00112-0.
- [28] K. Kim, J. Yoon, S. Shin, S. Lee, S.-A. Yang, and Y. Park, "Optical diffraction tomography techniques for the study of cell pathophysiology," *JBPE*, pp. 020201-1-020201–16, 2016, doi: 10.18287/JBPE16.02.020201.
- [29] Y. Park, C. Depeursinge, and G. Popescu, "Quantitative phase imaging in biomedicine," *Nature Photon*, vol. 12, no. 10, pp. 578–589, Oct. 2018, doi: 10.1038/s41566-018-0253-x.
- [30] E. Wolf, "Three-dimensional structure determination of semi-transparent objects from holographic data," *Optics Communications*, vol. 1, no. 4, pp. 153–156, Sep. 1969, doi: 10.1016/0030-4018(69)90052-2.
- [31] F. Charrière *et al.*, "Cell refractive index tomography by digital holographic microscopy," *Opt. Lett.*, vol. 31, no. 2, p. 178, Jan. 2006, doi: 10.1364/OL.31.000178.
- [32] W. Choi *et al.*, "Tomographic phase microscopy," *Nat Methods*, vol. 4, no. 9, pp. 717–719, Sep. 2007, doi: 10.1038/nmeth1078.
- [33] A. C. Kak and M. Slaney, *Principles of computerized tomographic imaging*. in Classics in applied mathematics, no. 33. Philadelphia: Society for Industrial and Applied Mathematics, 2001.
- [34] A. J. Devaney, "Inverse-scattering theory within the Rytov approximation," *Opt. Lett.*, vol. 6, no. 8, p. 374, Aug. 1981, doi: 10.1364/OL.6.000374.
- [35] Y. Sung, W. Choi, C. Fang-Yen, K. Badizadegan, R. R. Dasari, and M. S. Feld, "Optical diffraction tomography for high resolution live cell imaging," p. 12, 2009.
- [36] Y. Cotte *et al.*, "Marker-free phase nanoscopy," *Nature Photon*, vol. 7, no. 2, pp. 113–117, Feb. 2013, doi: 10.1038/nphoton.2012.329.
- [37] S. Vertu, J. Flügge, J.-J. Delaunay, and O. Haeberlé, "Improved and isotropic resolution in tomographic diffractive microscopy combining sample and illumination rotation," *Open Physics*, vol. 9, no. 4, pp. 969–974, Aug. 2011, doi: 10.2478/s11534-011-0018-3.
- [38] T. Kim *et al.*, "White-light diffraction tomography of unlabelled live cells," *Nature Photon*, vol. 8, no. 3, pp. 256–263, Mar. 2014, doi: 10.1038/nphoton.2013.350.
- [39] P. Hosseini, Y. Sung, Y. Choi, N. Lue, Z. Yaqoob, and P. So, "Scanning color optical tomography (SCOT)," *Opt. Express*, vol. 23, no. 15, p. 19752, Jul. 2015, doi: 10.1364/OE.23.019752.
- [40] A. Saba, J. Lim, A. B. Ayoub, E. E. Antoine, and D. Psaltis, "Polarization-sensitive optical diffraction tomography," *Optica*, vol. 8, no. 3, p. 402, Mar. 2021, doi: 10.1364/OPTICA.415343.
- [41] J. Lim *et al.*, "Comparative study of iterative reconstruction algorithms for missing cone problems in optical diffraction tomography," *Opt. Express*, vol. 23, no. 13, p. 16933, Jun. 2015, doi: 10.1364/OE.23.016933.
- [42] U. S. Kamilov *et al.*, "Learning approach to optical tomography," *Optica*, vol. 2, no. 6, p. 517, Jun. 2015, doi: 10.1364/OPTICA.2.000517.
- [43] J. Lim, A. B. Ayoub, E. E. Antoine, and D. Psaltis, "High-fidelity optical diffraction tomography of multiple scattering samples," *Light Sci Appl*, vol. 8, no. 1, p. 82, Dec. 2019, doi: 10.1038/s41377-019-0195-1.
- [44] S. Chowdhury *et al.*, "High-resolution 3D refractive index microscopy of multiple-scattering samples from intensity images," *Optica*, vol. 6, no. 9, p. 1211, Sep. 2019, doi: 10.1364/OPTICA.6.001211.
- [45] L. Tian and L. Waller, "3D intensity and phase imaging from light field measurements in an LED array microscope," *Optica*, vol. 2, no. 2, p. 104, Feb. 2015, doi: 10.1364/OPTICA.2.000104.
- [46] J. Lim, A. B. Ayoub, and D. Psaltis, "Three-dimensional tomography of red blood cells using deep learning," *Adv. Photon.*, vol. 2, no. 02, p. 1, Mar. 2020, doi: 10.1117/1.AP.2.2.026001.
- [47] B. Ge *et al.*, "Single-frame label-free cell tomography at speed of more than 10,000 volumes per second," p. 23.
- [48] A. Saba, C. Gigli, A. B. Ayoub, and D. Psaltis, "Physics-informed neural networks for diffraction tomography." arXiv, Jul. 28, 2022. Accessed: Aug. 22, 2022. [Online]. Available: <http://arxiv.org/abs/2207.14230>
- [49] J. Lim and D. Psaltis, "MaxwellNet: Physics-driven deep neural network training based on Maxwell's equations," *APL Photonics*, vol. 7, no. 1, p. 011301, Jan. 2022, doi: 10.1063/5.0071616.
- [50] T.-A. Pham *et al.*, "Versatile reconstruction framework for diffraction tomography with intensity measurements and multiple scattering," *Opt. Express*, vol. 26, no. 3, p. 2749, Feb. 2018, doi: 10.1364/OE.26.002749.
- [51] T. Pham, E. Soubies, A. Ayoub, J. Lim, D. Psaltis, and M. Unser, "Three-Dimensional Optical Diffraction Tomography With Lippmann-Schwinger Model," *IEEE Trans. Comput. Imaging*, vol. 6, pp. 727–738, 2020, doi: 10.1109/TCI.2020.2969070.
- [52] F. Träger, Ed., *Springer Handbook of Lasers and Optics*. Berlin, Heidelberg: Springer Berlin Heidelberg, 2012. doi: 10.1007/978-3-642-19409-2.
- [53] W. E. Moerner, W. Lenth, and G. C. Bjorklund, "Frequency Domain Optical Storage and Other Applications of Persistent Spectral Hole-Burning," in *Persistent Spectral Hole-Burning: Science and Applications*, vol. 44, W. E.

- Moerner, Ed., in *Topics in Current Physics*, vol. 44. , Berlin, Heidelberg: Springer Berlin Heidelberg, 1988, pp. 251–307. doi: 10.1007/978-3-642-83290-1\_7.
- [54] E. S. Maniloff, A. E. Johnson, and T. W. Mossberg, “Spectral Data Storage Using Rare-Earth-Doped Crystals,” *MRS Bull.*, vol. 24, no. 9, pp. 46–50, Sep. 1999, doi: 10.1557/S0883769400053069.
- [55] J. W. Goodman, *Fourier Optics Goodman.pdf*, 2nd ed. The McGraw-Hill companies Inc., 1988.
- [56] E. N. Leith, A. Kozma, J. Upatnieks, J. Marks, and N. Massey, “Holographic Data Storage in Three-Dimensional Media,” *Appl. Opt.*, vol. 5, no. 8, p. 1303, Aug. 1966, doi: 10.1364/AO.5.001303.
- [57] K. Curtis, A. Pu, and D. Psaltis, “Method for holographic storage using peristrophic multiplexing,” *Opt. Lett.*, vol. 19, no. 13, p. 993, Jul. 1994, doi: 10.1364/OL.19.000993.
- [58] D. Gabor, “Associative Holographic Memories,” *IBM J. Res. & Dev.*, vol. 13, no. 2, pp. 156–159, Mar. 1969, doi: 10.1147/rd.132.0156.
- [59] H.-Y. S. Li, Y. Qiao, and D. Psaltis, “Optical network for real-time face recognition,” *Appl. Opt.*, vol. 32, no. 26, p. 5026, Sep. 1993, doi: 10.1364/AO.32.005026.
- [60] C. Gu, J. Hong, and S. Campbell, “2-D shift-invariant volume holographic correlator,” *Optics Communications*, vol. 88, no. 4–6, pp. 309–314, Apr. 1992, doi: 10.1016/0030-4018(92)90047-U.
- [61] D. Brady and D. Psaltis, “Control of volume holograms,” *J. Opt. Soc. Am. A*, vol. 9, no. 7, p. 1167, Jul. 1992, doi: 10.1364/JOSAA.9.001167.
- [62] C. Moser, I. Maravic, B. Schupp, A. Adibi, and D. Psaltis, “Diffraction efficiency of localized holograms in doubly doped LiNbO<sub>3</sub> crystals,” *Opt. Lett.*, vol. 25, no. 17, p. 1243, Sep. 2000, doi: 10.1364/OL.25.001243.
- [63] C. Moser, B. Schupp, and D. Psaltis, “Localized holographic recording in doubly doped lithium niobate,” p. 3.
- [64] S. Kawata, H.-B. Sun, T. Tanaka, and K. Takada, *Nature*, vol. 412, pp. 697–698, doi: <https://doi.org/10.1038/35089130>.
- [65] X. Zhou, Y. Hou, and J. Lin, “A review on the processing accuracy of two-photon polymerization,” *AIP Advances*, vol. 5, no. 3, p. 030701, Mar. 2015, doi: 10.1063/1.4916886.
- [66] N. U. Dinc, J. Lim, E. Kakkava, C. Moser, and D. Psaltis, “Computer generated optical volume elements by additive manufacturing,” *Nanophotonics*, vol. 9, no. 13, pp. 4173–4181, Jun. 2020, doi: 10.1515/nanoph-2020-0196.
- [67] D. A. B. Miller, “Communicating with waves between volumes: evaluating orthogonal spatial channels and limits on coupling strengths,” *Appl. Opt.*, vol. 39, no. 11, p. 1681, Apr. 2000, doi: 10.1364/AO.39.001681.
- [68] R. Piestun and D. A. B. Miller, “Electromagnetic degrees of freedom of an optical system,” *J. Opt. Soc. Am. A*, vol. 17, no. 5, p. 892, May 2000, doi: 10.1364/JOSAA.17.000892.
- [69] D. Psaltis, D. Brady, and K. Wagner, “Adaptive optical networks using photorefractive crystals,” *Appl. Opt.*, vol. 27, no. 9, p. 1752, May 1988, doi: 10.1364/AO.27.001752.
- [70] H. Lee, X. Gu, and D. Psaltis, “Volume holographic interconnections with maximal capacity and minimal cross talk,” *Journal of Applied Physics*, vol. 65, no. 6, pp. 2191–2194, Mar. 1989, doi: 10.1063/1.342828.
- [71] T. D. Gerke and R. Piestun, “Aperiodic volume optics,” *Nature Photon*, vol. 4, no. 3, pp. 188–193, Mar. 2010, doi: 10.1038/nphoton.2009.290.
- [72] H. Wang and R. Piestun, “Dynamic 2D implementation of 3D diffractive optics,” *Optica*, vol. 5, no. 10, p. 1220, Oct. 2018, doi: 10.1364/OPTICA.5.001220.
- [73] J. Moughames, X. Porte, L. Larger, M. Jacquot, M. Kadic, and D. Brunner, “3D printed multimode-splitters for photonic interconnects,” *Opt. Mater. Express*, vol. 10, no. 11, p. 2952, Nov. 2020, doi: 10.1364/OME.402974.
- [74] J. Moughames *et al.*, “Three-dimensional waveguide interconnects for scalable integration of photonic neural networks,” *Optica*, *OPTICA*, vol. 7, no. 6, pp. 640–646, Jun. 2020, doi: 10.1364/OPTICA.388205.
- [75] M. Veli *et al.*, “Terahertz pulse shaping using diffractive surfaces,” *Nat Commun*, vol. 12, no. 1, p. 37, Dec. 2021, doi: 10.1038/s41467-020-20268-z.
- [76] Y. Luo *et al.*, “Computational imaging without a computer: seeing through random diffusers at the speed of light,” *eLight*, vol. 2, no. 1, p. 4, Dec. 2022, doi: 10.1186/s43593-022-00012-4.
- [77] D. Mengu and A. Ozcan, “All-Optical Phase Recovery: Diffractive Computing for Quantitative Phase Imaging,” *Advanced Optical Materials*, vol. 10, no. 15, p. 2200281, Aug. 2022, doi: 10.1002/adom.202200281.
- [78] Ç. Işıl *et al.*, “Super-resolution image display using diffractive decoders,” *Science Advances*, vol. 8, no. 48, p. eadd3433, Dec. 2022, doi: 10.1126/sciadv.add3433.
- [79] C. M. Lalau-Keraly, S. Bhargava, O. D. Miller, and E. Yablonovitch, “Adjoint shape optimization applied to electromagnetic design,” *Opt. Express*, vol. 21, no. 18, p. 21693, Sep. 2013, doi: 10.1364/OE.21.021693.
- [80] J. S. Jensen and O. Sigmund, “Topology optimization for nano-photonics,” *Laser & Photon. Rev.*, vol. 5, no. 2, pp. 308–321, Mar. 2011, doi: 10.1002/lpor.201000014.
- [81] S. Molesky, Z. Lin, A. Y. Piggott, W. Jin, J. Vucković, and A. W. Rodriguez, “Inverse design in nanophotonics,” *Nature Photon*, vol. 12, no. 11, pp. 659–670, Nov. 2018, doi: 10.1038/s41566-018-0246-9.

- [82] P. Camayd-Muñoz, C. Ballew, G. Roberts, and A. Faraon, "Multifunctional volumetric meta-optics for color and polarization image sensors," *Optica*, *OPTICA*, vol. 7, no. 4, pp. 280–283, Apr. 2020, doi: 10.1364/OP-TICA.384228.
- [83] M. Minkov *et al.*, "Inverse Design of Photonic Crystals through Automatic Differentiation," *ACS Photonics*, vol. 7, no. 7, pp. 1729–1741, Jul. 2020, doi: 10.1021/acsphotonics.0c00327.
- [84] W. Ma, Z. Liu, Z. A. Kudyshev, A. Boltasseva, W. Cai, and Y. Liu, "Deep learning for the design of photonic structures," *Nat. Photonics*, vol. 15, no. 2, pp. 77–90, Feb. 2021, doi: 10.1038/s41566-020-0685-y.
- [85] I. E. Lagaris, A. Likas, and D. I. Fotiadis, "Artificial neural networks for solving ordinary and partial differential equations," *IEEE Trans. Neural Netw.*, vol. 9, no. 5, pp. 987–1000, Sep. 1998, doi: 10.1109/72.712178.
- [86] M. Raissi, P. Perdikaris, and G. E. Karniadakis, "Physics-informed neural networks: A deep learning framework for solving forward and inverse problems involving nonlinear partial differential equations," *Journal of Computational Physics*, vol. 378, pp. 686–707, Feb. 2019, doi: 10.1016/j.jcp.2018.10.045.
- [87] Y. Chen, L. Lu, G. E. Karniadakis, and L. Dal Negro, "Physics-informed neural networks for inverse problems in nano-optics and metamaterials," *Opt. Express*, vol. 28, no. 8, p. 11618, Apr. 2020, doi: 10.1364/OE.384875.
- [88] J. J. Park, P. Florence, J. Straub, R. Newcombe, and S. Lovegrove, "DeepSDF: Learning Continuous Signed Distance Functions for Shape Representation," in *2019 IEEE/CVF Conference on Computer Vision and Pattern Recognition (CVPR)*, Long Beach, CA, USA: IEEE, Jun. 2019, pp. 165–174. doi: 10.1109/CVPR.2019.00025.
- [89] S. M. Popoff, G. Lerosey, R. Carminati, M. Fink, A. C. Boccarda, and S. Gigan, "Measuring the Transmission Matrix in Optics: An Approach to the Study and Control of Light Propagation in Disordered Media," *Phys. Rev. Lett.*, vol. 104, no. 10, p. 100601, Mar. 2010, doi: 10.1103/PhysRevLett.104.100601.
- [90] S. Rotter and S. Gigan, "Light fields in complex media: Mesoscopic scattering meets wave control," *Rev. Mod. Phys.*, vol. 89, no. 1, p. 015005, Mar. 2017, doi: 10.1103/RevModPhys.89.015005.
- [91] X. Porte *et al.*, "Direct (3+1)D laser writing of graded-index optical elements," *Optica*, vol. 8, no. 10, p. 1281, Oct. 2021, doi: 10.1364/OP-TICA.433475.
- [92] C. R. Ocier *et al.*, "Direct laser writing of volumetric gradient index lenses and waveguides," *Light Sci Appl*, vol. 9, no. 1, p. 196, Dec. 2020, doi: 10.1038/s41377-020-00431-3.
- [93] A. Grabulosa, J. Moughames, X. Porte, and D. Brunner, "Combining one and two photon polymerization for accelerated high performance (3 + 1)D photonic integration," *Nanophotonics*, vol. 11, no. 8, pp. 1591–1601, May 2022, doi: 10.1515/nanoph-2021-0733.
- [94] F. Mok and D. Psaltis, "Holographic Memories," *Scientific American*, vol. 273, p. 70, 1995.
- [95] G. J. Steckman, W. Liu, R. Platz, D. Schroeder, C. Moser, and F. Havermeyer, "Volume Holographic Grating Wavelength Stabilized Laser Diodes," *IEEE Journal of Selected Topics in Quantum Electronics*, vol. 13, no. 3, pp. 672–678, May 2007, doi: 10.1109/JSTQE.2007.896060.
- [96] S. Borgsmüller, S. Noehte, C. Dietrich, T. Kresse, and R. Männer, "Computer-generated stratified diffractive optical elements," *Appl Opt*, vol. 42, no. 26, pp. 5274–5283, Sep. 2003, doi: 10.1364/ao.42.005274.
- [97] T. Kämpfe, E.-B. Kley, A. Tünnermann, and P. Dannberg, "Design and fabrication of stacked, computer generated holograms for multicolor image generation," *Appl. Opt.*, *AO*, vol. 46, no. 22, pp. 5482–5488, Aug. 2007, doi: 10.1364/AO.46.005482.
- [98] T. Kämpfe, E.-B. Kley, and A. Tünnermann, "Designing multiplane computer-generated holograms with consideration of the pixel shape and the illumination wave," *J Opt Soc Am A Opt Image Sci Vis*, vol. 25, no. 7, pp. 1609–1622, Jul. 2008, doi: 10.1364/josaa.25.001609.
- [99] G. Labroille, B. Denolle, P. Jian, P. Genevieux, N. Treps, and J.-F. Morizur, "Efficient and mode selective spatial mode multiplexer based on multi-plane light conversion," *Opt. Express*, *OE*, vol. 22, no. 13, pp. 15599–15607, Jun. 2014, doi: 10.1364/OE.22.015599.
- [100] R. W. Gerchberg, "A practical algorithm for the determination of phase from image and diffraction plane pictures," *Optik*, Jan. 1972, Accessed: Oct. 18, 2023. [Online]. Available: <https://www.scinapse.io/papers/1484412996>
- [101] Y. Luo *et al.*, "Design of task-specific optical systems using broadband diffractive neural networks," *Light Sci Appl*, vol. 8, no. 1, Art. no. 1, Dec. 2019, doi: 10.1038/s41377-019-0223-1.
- [102] A. Beck and M. Teboulle, "Fast Gradient-Based Algorithms for Constrained Total Variation Image Denoising and Deblurring Problems," *IEEE Transactions on Image Processing*, vol. 18, no. 11, pp. 2419–2434, Nov. 2009, doi: 10.1109/TIP.2009.2028250.
- [103] Z. Wang, A. C. Bovik, H. R. Sheikh, and E. P. Simoncelli, "Image quality assessment: from error visibility to structural similarity," *IEEE Transactions on Image Processing*, vol. 13, no. 4, pp. 600–612, Apr. 2004, doi: 10.1109/TIP.2003.819861.



- [104] A. Žukauskas, I. Matulaitienė, D. Paipulas, G. Niaura, M. Malinauskas, and R. Gadonas, "Tuning the refractive index in 3D direct laser writing lithography: towards GRIN microoptics," *Laser & Photonics Reviews*, vol. 9, no. 6, pp. 706–712, 2015, doi: 10.1002/lpor.201500170.
- [105] G. Barbastathis and D. Psaltis, "Volume Holographic Multiplexing Methods," in *Holographic Data Storage*, H. J. Coufal, D. Psaltis, and G. T. Sincerbox, Eds., in Springer Series in Optical Sciences. , Berlin, Heidelberg: Springer, 2000, pp. 21–62. doi: 10.1007/978-3-540-47864-5\_2.
- [106] M. Sartison *et al.*, "3D printed micro-optics for quantum technology: Optimised coupling of single quantum dot emission into a single-mode fibre," *gxjzz*, vol. 2, no. 2, pp. 103–119, Jun. 2021, doi: 10.37188/lam.2021.006.
- [107] K. Markiewicz and P. Wasylczyk, "Photonic-chip-on-tip: compound photonic devices fabricated on optical fibers," *Opt. Express, OE*, vol. 27, no. 6, pp. 8440–8445, Mar. 2019, doi: 10.1364/OE.27.008440.
- [108] W. Hadibrata, H. Wei, S. Krishnaswamy, and K. Aydin, "Inverse Design and 3D Printing of a Metalens on an Optical Fiber Tip for Direct Laser Lithography," *Nano Lett.*, vol. 21, no. 6, pp. 2422–2428, Mar. 2021, doi: 10.1021/acs.nanolett.0c04463.
- [109] S. Ristok, S. Thiele, A. Toulouse, A. M. Herkommer, and H. Giessen, "Stitching-free 3D printing of millimeter-sized highly transparent spherical and aspherical optical components," *Opt. Mater. Express, OME*, vol. 10, no. 10, pp. 2370–2378, Oct. 2020, doi: 10.1364/OME.401724.
- [110] P.-I. Dietrich *et al.*, "In situ 3D nanoprinting of free-form coupling elements for hybrid photonic integration," *Nature Photon*, vol. 12, no. 4, Art. no. 4, Apr. 2018, doi: 10.1038/s41566-018-0133-4.
- [111] F. Mayer, S. Richter, J. Westhauser, E. Blasco, C. Barner-Kowollik, and M. Wegener, "Multimaterial 3D laser microprinting using an integrated microfluidic system," *Science Advances*, vol. 5, no. 2, p. eaau9160, Feb. 2019, doi: 10.1126/sciadv.aau9160.
- [112] A. Lamont, M. Restaino, M. Kim, and R. Sochol, "A facile multi-material direct laser writing strategy," *Lab on a Chip*, vol. 19, pp. 2340–2345, Jun. 2019, doi: 10.1039/C9LC00398C.
- [113] B. A. Kowalski and R. R. McLeod, "Design concepts for diffusive holographic photopolymers," *Journal of Polymer Science Part B: Polymer Physics*, vol. 54, no. 11, pp. 1021–1035, 2016, doi: 10.1002/polb.24011.
- [114] J. Guo, M. R. Gleeson, and J. T. Sheridan, "A Review of the Optimisation of Photopolymer Materials for Holographic Data Storage," *Physics Research International*, vol. 2012, p. e803439, Jun. 2012, doi: 10.1155/2012/803439.
- [115] K. Curtis, L. Dhar, A. Hill, W. Wilson, and M. Ayres, *Holographic Data Storage: From Theory to Practical Systems*. John Wiley and Sons, 2010. doi: 10.1002/9780470666531.
- [116] D. J. Glugla, M. B. Chosy, M. D. Alim, K. K. Childress, A. C. Sullivan, and R. R. McLeod, "Multiple patterning of holographic photopolymers for increased refractive index contrast," *Opt Lett*, vol. 43, no. 8, pp. 1866–1869, Apr. 2018, doi: 10.1364/OL.43.001866.
- [117] M. Ziemczonok, A. Kuś, P. Wasylczyk, and M. Kujawińska, "3D-printed biological cell phantom for testing 3D quantitative phase imaging systems," *Sci Rep*, vol. 9, no. 1, p. 18872, Dec. 2019, doi: 10.1038/s41598-019-55330-4.
- [118] S. Dottermusch, D. Busko, M. Langenhorst, U. W. Paetzold, and B. S. Richards, "Exposure-dependent refractive index of Nanoscribe IP-Dip photoresist layers," *Opt Lett*, vol. 44, no. 1, pp. 29–32, Jan. 2019, doi: 10.1364/OL.44.000029.
- [119] M. Schmid, D. Ludescher, and H. Giessen, "Optical properties of photoresists for femtosecond 3D printing: refractive index, extinction, luminescence-dose dependence, aging, heat treatment and comparison between 1-photon and 2-photon exposure," *Opt. Mater. Express*, vol. 9, no. 12, p. 4564, Dec. 2019, doi: 10.1364/OME.9.004564.
- [120] L. J. Jiang *et al.*, "Two-photon polymerization: investigation of chemical and mechanical properties of resins using Raman microspectroscopy," *Opt. Lett., OL*, vol. 39, no. 10, pp. 3034–3037, May 2014, doi: 10.1364/OL.39.003034.
- [121] N. Lindenmann *et al.*, "Photonic wire bonding: a novel concept for chip-scale interconnects," *Opt Express*, vol. 20, no. 16, pp. 17667–17677, Jul. 2012, doi: 10.1364/OE.20.017667.
- [122] M. Blaicher *et al.*, "Hybrid multi-chip assembly of optical communication engines by in situ 3D nano-lithography," *Light Sci Appl*, vol. 9, no. 1, Art. no. 1, Apr. 2020, doi: 10.1038/s41377-020-0272-5.
- [123] A. Bogucki, Ł. Zinkiewicz, W. Pacuski, P. Wasylczyk, and P. Kossacki, "Optical fiber micro-connector with nanometer positioning precision for rapid prototyping of photonic devices," *Opt Express*, vol. 26, no. 9, pp. 11513–11518, Apr. 2018, doi: 10.1364/OE.26.011513.
- [124] G. Panusa, Y. Pu, J. Wang, C. Moser, and D. Psaltis, "Fabrication of Sub-Micron Polymer Waveguides through Two-Photon Polymerization in Polydimethylsiloxane," *Polymers*, vol. 12, no. 11, Art. no. 11, Nov. 2020, doi: 10.3390/polym12112485.

- [125] P. Gašo *et al.*, “3D Polymer Based 1x4 Beam Splitter,” *Journal of Lightwave Technology*, vol. 39, no. 1, pp. 154–161, Jan. 2021, doi: 10.1109/JLT.2020.3026170.
- [126] A. Bertoincini and C. Liberale, “3D printed waveguides based on Photonic Crystal Fiber designs for complex fiber-end photonic devices.” arXiv, Sep. 07, 2020. doi: 10.48550/arXiv.2009.04209.
- [127] A. Nesic *et al.*, “Photonic-integrated circuits with non-planar topologies realized by 3D-printed waveguide overpasses,” *Opt. Express, OE*, vol. 27, no. 12, pp. 17402–17425, Jun. 2019, doi: 10.1364/OE.27.017402.
- [128] “Optical properties of photoresists for femtosecond 3D printing: refractive index, extinction, luminescence-dose dependence, aging, heat treatment and comparison between 1-photon and 2-photon exposure.” Accessed: Oct. 18, 2023. [Online]. Available: <https://opg.optica.org/ome/fulltext.cfm?uri=ome-9-12-4564&id=423069>
- [129] A. Ovsianikov, X. Shizhou, M. Farsari, M. Vamvakaki, C. Fotakis, and B. N. Chichkov, “Shrinkage of microstructures produced by two-photon polymerization of Zr-based hybrid photosensitive materials,” *Opt Express*, vol. 17, no. 4, pp. 2143–2148, Feb. 2009, doi: 10.1364/oe.17.002143.
- [130] S. Gallego, M. Ortuño, C. Neipp, C. García Llopis, A. Beléndez, and I. Pascual, “Overmodulation effects in volume holograms recorded on photopolymers,” Jan. 2003, doi: 10.1016/S0030-4018(02)02244-7.
- [131] H. Kogelnik, “Coupled Wave Theory for Thick Hologram Gratings,” *Bell System Technical Journal*, vol. 48, no. 9, pp. 2909–2947, Nov. 1969, doi: 10.1002/j.1538-7305.1969.tb01198.x.
- [132] Y. Wakayama, A. Okamoto, K. Kawabata, A. Tomita, and K. Sato, “Mode demultiplexer using angularly multiplexed volume holograms,” *Opt Express*, vol. 21, no. 10, pp. 12920–12933, May 2013, doi: 10.1364/OE.21.012920.
- [133] F. H. Mok, G. W. Burr, and D. Psaltis, “System metric for holographic memory systems,” *Opt Lett*, vol. 21, no. 12, pp. 896–898, Jun. 1996, doi: 10.1364/ol.21.000896.
- [134] E. S. Maniloff and K. M. Johnson, “Maximized photorefractive holographic storage,” *Journal of Applied Physics*, vol. 70, no. 9, pp. 4702–4707, Nov. 1991, doi: 10.1063/1.350340.
- [135] G. Zhao and P. Mouroulis, “Diffusion Model of Hologram Formation in Dry Photopolymer Materials,” *Journal of Modern Optics*, vol. 41, no. 10, pp. 1929–1939, Oct. 1994, doi: 10.1080/09500349414551831.
- [136] J. T. Sheridan, M. G. Gleeson, J. V. Kelly, and F. T. O’Neill, “Nonlocal polymerization-driven diffusion-model-based examination of the scaling law for holographic data storage,” *Opt Lett*, vol. 30, no. 3, pp. 239–241, Feb. 2005, doi: 10.1364/ol.30.000239.
- [137] A. W. Snyder and J. Love, *Optical Waveguide Theory*. Springer Science & Business Media, 1983.
- [138] A. C. Sullivan, M. D. Alim, D. J. Glugla, and R. R. McLeod, “Holographic analysis of photopolymers,” in *Holography: Advances and Modern Trends V*, SPIE, May 2017, pp. 56–63. doi: 10.1117/12.2265865.
- [139] A. Abou Khalil, W. Gebremichael, Y. Petit, and L. Canioni, “Refractive index change measurement by quantitative microscopy phase imaging for femtosecond laser written structures,” *Optics Communications*, vol. 485, p. 126731, Apr. 2021, doi: 10.1016/j.optcom.2020.126731.
- [140] N. U. Dinc *et al.*, “From 3D to 2D and back again,” *Nanophotonics*, vol. 12, no. 5, pp. 777–793, Mar. 2023, doi: 10.1515/nanoph-2022-0512.
- [141] R. T. Ingwall and D. Waldman, “Photopolymer Systems,” in *Holographic Data Storage*, H. J. Coufal, D. Psaltis, and G. T. Sincerbox, Eds., in Springer Series in Optical Sciences. , Berlin, Heidelberg: Springer, 2000, pp. 171–197. doi: 10.1007/978-3-540-47864-5\_10.
- [142] N. U. Dinc, C. Moser, and D. Psaltis, “(3+1)D Printing of Volume Holograms,” in *Digital Holography and 3-D Imaging 2022 (2022)*, paper Tu2A.5, Optica Publishing Group, Aug. 2022, p. Tu2A.5. doi: 10.1364/DH.2022.Tu2A.5.
- [143] A. Grabulosa, X. Porte, E. Jung, J. Moughames, M. Kadic, and D. Brunner, “(3+1)D printed adiabatic 1-to-M broadband couplers and fractal splitter networks,” *Opt. Express*, vol. 31, no. 12, p. 20256, Jun. 2023, doi: 10.1364/OE.486235.
- [144] G. Panusa, N. U. Dinc, and D. Psaltis, “Photonic waveguide bundles using 3D laser writing and deep neural network image reconstruction,” *Opt. Express*, vol. 30, no. 2, p. 2564, Jan. 2022, doi: 10.1364/OE.446775.
- [145] L. Siegle, S. Ristok, and H. Giessen, “Complex aspherical singlet and doublet microoptics by grayscale 3D printing,” *Opt. Express*, vol. 31, no. 3, p. 4179, Jan. 2023, doi: 10.1364/OE.480472.
- [146] N. McKeown *et al.*, “OpenFlow: enabling innovation in campus networks,” *SIGCOMM Comput. Commun. Rev.*, vol. 38, no. 2, pp. 69–74, Mar. 2008, doi: 10.1145/1355734.1355746.
- [147] N. Farrington *et al.*, “Helios: a hybrid electrical/optical switch architecture for modular data centers,” *SIGCOMM Comput. Commun. Rev.*, vol. 40, no. 4, pp. 339–350, Aug. 2010, doi: 10.1145/1851275.1851223.
- [148] M. Stepanovsky, “A Comparative Review of MEMS-Based Optical Cross-Connects for All-Optical Networks From the Past to the Present Day,” *IEEE Communications Surveys & Tutorials*, vol. 21, no. 3, pp. 2928–2946, 2019, doi: 10.1109/COMST.2019.2895817.

- [149] L. Poutievski *et al.*, “Jupiter evolving: transforming google’s datacenter network via optical circuit switches and software-defined networking,” in *Proceedings of the ACM SIGCOMM 2022 Conference*, Amsterdam Netherlands: ACM, Aug. 2022, pp. 66–85. doi: 10.1145/3544216.3544265.
- [150] R. Urata *et al.*, “Mission Apollo: Landing Optical Circuit Switching at Datacenter Scale”.
- [151] D. M. Marom, Y. Miyamoto, D. T. Neilson, and I. Tomkos, “Optical Switching in Future Fiber-Optic Networks Utilizing Spectral and Spatial Degrees of Freedom,” *Proceedings of the IEEE*, vol. 110, no. 11, pp. 1835–1852, Nov. 2022, doi: 10.1109/JPROC.2022.3207576.
- [152] D. M. Marom *et al.*, “Survey of Photonic Switching Architectures and Technologies in Support of Spatially and Spectrally Flexible Optical Networking [Invited],” *J. Opt. Commun. Netw., JOCN*, vol. 9, no. 1, pp. 1–26, Jan. 2017, doi: 10.1364/JOCN.9.000001.
- [153] Y. Xia, T. S. E. Ng, and X. S. Sun, “Blast: Accelerating high-performance data analytics applications by optical multicast,” in *2015 IEEE Conference on Computer Communications (INFOCOM)*, Kowloon, Hong Kong: IEEE, Apr. 2015, pp. 1930–1938. doi: 10.1109/INFOCOM.2015.7218576.
- [154] S. Das *et al.*, “Shufflecast: An Optical, Data-Rate Agnostic, and Low-Power Multicast Architecture for Next-Generation Compute Clusters,” *IEEE/ACM Trans. Networking*, vol. 30, no. 5, pp. 1970–1985, Oct. 2022, doi: 10.1109/TNET.2022.3158899.
- [155] P. Samadi, V. Gupta, J. Xu, H. Wang, G. Zussman, and K. Bergman, “Optical multicast system for data center networks,” *Opt. Express, OE*, vol. 23, no. 17, pp. 22162–22180, Aug. 2015, doi: 10.1364/OE.23.022162.
- [156] J. Li, T. Gan, B. Bai, Y. Luo, M. Jarrahi, and A. Ozcan, “Massively parallel universal linear transformations using a wavelength-multiplexed diffractive optical network,” *AP*, vol. 5, no. 1, p. 016003, Jan. 2023, doi: 10.1117/1.AP.5.1.016003.
- [157] N. K. Fontaine, R. Ryf, H. Chen, D. T. Neilson, K. Kim, and J. Carpenter, “Laguerre-Gaussian mode sorter,” *Nat Commun*, vol. 10, no. 1, Art. no. 1, Apr. 2019, doi: 10.1038/s41467-019-09840-4.
- [158] C. M. Valensise, I. Grecco, D. Pierangeli, and C. Conti, “Large-scale photonic natural language processing.” arXiv, Aug. 29, 2022. doi: 10.48550/arXiv.2208.13649.
- [159] M. Rafayelyan, J. Dong, Y. Tan, F. Krzakala, and S. Gigan, “Large-Scale Optical Reservoir Computing for Spatiotemporal Chaotic Systems Prediction,” *Phys. Rev. X*, vol. 10, no. 4, p. 041037, Nov. 2020, doi: 10.1103/PhysRevX.10.041037.
- [160] O. Kulce, D. Mengü, Y. Rivenson, and A. Ozcan, “All-optical information-processing capacity of diffractive surfaces,” *Light Sci Appl*, vol. 10, no. 1, Art. no. 1, Jan. 2021, doi: 10.1038/s41377-020-00439-9.
- [161] I. Oguz *et al.*, “Programming Nonlinear Propagation for Efficient Optical Learning Machines.” arXiv, Aug. 09, 2022. doi: 10.48550/arXiv.2208.04951.
- [162] Y. Eliezer, U. Ruhmair, N. Wisioł, S. Bittner, and H. Cao, “Exploiting structural nonlinearity of a reconfigurable multiple-scattering system.” arXiv, Aug. 18, 2022. doi: 10.48550/arXiv.2208.08906.
- [163] F. Xia, K. Kim, Y. Eliezer, L. Shaughnessy, S. Gigan, and H. Cao, “Deep Learning with Passive Optical Nonlinear Mapping.” arXiv, Jul. 18, 2023. doi: 10.48550/arXiv.2307.08558.
- [164] M. Yildirim, N. U. Dinc, I. Oguz, D. Psaltis, and C. Moser, “Nonlinear Processing with Linear Optics.” arXiv, Jul. 18, 2023. doi: 10.48550/arXiv.2307.08533.
- [165] C. Denz, *Optical Neural Networks*. Springer Science & Business Media, 2013.
- [166] A. N. Tait *et al.*, “Neuromorphic photonic networks using silicon photonic weight banks,” *Sci Rep*, vol. 7, no. 1, Art. no. 1, Aug. 2017, doi: 10.1038/s41598-017-07754-z.
- [167] C. Gao, P. Gaur, S. Rubin, and Y. Fainman, “Thin liquid film as an optical nonlinear-nonlocal medium and memory element in integrated optofluidic reservoir computer.” arXiv, Jul. 27, 2022. doi: 10.48550/arXiv.2110.03066.
- [168] G. Marcucci, D. Pierangeli, and C. Conti, “Theory of Neuromorphic Computing by Waves: Machine Learning by Rogue Waves, Dispersive Shocks, and Solitons,” *Phys. Rev. Lett.*, vol. 125, no. 9, p. 093901, Aug. 2020, doi: 10.1103/PhysRevLett.125.093901.
- [169] T. Zhou, F. Scalzo, and B. Jalali, “Nonlinear Schrödinger Kernel for Hardware Acceleration of Machine Learning,” *J. Lightwave Technol., JLT*, vol. 40, no. 5, pp. 1308–1319, Mar. 2022.
- [170] M. Yildirim *et al.*, “Nonlinear optical feature generator for machine learning,” *APL Photonics*, vol. 8, no. 10, p. 106104, Oct. 2023, doi: 10.1063/5.0158611.
- [171] O. Kulce, D. Mengü, Y. Rivenson, and A. Ozcan, “All-optical synthesis of an arbitrary linear transformation using diffractive surfaces,” *Light Sci Appl*, vol. 10, no. 1, Art. no. 1, Sep. 2021, doi: 10.1038/s41377-021-00623-5.
- [172] C. Huang *et al.*, “Demonstration of scalable microring weight bank control for large-scale photonic integrated circuits,” *APL Photonics*, vol. 5, no. 4, p. 040803, Apr. 2020, doi: 10.1063/1.5144121.

- 
- [173] J. Spall, X. Guo, T. D. Barrett, and A. I. Lvovsky, "Fully reconfigurable coherent optical vector–matrix multiplication," *Opt. Lett., OL*, vol. 45, no. 20, pp. 5752–5755, Oct. 2020, doi: 10.1364/OL.401675.
- [174] K. H. Wagner and S. McComb, "Optical Rectifying Linear Units for Back-Propagation Learning in a Deep Holographic Convolutional Neural Network," *IEEE J. Select. Topics Quantum Electron.*, vol. 26, no. 1, pp. 1–18, Jan. 2020, doi: 10.1109/JSTQE.2019.2946655.
- [175] H. Xiao, K. Rasul, and R. Vollgraf, "Fashion-MNIST: a Novel Image Dataset for Benchmarking Machine Learning Algorithms." arXiv, Sep. 15, 2017. doi: 10.48550/arXiv.1708.07747.
- [176] Y. Lecun, L. Bottou, Y. Bengio, and P. Haffner, "Gradient-based learning applied to document recognition," *Proceedings of the IEEE*, vol. 86, no. 11, pp. 2278–2324, Nov. 1998, doi: 10.1109/5.726791.
- [177] J. Howard and S. Gugger, "Fastai: A Layered API for Deep Learning," *Information*, vol. 11, no. 2, Art. no. 2, Feb. 2020, doi: 10.3390/info11020108.
- [178] B. Scellier and Y. Bengio, "Equilibrium Propagation: Bridging the Gap between Energy-Based Models and Backpropagation," *Frontiers in Computational Neuroscience*, vol. 11, 2017, Accessed: Oct. 18, 2023. [Online]. Available: <https://www.frontiersin.org/articles/10.3389/fncom.2017.00024>
- [179] D. Loterie, P. Delrot, and C. Moser, "High-resolution tomographic volumetric additive manufacturing," *Nat Commun*, vol. 11, no. 1, p. 852, Dec. 2020, doi: 10.1038/s41467-020-14630-4.
- [180] C. L. Panuski *et al.*, "A full degree-of-freedom spatiotemporal light modulator," *Nature Photonics*, vol. 16, no. 12, pp. 834–842, Dec. 2022, doi: 10.1038/s41566-022-01086-9.
- [181] U. S. Kamilov *et al.*, "Optical Tomographic Image Reconstruction Based on Beam Propagation and Sparse Regularization," *IEEE Transactions on Computational Imaging*, vol. 2, no. 1, pp. 59–70, Mar. 2016, doi: 10.1109/TCI.2016.2519261.
- [182] J. M. Bioucas-Dias and G. Valadao, "Phase Unwrapping via Graph Cuts," *IEEE Transactions on Image Processing*, vol. 16, no. 3, pp. 698–709, Mar. 2007, doi: 10.1109/TIP.2006.888351.
- [183] Y. LeCun *et al.*, "Backpropagation Applied to Handwritten Zip Code Recognition," *Neural Computation*, vol. 1, no. 4, pp. 541–551, Dec. 1989, doi: 10.1162/neco.1989.1.4.541.

# Curriculum Vitae

## Niyazi Ulaş Dinç

E-mail: niyazi.dinc@epfl.ch

Adress: EPFL STI IMT LAPD, BM 4106, CH-1015 Lausanne, Switzerland

### Education

PhD / Dr.: Photonics Thesis advisors: Demetri Psaltis and Christophe Moser	EPF Lausanne – EPFL Lausanne/CH School of Engineering	09.2019 - Present
Master: Microengineering Thesis advisor: Demetri Psaltis	EPF Lausanne – EPFL Lausanne/CH School of Engineering	09.2017 - 08.2019
Bachelor: Physics (Double Major) High honors degree	Middle East Technical University Ankara/TR Faculty of Arts and Science	09.2014 - 06.2017
Bachelor: Electrical and Electronics Engineering (Major) High honors degree	Middle East Technical University Ankara/TR Faculty of Engineering	09.2013 - 06.2017
High School	Bahcesehir High School Istanbul/TR	09.2008 – 06.2013

### Employment

Research Assistant	EPFL, Lausanne/CH Laboratory of Optics (LO) Laboratory of Applied Photonics Devices (LAPD)	09.2019 - Present
Teaching Assistant	EPFL, Lausanne/CH Imaging optics by Demetri Psaltis Deep learning for optical imaging by Demetri Psaltis	09.2019 - Present
Intern	Logitech, Lausanne/CH Compact Optics with Microlens Array and Freeform/Fresnel Surfaces	02.2019 – 08.2019

### Technical skills

Software and programming	Proficient: MATLAB, Python, Pytorch, CUDA, MS Office Basic knowledge: CAD softwares, COMSOL, Meep(FDTD) Mathematica, circuit modeling with computer tools (LTSpice, Multisim, etc.), Hardware description languages
Fabrication	Clean-room experience (such as sputtering, etching, characterization with electron microscopy, etc), 2-photon polymerization (custom and commercial tools such as Nanoscribe), custom Melt-ElectroWriting (MEW) system.
Optical instruments	High experience with optical setups both with CW and pulsed lasers for imaging, off-axis digital holography, and characterization using liquid crystal SLMs, Galvo mirrors, DMDs, high resolution stages, etc.

## Languages

Turkish	Native	
English	Advanced	Fluent in writing and speaking
French	Elementary	Basic words and phrases

## Publications

1. Volume holograms with linear diffraction efficiency relation by (3+1)D printing 2023  
**NU Dinc**, C Moser, D Psaltis  
arXiv preprint arXiv:2310.06350
2. Nonlinear Processing with Linear Optics 2023  
M Yildirim†, **NU Dinc†**, I Oguz, D Psaltis, C Moser  
arXiv preprint arXiv:2307.08533
3. Forward-Forward Training of an Optical Neural Network 2023  
I Oguz, J Ke, Q Wang, F Yang, M Yildirim, **NU Dinc**, JL Hsieh, C Moser, D Psaltis  
Optics Letters 48 (20), 5249-5252
4. From 3D to 2D and back again 2023  
**NU Dinc**, A Saba, J Madrid-Wolff, C Gigli, A Boniface, C Moser, D Psaltis  
Nanophotonics 12 (5), 777-793
5. Programming nonlinear propagation for efficient optical learning machines 2022  
I Oguz, JL Hsieh, **NU Dinc**, U Teğin, M Yildirim, C Gigli, C Moser, D Psaltis  
arXiv preprint arXiv:2208.04951
6. Photonic waveguide bundles using 3D laser writing and deep neural network image Reconstruction 2022  
G Panusa†, **NU Dinc†**, D Psaltis  
Optics Express 30 (2), 2564-2577
7. Direct (3+ 1) D laser writing of graded-index optical elements 2021  
X Porte†, **NU Dinc†**, J Moughames, G Panusa, C Juliano, M Kadic, C Moser, D Brunner, D Psaltis  
Optica 8 (10), 1281-1287
8. Reusability report: Predicting spatiotemporal nonlinear dynamics in multimode fibre optics with a recurrent neural network 2021  
U Teğin, **NU Dinc**, C Moser, D Psaltis  
Nature Machine Intelligence 3 (5), 387-391
9. Optical neural networks: the 3D connection 2020  
**NU Dinc**, D Psaltis, D Brunner  
Photoniques, 34-38
10. Computer generated optical volume elements by additive manufacturing 2020  
**NU Dinc**, J Lim, E Kakkava, C Moser, D Psaltis  
Nanophotonics 9 (13), 4173-4181

† Equally contributing authors

## Conference talks

1. (3+1)D printing of volume holograms. N.U. Dinc, C. Moser, & D. Psaltis, (2022, August). In Holographic Optical Elements and Applications. Optica Digital Holography and Three-Dimensional Imaging Topical Meeting (Cambridge UK).
2. Optimization and 3D printing of waveguide bundles for imaging. N.U. Dinc, G. Panusa, & D. Psaltis, (2022, March). In Optical Fibers and Sensors for Medical Diagnostics, Treatment and Environmental Applications XXII. SPIE Photonics West (San Francisco, USA).
3. Gradient-index volume holograms by 2-photon polymerization. N.U. Dinc, G. Panusa, C., Moser, & D. Psaltis, (2021, August). In Liquid Crystals XXV. SPIE Optics+Photonics (San Diego, USA).
4. Digitally optimized gradient-index optics by additive manufacturing. N.U. Dinc, G. Panusa, C. Moser, & D. Psaltis, (2021, June). In Digital Optical Technologies SPIE (Munich, Germany)
5. 3D printed computer generated volume holograms. N.U. Dinc, J. Lim, E. Kakkava, C. Moser, & D. Psaltis, (2020, August). In Liquid Crystals XXIV. SPIE Optics+Photonics (San Diego, USA).